Doctoral Thesis

Effective kinetic description of non-equilibrium dynamics in small and large collision systems

Author:
Clemens Werthmann

Supervisor & 1st Examiner:
Prof. Dr. Sören Schlichting

2nd Examiner:
Prof. Dr. Nicolas Borghini

A thesis submitted in partial fulfillment of the requirements for the degree of Doctor rerum naturalium

Fakultät für Physik
Universität Bielefeld

November 7, 2022

Gedruckt auf alterungsbeständigem Papier °° ISO 9706

Declaration of Authorship

I, Clemens Werthmann, declare that this thesis titled, "Effective kinetic description of non-equilibrium dynamics in small and large collision systems" and the work presented in it are my own. The thesis has not been previously submitted to any examination office. Only the sources and literature indicated have been used. The results presented in the thesis are largely based on

- V. E. Ambruș, S. Schlichting, and C. Werthmann, "Development of transverse flow at small and large opacities in conformal kinetic theory," Phys. Rev. D, vol. 105, no. 1, p. 014 031, 2022. doi: 10.1103/PhysRevD.105.014031. arXiv: 2109.03290 [hep-ph] [1]
- V. E. Ambruș, S. Schlichting, and C. Werthmann, "Opacity dependence of transverse flow, pre-equilibrium and applicability of hydrodynamics in heavy-ion collisions", in preparation.

Signed: 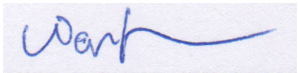

Date: 08.11.2022

Abstract

In current times, the study hadronic collisions is a prominent research field in experimental and theoretical physics. Simulations of hadronic collisions are typically based on a hydrodynamic description that relies on equilibration. But accurate depictions of the early time period or of collisions with few produced particles may require a non-equilibrium description of the dynamics. In this work we describe equilibrium and non-equilibrium effects in hadronic collisions ranging from small to large systems within model descriptions based on kinetic theory and compare to hydrodynamics. We focus on results for cooling due to longitudinal expansion and radial as well as anisotropic flow.

We employ an effective kinetic description, based on the Boltzmann equation in the relaxation time approximation, to study the space-time dynamics and development of transverse flow of small and large collision systems. By combining analytical insights in the small opacity limit with numerical simulations at larger opacities, we are able to describe the development of transverse flow from very small to very large opacities. Suprisingly, we find that deviations between kinetic theory and hydrodynamics persist even in the limit of very large opacities, which can be attributed to the presence of the early pre-equilibrium phase.

For decades hydrodynamics has been used as the main tool for simulating heavy ion collisions, being highly successful in describing their phenomenology. However, a priori it is not clear why this description should be as accurate as it is in simulating a system whose size is not necessarily large compared to the mean free path of its constituents, with possibly sizable local fluctuations involving large gradients and a far-from-equilibrium initial state. A rigorous global examination of possible problems of this description has yet to be performed. In this work, we present our results of comparing hydrodynamic and hybrid simulations to kinetic theory in a simplified dynamical model. We point out inaccuracies of hydrodynamical models and present modified setups that can improve them.

Acknowledgements

Firstly, I would like to thank Sören Schlichting for the opportunity to work in his team, for the continued and detailed scientific advise and supervision of my projects and for pushing me to take on many challenges to expand my scientific capabilities.

I am also thankful to Victor Ambruș, Nicolas Borghini and Hannah Elfner for insightful discussions as well as guidance in scientific matters and carrer planning.

Thanks to my colleagues on the D6/E6 floor and the other members of the "Non-equilibrium QCD" group, especially to my (former) office mates Ismail Soudi, Pragya Singh, Xiaojian Du and Frederik Klette for interesting discussions and for the relaxed pleasant working atmosphere.

Furthermore I would like to thank Gudrun Eickmeyer, Irene Kehler and Susi v. Reder for their assistance with administrative matters.

I am grateful to the CRC-TR 211 for many interesting talks, workshops and colloquia and for the networking and carreer opportunities.

I acknowledge the support by the Deutsche Forschungsgemeinschaft (DFG, German Research Foundation) through the CRC-TR 211 'Strong-interaction matter under extreme conditions'– project number 315477589 – TRR 211, as well as computational resources provided by the Paderborn Center for Parallel Computing (PC2) and the Center for Scientific Computing (CSC) at the Goethe-University of Frankfurt.

Contents

Chapter 1

Introduction

One of the main tasks of modern physics is to assess the question of the makeup of the universe on the most fundamental level, in order to improve the capability of scientific theories to explain why the world behaves the way it does. As this quest has progressed, its objects of interest have become smaller and smaller as they have been found to be made up of more fundamental objects. First, it was discovered that atoms are made up of a bunch of negatively charged electrons surrounding a positively charged atomic core, the nucleus, which are held together via the electromagnetic interaction. The latter has been found to consist of so-called nucleons, which fall into the categories of neutrons and protons. They are bound by a short-range internucleonic force that is mostly attractive but repulsive at very small distances. The contemporary consensus on the most fundamental objects of nature as described in the standard model of particle physics is that elementary particles called quarks and gluons are what makes up nucleons by binding together via the strong interaction, which is described by a non-abelian gauge theory called quantum chromodynamics (QCD). It remains to be seen whether this picture will again be challenged by the discovery of even more elementary building blocks.

As it stands currently, the behaviour of strongly interacting particles is not yet fully understood. This is in part due to the fact that under ordinary circumstances, quarks and gluons can not be observed in their free state due to the binding strength of the strong interaction. However, recent findings have verified that at high temperatures or densities, strongly interacting particles can collectively form a medium in which they can propagate more freely, the so-called Quark Gluon Plasma (QGP). The study of its properties is in the focus of many areas of high energy physics.

Due to the extreme conditions that are required for a QGP to form, it is hard to study it experimentally. The main means to do this is by artificially creating small droplets of QGP in a highly energetic collision of hadronic particles. These take place on very short time and energy scales, such that the QGP cannot be measured directly and information of its properties has to be extracted from the distribution of particles coming from the collision. This requires a large amount of statistics and the extraction of specific observables that can be related to the collective behaviour in the QGP medium, such as anisotropies in the angular distribution of the particle momenta, which is referred to as anisotropic flow. The fact that these collisions undergo a complicated evolution from excited far-from-equilibrium quantum fields over the QGP back to hadronic particles makes the theoretical modelling of this process a complex task, which nevertheless is required to make sense of the measurements. Modern simulation frameworks utilizing different model setups for different stages of the collision are able to extract properties of the created medium by comparing with experimental results [2–6].

The dynamics of the QGP is commonly described in terms of relativistic viscous

hydrodynamics, which provides an accurate description of many of the observed collective phenomena [7–12]. However, hydrodynamics is an effective model that by construction relies on some degree of equilibration of the system it describes. This is certainly not the case in the very early stages of the collision, where the system is very far from equilibrium. Similarly, at late times the expansion will drive it out of equilibrium and render hydrodynamics inapplicable. Thus, it has to be complemented with additional dynamical models describing these stages of the collision. Many recent works have investigated how and on what timescales the system equilibrates to a point where hydrodynamics becomes applicable [13–15] (see also [16, 17] for recent reviews). Theoretical assessments of the early-time stage have led to the discovery of a universal attractor behaviour [18–33], where the time evolution of several quantities related to pressure and energy for different initial conditions quickly collapses to a universal attractor curve. This behaviour is observed in a variety of model descriptions. Still, many of the details are yet unclear.

Another recent topic of interest has been the discovery of anisotropic flow in small collision systems [34–39]. This term refers to collisions with protons or very small ions like hydrogen or helium, as opposed to the so-called large systems, where heavy ions like lead or gold are collided. In hadronic collisions with protons, very few particles are expected to be created which would form a medium that is too dilute to equilibrate and form a QGP phase. Hence, small systems were conceptually understood as a baseline measurement of hadronic collisions without collective effects, that measurements from large systems could be compared to. Theoretical models of p-p collisions often times describe them via high energy physics event generators that are based on the factorization of perturbative QCD [40, 41], which is in sharp contrast to the modelling of heavy ion collisions [42]. Thus, small systems developing anisotropic flow was an unexpected discovery and called for theoretical studies of its origin, which have been performed in a variety of different evolution models [1, 15, 37–39, 43–86].

Both the pre-equilibrium stage of heavy ion collisions as well as the dilute medium in small systems are not necessarily compatible with the theoretical foundation of hydrodynamics, which is based on an expansion around thermal equilibrium. An appropriate alternative dynamical model is kinetic theory, which is a mesoscopic description of the phase space distribution of interacting particles and is therefore less constrained in its applicability to very dilute systems and far-from-equilibrium dynamics. Applications of kinetic theory to heavy ion collisions have been proposed already 30 years ago [87–91] and have been used in different model scenarios to various levels in complexity. This has lead to the development of several simulation codes based on these dynamics, like UrQMD [92], BAMPS [93, 94], AMPT [95], PHSD [96] and SMASH [97]. Based on these codes as well as analytical considerations, also in recent years applications of kinetic theory have been used to gain further insights into many aspects of non-equilibrium dynamics in hadronic collisions.

This work is concerned with employing a simplified version of kinetic theory to describe the time evolution of hadronic collisions from very small to very large systems in order to asses the questions of how collective flow emerges in small systems and how large systems evolve towards hydrodynamic behaviour. In Chapter 2, we provide additional details on the motivation for heavy ion collisions, the experimental setup and the extraction and interpretation of observables. Chapter 3 provides an overview of the theoretical description of the dynamics in heavy ion collisions in kinetic theory and hydrodynamics, including specifications of the modelling choices that were made in this work. We then proceed to the practical part of this work, starting in Chapter 4 with a detailed discussion of the Bjorken flow attractor and how it can be applied to

early times of simulations with transverse expansion. Chapter 5 discusses the development of anisotropic flow and cooling as a function of the size of the collision system, with a comparison to a linearized scheme for small opacities and hydrodynamics at large opacities. While the former provides a very accurate description in its realm of applicability, hydrodynamics is observed to be in disagreement with kinetic theory due to its pre-equilibrium behaviour. Thus in Chapter 6, we go on to perform a more global comparison of the two model descriptions where we present an alternative initialization scheme of hydrodynamics tht can counteract the differences in pre-equilibrium. We also compare with hybrid models using kinetic theory for early time and switching to hydrodynamics at later time. We provide a criterion of when hydrodynamics becomes applicable, which is corroborated by comparing hybrid simulation results at various switching times. In Chapter 7 we provide a global summary of our findings, discuss possible extensions of our work and point out connections to related topics in the current research on heavy ion collisions. There are several Appendices that provide additional details for the results presented in Chapters 5 and 6.

Chapter 2

Studying Heavy Ion Collisions

The introduction has already provided a global overview of the scientific basis of this work. We will now discuss further details of the purpose of heavy ion collisions in general and this work in particular.

2.1 Motivation for HICs

As physics has progressed to study smaller and smaller objects, direct measurements of their internal structure have become impossible. Instead, one has to perform scattering experiments in which a large number of particles are accelerated to high speeds and then collided which each other. The scattering products and their angular distribution then allow to indirectly measure the structure of the colliding particles. The first experiment of this type was Rutherford's scattering experiment [98], where a beam of α-particles was scattered on a thin piece of gold foil. The measured distribution of outgoing particles led to the conclusion that the positive charges in the atom are contained in a small area making up a tiny fraction of its volume: the nucleus.

Nowadays, scattering experiments are one of the main ways to probe models of particle physics. The study of deep inelastic scattering processes, in which a lepton - typically an electron - is scattered off of hadronic particles, has led to a precise picture of the internal structure of a proton. It can be viewed as a collection of pointlike scattering centers of different types, the so-called "partons". The partons have since been found to be different kinds of elementary particles, the quarks and gluons. When probing the proton at different scales, its makeup is also different. This is expressed by the "parton distribution functions" (pdfs) $f_\alpha(x, Q^2)$, which gives for a parton carrying the fraction x of the total momentum of the proton its probability to be of type α. In principle, this also depends on the resolution scale Q^2 of the probing scattering process, however according to the Bjorken scaling argument [99], this dependence drops out at high Q^2 due to the pointlike structure of the partons. Experimental results reveal this behaviour to be approximately true in nature [100], however there are logarithmic corrections to perfect scaling [101–103] due to higher order corrections to the scattering processes. Figure 2.1 shows at a resolution scale $Q^2 = 10$ GeV the proton pdfs for valence up (u) and down (d) quarks, as well as for sea quarks (S) and gluons (g). At small x, the gluon pdf dominates over the others. At these scales, the proton is made up of a fluctuating sea of lots of gluons.

Deep inelastic scattering probes the proton via electroweak interactions. Different insights might be obtained by performing scattering experiments also with two hadrons, which will mainly proceed via the strong interaction. As it turns out, these scatterings have a very rich phenomenology due to the amount and variety of produced

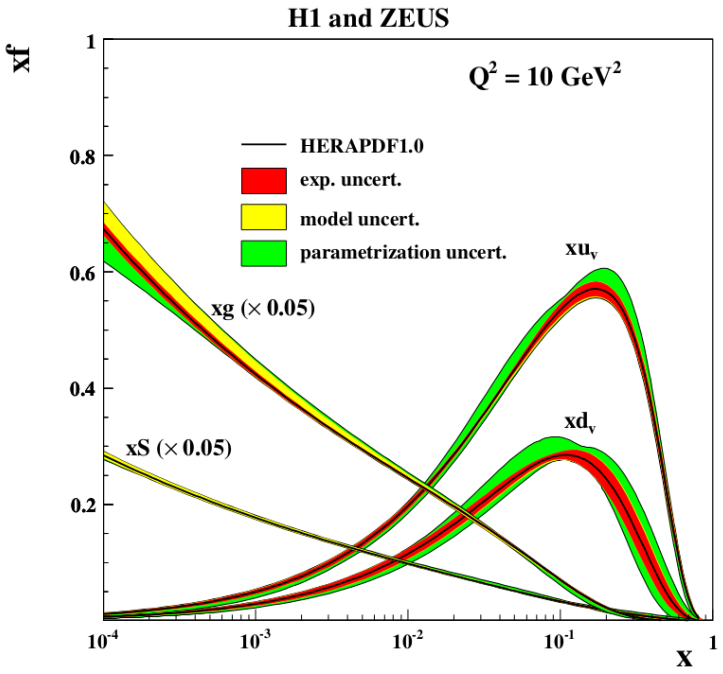

FIGURE 2.1: Plot of the parton distribution functions for the proton as a function of the longitudinal momentum fraction x at a squared probing energy scale of $Q^2 = 10$ GeV^2. The parton types considered here are valence up (u_v) and down (d_v) quarks as well as sea quarks (S) and gluons (g). Figure taken from [104].

particles[1]. When colliding heavy ions, the detectors typically measure thousands of particles coming from a single collision. Naturally, the produced particles will also interact with each other, making it harder to interpret the distributions of outgoing particles. However, these circumstances also allow to study the collective properties of strongly interacting matter, which is rich in possibilities, as described in the following sections of this chapter.

2.2 Heavy Ion Collisions in Experiment

HICs are performed in a large variety of different systems in order to vary several different paramters that govern its behaviour. However, these experimental parameters do not translate directly into parameters of the theoretical description. Instead, one typically adjusts the theoretical parameters in order to reproduce the experimental ones, such that a comparison of theory and experiment can be performed.

By varying the type of ions that are collided, one can adjust the typical number of particles created in a collision and its geometrical properties. For the latter, one can vary the typical spatial extent of the created medium, but also its anisotropy. For example, deformed nuclei will on average produce larger spatial anisotropies in the created medium than spherical ones.

One can adjust the energy of the collision, which is quantified in terms of the center of mass collisional energy $\sqrt{s_{NN}}$ per nucleon-nucleon pair in the colliding nuclei. For larger $\sqrt{s_{NN}}$, one expects a higher temperature of the created medium, but also a

[1] The pdfs are universal and the results from deep inelastic scattering can still be used to describe hard processes in hadronic collisions. However, as will be described shortly, there are other effects that cannot be described as straightforwardly.

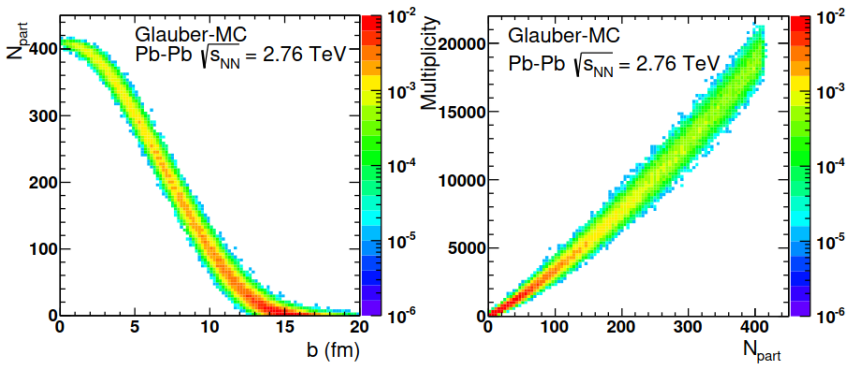

FIGURE 2.2: Heatmap of the probability distribution of simulated Pb-Pb collision events at $\sqrt{s_{NN}} = 2.76$ TeV in terms of two pairs of observables to illustrate the correlation of impact parameter b with number of participants N_{part} and of N_{part} with the event multiplicity. Figure taken from [105].

lower baryon chemical potential. This is because the total baryon number is fixed by the colliding nuclei and at higher energies fewer baryons are stopped in the collision and most of them quickly leave the collision area in directions close to the beam axis.

The difference between theoretical and experimental parameters becomes very apparent when it comes to the impact parameter b. In theoretical descriptions, this is the transverse distance of the centerpoints of the two colliding nuclei, which strongly affects how many nucleons will partake in the collision, how much energy will be deposited in the medium and how anisotropic the medium is. In experiment, nuclei collide at high frequency with random impact parameters that can not be determined in measurements. Instead, the collisions are classified by the number of outgoing particles that are measured in the detector, the so-called multiplicity. This is then re-expressed in terms of the so called "centrality percentile", defined as the fraction of collision events that have an equal or higher number of produced particles than the event in question. The expectation is that events with lower centrality percentile should typically have a smaller impact parameter.

While this quantity does correlate with the impact parameter, the correlation is not perfect. For fixed impact parameter b, one expects a washed-out distribution in multiplicity and vice-versa. This is illustrated by Fig. 2.2, which shows heatmap plots of the probability distributions of simulated collision events in the $b - N_{\text{part}}$ as well as $N_{\text{part}}-$Multiplicity planes for Pb-Pb collisions at $\sqrt{s_{NN}} = 2.76$ TeV. N_{part} is the total number of nuleons in the two nuclei that participate in the collision. In both cases, there is some correlation between the quantities, but the distribution is by no means a narrow line. The quality of this correlation also depends on the type of nuclei that are collided and is worse for smaller nuclei [105]. Hence, one typically considers a coarse-grained parametrization via bins in the centrality percentile, so-called "centrality classes", where all events in a given range of the centrality percentile are grouped together. The analysis is then restricted to statistical statements about the centrality classes.

2.3 Strong interaction

The strong interaction is one of the four known fundamental forces in physics. It binds quarks to bound states like nucleons. The residual forces of the strong interaction are what hold nucleons together in nuclei, similar to how in the case of the electromagnetic interaction, the Van-der-Waals force holds molecules together. The quantum field

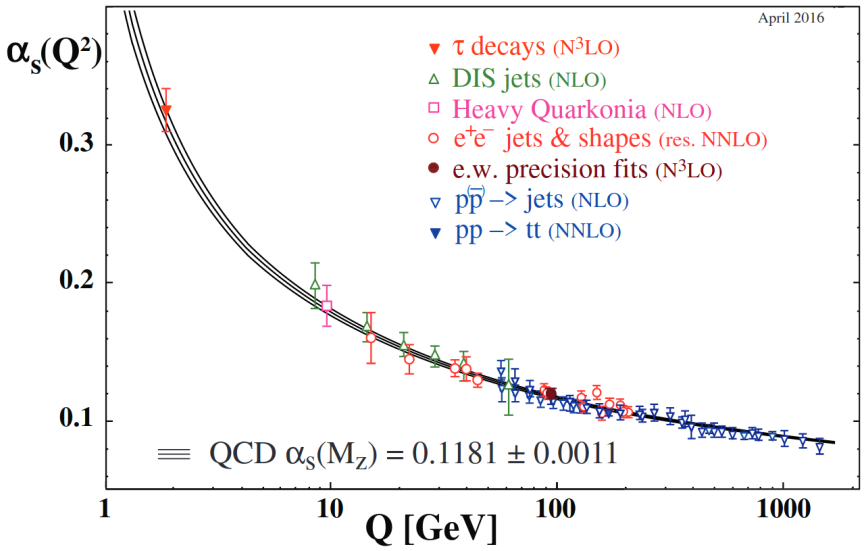

FIGURE 2.3: Plot showing experimental results and a fit curve for the dependence of the strong coupling $\alpha_s = g_s^2/4\pi$ on the energy scale Q of scattering processes. Figure taken from [107]

theory of the strong interaction is called Quantum Chromo Dynamics (QCD). In this theory, the strong interaction is described by an SU(3) gauge interaction of the quark and gluon fields, where the gluons are the gauge bosons. In order to gain a heuristic understanding of the three involved quantum charges, one typically associates them with the colors green, blue and red, hence the name QCD. The bound states of QCD are called hadrons and are made up of multiple quarks that alltogether are color neutral. They can be formed e.g. by a blue and an anti-blue or by a red, a blue and a green quark. Particles made up of two quarks are called mesons, while particles containing three quarks are called baryons.

There are six different quark flavors, which from lightest to heaviest are called up, down, strange, charm, bottom and top. Each of them has three color variants, which form a triplet of the SU(3) gauge group. For the gauge bosons, there are $3^2 - 1 = 8$ possibilities of their color state as given by the generators of SU(3). Additionally, since they are spin-1 particles, there are different possibilities for their spin polarization.

Despite the theoretical model description leading to an explanation for the large variety of observed hadron types, many of the properties of strongly interacting matter remain unclear. This is because the coupling of the strong interaction is typically too large for perturbation theory to be applicable. Hence, it is not straightforward to calculate these properties from the QCD Lagrangian. Non-perturbative ab-initio calculations require to simulate QCD on a lattice in spacetime, which at present is restricted to small net baryon densities. Other than that, QCD at large coupling can only be described in effective model descriptions, such as the linear σ Model [106].

2.4 Quark Gluon Plasma

On ordinary scales of temperature and density, strongly interacting particles occur exclusively in bound states that have a neutral net color charge. This is referred to as confinement of the color charges. The reason is the large size of the strong coupling, which gives rise to non-perturbative behaviour. The force between strongly interacting particles is in fact so strong, that the energy required for separating them is sufficient

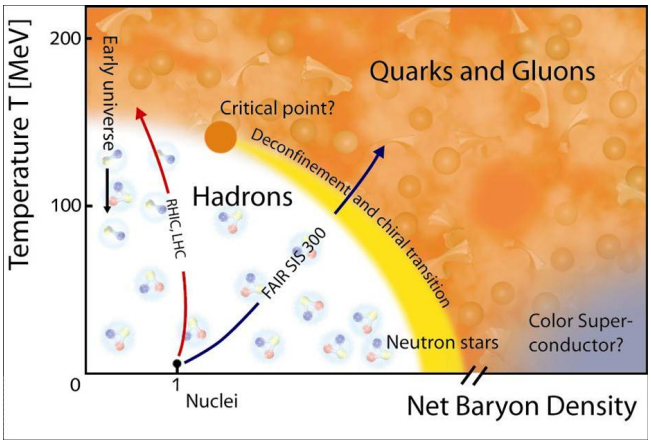

FIGURE 2.4: Sketch of popular conjectures on the structure of the QCD phase diagram in the baryon-density temperature plane. Figure originally taken from the website of the GSI Helmholtzzentrum für Schwerionenforschung (www.gsi.de).

to produce additional strongly interacting particles. Thus, instead of separating color charges, a color neutral bound object will split into two neutral objects and the color charges remain confined.

However, the coupling constant depends on the energy scale of strong interaction processes. This is illustrated by Fig. 2.3, which shows experimental measurements and a fit curve for the size of $\alpha_s = g_s^2/4\pi$ as a function of the negative four-momentum transfer squared Q^2 of the examined scattering processes. On large energy scales, the coupling becomes small and can be treated perturbatively. This phenomenon is referred to as "asymptotic freedom".

For the macroscopic behaviour of a system of strongly interacting matter, this means that the coupling becomes weak at large temperatures or densities. In these cases, particles with color charges are supposed to be able to move freely inside of a thermal medium of strongly interacting matter. This state is called the Quark Gluon Plasma (QGP), because similarly to a plasma of electrons and ions, the quarks and gluons do not form bound states. However, the picture of a very dilute state of matter does not apply to the QGP, as it is essential for its existence to have a dense background medium. The transition from hadronic matter with confined color charges to the QGP is called the "deconfinement phase transition".

The QGP is one of the most recent discoveries of exotic phases of matter and a lot of its properties are still not known in detail. Its experimental, theoretical and phenomenological study is a large and active area of research. One important aspect of this research is to unveil the structure of the QCD phase diagram, which is illustrated schematically in Fig. 2.4. Despite giving a quite detailed view, many of the aspects of this diagram are only conjectured but not known. We do know that strongly interacting matter consists of hadrons at small temperature and density, which transitions to the QGP when increasing temperature or density. Simulations of QCD on the Lattice have shown, that for small chemical potential, the transition is a crossover.

However, in the case of at least three vanishing quark masses, the transition is always first order [108]. More realistic model studies suggest that a first order transition line exists also in the physical case, which ends in a second order critical point. Other predictions about the phase diagram include for example a color superconducting phase at large densities or an inhomogeneous chiral phase inbetween the hadronic and QGP phases.

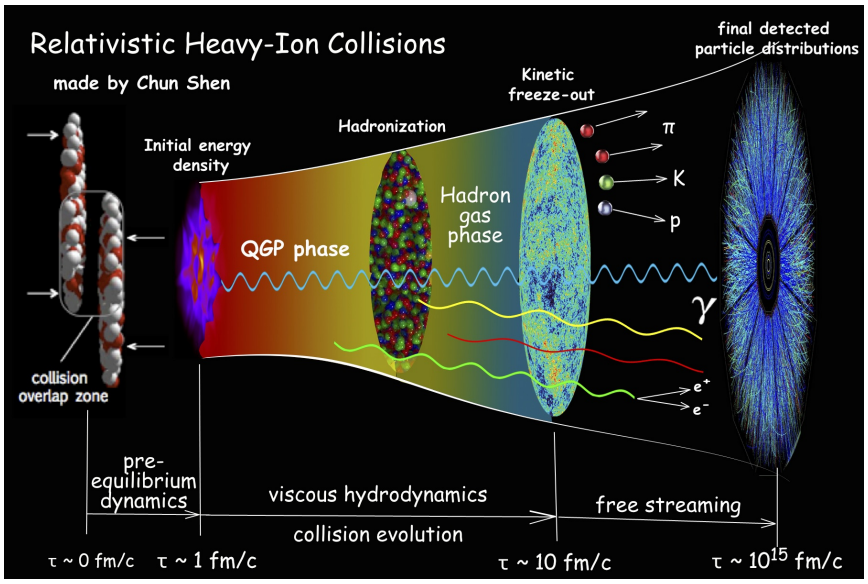

FIGURE 2.5: Illustration of the theoretical modelling of the stages of a heavy ion collision and their time scales. Figure taken from [111].

Another crucial topic in the research of the QGP are its equilibrium and dynamical properties, quantified by equations of state and the so-called transport coefficients. These can be calculated in Lattice QCD[2], but experimental measurements are difficult, as in heavy ion collisions the QGP is created only for a short amount of time and cannot be measured directly. Instead, one has to infer their values by comparing results of simulations with experimental data in a Bayesian analysis framework. Another way to deduce the properties of the QGP is to study neutron stars, which are hypothesised to contain a QGP in their core. By comparing theoretical stability constraints with observed stars, it is possible to extract information on the equations of state at high density and low temperature. It is also possible to extract information on QGP properties from the gravitational wave signal of neutron star mergers.

2.5 Stages of a HIC

In a heavy ion collision, extreme conditions are created on small time- and length scales on the order of 10 fm. During this time, the created medium rapidly transitions through several orders of magnitude in its effective temperature and departure from equilibrium and therefore also different regimes of its dynamical behaviour. Modern simulation setups for the evolution of the system therefore use different model descriptions of the different stages of this evolution, some of which are introduced in more detail in Chapter 3. Fig. 2.5 nicely illustrates these stages.

To start off, an initial state has to be generated. Viewing nuclei as having a static internal structure, the initial condition is motivated purely by the geometric argument of the transverse overlap area and thickness distribution of the two colliding nuclei. However, nuclei are quantum objects, and their internal structure undergoes quantum fluctuations, such that the precise structure at the moment of the collision varies between events. Modern initial state generators typically model these fluctuations in

[2]Technically Lattice QCD only describes the equilibrium state. In order to extract transport coefficients, the close-to-equilibrium behaviour has to be related to the in-equilibrium one in a non-straightforward way [109, 110].

the geometry of the colliding nuclei by randomly sampling hot spots from an average density distribution. Simulations using this type of initial condition are called "event-by-event" simulations. Due to the complex time evolution of the collision, the properties of the initial state are hard to constrain. Hence, there are several different initial state models in use today [112–115] that may vary a lot in the distinct local features of the initial states they produce.

The dynamics at times $\tau \lesssim 1$ fm is typically described by a model based on kinetic theory, a mesoscopic description of the particle distribution in phase space, which typically assumes some degree of diluteness but can describe even systems that are far away from equilibrium. Phenomenologically, it has been shown that the pre-equilibrium stage has a non-negligible influence on final state observables [1, 116, 117] and it is therefore crucial to employ realistic descriptions thereof.

During these early times, the system quickly equilibrates, such that after an evolution time of typically $\tau \sim 1$ fm, the system is further evolved using hydrodynamics, which is the centerpiece of the simulation. In this time, the system forms a strongly interacting close-to-thermal medium, which reflects itself in many of the measured observables like collective flow, jet quenching and quarkonium suppression, as explained in the following subsection.

Eventually, at times $\tau \sim 10$ fm, the medium cools down to the point where color charged particles become confined in hadronic bound states again. In theoretical simulations, at this point a thermal particle distribution is sampled, which is then further propagated in a hadronic transport description based on kinetic theory. In the further evolution, the hadrons scatter among each other and decay into lighter hadrons. Eventually, all hadrons will decay into stable (or long-lived) states and propagate without further interactions.

2.6 How to make sense of the measurements

The detectors placed around the collision points in experimental setups of HICs can only measure the outgoing particles, long after interactions have taken place. On these scales, spatial distances of the particles in that phase can not be resolved. The detectors can only measure the momentum distribution for different species X of produced particles in a collision of the hadrons Y and Z, denoted as $\mathrm{d}N^X_{YZ}/\mathrm{d}^2\mathbf{p}_\perp \mathrm{d}y$. $\mathbf{p}_\perp$ is the momentum in the transverse plane to the beam axis, while y is a measure of the longitudinal momentum. The momentum coordinates used in heavy ion collisions are introduced in more detail in Sec. 3.1. From these distributions, many different observables can be computed that allow more direct insights into the collective behaviour of the particles in the collision.

The type of observable that is studied most extensively are the nuclear modification factors $R^X_{YZ}(\mathbf{p}_\perp, y)$, which are ratios of the distribution of produced particles of type X in collisions of hadrons Y and Z to the same distribution in proton-proton collisions, normalized to the average number N_{YZ} of colliding nucleon pairs in a given centrality class of collisions of Y and Z. This can be mathematically expressed as

$$R^X_{YZ}(\mathbf{p}_\perp, y) = \frac{1}{N_{YZ}} \frac{\frac{\mathrm{d}N^X_{YZ}}{\mathrm{d}^2\mathbf{p}_\perp \mathrm{d}y}}{\frac{\mathrm{d}N^X_{pp}}{\mathrm{d}^2\mathbf{p}_\perp \mathrm{d}y}} \,. \tag{2.1}$$

This ratio quantifies how much the interacting medium that is produced in the collision of Y and Z modifies the particle distribution and therefore measures some aspects

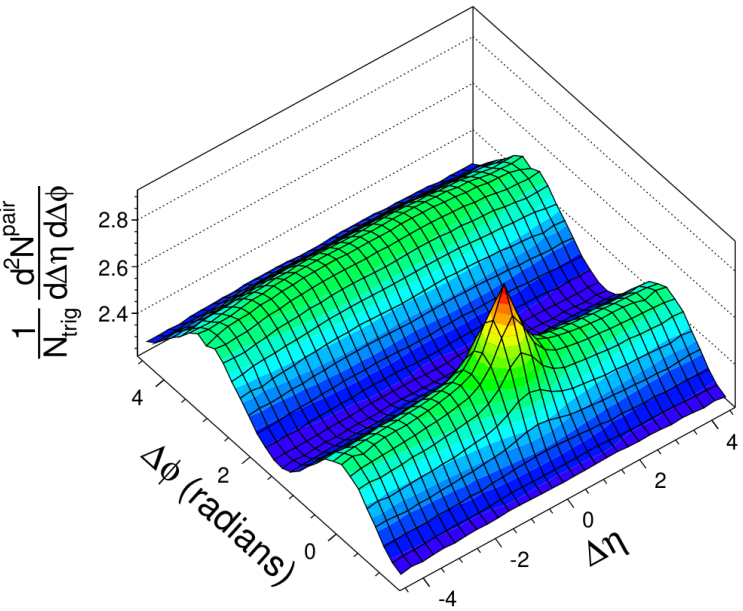

FIGURE 2.6: 2D distribution of pairs of particles in relative azimuthal angle $\Delta\phi$ and relative pseudorapidity $\Delta\eta$ as measured in Pb-Pb collisions at $\sqrt{s_{NN}} = 2.76$ TeV. Figure taken from [118].

of the collective behaviour in a QGP. Some examples of such effects that are studied on the basis of nuclear modification factors are jet quenching and quarkonium suppression.

High-momentum particles carrying a color charge propagate in bunches together with similarly high-momentum particles, which are called jets. These particles lose energy by fragmentation, i.e. by splitting off low-momentum particles. When propagating in a strongly interacting medium, there is additional medium induced radiation and the jet undergoes interactions with the medium which leads to an extra deposition of energy and momentum, such that the jet loses energy at a higher rate compared to propagation in vacuum. This is referred to as jet quenching.

Quarkonia are bound states of a quark and the corresponding anti-quark. Inside of a strongly interacting medium, the binding forces are modified and not as strong as in vacuum. Due to interactions with the medium, the quark-antiquark pair may be split up and separated. This is the explanation for the fact that in the final distribution of particles, heavy ion collisions are observed to produce a lower amount of quarkonia than expected from proton-proton collisions.

Another crucial aspect of the studies of produced particle distributions is their anisotropy in transverse momentum. Fig. 2.6 shows results for the distribution of particle pairs in Pb-Pb collisions at $\sqrt{s_{NN}} = 2.76$ TeV as a function of their difference in longitudinal momentum $\Delta\eta$ and in azimuthal angle $\Delta\phi_p$. The peak at zero difference comes from genuine two-particle correlations such as those between particles coming from the same decay of another particle. However, there is also a more global angular correlation that is approximately independent of $\Delta\eta$. This is commonly referred to as "the ridge". These global momentum anisotropies can be described by the hydrodynamic response of the medium to the geometric properties of the colliding nuclei, which is explained in more detail in Sec. 3.8. Therefore, they are interpreted as another measure of the collective behaviour inside the thermal QGP medium.

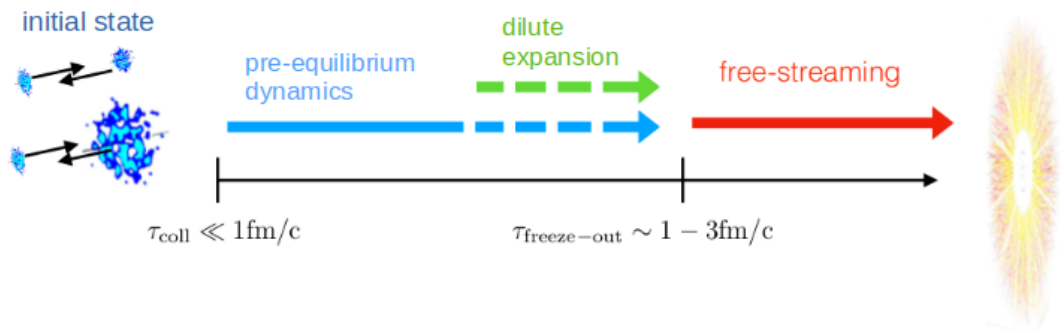

FIGURE 2.7: Sketch of the theoretical modelling framework of small systems showing the different stages and their timescales. Figure taken from [119].

2.7 Small systems

The term small systems refers to collisions involving protons or ions of hydrogen or helium. In these collisions, very few particles are created and it is unlikely that an equilibrated medium could emerge. As illustrated in Fig 2.7 the image of how to describe small systems is different to the case of heavy ion collisions, since due to the presumably low degree of equilibration, hydrodynamics can not be expected to be applicable. Instead, the evolution of the medium has to be fully modelled in a non-equilibrium description. Due to the smaller size, the system will also cool down faster and transition to hadrons at times $\tau \sim 1-3$ fm.

Originally, p-p collisions were considered as a baseline of collisions without collective effects, which one can compare results from other collision systems to, hence many observables are defined as a ratio between nucleus-nucleus and p-p collisions. Indeed, while experiments have found quarkonium suppression in p-A collisions, in p-p collisions they have so far found no conclusive evidence of many in-medium effects such as jet quenching or quarkonium suppression [38]. However, the detection of collective flow effects has challenged this paradigm. Figure 2.8 shows the distribution of particle pairs in relative azimuthal angle $\Delta\phi_p$ and relative longitudinal momentum quantified by $\Delta\eta$ for p-p collisions at a collisional energy of $\sqrt{s_{NN}} = 13$ TeV. While it is much more faint than in the case of Pb-Pb collisions as seen in Fig. 2.6, a global "ridge" also appears in this plot.

It has been in the recent focus of the research field to explain this collective behaviour. Some efforts have been concerned with applying hydrodynamics also for the dynamical description of small systems [43–50, 52–58], which were able to describe experimental results for collective flow in p-A and p-p collisions[37–39]. However, they suffer from poor constraints on the initial condition [53, 59, 60]. More importantly, it remains the question of whether one can reconcile its theoretical foundation with the properties of the medium in small systems. Others have put forward the argument that flow could already be present in the initial state and explored this possibility in Color Glass Condensate descriptions [61–72]. Ultimately, these efforts have resulted in the realization that the model fails to describe important features and that correlations in the initial state are too short-range to account for the phenomenon [73].

An appropriate alternative dynamical model for small systems is kinetic theory, which is a mesoscopic description of the phase space distribution of interacting particles and is therefore less constrained in its applicability to very dilute systems and far-from-equilibrium dynamics. Several efforts have succeeded in describing transverse dynamics and the buildup of transverse flow within this description [1, 74–84], in some

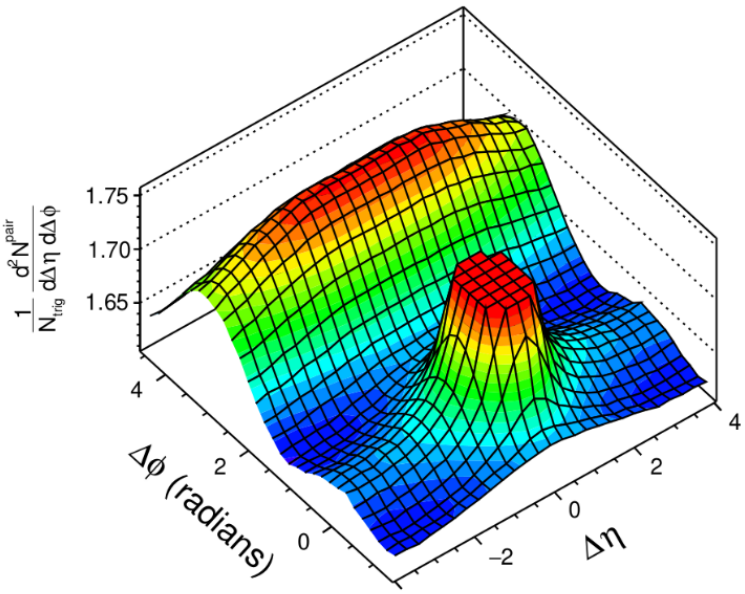

FIGURE 2.8: 2D distribution of pairs of particles in relative azimuthal angle $\Delta\phi$ and relative pseudorapidity $\Delta\eta$ as measured in p-p collisions at $\sqrt{s_{NN}} = 13$ TeV. Figure taken from [120].

cases even with event-by-event simulations [15, 66, 85, 86].

Chapter 3

Dynamical description of hadronic collisions

After giving a general introduction into the topic of hadronic collisions, we will now provide an overview of the theoretical foundation for the model descriptions used in this work. We will use descriptions based on kinetic theory as well as hydrodynamics, which are introduced below. For more detailed discussions and derivations, we refer to textbooks on these topics [121–124].

3.1 Coordinates

As is often the case in physics, the theoretical description of the expaning plasma created in a hadronic collision takes a simpler form if described in a fitting set of coordinates. The set of spatial coordinates $x^\mu = (\tau, \mathbf{x}_\perp, \eta)$ that are commonly used in this context are called Milne coordinates and are defined in the following way. The plane transverse to the particle beam is parametrized via cartesian coordinates $\mathbf{x}_\perp = (x^1, x^2)$. The time x^0 and the longitudinal x^3-coordinate along the beam direction are transformed to the new coordinates

$$\tau = \sqrt{(x^0)^2 - (x^3)^2}\,, \quad \eta = \operatorname{artanh}(x^3/x^0)\,, \tag{3.1}$$

where τ is called the proper time and η is called the spacetime rapidity. For the momentum coordinates, one can define the rapidity

$$y = \operatorname{artanh}(p^3/p^0)\,. \tag{3.2}$$

This definition of the rapidity takes into account only the longitudinal momentum component, which is useful when describing particle collisions. In some other physics contexts, the rapidity is defined alternatively as $w = \operatorname{artanh}(|\vec{p}|/p^0)$.

The benefit of this coordinate system becomes apparent from the behaviour under boosts in the longitudinal direction: these will keep τ invariant and modify η and y by an additive constant, specifically the rapidity of the boost. This behaviour is especially useful when describing a boost-invariant system. Its symmetry simply translates to phase space densities depending only on the difference $y - \eta$, while spatial densities cannot depend on η at all.

In Milne coordinates, the metric becomes

$$g_{\mu\nu} = \operatorname{diag}(1, -1, -1, -\tau^2)\,. \tag{3.3}$$

The corresponding covariant momentum coordinates are $p^\mu = (p^\tau, \mathbf{p}_\perp, p^\eta)$, where $\mathbf{p}_\perp = (p^1, p^2)$ is the cartesian transverse momentum and

$$p^\tau = p_\perp \cosh(y - \eta) \ , \quad p^\eta = \frac{p_\perp}{\tau} \sinh(y - \eta) \ . \tag{3.4}$$

with $p_\perp = |\mathbf{p}_\perp|$. Similarly, we also define $x_\perp = |\mathbf{x}_\perp|$ as well as ϕ_x and ϕ_p as the azimuthal angles in transverse position and momentum space.

3.2 Kinetic theory and the Boltzmann equation

Kinetic theory describes the evolution of the phase space distribution f of particles or quasiparticles, which can be mathematically expressed as

$$f(t, x, p) = (2\pi)^3 \nu \frac{\mathrm{d}N}{\mathrm{d}^3x \mathrm{d}^3p}(t) \ , \tag{3.5}$$

where ν is the number of degrees of freedom, e.g. polarization states, for the given type of particle. Here, f is to be understood as a probability distribution representing the probability to find a particle in the phase space volume element $\mathrm{d}^3x\mathrm{d}^3p$, meaning that kinetic theory does not deal with exact microscopic states of the system but with a statistical description thereof.

Depending on the context, one may also introduce multiple different phase space distributions f_i to distinguish multiple particle types labelled by i. In this work, we will describe massless bosonic degrees of freedom, which could technically be distinguished into different particle types according to their associated quantum charges. However, we will use a simplified model of the time evolution that treats all particle types in the same way. Therefore, we do not need to distinguish them and instead describe them via an average distribution

$$f(t, x, p) = \frac{(2\pi)^3}{\nu_{\text{eff}}} \frac{\mathrm{d}N}{\mathrm{d}^3x \mathrm{d}^3p} \tag{3.6}$$

where "N" now counts all particle types and the factor $\frac{1}{\nu_{\text{eff}}}$ indicates the average over particle types by dividing by the effective number of degrees of freedom.

The time evolution of the phase space distribution f is described by the Boltzmann equation. Its relativistic formulation is given as

$$\left(p^\mu \partial_\mu + m \frac{\partial}{\partial p^\mu} K^\mu \right) f = C[f] \ . \tag{3.7}$$

This equation contains three terms describing different sources of changes in f. $p^i \partial_i f$ describes changes due to the movement of particles according to their momenta. $m\partial/\partial p^\mu (K^\mu f)$ describes the reaction of the system to external forces K^μ, which change the momenta of the particles. In many model descriptions such as the one we will use in this work, external forces can be neglected and this term is dropped. Finally, $C[f]$ is called the collision kernel or collision integral and encodes changes due to the interaction of the particles described by the phase space distribution f. The specific form of $C[f]$ is a choice of physics modelling. Particle interactions can be described for example by scatterings of hard spheres, by scattering crosssections obtained from transition amplitudes that can be computed in more fundamental models like a non-equilibrium quantum field theoretical description of QCD, or by an effective model that approximates the effect of the microscopic dynamics. It is a functional of

f, making the Boltzmann equation an integro-differential equation for f. Typically, the interactions encoded in the collision kernel drive the system to equilibrium, and the equilibrium distribution f_{eq} remains unchanged under scatterings, $C[f_{\text{eq}}] = 0$.

Technically the Boltzmann equation can be derived as a special case of more general descriptions. We do not go into further details here, but we state the conditions under which we can accurately approximate the system's dynamics by using the Boltzmann equation.

As the formulation of kinetic theory discussed here describes a particle distribution in phase space with three momentum coordinates, it deals with on-shell particles whose energy is fully determined by their momentum. Strictly speaking, for this picture to be applicable the notion at the very least of quasiparticles has to be sensible, as an arbitrary state of excited quantum fields as might be realized shortly after the collision, before these particles have formed, technically can not be exactly described. Still, this model can be used to obtain at least some approximation of the early time dynamics.

Furthermore, we restrict the model to a one-particle distribution, meaning we neglect n-particle correlations when considering the microscopic scatterings of the particles. One might also consider dynamics of joint distributions of n particles, which can systematically be truncated to distributions of fewer particles. This hierarchy of particle distribution functions is called the BBGKY hierarchy. Here, we truncate this hierarchy already at the one-particle level. Specifically, the underlying assumption is that correlations between particles decay dynamically on timescales that are much shorter than the typical time between interactions. This also means that interactions are assumed to be short-range and involve only two particles at a time. The notion of the collision kernel typically assumes that interactions happen on small time and length scales compared to the typical interparticle distance and can be assumed to be local and instantaneous, in a coarse-grained picture of the particle distribution. In this sense, the Boltzmann equation describes a "dilute gas".

3.2.1 Relaxation Time Approximation

When introducing the Boltzmann equation, we stated that there are different possible modelling choices for the collision kernel $C[f]$. The Relaxation Time Approximation (RTA) falls into the category of effective descriptions of the microscopic scattering dynamics and is often used in practice due to its simple form. In RTA, the collision kernel is approximated as [125, 126]

$$C_{\text{RTA}}[f] = -\frac{p^\mu u_\mu}{\tau_R}(f - f_{\text{eq}}) \,. \tag{3.8}$$

The key feature of this description is the fact that the change of f is proportional to the difference to the local equilibrium distribution f_{eq}, meaning that all deviations from this equilibrium distribution will decay exponentially in a similar way, governed by the relaxation time τ_R. The quantity u^μ appearing in this equation denites the local restframe flow velocity of the collective medium. The factor $p^\mu u_\mu$ simply comes from the fact that Lorentz invariance requires to consider the dynamics of each part of the system in its local restframe.

There are multiple modelling choices for the relaxation time τ_R with different degrees of complexity, some of which even take into account dependencies on the particle momenta [127]. The simplest choice certainly is that of a constant relaxation time.

However, this choice introduces a scale into the system. If we want to describe a conformal system[1], the natural relation of the relaxation time to the local thermodynamic properties is an inverse proportionality to temperature. Within conformal RTA, the shear viscosity is given as $\eta = 4\tau_R P/5$ and the entropy density as $s = 4P/T$, where P is the pressure. These relations can be inverted to fix the prefactor of the relaxation time in terms of the specific shear viscosity η/s as

$$\tau_R = 5\frac{\eta}{s}T^{-1} \,. \tag{3.9}$$

Another object in the RTA collision kernel that allows some freedom of choice is the local equilibrium distribution f_{eq}. Its form should be chosen according to the conserved quantities in the model description, like particle numbers. The local equilibrium distribution is then adjusted to reproduce the same local density of these quantities as the phase space density f and thereby locally depends on f. We will focus on the simplest case, where only energy is conserved and the local equilibrium distribution matches the local effective temperature T of the system. To do this, one first has to establish a sensible notion of temperature for a system that is out of equilibrium. We postpone this discussion to Sec. 3.6.

f_{eq} also depends on the type of particles that are described. When modelling particles that behave classically, it is simply the Boltzmann distribution.

$$f_{\text{eq}} = \exp\left(-\frac{p^\mu u_\mu}{T}\right) \tag{3.10}$$

In the case of fermions resp. bosons, quantum statistics have to be considered and the equilibrium distribution is given as the Fermi-Dirac distribution resp. Bose-Einstein distribution:

$$f_{\text{eq}} = \frac{1}{\exp\left(\frac{p^\mu u_\mu}{T}\right) \pm 1} \,. \tag{3.11}$$

As stated before, we will describe the medium created in a heavy-ion collision by kinetic theory in RTA for bosonic degrees of freedom and hence the equilibrium distribution will be given as the Bose-Einstein distribution. However, the actual QGP in nature has many gluonic and quarkionic constituents. If one is to describe its physical properties as accurately as possible, it is not immediately clear how many bosonic degrees of freedom (ν_{eff}) one should choose the model to have, especially since some particles carry a mass, which does not fit our model description of a conformal system. However, we can certainly choose to reproduce one of the QGPs most defining properties, its equation of state as determined from high temperature Lattice QCD [128, 129]. In our model, the conformal equation of state is given as

$$\epsilon = \nu_{\text{eff}}\frac{\pi^2}{30}T^4 \,, \tag{3.12}$$

so we simply adjust ν_{eff} to reproduce the physical value, which comes out to be $\nu_{\text{eff}} \approx 40$[2].

[1] This means that one assumes that conformal symmetry holds. As we will only deal with implications of this symmetry, we only give a rough idea of what this means. Among other features, conformal symmetry requires scale invariance, such that no extra scales like particle masses can be present. This symmetry holds for $N = 4$ supersymmetric Yang-Mills theory, which is in some ways similar to QCD. This led to the belief that QCD could behave similarly to a conformal field theory.

[2] Specifically, we used $\nu_{\text{eff}} = 40$ in Chapter 5 and $\nu_{\text{eff}} = 42.25$ in Chapter 6

As we will explain in more detail in Section 5.1.2, one can show [80] that in boost-invariant conformal RTA, the time evolution of the system depends only on one single parameter, the opacity $\hat{\gamma}$ defined as

$$\hat{\gamma} = \frac{1}{5\eta/s}\left(\frac{R}{\pi}\frac{30}{\nu_{\text{eff}}\pi^2}\frac{\mathrm{d}E_\perp^0}{\mathrm{d}\eta}\right)^{1/4} , \tag{3.13}$$

where R as introduced in Eq. 3.48 is a measure of the system size in transverse space. The opacity is a measure of the typical size of interaction effects in the system.

Evidently, in RTA the dynamics are radically simplified, which is not always a good approximation. Modelling all non-equilibrium modes to decay in the same way neglects e.g. kinematic constraints of scatterings. For example, in more realistic descriptions, high-energy excitations are more long-lived than low-energy ones. When applying this model to heavy ion collisions, it can only describe the soft bath of excitations, but not localizes hard modes. Jets evolve by splitting into a lot of soft particles and low-$p_\perp$ heavy quarks experience only small changes in momentum via interactions with the medium and undergo a Brownian-like motion. Neither of these two processes can be expected to be well described in RTA. However, in our study we focus on the cooling and flow properties of the system, which are collective effects that are mainly dictated by the soft bath. Hence, we can neglect the dynamics of hard excitations.

3.2.2 Opacity expansion for dilute systems

The Boltzmann equation as an integro-differential equation is in general too complicated to solve analytically. However analytical solutions can be computed in certain special cases, like the free-streaming case of a system without interactions

$$p^\mu \partial_\mu f = 0 , \tag{3.14}$$

where all particles move on straight lines according to their momentum, so in cartesian coordinates the solution is given as

$$f(t,x,p) = f\left(t_0, x - \frac{p}{|p|}(t-t_0), p\right) . \tag{3.15}$$

If one wants to describe a system in the weakly interacting regime close to free-streaming, which corresponds to the limit of small opacities, one may devise an appropriate expansion scheme [74, 75] that allows to find an analytical approximate solution also for this system. To do this, we expand around the free-streaming limit corresponding to zero opacity, denoted as $f^{(0)}$, which satisfies Eq. (3.14). The first order correction $f^{(1)}$ is obtained by approximating the effect of particle collisions by computing the scattering rate from the zeroth order result.

$$p^\mu \partial_\mu f^{(1)} = C[f^{(0)}] \tag{3.16}$$

The simplification of this equation when compared to the full Boltzmann now lies in the fact that $f^{(0)}$ is already known and thus the right-hand-side of the equation is fully determined and just constitutes an inhomogeneous term for the partial differential equation in Eq. (3.14), which can be treated e.g. with the method of Green's functions.

In cartesian coordinates, one obtains the solution

$$f^{(1)}(t,x,p) = \int_{t_0}^{t} \mathrm{d}t' \frac{C[f]}{|p|}\left(t', x - \frac{p}{|p|}(t-t'), p\right) . \tag{3.17}$$

This expansion can be continued by considering in the next step the effect of the scattering rates of the first order solution. However, in practice typically one stops at first order because the exact computation of higher order corrections becomes more complex.

3.3 Hydrodynamics

Relativistic hydrodynamics is an effective macroscopic description based on conservation laws and a gradient expansion scheme around the equilibrium case. When only the conservation of energy and momentum is considered, hydrodynamics describes only the dynamics of the energy-momentum tensor $T^{\mu\nu}$ via the conservation equations

$$\nabla_\mu T^{\mu\nu} = 0 . \tag{3.18}$$

A priori, this is a system of four dynamical equations for a total of ten independent components of $T^{\mu\nu}$, as it is a symmetric 4×4 matrix. In order to find unique solutions, some extra equations have to be provided. This should not be surprising, as clearly, the dynamical behaviour of a fluid depends on its physical properties, as for example honey does not move in the same way as water does. The additional properties of the system have to be supplied in the form of equations that relate the independent components of $T^{\mu\nu}$ to each other.

In order to be able to identify things like the local restframe energy density ϵ or the local flow velocity u^μ, which play a huge role in the decomposition of the energy-momentum tensor, these equations typically have to be defined in a specific reference frame of the fluid, i.e. a specific choice of ho to define the local restframe, or equivalently, a choice of how to define the local flow velocity u^μ. It should be noted that while mathematically this choice is arbitrary, as redefinitions shift the decomposition of $T^{\mu\nu}$ only in the presence of gradients and equilibrium definitions are always the same, however it does have a physical meaning: by choosing a reference frame, one fixes the frame in which the system will equilibrate [130]. A common choice is the Landau frame, which defines the local flow velocity as the flow of energy as expressed by Eq. 3.45, such that energy currents vanish in the local restframe. The energy-momentum tensor can then be decomposed into different tensor structures derived from u^μ. In the Landau frame, this decomposition takes the following form:

$$T^{\mu\nu} = \epsilon u^\mu u^\nu - (P+\Pi)\Delta^{\mu\nu} + \pi^{\mu\nu} . \tag{3.19}$$

The term $u^\mu u^\nu$ projects onto the local flow velocity, and ϵ is the local restframe energy density. $\Delta^{\mu\nu} = g^{\mu\nu} - u^\mu u^\nu$ is a projection onto the orthogonal parts to u^μ, i.e. the spatial directions in the fluid restframe. Thus, $P+\Pi$ is the physical pressure of the system, which is divided into a hydrostatic part P and a dynamical part Π, the so-called bulk pressure. The hydrostatic pressure relates to the local restframe energy density via an equilibrium equation of state $P = P(\epsilon)$, which is one of the additional equations required to close the system of evolution equations. In our work, $P = \epsilon/3$ for a conformal system. The bulk viscous pressure describes the deviation from the hydrostatic pressure due to the movement of the fluid. Finally, the shear stress tensor

$\pi^{\mu\nu}$ is symmetric, traceless and transverse to u^μ. It describes the stress due to velocity differences between neighboring fluid layers.

By construction, hydrodynamics is a coarse-grained macroscopic effective theory, even more so than kinetic theory in RTA, as it discards information on the momentum distribution of microscopic constituents. Hence it has the same limitation of being suited only to describe the soft bulk of the system, which however is sufficient for describing observables related to the collective behaviour. On top of that, by construction its applicability can only be assured for systems that are close to equilibrium. Though "non-hydrodynamic" excitations [80, 131, 132], i.e. non-equilibrium modes that hydrodynamics can not describe, may decay quickly and render hydrodynamics applicable within a fraction of the lifetime of the system, one certainly can not expect it to accurately describe the far-from-equilibrium initial state. Therefore in practice it is only applied after some "hydrodynamization time" has passed, which is typically assumed to be $\mathcal{O}(1\ \mathrm{fm/c})$. The early time behaviour has to be described in a non-equilibrium time evolution, for example with the KøMPøST-code that is discussed in Sec. 3.4.

3.3.1 Ideal hydrodynamics

In ideal hydrodynamics, the system is assumed to always be in equilibrium. Microscopically, this assumption means that particle interactions are so frequent, that in response to any macroscopic change of the system's state due to fluid motion, they immediately bring the system into the new associated equilibrium state, i.e. the interaction rate is assumed to be infinite. For the different components of the energy-momentum tensor, the assumption of equilibrium means that the pressure is always fully determined by the equation of state, i.e. the bulk pressure vanishes, and that the system is fully isotropic and there is no shear stress. Thus, the energy-momentum tensor is fully determined by ϵ, P and u^μ,

$$T^{\mu\nu} = \epsilon u^\mu u^\nu - P\Delta^{\mu\nu} \,, \tag{3.20}$$

and therefore contains only five independent components. Together with the equation of state $P = P(\epsilon)$, the conservation equations (3.18) now constitute a closed set of evolution equations.

3.3.2 Viscous hydrodynamics

In viscous hydrodynamics, the quantities Π and $\pi^{\mu\nu}$ are nonzero. Here one no longer assumes that the microscopic state of the system can immediately respond to changes due to fluid motion and Π as well as $\pi^{\mu\nu}$ are determined in terms of gradients of the flow velocity u^μ. Conceptually, one collects all independent scalar resp. traceless symmetric transverse tensor structures that can be formed with these gradients. There are different "orders" of viscous hydrodynamics, which refers to the order to which one performs the expansion in gradients. In the case of the simplest first order hydrodynamics, sometimes referred to as Navier-Stokes hydrodynamics due to its non-relativistic counterpart, the bulk pressure and shear stress tensor are given as

$$\Pi = -\zeta\theta = -\zeta\nabla_\mu u^\mu \,, \tag{3.21}$$

$$\pi^{\mu\nu} = 2\eta\sigma^{\mu\nu} = 2\eta\nabla^{\langle\mu}u^{\nu\rangle} = 2\eta\left(\frac{1}{2}\Delta^\mu_\alpha\Delta^\nu_\beta + \frac{1}{2}\Delta^\nu_\alpha\Delta^\mu_\beta - \frac{1}{3}\Delta^{\mu\nu}\Delta_{\alpha\beta}\right)\nabla^\alpha u^\beta \,. \tag{3.22}$$

The bulk viscosity ζ and shear viscosity η are properties of the medium that have to be measured or computed in a more fundamental description of its equilibrium state and then fed into the hydrodynamic equations. Generally, the coefficients that show up in the hydrodynamic expansion scheme are referred to as transport coefficients. In Navier-Stokes hydrodynamics, some excitations violate causality as they propagate faster than the speed of light. Recently, it has been shown that these non-causalities can be eliminated in certain choices of the reference frame [130, 133].But this problem has also led to other formulations of hydrodynamics called Müller-Israel-Stewart hydrodynamics [134–136] that promote Π and $\pi^{\mu\nu}$ to dynamical quantities with their own evolution equations

$$\tau_\Pi \dot{\Pi} + \Pi = -\zeta\theta + \text{extra terms} \,, \tag{3.23}$$

$$\tau_\pi \dot{\pi}^{\langle\mu\nu\rangle} + \pi^{\mu\nu} = 2\eta\sigma^{\mu\nu} + \text{extra terms} \,, \tag{3.24}$$

which introduces the relaxation timescales τ_Π and τ_π for these quantities as additional medium properties. The extra terms are again determined in a gradient expansion scheme according to the type of hydrodynamics that is considered, but can now also depend on Π and $\pi^{\mu\nu}$.

In this work, we will apply second order Müller-Israel-Stewart hydrodynamics for the case of conformal symmetry, which brings simplifications [137] such as vanishing bulk viscous pressure $\Pi \equiv 0$. In this case, the evolution equation for $\pi^{\mu\nu}$ is

$$\tau_\pi \dot{\pi}^{\langle\mu\nu\rangle} + \pi^{\mu\nu} = 2\eta\sigma^{\mu\nu} + 2\tau_\pi \pi_\lambda^{\langle\mu}\omega^{\nu\rangle\lambda} - \delta_{\pi\pi}\pi^{\mu\nu}\theta - \tau_{\pi\pi}\pi^{\lambda\langle\mu}\sigma_\lambda^{\nu\rangle} + \phi_7 \pi_\alpha^{\langle\mu}\pi^{\nu\rangle\alpha} \,, \tag{3.25}$$

where $\omega^{\mu\nu}$ is the vorticity tensor, defined as

$$\omega^{\mu\nu} = \frac{1}{2}(\nabla^\mu u^\nu - \nabla^\nu u^\mu) \,. \tag{3.26}$$

This equation again introduces some more transport coefficients $\delta_{\pi\pi}$, $\tau_{\pi\pi}$ and ϕ_7 . In order to meaningfully compare results from hydrodynamics and kinetic theory in RTA, which is one of the goals of this work, all transport coefficients must be set to those of a system that obeys the dynamical laws of said kinetic theory. The next section briefly explains how to do this.

3.3.3 Obtaining Hydrodynamics from kinetic theory

For this work, only the conceptional relation between kinetic theory and hydrodynamics is important, but not the details. We will therefore give only a rough outline of this connection. The main idea is the following: hydrodynamics is an expansion around equilibrium, which can also be accurately described in a suitable version of kinetic theory. But for the latter, all medium properties are already determined by the properties of the microscopic interactions, i.e. by the collision kernel. Therefore, we can match hydrodynamics to the model description of a given kinetic theory by computing its transport coefficients. Here, "suitable" means that in the kinetic theory description, effects that drive the system out of equilibrium, like e.g. expansion, should be negligible compared to the effect of interactions that drive it towards equilibrium. Mathematically, one writes

$$\left(p^\mu \partial_\mu + m\frac{\partial}{\partial p^\mu}K^\mu\right) f = \frac{1}{\epsilon}C[f] \,, \tag{3.27}$$

such that interaction rates are large when ϵ is small. We can then consider the time evolution of a phase space distribution that slightly deviates from the equilibrium distribution $f^{(0)}_{\mathrm{C-E}} = f_{\mathrm{eq}}$ and expand it in ϵ.

$$f = f^{(0)}_{\mathrm{C-E}} + \epsilon f^{(1)}_{\mathrm{C-E}} + \epsilon^2 f^{(2)}_{\mathrm{C-E}} + ... \tag{3.28}$$

This type of expansion is known as Chapman-Enskog expansion. In this setup, the equilibrium transport properties of the given kinetic theory can be computed. For RTA, the transport coefficients required in the second order viscous hydrodynamics scheme we want to employ take on the values [138–140]

$$\tau_\pi = \tau_R \,, \quad \eta = \frac{4}{5}\tau_R P \,, \quad \delta_{\pi\pi} = \frac{4\tau_R}{3} \,, \quad \tau_{\pi\pi} = \frac{10\tau_R}{7} \,, \quad \phi_7 = 0 \,. \tag{3.29}$$

Generally, when describing any arbitrary system in a kinetic theory model as well as in hydrodynamics matched to that kinetic theory model, one should thus expect that the two descriptions agree whenever interaction rates in the kinetic theory model are large compared to non-equilibrium effects.

3.4 KøMPøST

Since they describe the dynamics of phase space distributions, models based on kinetic theory a priori have more degrees of freedom than effective macroscopic descriptions like hydrodynamics. In order to make these models viable for realistic simulations, some simplifications have to be applied in order to reduce the computational effort. This is especially true in the case of event-by-event heavy ion collision simulations, where it is required to run thousands of simulations in a reasonable amount of time to produce accurate statistics. Since here most of the time evolution can be described in hydrodynamics, it is sufficient to employ a suitable approximate early time description for the pre-equilibrium stage that can subsequently be matched to hydro.

The open-source simulation code KøMPøST [141] implements a linearized non-equilibrium time evolution of the energy-momentum tensor $T^{\mu\nu}$ based on the dynamics of a kinetic theory description. It has been developed as a practical tool for describing the early-time far-from-equilibrium dynamics of heavy ion collisions, where the system has not yet hydrodynamized and a non-equilibrium description is required. The original version of KøMPøST was based specifically on the effective kinetic theory for pure glue QCD [142, 143]. To perform accurate comparisons with the other evolution models used in this paper, a modified version based on the dynamics of RTA was used. For this, we imported the RTA Green's functions calculated in [144]. This version of KøMPøST is available on Github [145].

KøMPøST evolves a given input initial state from an initial time τ_0 to a final time τ in a single propagation step. Conceptionally, the output is expected to describe a hydrodynamized system and can be used as input for a subsequent hydrodynamic evolution model. Since the computation of this step involves linearizations in perturbations around a local average value, KøMPøST has a limited range of applicability in the evolution time.

More specifically, in its default mode with energy perturbations, KøMPøST propagates the energy momentum tensor in the following way: the values at each point $\mathbf{x}$ in the final state are computed from the initial values of $T^{\mu\nu}$ at all causally connected points $\mathbf{x}'$ in the initial state, meaning points that fulfill $|\mathbf{x} - \mathbf{x}'| < c(\tau - \tau_0)$. The energy-momentum tensor is divided into a spatial average of the causal past and

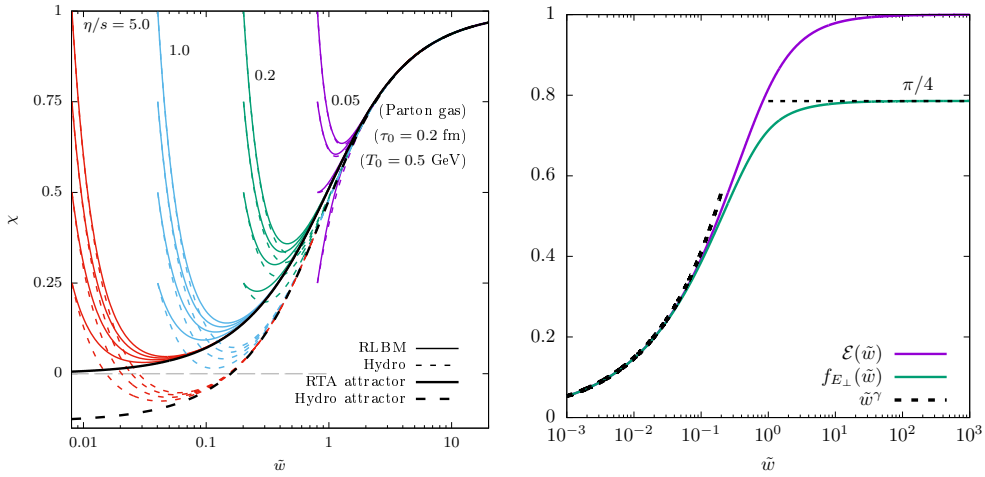

FIGURE 3.1: Approach to the universal attractor curve for the ratio $\chi = P_L/P_T$ of longitudinal and transverse pressure as a function of the scaling variable $\tilde{w} = \frac{T\tau}{4\pi\eta/s}$ for various initial conditions and values of the specific shear viscosity η/s for a parton gas simulated in hydrodynamics and kinetic theory (left) and energy $\mathcal{E}(\tilde{w})$ as well as transverse energy $f_{E_\perp}(\tilde{w})$ attractor curves for RTA kinetic theory (right). Left plot adapted from [146].

perturbations around this average:

$$T^{\mu\nu}_{\mathbf{x}}(\tau_0, \mathbf{x}') = \bar{T}^{\mu\nu}_{\mathbf{x}}(\tau_0) + \delta T^{\mu\nu}_{\mathbf{x}}(\tau_0, \mathbf{x}') \,,$$

where the subscribt $\mathbf{x}$ denotes the fact that the average depends on the position for which the causal past is considered. The average value is evolved according to the laws of Bjorken flow dynamics, assuming local homogeneity in the transverse plane and boost invariance, while the perturbations are propagated in a linear response scheme:

$$\delta T^{\mu\nu}(\tau, \mathbf{x}) = \int \mathrm{d}^2\mathbf{x}' \; G^{\mu\nu}_{\alpha\beta}(\mathbf{x}, \mathbf{x}', \tau, \tau_0) \delta T^{\alpha\beta}_{\mathbf{x}}(\tau_0, \mathbf{x}') \frac{\bar{T}^{\tau\tau}_{\mathbf{x}}(\tau)}{\bar{T}^{\tau\tau}_{\mathbf{x}}(\tau_0)} \,. \tag{3.30}$$

The Green's functions $G^{\mu\nu}_{\alpha\beta}(\mathbf{x}, \mathbf{x}', \tau, \tau')$ have been computed in the respective underlying kinetic theory description and are included in KøMPøST.

Energy perturbations ($\delta T^{\mu\nu}$) can also be switched off, in which case KøMPøST propagates only the average energy-momentum tensor taken over the causal past, as discussed above.

3.5 Bjorken Flow attractor

The dynamics of the medium created in a hadronic collision can be described in many different models with varying degrees of complexity. Bjorken flow is a simplistic model description that assumes boost invariance and homogeneity in the transverse plane, such that the dynamics is restricted to one dimension only. In Bjorken flow, the energy-momentum tensor is diagonal,

$$T^{\mu\nu} = \mathrm{diag}(\epsilon, P_T, P_T, P_L) \,, \tag{3.31}$$

where P_T is the transverse pressure and P_L is the longitudinal pressure. A recent finding of its theoretical treatment is the realization that conformal Bjorken Flow

features a universal attractor behaviour [18–33] across different initial states and even different model descriptions. In particular, for several observables related to pressure and energy, the time evolution curves of different initial states will quickly collapse onto a common attractor curve, if the time dependence is expressed via the conformal scaling variable $\tilde{w}$ defined as

$$\tilde{w} = \frac{T\tau}{4\pi\eta/s} , \tag{3.32}$$

where η/s is the specific shear viscosity of the system and T is its (effective) temperature, which itself depends on time, such that the total time dependence is nonlinear.

The left plot in Figure 3.1 shows this collapsing behaviour of time evolutions for different initial conditions and different specific shear viscosities for the example of the ratio $\chi = P_L/P_T$ in a parton gas described in kinetic theory (solid lines) as well as hydrodynamics (dashed lines). The attractor curves plotted in black have a slightly different early time ($\tilde{w} \ll 1$) behaviour in the two different model descriptions. The early time limit of the curve is $\chi = 0$ for kinetic theory, but in hydrodynamics, it takes a negative value of $\chi = \frac{-23+\sqrt{505}}{4} \approx -0.132$ [31, 147]. The (close-to-)equilibrium behaviour at late times $\tilde{w} \gtrsim 1$ is the same in both descriptions and the curves converge. The fact that longitudinal pressure vanishes at early times was discovered early on after physicist started modelling hadronic collisions in kinetic theory [148], but the attractor behaviour was discovered only recently [20].

Similar attractor curves exist also for energy and transverse energy. The existence of each of these curves is not separate from the others, but rather ties into each other. As an example, following a discussion in [30] we outline how to relate the attractor curve of χ to the one for energy.

As can be derived from energy momentum conservation, Bjorken flow follows the evolution equation

$$\tau\partial_\tau\epsilon = -(\epsilon + P_L) . \tag{3.33}$$

If we rewrite χ to $P_L/\epsilon = \chi/(\chi+2)$ and denote the attractor curve for this quantity as $f(\tilde{w})$, then on this attractor the evolution equation becomes

$$\tau\partial_\tau\epsilon = -\epsilon(1 + f(\tilde{w})) . \tag{3.34}$$

The possibility to write the time derivative of energy as a function of $\tilde{w}$ in this way directly extends also to the temperature, as $T = \text{const.} \times \epsilon^{1/4}$. Since $\tilde{w}$ is defined as a product of time and temperature, this property then allows to rewrite time derivatives to derivatives in $\tilde{w}$:

$$\tau\partial_\tau = a(\tilde{w})\tilde{w}\partial_{\tilde{w}} , \quad a(\tilde{w}) = \frac{3}{4} - \frac{1}{4}f(\tilde{w}) . \tag{3.35}$$

Thus, the existence of the attractor curve for χ also implies the existence of an energy attractor curve, which is the solution of Eq. 3.34 in terms of $\tilde{w}$ and can be obtained by integration.

$$\epsilon(\tilde{w}) = \epsilon(\tilde{w}_0)\exp\left(-\int_{\tilde{w}_0}^{\tilde{w}} \frac{\mathrm{d}\tilde{w}}{\tilde{w}} \frac{1+f(\tilde{w})}{a(\tilde{w})}\right) \tag{3.36}$$

To make the late time equilibrium behaviour manifest, it is useful to consider quantities scaled by a fitting power of time. The attractor curves $\mathcal{E}(\tilde{w}) \propto \tau^{4/3}\epsilon$ and

$f_{E_\perp}(\tilde{w}) \propto \tau^{1/3} \mathrm{d}E_\perp/\mathrm{d}\eta$ for the case of RTA kinetic theory are shown in the right plot of Figure 3.1. They interpolate between a constant in the late time equilibrium case ($\tilde{w} \gg 1$) and a power law $\sim \tilde{w}^\gamma$ for early times ($\tilde{w} \ll 1$). The exponent γ in this power law is model dependent, meaning that different model descriptions feature different pre-equilibrium behaviour of the attractor curve. γ takes on a value of $4/9$ in kinetic theory, which means that $\mathrm{d}E_\perp/\mathrm{d}\eta$ is constant at early times. More generally, it is known that kinetic theory features an early time free-streaming period [26].

We will give a more detailed mathematical description of the attractor curve in Chapter 4, including a discussion of how we apply it to systems with transverse expansion. In Chapters 5 and 6, we will present some results from this discussion, however for an understanding of the conceptual idea the basic explanation provided above is already sufficient.

3.6 Observables

We have discussed how to describe the time evolution of either the phase space density f or the energy-momentum tensor $T^{\mu\nu}$ as the fundamental objects of a given model description. In order to gain a better physical understanding of the state of the system at each point in time, we will derive certain observables from these fundamental quantities that carry specific physical meaning.

As the phase space density is a probability density of microscopic constituents in phase space, it is fairly straightforward to define momentum-integrated totals of local momentum observables $\mathcal{O}(p)$ as

$$\langle \mathcal{O} \rangle \equiv \int \mathrm{d}P f \mathcal{O} \,, \tag{3.37}$$

where $dP = \nu_{\mathrm{eff}} \sqrt{-g} d^3p/[(2\pi)^3 p_0]$ is the generally-covariant integration measure in momentum space. For example, we can compute the transverse energy per unit rapidity and area in transverse space as the total transverse momentum of all particles. Naturally, the total transverse energy per unit rapidity $\mathrm{d}E/\mathrm{d}\eta$ can then be obtained via integration over transverse space $\int_{\mathbf{x}_\perp} \equiv \int \mathrm{d}^2\mathbf{x}_\perp$.

$$\frac{\mathrm{d}E_\perp}{\mathrm{d}\eta \mathrm{d}^2\mathbf{x}_\perp} = \langle p^\tau p_\perp \rangle \quad \Rightarrow \quad \frac{\mathrm{d}E_\perp}{\mathrm{d}\eta} = \int_{\mathbf{x}_\perp} \langle p^\tau p_\perp \rangle \,. \tag{3.38}$$

This observable will play a role in defining the initial state in kinetic theory.

Conversely, we can also integrate over space to obtain the momentum distribution of all particles in the system at fixed proper time τ. in Milne coordinates, the four-volume transformation entails an extra functional determinant for the 3d hypersurface integration at fixed proper time τ, such that

$$\frac{\mathrm{d}N}{\mathrm{d}^2\mathbf{p}_\perp \mathrm{d}y} = \frac{\nu_{\mathrm{eff}}}{(2\pi)^3} \int_{\mathbf{x}_\perp} \int \mathrm{d}\eta \; p_\perp \tau \cosh(y - \eta) \, f \quad . \tag{3.39}$$

As in heavy ion collisions, only the final momentum distributions of particles can be measured, $\mathrm{d}N/\mathrm{d}y\mathrm{d}^2\mathbf{p}_\perp(\tau \to \infty)$ is closely related to experiment and many observables are derived from it. As the distribution is observed to be anisotropic in momentum space, one defines the so-called flow harmonics $v_n(p_\perp)$ as the normalized

Fourier coefficients in the azimuthal angle [149–151].

$$v_n(p_\perp) = \frac{\int \mathrm{d}\phi_p \cos[n(\phi_p - \Psi_n)] \frac{\mathrm{d}N}{\mathrm{d}y\mathrm{d}^2\mathbf{p}_\perp}}{\int \mathrm{d}\phi_p \frac{\mathrm{d}N}{\mathrm{d}y\mathrm{d}^2\mathbf{p}_\perp}} , \quad n \geq 1. \tag{3.40}$$

Ψ_n is the n-th symmetry plane angle defined by the maximum of the n-th harmonic in the spectrum. Alternatively, one can define the flow harmonics with a complex weight $e^{in\phi_p}$ and study the real and imaginary part (or sine and cosine part). In systems without boost symmetry, where the phase space density can depend on y and η independently instead of just on their difference, the flow harmonics v_n may also depend on y.

In practice, depending on the method of how the distributions are obtained, in some cases it might be impossible or at least unreasonably hard to obtain a $p_\perp$-differential theoretical result in the out-of-equilibrium case. Therefore one often considers weighted moments of these functions, e.g. their expectation value under the particle distribution, which we will refer to as the particle-number-weighted flow harmonics v_n^N. In this work, we will mostly consider energy-weighted flow harmonics, defined as

$$v_n^E = \frac{\int_{\mathbf{x}_\perp} \int \frac{d^3p}{(2\pi)^3}\, p_\perp\, e^{in\phi_p}\, f}{\int_{\mathbf{x}_\perp} \int \frac{d^3p}{(2\pi)^3}\, p_\perp\, f} = \frac{\int_{\mathbf{x}_\perp} \left\langle (p^\tau)^2 \sqrt{1-v_z^2} e^{in\phi_p} \right\rangle}{\int_{\mathbf{x}_\perp} \left\langle (p^\tau)^2 \sqrt{1-v_z^2} \right\rangle} , \tag{3.41}$$

If one wants to compare hydrodynamics and kinetic theory, it is convenient to define observables on the basis of the energy-momentum tensor $T^{\mu\nu}$, which is the fundamental dynamical object in hydrodynamics and can be obtained in kinetic theory as

$$T^{\mu\nu} = \langle p^\mu p^\nu \rangle . \tag{3.42}$$

As a substitute for $\mathrm{d}E_\perp/\mathrm{d}\eta$, one may define the integral of the transverse part of the trace of the energy-momentum tensor, $\epsilon_{\mathrm{tr}} \equiv T^{\tau\tau} - \tau^2 T^{\eta\eta} = T^{xx} + T^{yy}$, computed as

$$\frac{\mathrm{d}E_{\mathrm{tr}}}{d\eta} = \tau \int_{\mathbf{x}_\perp} (T^{xx} + T^{yy}), \tag{3.43}$$

which is equal to the actual transverse energy per rapidity $\mathrm{d}E_\perp/\mathrm{d}\eta$ whenever the rapidity component of the particles' momenta is negligible, $p^\eta \simeq 0$. Similarly, as a substitute for the flow harmonics v_n, one may define the ellipticity of the energy flow ϵ_p in terms of the transverse components of the energy-momentum tensor as [152, 153]

$$\epsilon_p e^{2i\Psi_p} = \frac{\int_{\mathbf{x}_\perp} (T^{xx} - T^{yy} + 2iT^{xy})}{\int_{\mathbf{x}_\perp} (T^{xx} + T^{yy})} , \tag{3.44}$$

where Ψ_p is the symmetry plane angle of the elliptic flow ϵ_p. It is harder to define suitable analogues of the other flow harmonics v_n with $n \neq 2$, since according to Eq. 3.42 the energy-momentum tensor depends quadratically on the momentum components p^μ, while v_n depends on a polynomial of the momentum components of degree n, e.g. $v_3 \sim \langle p_x^3 - 3p_x p_y^2 \rangle$ (for $\Psi_3 = 0$). These polynomials are related to the Chebyshev polynomials T_n [154, Ch. 18] fulfilling $\cos(n\phi) = T_n(\cos(\phi))$.

Defining the local restframe as the frame where energy flow vanishes, we can also obtain observables that are defined in this restframe. In this case, the local restframe

energy density ϵ and the local flow velocity u^μ can be determined as the timelike ($u_\mu u^\mu = +1$) eigenvalue and -vector of the energy-momentum tensor $T^{\mu\nu}$:

$$u_\mu T^{\mu\nu} = \epsilon u^\nu \ . \tag{3.45}$$

Now we can also establish the notion of an effective temperature by assuming that ϵ is the energy density that the system would have if it was in equilibrium and employ an equation of state $\epsilon = \epsilon(T)$ to obtain the effective temperature. As already stated in Section 3.2.1, we work with the conformal equation of state

$$\epsilon = \nu_{\text{eff}} \frac{\pi^2}{30} T^4 \ . \tag{3.46}$$

The energy density is often used to quantify the spatial distribution of the system. After normalization, it can be interpreted as a spatial probability distribution. We define the energy-weighted spatial average of observables $O(\tau, \mathbf{x}_\perp)$ by

$$\langle O \rangle_\epsilon (\tau) = \frac{\int_{\mathbf{x}_\perp} O(\tau, \mathbf{x}_\perp)\epsilon(\tau, \mathbf{x}_\perp)}{\int_{\mathbf{x}_\perp} \epsilon(\tau, \mathbf{x}_\perp)} \ . \tag{3.47}$$

This allows to define several observables related to the geometry of the system. Technically, these are mostly used to characterize the initial state at $\tau = \tau_0$, but they can be computed at arbitrary times. We can define the RMS radius of the system as

$$R^2 = \left\langle {\mathbf{x}_\perp}^2 \right\rangle_\epsilon \ . \tag{3.48}$$

As we will not examine its time dependence, in the following we will denote by R the RMS radius of the initial state. Spatial anisotropies of the system are quantified by the eccentricites [155, 156]

$$\epsilon_n e^{in\Psi_n} = -\frac{\left\langle e^{in\phi_x} x_\perp^n \right\rangle_\epsilon}{\left\langle x_\perp^n \right\rangle_\epsilon} \ , \quad n \geq 2 \ , \tag{3.49}$$

where ϵ_n describes the size of modes with n-fold rotational symmetry and takes values between zero and one, while Ψ_n is the n-th symmetry plane angle defined by the direction of the minimum of the corresponding mode. The minus sign is a convention that will be explained in Sec. 3.8.

Going back to the energy-momentum tensor, we can define its equilibrium part in the Landau frame as

$$T^{\mu\nu}_{\text{eq}} = (\epsilon + P)u^\mu u^\nu - P g^{\mu\nu} \ , \tag{3.50}$$

where for this work the pressure is given as $P = \epsilon/3$ for a conformal system. Accordingly, the non-equilibrium part, i.e. the shear stress tensor, is given as

$$\pi^{\mu\nu} = T^{\mu\nu} - T^{\mu\nu}_{\text{eq}} \ . \tag{3.51}$$

The local departure from equilibrium can then be characterized in terms of the inverse Reynolds number,

$$\text{Re}^{-1}(\tau, \mathbf{x}_\perp) = \left[\frac{6\pi^{\mu\nu}(\tau, \mathbf{x}_\perp)\pi_{\mu\nu}(\tau, \mathbf{x}_\perp)}{\epsilon^2(\tau, \mathbf{x}_\perp)} \right]^{1/2} \ . \tag{3.52}$$

With the above normalization, $\mathrm{Re}^{-1} = 1$ when $T^{\mu\nu} = \mathrm{diag}(\epsilon, \epsilon/2, \epsilon/2, 0)$, corresponding to the initial pre-equilibrium free-streaming limit, which is given in more detail in Sec. 3.5. This quantity is reduced whenever there are frequent interactions, but can be increased in expansion, especially in free-streaming. To characterize the average shear in the entire system, we will use the energy-weighted average $\left\langle \mathrm{Re}^{-1} \right\rangle_\epsilon$. Similarly, we will study the average transverse flow velocity given as

$$\langle u_\perp \rangle_\epsilon = \left\langle \left(u_x^2 + u_y^2\right)^{1/2} \right\rangle_\epsilon \tag{3.53}$$

to characterize the rate of transverse expansion.

3.7 Initial state

Of course, dynamical descriptions of hadronic collisions have to be provided with a suitable initial state. However, its form can not be assessed in experiment and has to be computed in a theoretical model description. Technically the features of these models should be tested by comparing simulation results to actual data, but due to the nonlinear time evolution as well as the uncertainties of the actual detailed properties of the QGP medium, the initial state is not well constrained by data. Hence, there are very different models for event-by-event initial states.

Here, we will not go into further detail about the intricacies of initial state models. As we are interested in the typical behaviour of cooling and development of transverse flow at different opacities, we neglect event-by-event fluctuations and consider more well-behaved initial states. In Chapter 5, we will consider an academic form of the initial condition that is not necessarily realistic, but easy to treat in dynamical models. Chapter 6 will deal with a smooth initial condition that was obtained as an average of events. Both will be described in more details in the respective chapters.

One thing that many models of the initial state have in common is that they only provide an initial energy density profile. Despite the fact that kinetic theory describes a distribution in 6D phase space, under reasonable assumptions, the initial state is nevertheless sufficiently determined by specifying $\epsilon(\tau_0, \mathbf{x}_\perp)$, as we will now argue.

At early times, particles can be assumed to have vanishing longitudinal momentum, $p^\eta = 0$. This is the case for the early time attractor of Bjorken flow in kinetic theory, but also emerges in Color Glass Condensate descriptions [157]. Assuming also boost invariance, the initial condition for the phase space distribution takes the form

$$f(\tau_0, \mathbf{x}_\perp, \mathbf{p}_\perp, y - \eta) = \frac{(2\pi)^3}{\nu_{\mathrm{eff}}} \frac{\delta(y - \eta)}{\tau_0 p_\perp} \frac{\mathrm{d}N_0}{\mathrm{d}^2\mathbf{x}_\perp \mathrm{d}^2\mathbf{p}_\perp \mathrm{d}y} \,, \tag{3.54}$$

where the particle density on the right hand side no longer depends on y. Assuming an isotropic distribution in transverse momentum, it also does not depend on ϕ_p. Under the given assumptions, the particle distribution relates to the energy density via

$$\epsilon(\tau_0, \mathbf{x}_\perp) = \frac{1}{\tau_0} \int d^2\mathbf{p}_\perp \; p_\perp \; \frac{\mathrm{d}N_0}{\mathrm{d}^2\mathbf{x}_\perp \mathrm{d}^2\mathbf{p}_\perp \mathrm{d}y} \,. \tag{3.55}$$

Due to the particularly simple nature of RTA, as will be explained in more detail in Sec. 5.1.2, we need not specify the remaining dependence on $p_\perp$ and instead choose to describe a reduced distribution function $\mathcal{F}$ given by

$$\mathcal{F}(\tau, \mathbf{x}_\perp, \phi_p, y - \eta) \propto \int \mathrm{d}p \; p^3 f(\tau, \mathbf{x}_\perp, \mathbf{p}_\perp, y - \eta) \,, \tag{3.56}$$

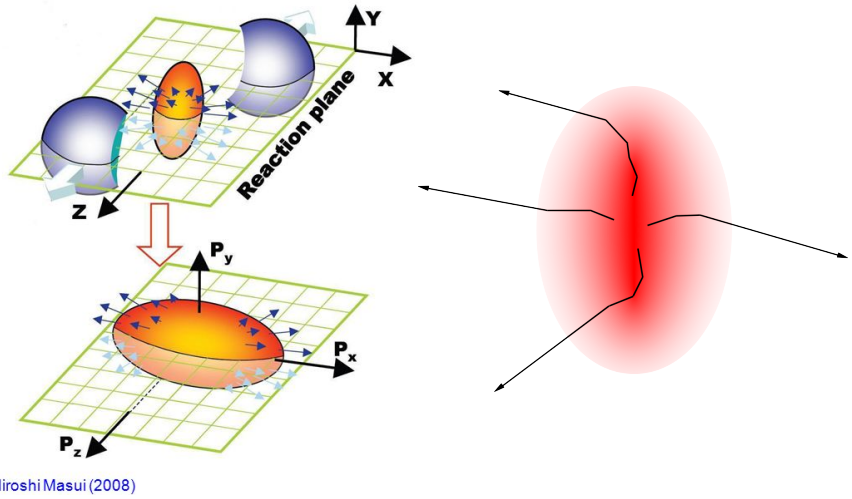

FIGURE 3.2: Sketch of the mechanisms that convert spatial anisotropies in the energy density distribution to momentum anisotropies in the pictures of hydrodynamics (left) and kinetic theory (right). Left Figure taken from [165].

such that at initial time

$$\mathcal{F}(\tau_0, \mathbf{x}_\perp, \phi_p, y - \eta) \propto \delta(y - \eta)\epsilon(\tau_0, \mathbf{x}_\perp) \tag{3.57}$$

3.8 Relation of Eccentricities and Flow

It is well understood that typically, the main source of the measured momentum anisotropies in the final state is the systems collective dynamical response to spatial anisotropies in the initial state [149, 155, 158–160]. Technically, the relation between these anisotropies, as quantified by many kinds of observables even beyond the eccentricities and flow hamonics we discuss here, have been examined in detail by studying their correlations in event-by-event simulations [86, 161–164]. But our work is restricted to idealised initial states, so here, we will only state the underlying conceptional idea, especially when it comes to nonlinear responses.

In the hydrodynamic picture, this relation can be understood as follows [10]. The smaller the systems spatial extent in a given direction, the larger the pressure gradient in that direction. The pressure gradient is what drives the hydrodynamic expansion, i.e. a larger pressure gradient will cause a larger expansion rate. If the spatial extent of the system is initially anisotropic, then during its evolution so will be the expansion rate and therefore also the microscopic momenta of the particles. This is illustrated by the left part of Fig. 3.2.

The relation can also be understood in the microscopic picture of kinetic theory [75]. A particle that is emitted into a direction where the system has a smaller spatial extent, then it is less probable that it will scatter on its path and change directions. Therefore, more particles going into directions of a denser part of the system are scattered into directions of a more dilute part of the system than the other way around, causing the final momentum anisotropy. This mechanism is illustrated by the right schematic in Fig. 3.2.

As discussed in Section 3.6, spatial anisotropies are quantified via the eccentricities ϵ_n and momentum anisotropies are measured as the flow harmonics v_n. Note that in the dynamical process described above, the momentum anisotropy develops maxima in the directions where the spatial distribution had its minima. This is the reason

why the definition of ϵ_n in equation 3.49 contains a minus sign. In this way, typically the v_n and ϵ_n will have the same sign.

The mechanism discussed above describes the immediate response to the intial state. However, the spatial distribution of the system also evolves in time. For example, the anisotropy in expansion rate will at later times have an effect back on the spatial anisotropies of the system. But it is also possible that the initial response couples again to anisotropies in the system and produce higher order responses [163, 164, 166, 167]. One can expect the initial response to be linear in the initial state eccentricities and the "response to the response" to be quadratic. It is also possible that a mixed response to two different initial state eccentricities develops, e.g. a v_5 in response to $\epsilon_2\epsilon_3$. Similarly, there can be even higher order responses that scale with higher powers of the eccentricities. In particular, in addition to the linear response of elliptic flow to initial state ellipticity, there can also be an additional contribution that is cubic in the ellipticity.

Chapter 4

Early Time Attractor in systems with Transverse Dynamics

Before studying the global dynamics in hadronic collisions, we first focus on early times, where the presence of universal behaviour simplifies the dynamics. Understanding this behaviour will provide insights into the results obtained in simulations of the full dynamics.

The attractor behaviour described in Sec. 3.5 a priori only exists in Bjorken flow. However, it turns out that it can also be used as a local early time approximation of the dynamics in systems with transverse expansion. This is because before the onset of transverse expansion, at times $\tau \ll R$, the system's dynamics is dominated by longitudinal expansion and the effects of transverse expansion can be neglected. Under these conditions, at each point in the transverse plane the system evolves independently of the transverse neighbourhood and can locally be described by $0+1$-D longitudinally boost-invariant Bjorken flow. After equilibration during this period, the system always evolves in the same way. And if it is initialized on the attractor, then its entire time evolution is given by the attractor curve. We will describe the features of the attractor scaling solution for both the Müller-Israel-Stewart-type second-order hydrodynamics theory and for conformal kinetic theory in RTA. In Subsection 4.1, the quantities describing the attractor solutions are introduced. Subsection 4.1.1 and 4.1.2 discuss how the pre-equilibrium evolution impacts the observables of interest, highlighting the possible discrepancies between RTA, viscous hydrodynamics and ideal hydrodynamics. Finally, in Subsec. 6.3.2, we discuss how viscous and ideal hydrodynamics can be brought in agreement with RTA at late times by scaling the initial conditions.

4.1 Detailed description of the Bjorken flow attractor

The $0+1$-D Bjorken flow can be described in terms of the Milne coordiantes (τ, x, y, η), with respect to which the velocity becomes $u^\mu \partial_\mu = \partial_\tau$. The energy-momentum tensor takes the diagonal form

$$T^{\mu\nu} = \mathrm{diag}(\epsilon, P_T, P_T, \tau^{-2} P_L), \tag{4.1}$$

where P_T and P_L are the transverse and longitudinal pressures, respectively. The shear-stress tensor also becomes diagonal,

$$\pi^{\mu\nu} = \mathrm{diag}\left(0, -\frac{1}{2}\pi_d, -\frac{1}{2}\pi_d, \frac{1}{\tau^2}\pi_d\right), \tag{4.2}$$

where π_d can be related to P_T and P_L via

$$P_T = P - \frac{\pi_d}{2}, \quad P_L = P + \pi_d, \tag{4.3}$$

such that $\pi_d = \frac{2}{3}(P_L - P_T)$. The observable of interest for the following section are the inverse Reynolds number defined in Eq. (3.52), and the sum $\epsilon_{\rm tr} = T^{xx} + T^{yy}$, which become:

$$\mathrm{Re}^{-1} = -\frac{3\pi_d}{\epsilon}, \qquad \epsilon_{\rm tr} = \frac{2\epsilon}{3} - \pi_d = \frac{2\epsilon}{3}(1 + \mathrm{Re}^{-1}). \tag{4.4}$$

The evolution of the energy density ϵ is governed by the conservation equation $\nabla_\mu T^{\mu\nu}$, where ∇_μ is the covariant derivative, which reduces to

$$\tau\frac{\partial\epsilon}{\partial\tau} + \frac{4}{3}\epsilon + \pi_d = 0. \tag{4.5}$$

In ideal hydrodynamics, $\pi_d = 0$ and $\tau^{4/3}\epsilon(\tau) = \tau_0^{4/3}\epsilon_0$, where ϵ_0 is the energy density at initial time τ_0.

In RTA, the dynamics of π_d is governed directly by the Boltzmann equation. In viscous hydrodynamics, the evolution of π_d can be found from Eq. (3.25) and reads:

$$\tau\frac{\partial\pi_d}{\partial\tau} + \left(\lambda + \frac{4\pi\tilde{w}}{5} + \frac{2\pi\tilde{w}}{5}\phi_7\pi_d\right)\pi_d + \frac{16\epsilon}{45} = 0, \tag{4.6}$$

where $\tilde{w}$ is the conformal parameter,

$$\tilde{w} = \frac{5\tau}{4\pi\tau_\pi} = \frac{\tau T}{4\pi\eta/s}. \tag{4.7}$$

In the above, $s = (\epsilon + P)/T$ is the entropy density for an ultrarelativistic gas at vanishing chemical potential, while $\eta = \frac{4}{5}\tau_\pi P$, as shown in Eq. (3.29). In Eq. (4.6), we introduced the notation

$$\lambda = \frac{\delta_{\pi\pi}}{\tau_\pi} + \frac{\tau_{\pi\pi}}{3\tau_\pi}, \tag{4.8}$$

which evaluates to 38/21 when using the values for the second-order transport coefficients given in Eq. (3.29). We note that in the original MIS theory, λ evaluates to 4/3, while the value 31/15 was advocated in Ref. [31] in order to mimic the early time attractor of RTA.

Equations (4.5) and (4.6) admit scaling solutions with respect to the conformal parameter $\tilde{w}$. To see this, we note that the time derivative of $\tilde{w}$ satisfies

$$\tau\frac{\mathrm{d}\tilde{w}}{\mathrm{d}\tau} = \tilde{w}\left(\frac{2}{3} - \frac{f_\pi}{4}\right), \tag{4.9}$$

where we defined

$$f_\pi = \frac{\pi_d}{\epsilon}. \tag{4.10}$$

Assuming now that f_π depends only on $\tilde{w}$, Eq. (4.6) becomes

$$\tilde{w}\left(\frac{2}{3} - \frac{f_\pi}{4}\right)\frac{\mathrm{d}f_\pi}{\mathrm{d}\tilde{w}} + \frac{16}{45} + \left(\lambda - \frac{4}{3} + \frac{4\pi\tilde{w}}{5} + \frac{2\pi\tilde{w}}{5}\phi_7\epsilon f_\pi - f_\pi\right)f_\pi = 0, \tag{4.11}$$

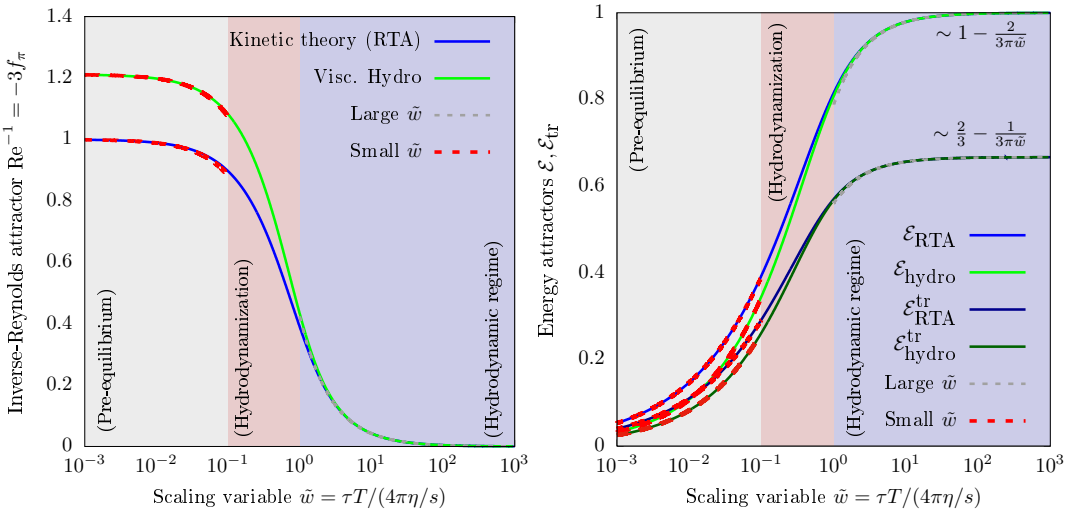

FIGURE 4.1: Attractor curves for the scaling functions (top) Re^{-1} [cf. Eq. (4.4)]; and (bottom) $\mathcal{E}(\tilde{w})$ [upper two curves, light colors, cf. Eq. (4.15)] and $\mathcal{E}_{\rm tr}(\tilde{w})$ [lower two curves, dark colors, cf. Eq. (4.17)], obtained for RTA (blue) and for second-order hydrodynamics (green). The large-$\tilde{w}$ asymptotics are shown with dashed gray curves. The small-$\tilde{w}$ asymptotics are shown with black and red dashed curves for RTA and hydro, respectively.

where $\phi_7\epsilon = 27/70$ evaluates to a constant according to Eq. (3.29). Demanding that f_π remains finite when $\tilde{w} \to 0$, its early-time behavior can be obtained as

$$f_\pi(\tilde{w} \ll 1) = f_{\pi;0} + f_{\pi;1}\tilde{w} + O(\tilde{w}^2) + \ldots, \tag{4.12}$$

where

$$\begin{aligned} f_{\pi;0} =& \frac{1}{2}\left[\lambda - \frac{4}{3} - \sqrt{\left(\lambda - \frac{4}{3}\right)^2 + \frac{64}{45}}\right], \\ f_{\pi;1} =& \frac{\frac{16\pi}{25} f_{\pi;0}^2}{(f_{\pi;0} - \frac{4}{15})^2 + \frac{16}{75}} \left(1 + \frac{1}{2}\phi_7\epsilon f_{\pi;0}\right). \end{aligned} \tag{4.13}$$

When $\lambda = 38/21$, we find $f_{\pi;0} = \frac{1}{105}(25 - 3\sqrt{505}) \simeq -0.404$, which is different from the limit $-1/3$ in kinetic theory[1]. At large values of $\tilde{w}$, $f_\pi(\tilde{w})$ behaves like

$$f_\pi(\tilde{w} \gg 1) = -\frac{4}{9\pi\tilde{w}} + O(\tilde{w}^{-2}), \tag{4.14}$$

which is the leading order gradient expansion [20] and therefore valid in both viscous hydrodynamics and in RTA. Due to the relations in Eq. (4.4), our observable $\mathrm{Re}^{-1} = -3f_\pi$ also exhibits attractor behaviour. Its attractor curve is represented as a function of $\tilde{w}$ in the top panel of Fig. 4.1. Its asymptotic forms at small and large $\tilde{w}$ can be found from Eqs. (4.12) and (4.14), respectively.

[1]Expressing $\lambda = f_{\pi;0} + \frac{4}{3} - \frac{16}{45 f_{\pi;0}}$, it can be seen that $f_{\pi;0} = -1/3$ leads to $\lambda = 31/15$, as pointed out in Ref. [31].

We now turn to the energy equation, Eq. (4.5). On the attractor, when f_π depends only on $\tilde{w}$, it is possible to write (cf. [25, 33])

$$\tau^{4/3}\epsilon(\tau) = \frac{\tau_0^{4/3}\epsilon_0}{\mathcal{E}(\tilde{w}_0)}\mathcal{E}(\tilde{w}), \tag{4.15}$$

where the scaling function $\mathcal{E}(\tilde{w})$ satisfies

$$\tilde{w}\left(\frac{2}{3} - \frac{f_\pi}{4}\right)\frac{\mathrm{d}\mathcal{E}}{\mathrm{d}\tilde{w}} + f_\pi\mathcal{E} = 0. \tag{4.16}$$

Due to Eq. (4.4), $\epsilon_{\rm tr}$ also admits a scaling solution,

$$\tau^{4/3}\epsilon_{\rm tr}(\tau) = \frac{\tau_0^{4/3}\epsilon_0}{\mathcal{E}(\tilde{w}_0)}\mathcal{E}_{\rm tr}(\tilde{w}), \mathcal{E}_{\rm tr}(\tilde{w}) \qquad = \left(\frac{2}{3} - \frac{f_\pi(\tilde{w})}{4}\right)\mathcal{E}(\tilde{w}). \tag{4.17}$$

For $\tilde{w} \ll 1$, $\mathcal{E}(\tilde{w})$ can be obtained as

$$\mathcal{E}(\tilde{w} \ll 1) = C_\infty^{-1}\tilde{w}^\gamma(1 + \mathcal{E}_1\tilde{w} + \dots), \tag{4.18}$$

where the exponent γ and the correction $\mathcal{E}_1$ are given by

$$\gamma = \frac{12 f_{\pi;0}}{3f_{\pi;0} - 8}, \quad \mathcal{E}_1 = -\frac{\frac{32}{3}f_{\pi;1}}{(f_{\pi;0} - \frac{8}{3})^2}. \tag{4.19}$$

The constant C_∞ appearing in Eq. (4.18) is taken such that $\lim_{\tilde{w}\to\infty}\mathcal{E}(\tilde{w}) = 1$, in which case $\mathcal{E}$ has the following late-time asymptotic behavior:

$$\mathcal{E}(\tilde{w} \gg 1) = 1 - \frac{2}{3\pi\tilde{w}}. \tag{4.20}$$

In the case of ideal hydrodynamics, obviously $f_\pi = 0$ (such that $f_{\pi;0} = \gamma = 0$) and $\mathcal{E}(\tilde{w}) = C_\infty = 1$. The functions $\mathcal{E}(\tilde{w})$ and $\mathcal{E}_{\rm tr}(\tilde{w})$ are shown in the bottom panel of Fig. 4.1 for both viscous hydrodynamics and for kinetic theory. The normalization factor C_∞ can be obtained in each theory by computing the attractor curve [25]. For completeness, we list below the values of γ and C_∞ in the relevant theories:

$$\text{RTA}: \qquad \gamma = \frac{4}{9}, \qquad C_\infty \simeq 0.88, \tag{4.21a}$$

$$\text{Visc. Hydro}: \qquad \gamma = \frac{\sqrt{505} - 13}{18}, \qquad C_\infty \simeq 0.82, \tag{4.21b}$$

$$\text{Ideal Hydro}: \qquad \gamma = 0, \qquad C_\infty = 1. \tag{4.21c}$$

Due to the normalization $\lim_{\tilde{w}\to\infty}\mathcal{E}(\tilde{w}) = 1$, the quantities $\tau^{-2/3}\tilde{w}$ and $\tau^{4/3}\epsilon$ can be rewritten as

$$\tau^{-2/3}\tilde{w} = (\tau^{-2/3}\tilde{w})_\infty\mathcal{E}^{1/4}(\tilde{w}), \tag{4.22a}$$

$$\tau^{4/3}\epsilon = (\tau^{4/3}\epsilon)_\infty\mathcal{E}(\tilde{w}), \tag{4.22b}$$

where $(\tau^{-2/3}\tilde{w})_\infty$ and $(\tau^{4/3}\epsilon)_\infty$ represent the corresponding asymptotic, late-time hydrodynamic limits, satisfying

$$(\tau^{-2/3}\tilde{w})_\infty = \frac{(\tau^{4/3}\epsilon)_\infty^{1/4}}{a^{1/4}4\pi\eta/s}, \qquad (\tau^{4/3}\epsilon)_\infty = \frac{\tau_0^{4/3}\epsilon_0}{\mathcal{E}(\tilde{w}_0)}. \tag{4.23}$$

Taking now the initial time such that $\tilde{w}_0 \ll 1$, Eq. (4.18) can be used to obtain

$$(\tau^{4/3}\epsilon)_\infty \simeq C_\infty \left(\frac{4\pi\eta}{s}a^{1/4}\right)^{\gamma} \left(\tau_0^{(\frac{4}{3}-\gamma)/(1-\gamma/4)}\epsilon_0\right)^{1-\gamma/4}. \tag{4.24}$$

Equation (4.24) tells us that the equilibration dynamics introduce a nontrivial relation between energy densities in equilibrium and in the initial state, as the dependence is nonlinear and the exponents depend on the model description, which was one of the main points of Ref. [25].

In the pre-equilibrium regime, $\tilde{w} \ll 1$. Under the early-time approximation (4.18), $\tilde{w}$ can be written in terms of $(\tau^{-2/3}\tilde{w})_\infty$ as

$$\tilde{w} \simeq \tau^{\frac{2}{3}/(1-\gamma/4)} \left[C_\infty^{-1/4}(\tau^{-2/3}\tilde{w})_\infty\right]^{1/(1-\gamma/4)}, \tag{4.25}$$

which allows $\epsilon(\tilde{w} \ll 1)$ to be obtained as

$$\epsilon(\tilde{w} \ll 1) \simeq \tau^{(\gamma-\frac{4}{3})/(1-\gamma/4)} \left[C_\infty^{-1}\left(\frac{4\pi\eta}{s}a^{1/4}\right)^{-\gamma}(\tau^{4/3}\epsilon)_\infty\right]^{1/(1-\gamma/4)}. \tag{4.26}$$

Substituting the expression (4.24) for $(\tau^{4/3}\epsilon)_\infty$ manifestly shows that $\tau^{(\frac{4}{3}-\gamma)/(1-\gamma/4)}\epsilon$ becomes independent of τ as $\tau \to 0$:

$$\epsilon(\tilde{w} \ll 1) \simeq \left(\frac{\tau_0}{\tau}\right)^{(\frac{4}{3}-\gamma)/(1-\frac{\gamma}{4})}\epsilon_0. \tag{4.27}$$

4.1.1 Pre-equilibrium evolution

We now consider a system which is no longer homogeneous in the transverse plane, such that the energy density becomes a function of both τ and $\mathbf{x}_\perp$, $\epsilon \equiv \epsilon(\tau, \mathbf{x}_\perp)$. At early times $\tau \ll R$ we can neglect transverse dynamics and describe the dynamics locally by Bjorken flow (we will discuss early-time transverse expansion effects on the build-up of flow in the Subsec. 4.1.2). Under this approximation, at each point $\mathbf{x}_\perp$ of the transverse plane, we can assume that $\epsilon(\tau, \mathbf{x}_\perp)$ follows an evolution along the attractor curve according to the local value of the conformal variable, $\tilde{w} \equiv \tilde{w}(\tau, \mathbf{x}_\perp)$. Morevoer, we consider that $\tilde{w}_0(\mathbf{x}_\perp) \ll 1$ throughout the system, such that the full pre-equilibrium evolution is captured during the system's evolution.

Neglecting the dynamics in the transverse plane, such that $T^{xx} = T^{yy} = \frac{1}{2}\epsilon_{\rm tr}$, $\mathrm{d}E_{\rm tr}/\mathrm{d}\eta$ defined in Eq. (3.43) can be written as

$$\frac{\mathrm{d}E_{\rm tr}}{\mathrm{d}\eta} = \tau \int_{\mathbf{x}_\perp} \left(\frac{2}{3} - f_\pi\right)\epsilon, \tag{4.28}$$

where Eq. (4.4) was employed to replace $\epsilon_{\rm tr}$ and $f_\pi = -{\rm Re}^{-1}/3$. Using now Eqs. (4.22b) and (4.24) to replace ϵ, we arrive at

$$\frac{{\rm d}E_{\rm tr}}{{\rm d}\eta} = \tau^{-1/3} a \left(\frac{4\pi\eta}{s}\right)^{\gamma} \int_{\mathbf{x}_\perp} \left(\tau_0^{(\frac{4}{3}-\gamma)/(1-\gamma/4)} \frac{\epsilon_0}{a}\right)^{1-\frac{\gamma}{4}} \left(\frac{2}{3} - f_\pi\right) C_\infty \mathcal{E}. \tag{4.29}$$

The above equation can be employed to estimate the evolution of ${\rm d}E_{\rm tr}/{\rm d}\eta$ due solely to longitudinal expansion over the whole range of τ.

At a fixed value of τ, the conformal parameter $\tilde{w}$ spans the interval 0 (reached at infinitely large distances from the system's center of mass) up to the value $\tilde{w}_{\rm max}$ corresponding to the maximum value of the temperature. For sufficiently small values of τ, $\tilde{w}_{\rm max} \ll 1$ and Eqs. (4.12), (4.27) can be used to approximate f_π and ϵ, leading to

$$\frac{{\rm d}E_{\rm tr}}{{\rm d}\eta} \simeq \left(\frac{\tau_0}{\tau}\right)^{\frac{1}{3}(1-9\gamma/4)/(1-\gamma/4)} \frac{{\rm d}E^0_{\rm tr}}{{\rm d}\eta}. \tag{4.30}$$

The above relation shows that in RTA ($\gamma = 4/9$), ${\rm d}E_{\rm tr}/{\rm d}\eta$ remains constant during pre-equilibrium. Conversely, in viscous hydrodynamics, $\gamma > 4/9$ and consequently ${\rm d}E_{\rm tr}/{\rm d}\eta$ increases with time. As expected, in ideal hydrodynamics, ${\rm d}E_{\rm tr}/{\rm d}\eta$ decreases as $\tau^{-1/3}$.

In the limit $\tilde{w} \gg 1$, $f_\pi \sim \tilde{w}^{-1}$ and $\mathcal{E} \simeq 1$, as shown in Eqs. (4.14) and (4.20), such that $\tau^{4/3}\epsilon$ can be approximated by $(\tau^{4/3}\epsilon)_\infty$ by virtue of Eq. (4.22b). Using Eq. (4.24), ${\rm d}E_{\rm tr}/{\rm d}\eta$ reduces to

$$\frac{{\rm d}E_{\rm tr}}{{\rm d}\eta} \simeq \frac{2\tau^{-1/3}}{3} C_\infty \left(\frac{4\pi\eta}{s} a^{1/4}\right)^{\gamma} \tau_0^{\frac{4}{3}-\gamma} \int_{\mathbf{x}_\perp} \epsilon_0^{1-\gamma/4}. \tag{4.31}$$

The above equation shows that at late times, ${\rm d}E_{\rm tr}/{\rm d}\eta$ decrease as $\tau^{-1/3}$. The amount of energy available at a given time τ depends explicitly on the dynamical theory (ideal and viscous hydrodynamics, RTA).

We now consider another important effect arising due to the pre-equilibrium evolution, namely inhomogeneous cooling. During pre-equilibrium, neighbouring points in the transverse plane undergo cooling at differing rates according to their local attractors. As pointed out in Refs. [1, 25], the characteristics of the inhomogeneities in the transverse plane change during pre-equilibrium, as can be seen by looking at the eccentricity ϵ_n, defined as

$$\epsilon_n = -\frac{\displaystyle\int_{\mathbf{x}_\perp} x_\perp^n \epsilon \cos[n(\phi_x - \Psi_n)]}{\displaystyle\int_{\mathbf{x}_\perp} x_\perp^n \epsilon} \tag{4.32}$$

When $\tilde{w} \ll 1$, Eq. (4.27) can be employed to show that $\epsilon_n(\tau) \simeq \epsilon_n(\tau_0)$ and the eccentricities ϵ_n remain constant during pre-equilibrium. When $\tilde{w} \gg 1$, ϵ_n is modified to

$$\epsilon_n \simeq -\frac{\displaystyle\int_{\mathbf{x}_\perp} x_\perp^n \epsilon_0^{1-\gamma/4} \cos[n(\phi_x - \Psi_n)]}{\displaystyle\int_{\mathbf{x}_\perp} x_\perp^n \epsilon_0^{1-\gamma/4}}. \tag{4.33}$$

The above relation shows that inhomogeneous cooling leads to modifications of all eccentricities of the initial profile, except in the case of ideal hydrodynamics ($\gamma = 0$).

The effects of the different behaviour for global and inhomogeneous cooling in

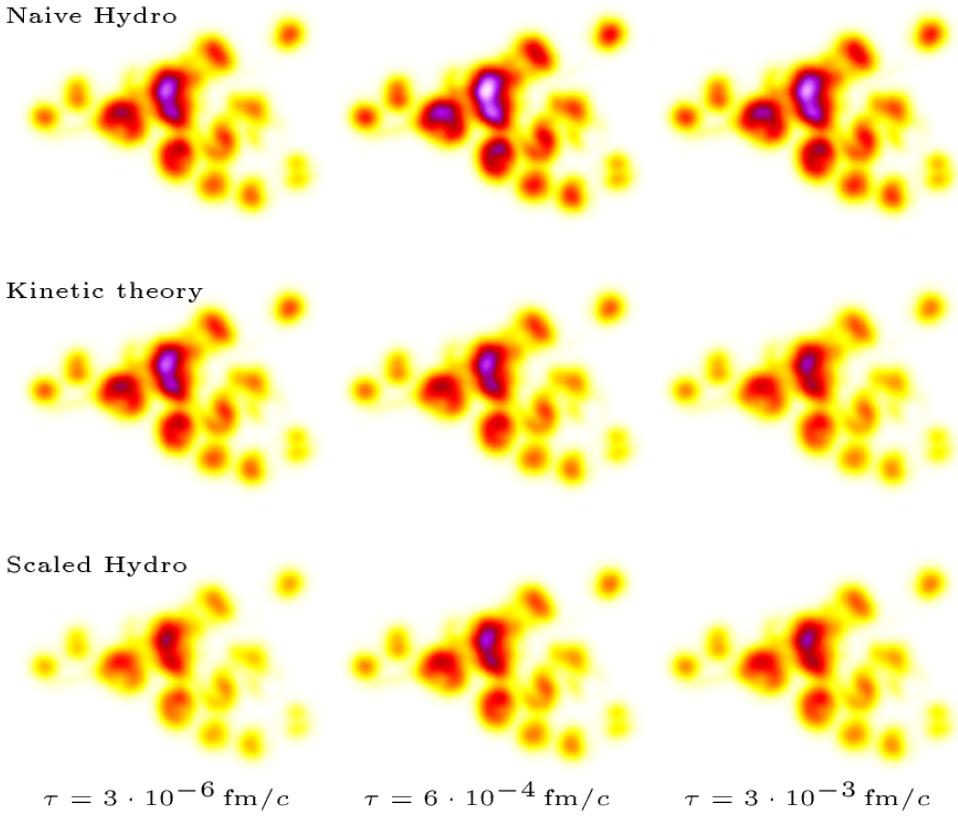

FIGURE 4.2: Early time evolution of the transverse profile of the restframe energy density $\tau\epsilon$ for an example event in the 30-40% centrality class of PbPb collisions in naive viscous hydrodynamics (top), kinetic theory (middle) and scaled viscous hydrodynamics (bottom) at an opacity $4\pi\eta/s = 0.05$.

different model descriptions are illustrated in Fig. 4.2. It shows the pre-equilibrium evolution of the energy density profile multiplied by the Bjorken time, $\tau\epsilon$, for an example event in the 30-40% centrality class of PbPb collisions in kinetic theory and viscous hydrodynamics with either the same or a scaled initial condition. At very early times, this quantity is constant in kinetic theory, but later it decreases slightly due to equilibration. Meanwhile, in hydrodynamics it increases first before transitioning to a decreasing trend. The speed of these transitions in both cases depends on the local temperature, meaning that e.g. the peak values will start decreasing earlier than the values in the outskirts of the system, i.e. the system cools inhomogeneously. After equilibration, the time evolution will uniformly follow the same power law in both models, but the differences due to the different pre-equilibrium evolution will persist. But the knowledge of the local attractor scaling behaviour allows to anticipate the differences between kinetic theory and hydrodynamics and apply a corresponding local scaling prescription to the initial condition of hydro. It then initially takes smaller values than in kinetic theory but dynamically approaches it during pre-equilibrium and reaches agreement after equilibration. This initialization scheme is explained in more detail in Sec. 6.3.2 of Chapter 6 which discusses comparisons of kinetic theory and hydrodynamics.

The local scaling result can also be applied to the more common measure of transverse energy, $\mathrm{d}E_\perp/\mathrm{d}\eta$. While this quantity does not exist in hydrodynamics, a similar scaling law to Eq. 4.15 can be derived in kinetic theory:

$$\tau^{1/3}\frac{\mathrm{d}E_\perp}{d^2\mathbf{x}_\perp \mathrm{d}\eta} = (4\pi\eta/s)^{4/9} a^{1/9} (\epsilon\tau)_0^{8/9}\; C_\infty\; f_{E_\perp}(\tilde{w}) \tag{4.34}$$

where the early time behaviour of $f_{E_\perp}$ is the same as that of $\mathcal{E}$ as longitudinal pressure vanishes, while the late time constant value that it approaches can be deduced from an intregal of the thermal equilibrium distribution.

$$f_{E_\perp}(\tilde{w} \gg 1) = \frac{\pi}{4}\,, \quad f_{E_\perp}(\tilde{w} \ll 1) = C_\infty^{-1}\tilde{w}^{4/9}\,. \tag{4.35}$$

In the same way as e and $\mathrm{d}E_{\mathrm{tr}}/\mathrm{d}\eta$, the total $\mathrm{d}E_\perp/\mathrm{d}\eta$ can be obtained by transverse integration over local Bjorken flows that were propagated on their attractor according to the local value of the scaling variable $\tilde{w}(\tau, \mathbf{x}_\perp)$.

$$\frac{dE_\perp}{d\eta} = \quad \tau^{-1/3}(4\pi\eta/s)^{4/9} a^{1/9} C_\infty \int_{\mathbf{x}_\perp} f_{E_\perp}(\tilde{w}(\tau, \mathbf{x}_\perp))\; (\epsilon\tau)_0^{8/9}(\mathbf{x}_\perp)\,. \tag{4.36}$$

The early and late time behaviour of $f_{E_\perp}$ translate to early and late time behaviour of the integrated quantity $\mathrm{d}E_\perp/\mathrm{d}\eta$ in the cases where the majority of the system (in an energy density weighted sense) resides in the respective limiting cases. For $\hat{\gamma}(\tau/R)^{3/4} \ll 1$, the system is free-streaming and $\mathrm{d}E_\perp/\mathrm{d}\eta$ is constant, while for $\hat{\gamma}(\tau/R)^{3/4} \gg 1$ the majority of the system is in equilibrium and $\mathrm{d}E_\perp/\mathrm{d}\eta \propto \tau^{-1/3}$. The full result for the late time limit is given as

$$\frac{dE_\perp/d\eta}{dE_\perp^0/d\eta} = \frac{9}{8}\left(\frac{4\pi}{5\hat{\gamma}}\right)^{4/9}\left(\frac{R}{\tau}\right)^{1/3} C_\infty f_{E_\perp}(\infty)\,, \tag{4.37}$$

which also means that in Bjorken flow, $\mathrm{d}E_\perp/\mathrm{d}\eta$ decreases with increasing opacity according to a power law $\propto \hat{\gamma}^{-4/9}$.

4.1.2 Pre-flow estimation

We now estimate the build-up of flow during the pre-equilibrium evolution, which we quantify via the observable $\langle u_\perp \rangle_\epsilon$ defined in Eq. (3.53). The basis of our analysis is to consider that the transverse dynamics represent a small perturbation on top of the purely-longitudinal dynamics discussed in Subsecs. 4.1 and 4.1.1, which we consider to be dominant. The idea of this calculation is similar to the one presented in Ref. [168].

At early times $\tau \ll R$, when the transverse flow is negligible, we can write $T^{\mu\nu} = T^{\mu\nu}_B + \delta T^{\mu\nu}$, where $T^{\mu\nu}_B = \mathrm{diag}(\epsilon_B, P_{B;T}, P_{B;T}, P_{B;L})$ is the background (Bjorken) solution of the local, equivalent $0+1$-D system (we also consider that at initial time, $\tilde{w}_0 \ll 1$ throughout the transverse plane). Further assuming that $\delta T^{\mu\nu}$ is small and imposing the Landau frame condition, $T^\mu_\nu u^\nu = \epsilon u^\mu$, we write $u^\mu = u^\mu_B + \delta u^\mu$ and $\epsilon = \epsilon_B + \delta\epsilon$ and find

$$\delta\epsilon = \delta T^{\tau\tau}, \qquad \delta u^i = \frac{\delta T^{\tau i}}{\epsilon_B + P_{B;T}}, \tag{4.38}$$

while $\delta u^\tau = 0$ as required by $u^\mu_B \delta u_\mu = 0$. Thus, the flow build-up can be estimated from the build-up of $\delta T^{\tau i}$.

We can now derive a dynamical equation for $T^{\tau i}$ via the conservation equation $\nabla_\mu T^{\mu\nu} = 0$, which in a general coordinate system reads

$$\nabla_\mu T^{\mu\nu} = \partial_\mu T^{\mu\nu} + \Gamma^\mu{}_{\lambda\mu} T^{\lambda\nu} + \Gamma^\nu{}_{\lambda\mu} T^{\mu\lambda} \,, \tag{4.39}$$

where $\Gamma^\lambda{}_{\mu\nu} = \frac{1}{2} g^{\lambda\rho}(\partial_\nu g_{\rho\mu} + \partial_\mu g_{\rho\nu} - \partial_\rho g_{\mu\nu})$ are the Christoffel symbols. In the Bjorken coordinate system (τ, x, y, η), the only non-vanishing Christoffel symbols are $\Gamma^\tau{}_{\eta\eta} = \tau$ and $\Gamma^\eta{}_{\tau\eta} = \Gamma^\eta{}_{\eta\tau} = \tau^{-1}$, such that the equation for $\nu = i$ becomes:

$$\frac{1}{\tau}\frac{\partial(\tau T^{\tau i})}{\partial\tau} + \partial_j T^{ij} = 0 \,. \tag{4.40}$$

Splitting the energy-momentum tensor into a local Bjorken flow part and a small perturbation as discussed above, we find:

$$\frac{1}{\tau}\frac{\partial(\tau \delta T^{\tau i})}{\partial\tau} + \partial_i P_{B;T} + \partial_j \delta T^{ij} = 0 \,. \tag{4.41}$$

Noting that δT^{ij} represents a higher-order correction, the leading-order contribution to $\delta T^{\tau i}$ can be obtained by solving

$$\frac{\partial(\tau \delta T^{\tau i})}{\partial\tau} \simeq -\tau \partial_i P_{B;T}. \tag{4.42}$$

To leading order, $P_{B;T}$ evolves according to the local Bjorken attractor, such that $P_{B;T} \simeq \epsilon_B \left(\frac{1}{3} - \frac{1}{2} f_{\pi;B}\right)$. Using Eq. (4.22b) to replace ϵ_B, the spatial gradient of $P_{B;T}$ can be obtained as:

$$\frac{\partial_i P_T}{P_T} = \frac{\partial_i (\tau^{4/3}\epsilon)_\infty}{(\tau^{4/3}\epsilon)_\infty} + \left(\frac{\mathcal{E}'}{\mathcal{E}} - \frac{\frac{1}{2} f'_\pi}{\frac{1}{3} - \frac{1}{2} f_\pi}\right) \partial_i \tilde{w}, \tag{4.43}$$

where the prime denotes differentiation with respect to $\tilde{w}$. Here and henceforth, we will drop the B subscript for brevity, keeping in mind that all instances of P_T, ϵ, f_π and the corresponding conformal variable $\tilde{w}$ are evaluated according to the background $0+1$-D Bjorken attractor.

Since $(\tau^{4/3}\epsilon)_\infty$ depends on the transverse coordinates only through the initial

profile [see Eq. (4.24)], the first term on the right-hand side of the above relation evaluates in the limit $\tilde{w}_0 \ll 1$ to

$$\frac{\partial_i(\tau^{4/3}\epsilon)_\infty}{(\tau^{4/3}\epsilon)_\infty} = \left(1-\frac{\gamma}{4}\right)\frac{\partial_i\epsilon_0}{\epsilon_0}. \tag{4.44}$$

The gradient of $\tilde{w}$ appearing in Eq. (4.43) can be written in terms of that of $(\tau^{-2/3}\tilde{w})_\infty$ starting from Eq. (4.22a),

$$\begin{aligned}\frac{\partial_i\tilde{w}}{\tilde{w}} &= \left(1-\frac{\tilde{w}\mathcal{E}'}{4\mathcal{E}}\right)^{-1}\frac{\partial_i(\tau^{-2/3}\tilde{w})_\infty}{(\tau^{-2/3}\tilde{w})_\infty} \\ &= \frac{1}{4}\left(1-\frac{\gamma}{4}\right)\left(1-\frac{\tilde{w}\mathcal{E}'}{4\mathcal{E}}\right)^{-1}\frac{\partial_i\epsilon_0}{\epsilon_0},\end{aligned} \tag{4.45}$$

where the equality on the second line is established using the relations (4.23) and (4.44). Substituting Eqs. (4.44) and (4.45) into Eq. (4.43) gives

$$\frac{\partial_i P_T}{P_T} = \frac{1-\gamma/4}{1-\frac{\tilde{w}\mathcal{E}'}{4\mathcal{E}}}\left(1-\frac{\tilde{w}f_\pi'}{\frac{8}{3}-4f_\pi}\right)\frac{\partial_i\epsilon_0}{\epsilon_0}. \tag{4.46}$$

Substituting Eq. (4.46) in Eq. (4.42) and integrating with respect to τ, we arrive at

$$\delta T^{\tau i} = -\frac{1}{\tau}\left(1-\frac{\gamma}{4}\right)\frac{\partial_i\epsilon_0}{\epsilon_0}\int_{\tau_0}^{\tau} d\tau \frac{\frac{1}{3}-\frac{1}{2}f_\pi-\frac{\tilde{w}}{8}f_\pi'}{1-\frac{\tilde{w}}{4\mathcal{E}}\mathcal{E}'}\tau\epsilon\,. \tag{4.47}$$

Considering now that $\tilde{w} \ll 1$ throughout the system, we can use Eqs. (4.18), (4.12) and (4.27) to approximate $f_\pi \simeq f_{\pi;0} = -(2\gamma/3)/(1-\gamma/4)$, $\mathcal{E} \simeq C_\infty^{-1}\tilde{w}^\gamma$ and $\epsilon = (\tau_0/\tau)^{2-\alpha}\epsilon_0$, where $\alpha = (\gamma+4/3)/[2(1-\gamma/4)]$, which reduces to $\alpha = 2/3$, 1 and 1.071 in ideal hydro, RTA and viscous hydro, respectively. To leading order, we find

$$\tau^{2-\alpha}\delta T^{\tau i} = -\frac{\tau}{2}\left[1-\left(\frac{\tau_0}{\tau}\right)^\alpha\right]\partial_i(\tau_0^{2-\alpha}\epsilon_0), \tag{4.48}$$

which allows the macroscopic velocity to be estimated as

$$\delta u^i(\tilde{w}\ll 1) \simeq -\frac{3\tau}{8}\left(1-\frac{\gamma}{4}\right)\left[1-\left(\frac{\tau_0}{\tau}\right)^\alpha\right]\frac{\partial_i\epsilon_0}{\epsilon_0}. \tag{4.49}$$

As expected, the flow velocity is driven by the gradients of the initial energy density profile. In addition, when $\tau \gg \tau_0$, δu^i exhibits a linear increase with τ, independently of the value of γ. The prefactor governing the overall amplitude of δu^i is however γ-dependent. We can now estimate the early-time evolution of $\langle u_\perp\rangle_\epsilon$, defined in Eq. (3.53), as follows:

$$\langle u_\perp\rangle_{\epsilon,\text{early}} \simeq \frac{3\tau}{8}\left(1-\frac{\gamma}{4}\right)\left[1-\left(\frac{\tau_0}{\tau}\right)^\alpha\right]\left(\int_{\mathbf{x}_\perp}\epsilon_0\right)^{-1}\int_{\mathbf{x}_\perp}|\nabla_\perp\epsilon_0|, \tag{4.50}$$

where $|\nabla_\perp\epsilon_0| = [(\partial_x\epsilon_0)^2+(\partial_y\epsilon_0)^2]^{1/2}$.

In general, the time dependence of the integrand in Eq. (4.47) is too complicated to integrate analytically. But it again takes a simple form in the Bjorken flow equilibrium stage, where $\tau^{4/3}P_{B;T} \simeq \frac{1}{3}(\tau^{4/3}\epsilon)_\infty$. At late times, when the duration of pre-equilibrium is small compared to the elapsed time, its contribution in the time

integration is negligible and $\delta T^{\tau i}$ and δu^i asymptote to

$$\delta T^{\tau i}(\tilde{w} \gg 1) \simeq -\frac{1}{2\tau^{1/3}} \left[1 - \left(\frac{\tau_0}{\tau}\right)^{2/3}\right] \partial_i (\tau^{4/3}\epsilon)_\infty, \tag{4.51a}$$

$$\delta u^i(\tilde{w} \gg 1) \simeq -\frac{3\tau}{8} \left[1 - \left(\frac{\tau_0}{\tau}\right)^{2/3}\right] \frac{\partial_i (\tau^{4/3}\epsilon)_\infty}{(\tau^{4/3}\epsilon)_\infty}, \tag{4.51b}$$

such that $\langle u_\perp \rangle_\epsilon$ becomes

$$\langle u_\perp \rangle_{\epsilon,\text{late}} \simeq \frac{3\tau}{8} \left[1 - \left(\frac{\tau_0}{\tau}\right)^{2/3}\right] \frac{\int_{\mathbf{x}_\perp} |\nabla_\perp \epsilon_0^{1-\gamma/4}|}{\int_{\mathbf{x}_\perp} \epsilon_0^{1-\gamma/4}}. \tag{4.52}$$

Note that the above equation was derived under the assumption that δu^i is small and thus holds only when the system hydrodynamizes before transverse expansion sets in.

Chapter 5

Development of transverse flow at small and large opacities

We will now employ the RTA Boltzmann effective kinetic theory as described in Section 3.2.1 to study the space-time dynamics and development of transverse flow in small and large collision systems. Our simplified setup is introduced and discussed in Section 5.1.1. We perform (semi-)analytic calculations to leading order in opacity in Sec. 5.2 and subsequently in Sec. 5.3 develop two different numerical schemes that allow us to study the evolution of the system all the way from very low to very high opacity. Numerical results are presented in Sec. 5.4, where we analyze the longitudinal cooling and flow response in kinetic theory as a function of opacity and compare it to analogous calculations in ideal and viscous hydrodynamics. Sec. 5.5 provides a short discussion of the results of this Chapter. Appendices A-D contain additional details and explicit expressions for the (semi-) analytic calculations.

5.1 Effective kinetic description of anisotropic flow

5.1.1 Setup

We will describe a boost invariant system with vanishing initial momentum anisotropies via RTA kinetic theory as described in Chapter 3, i.e. we describe the time evolution of the phase space distribution f via

$$p^\mu \partial_\mu f = -\frac{p_\mu u^\mu}{\tau_R}\left[f - f_{eq}\left(\frac{p_\mu u^\mu}{T}\right)\right], \tag{5.1}$$

where we choose a temperature dependent relaxation time

$$\tau_R = \frac{5\eta/s}{T}\,. \tag{5.2}$$

As described in Sec. 3.7, the initial condition we consider is of the form

$$f(\tau_0, \mathbf{x}_\perp, \mathbf{p}_\perp, y-\eta) = \frac{(2\pi)^3}{\nu_{\text{eff}}}\frac{\delta(y-\eta)}{\tau_0 p_\perp}\frac{\mathrm{d}N_0}{\mathrm{d}^2\mathbf{x}_\perp \mathrm{d}^2\mathbf{p}_\perp \mathrm{d}y}, \tag{5.3}$$

which has vanishing longitudinal pressure ($T^\eta_\eta = 0$). Strikingly, it can be shown (c.f. Sec. 5.1.2) that – due to the particularly simple nature of RTA – certain energy weighted observables do not depend on a particular form of the (isotropic) momentum distribution $\frac{\mathrm{d}N_0}{\mathrm{d}^2\mathbf{x}_\perp \mathrm{d}^2\mathbf{p}_\perp \mathrm{d}y}$ [80], and we will therefore not specify it further. Instead the

dynamics is entirely described by the initial energy density distribution, which for the initial conditions in Eq. (5.3) is determined by[1]

$$\epsilon(\tau_0, \mathbf{x}_\perp) = \frac{1}{\tau_0} \int d^2\mathbf{p}_\perp \; p_\perp \; \frac{\mathrm{d}N_0}{\mathrm{d}^2\mathbf{x}_\perp \mathrm{d}^2\mathbf{p}_\perp \mathrm{d}y} \; . \tag{5.4}$$

We take the initial energy density $\epsilon(\tau_0, \mathbf{x}_\perp)$ as a superposition of an isotropic background $\bar{\epsilon}(\tau_0, x_\perp)$ depending only on $x_\perp = |\mathbf{x}_\perp|$ and an anisotropic component $\delta\epsilon(\tau_0, \mathbf{x}_\perp)$, i.e.

$$\epsilon(\tau_0, \mathbf{x}_\perp) = \bar{\epsilon}(\tau_0, x_\perp) + \delta\epsilon(\tau_0, \mathbf{x}_\perp) \; . \tag{5.5}$$

We follow previous works [15, 77] and consider the background to be of a rotationally symmetric Gaussian shape

$$\bar{\epsilon}(\tau_0, x_\perp) = \frac{1}{\pi R^2 \tau_0} \frac{\mathrm{d}E_\perp^{(0)}}{\mathrm{d}\eta} \exp\left(-\frac{x_\perp^2}{R^2}\right), \tag{5.6}$$

where R denotes the transverse system size and $\frac{\mathrm{d}E_\perp^{(0)}}{\mathrm{d}\eta}$ denotes the initial energy per unit rapidity. Similarly, the anisotropic perturbations are taken as[2]

$$\delta\epsilon(\tau_0, \mathbf{x}_\perp) = \bar{\epsilon}(\tau_0, x_\perp)\, \delta_n \exp\left(-\alpha \frac{x_\perp^2}{R^2}\right) \left(\frac{x_\perp}{R}\right)^n \cos(n\phi^{(n)}_{\mathbf{x}_\perp \mathbf{n}_\perp}) \; . \tag{5.7}$$

such that upon integrating over the transverse coordinates $\mathbf{x}_\perp$ the perturbations do not contribute to the total energy. By $\phi^{(n)}_{\mathbf{x}_\perp \mathbf{n}_\perp}$, we denote the angle

$$\phi^{(n)}_{\mathbf{x}_\perp \mathbf{n}_\perp} = \phi_x - \Psi_n \; , \tag{5.8}$$

where ϕ_x is the position space azimuthal angle, i.e. $\phi_x = \arctan(x^2/x^1)$, and Ψ_n is the symmetry plane angle of the n-th order angular harmonic mode. To compactify the notation, in the following we will drop the superscript (n) and write $\phi_{\mathbf{x}_\perp \mathbf{n}_\perp}$. We note that in accordance with Eq. (5.7), we will restrict ourselves to including only one anisotropic mode at a time, which means that we need not specify Ψ_n (or rather the relative angles between different symmetry planes). We leave the parameter α unspecified for analytical calculations, and if not stated otherwise employ $\alpha = 1/2$ when presenting numerical results.

By varying the amplitude δ_n of the anistropic perturbations, we can adjust the eccentricities ϵ_n of the initial state energy distribution. They can be computed analytically for our form of the initial condition. Defining $\bar{\alpha} = 1 + \alpha$, the results are

$$\epsilon_n = -\delta_n \frac{n!}{2\Gamma(\frac{n}{2}+1)} \bar{\alpha}^{-n-1} \; . \tag{5.9}$$

Values of the ratio ϵ_n/δ_n for $n = 2, \cdots, 6$ in the case $\alpha = \frac{1}{2}$ are summarized in Table 5.1, along with the maximally allowed values $\epsilon_n^{\max}$ for which a positive energy density is retained throughout the entire transverse plane.

[1] Strictly speaking, the integration in Eq. (5.4) yields a density in $\mathrm{d}^2\mathbf{x}_\perp \mathrm{d}y$. However, in the boost-invariant case, the phase-space distribution f only depends on $y - \eta$, meaning that integration over y and η is interchangeable and densities w.r.t.+ $\mathrm{d}y$ and $\mathrm{d}\eta$ are identical.

[2] Note that the anisotropic perturbations contains a variance modification factor α; a similar factor in the isotropic Gaussian could always be absorbed into the definition of R.

n	2	3	4	5	6
ϵ_n/δ_n	$-\frac{8}{27}$	$-\frac{64}{81\sqrt{\pi}}$	$-\frac{64}{81}$	$-\frac{2048}{729\sqrt{\pi}}$	$-\frac{2560}{729}$
$\epsilon_n^{\max}$	0.4027	0.3845	0.3649	0.3454	0.3265

TABLE 5.1: Eccentricities ϵ_n/δ_n and maximum allowed eccentricity $\epsilon_n^{\max}$ for which positivity of the initial energy density is satisfied.

5.1.2 Scaling properties

Based on the above setup, the development of anisotropic flow in small systems constitutes a complicated multi-scale problem, which in general is sensitive to the typical energy of quasi-particles Q_s, the total energy per unit rapidity $dE_\perp^{(0)}/d\eta$, the system size R, as well as the dimensionless coupling strength η/s. However, due to the particular simplicity of the conformal relaxation time approximation in Eq. (5.1), the entire dependence on these quantities can be expressed in terms of a single dimensionless opacity parameter $\hat{\gamma}$ [80], as we will now demonstrate.

The starting point is the Boltzmann equation (5.1), in which we assume that the phase-space distribution $f(x,p)$ can be expressed as an explicit function of the curvilinear coordinates τ and $\boldsymbol{x}_\perp$, as well as of the momentum space coordinates p^τ, v_z and ϕ_p, defined via

$$\begin{pmatrix} p^\tau \\ p^\eta \end{pmatrix} = p^\tau \begin{pmatrix} 1 \\ \tau^{-1} v_z \end{pmatrix}, \quad \mathbf{p}_\perp = p^\tau \sqrt{1-v_z^2} \begin{pmatrix} \cos\phi_p \\ \sin\phi_p \end{pmatrix}. \tag{5.10}$$

In this case, the Boltzmann equation (5.1) reduces to [80]

$$\left(\partial_\tau + \mathbf{v}_\perp \cdot \nabla_\perp - \frac{v_z(1-v_z^2)}{\tau}\partial_{v_z} - \frac{v_z^2 p^\tau}{\tau}\partial_{p^\tau}\right) f = -\left(5\frac{\eta}{s}\right)^{-1} T[f] v^\mu u_\mu[f](f - f_{eq}[f]), \tag{5.11}$$

where we denote $v^\mu = p^\mu/p^\tau$, while T and u^μ are determined from the phase-space distribution f via Landau matching, as described in the previous section.

Now the general strategy to establish the scaling properties of the system is to first integrate out the momentum dependence and subsequently express all quantities in terms of dimensionless variables. Since the Landau matching condition in Eq. (3.45) only requires the knowledge of energy weighted moments of the phase-space distribution, we reformulate the problem in terms of the reduced distribution [3]

$$\mathcal{F}(\tau, \mathbf{x}_\perp; \phi_p, v_z) \;=\; \frac{\nu_{\text{eff}}\ \pi R^2\ \tau}{(2\pi)^3}\left(\frac{\mathrm{d}E_\perp^{(0)}}{\mathrm{d}\eta}\right)^{-1} \int_0^\infty \mathrm{d}p^\tau (p^\tau)^3 f(\tau, \mathbf{x}_\perp; p^\tau, \phi_p, v_z). \tag{5.12}$$

where the constant prefactor is simply chosen to cancel explicit dependencies on ν_{eff} and $\frac{\mathrm{d}E_\perp^{(0)}}{\mathrm{d}\eta}$ in the resulting equations. Since Eq. (5.12) takes into account the correct energy (p^τ) weigthing, the energy momentum tensor $T^{\mu\nu}$ can simply be expressed in terms of the reduced distribution as

$$T^{\mu\nu}(\tau, \mathbf{x}_\perp) = \frac{1}{\tau R^2}\frac{\mathrm{d}E_\perp^{(0)}}{\mathrm{d}\eta}\int \mathrm{d}\Omega_p v^\mu v^\nu \mathcal{F}(\tau, \mathbf{x}_\perp; \phi_p, v_z), \tag{5.13}$$

[3] Note that our definition for $\mathcal{F}$ differs from the one in Ref. [80] by a factor of τ, which is introduced in order to absorb trivial effects of the longitudinal expansion.

where $\mathrm{d}\Omega_p = \mathrm{d}v_z \mathrm{d}\phi_p$ denotes the solid angle element in momentum space. By multiplying Eq. (5.11) with the appropriate pre-factors and performing the integration in Eq. (5.12), we then arrive at

$$\left(\tilde{\partial}_\tau + \vec{v}_\perp \cdot \tilde{\partial}_{\vec{x}_\perp} - \frac{v_z(1-v_z^2)}{\tilde{\tau}}\partial_{v_z} + \frac{4v_z^2-1}{\tilde{\tau}}\right)\mathcal{F} = -\hat{\gamma} v^\mu u_\mu[\mathcal{F}]\,\tilde{\tau}^{-1/4}\tilde{T}[\mathcal{F}]\,(\mathcal{F}-\mathcal{F}_{eq}[\mathcal{F}])\,, \quad (5.14)$$

where all quantities denoted with a tilde ˜ are explicitly dimensionless and defined as follows. Dimensionless coordinates are expressed with respect to the system size R as

$$\tilde{\tau} = \tau/R, \qquad \tilde{\mathbf{x}}_\perp = \mathbf{x}_\perp/R, \quad (5.15)$$

while the dimensionless energy density $\tilde{\epsilon}$ and temperature $\tilde{T}$ of the system are defined according to

$$\tilde{\epsilon} = \frac{\tau\pi R^2}{dE_\perp^{(0)}/d\eta}\,\epsilon\,, \qquad \tilde{T} = \left(\frac{\tau\pi R^2 \frac{\pi^2}{30}\nu_{\mathrm{eff}}}{dE_\perp^{(0)}/d\eta}\right)^{1/4} T\,. \quad (5.16)$$

Defining the stress-energy tensor with respect to the same non-dimensionalization employed for the energy density, we have

$$\widetilde{T}^{\mu\nu} = \frac{\tau\pi R^2}{dE_\perp^{(0)}/d\eta}\,T^{\mu\nu} = \int \mathrm{d}\Omega_p v^\mu v^\nu \mathcal{F} \quad (5.17)$$

such that the Landau macthing contion in Eq. (3.45) reduces to

$$u_\nu \widetilde{T}^{\mu\nu} = \tilde{\epsilon} u^\mu\,, \quad (5.18)$$

and the equation of state takes the particularly simple form $\tilde{\epsilon} = \tilde{T}^4$ in terms of the dimensionless variables. By considering the fact that the local equilibrium distribution is determined as $f_{eq}(x,p) = f_{eq}[p^\tau(v\cdot u)/T]$, the corresponding distribution $\mathcal{F}_{eq}$ can be expressed as

$$\mathcal{F}_{eq} = \frac{\nu_{\mathrm{eff}}\ \pi R^2\ \tau}{(2\pi)^3}\left(\frac{\mathrm{d}E_\perp^{(0)}}{\mathrm{d}\eta}\right)^{-1}\ \frac{T^4}{(u\cdot v)^4}\ \int_0^\infty dx\, x^3\, f_{eq}(x)\,, \quad (5.19)$$

where the last integral can be computed in terms of the energy density ϵ as

$$\int_0^\infty dx\, x^3\, f_{eq}(x) = \frac{(2\pi)^3\epsilon}{4\pi\ \nu_{\mathrm{eff}}\ T^4} \quad (5.20)$$

such that $\mathcal{F}_{eq}$ takes the simple form

$$\mathcal{F}_{eq} = \frac{\tilde{\epsilon}}{4\pi\ (u\cdot v)^4}. \quad (5.21)$$

Similarly, the initial condition for $\mathcal{F}$ can also be obtained by integrating Eq. (5.3), where assuming an azimuthally isotropic momentum distribution, one can express $\mathcal{F}$ in terms of the initial energy density as

$$\mathcal{F}(\tilde{\tau}_0, \tilde{\mathbf{x}}_\perp, \phi_p, v_z) = \frac{\delta(v_z)}{2\pi}\tilde{\epsilon}(\tilde{\tau}_0, \tilde{\mathbf{x}}_\perp)\,, \quad (5.22)$$

such that the pre-factors in the definition of $\tilde{\epsilon}(\tilde{\tau}_0, \tilde{\mathbf{x}}_\perp)$ in Eq. (5.16) cancel with the ones in Eq. (5.12).

By performing the above transformations, all dependencies on the system size R, initial energy $\frac{\mathrm{d}E_\perp^{(0)}}{\mathrm{d}\eta}$ and number of degrees of freedom ν_{eff} have thus been subsumed into a single dimensionless opactiy parameter

$$\hat{\gamma} = \left(5\frac{\eta}{s}\right)^{-1} R^{3/4} \left(\frac{1}{\pi R^2 \frac{\pi^2}{30}\nu_{\mathrm{eff}}} \frac{\mathrm{d}E_\perp^{(0)}}{\mathrm{d}\eta}\right)^{1/4} . \tag{5.23}$$

which appears on the right hand side of Eq. (5.14) and controls the relaxation towards equilibrium. In order to get an idea of the typical magnitude of $\hat{\gamma}$, we can estimate its value as

$$\hat{\gamma} \approx 0.88 \left(\frac{\eta/s}{0.16}\right)^{-1} \left(\frac{R}{0.4\,\mathrm{fm}}\right)^{1/4} \left(\frac{\mathrm{d}E_\perp^{(0)}/\mathrm{d}\eta}{5\,\mathrm{GeV}}\right)^{1/4} \left(\frac{\nu_{\mathrm{eff}}}{40}\right)^{-1/4} . \tag{5.24}$$

which indicates that in small systems realized in $p+p$ and $p+Pb$, one should typically expect $\hat{\gamma}$ of the order unity. Conversely, in large systems, the opacity can be significantly larger, such that e.g. in central $Pb+Pb$ collisions at LHC energies one obtains

$$\hat{\gamma} \approx 9.2 \left(\frac{\eta/s}{0.16}\right)^{-1} \left(\frac{R}{6\,\mathrm{fm}}\right)^{1/4} \left(\frac{\mathrm{d}E_\perp^{(0)}/\mathrm{d}\eta}{4000\,\mathrm{GeV}}\right)^{1/4} \left(\frac{\nu_{\mathrm{eff}}}{40}\right)^{-1/4} . \tag{5.25}$$

Based on a combination of (semi-)analytic and numerical studies, we will therefore explore the full range of opacities $\hat{\gamma} \ll 1$, $\hat{\gamma} \sim 1$ and $\hat{\gamma} \gg 1$ in order to investigate possible changes in the reaction dynamics for small and large systems.

5.2 Solution to linear order in opacity $\hat{\gamma}$ and eccentricity ϵ_n

We want to employ the opacity expansion scheme described in Sec. 3.2.2 to the setup discussed in this Chapter. We are primarily interested in the development of anisotropic flow, i.e. the final state momentum space anisotropy quantified by the harmonic coefficients v_n, in response to the initial state coordinate space eccentricity quantified by the amplitudes ϵ_n (or equivalently δ_n) of the harmonic perturbations introduced in Eq. (5.7). Starting from the free-streaming regime, where there is no production of v_n, we seek to follow previous works [74–76, 78, 79, 81] in deriving analytical expressions for $v_n(\tilde{\tau})$ which are accurate to linear order for small $\hat{\gamma}$ and small ϵ_n.

Since in the free-streaming system, the momenta of the particles remain unchanged, the free-streaming dynamics is effectively 2+1 dimensional, and we will continue to work in spatial Milne coordinates, where in contrast to other sections, we use y for longitudinal momentum parametrization instead of p^η or v_z. Another feature is that the analytical setup will quite straightforwardly also allow to treat the problem more generally without restricting it to energy-weighted degrees of freedom. However, this requires to specify the initial condition in (5.3) in more detail – in particular with regards to the initial momentum distribution $\mathrm{d}N_0/\mathrm{d}^2\mathbf{x}_\perp \mathrm{d}^2\mathbf{p}_\perp \mathrm{d}y$, which will introduce additional scales that non-energy-weighted degrees of freedom will depend on. We will assume that this distribution is (initially) isotropic in transverse momentum and depends only on some non-specific but fixed function F of the ratio

of $p_\perp$ to the momentum scale $Q_s(\mathbf{x}_\perp)$, i.e.

$$\frac{\mathrm{d}N_0}{\mathrm{d}^2\mathbf{x}_\perp \mathrm{d}^2\mathbf{p}_\perp \mathrm{d}y} = F\left(\frac{Q_s(\mathbf{x}_\perp)}{p_\perp}\right) \quad . \tag{5.26}$$

where the characteristic energy scale $Q_s(\mathbf{x}_\perp)$ is related to the local energy density $\epsilon(\tau_0, \mathbf{x}_\perp)$ via Eq. (5.4).

Below, we outline the calculation of observables to leading order in an expansion in opacity $\hat{\gamma}$ and eccentricity ϵ_n and quote the results for the flow harmonics v_n and the longitudinal cooling of $dE_\perp/d\eta$. Details of the analytic calculation are compiled in Appendices A-C.

5.2.1 Expansion scheme

The zeroth and first order results in the opacity expansion are obtained as

$$p^\mu \partial_\mu f^{(0)} = 0 \,, \tag{5.27}$$

$$p^\mu \partial_\mu f^{(1)} = C[f^{(0)}] \,. \tag{5.28}$$

As reasoned in the previous section, we can factor out from $C[f]$ the opacity parameter $\hat{\gamma}$ as a proportionality constant containing all parametric dependencies. Therefore $\hat{\gamma}$ can be identified as the expansion parameter of this expansion scheme. In the following, we will denote observables X computed in the free-streaming limit as $X^{(0)}$ and their first order corrections in opacity by $X^{(1)}$.

Similarly, for the expansion in eccentricity, we recall from Section 5.1.1 that the initial energy density is of the form

$$\epsilon(\tau_0, \mathbf{x}_\perp) = \bar{\epsilon}(\tau_0, x_\perp) + \delta\epsilon(\tau_0, \mathbf{x}_\perp) \tag{5.29}$$

with isotropic $\bar{\epsilon}$ and purely anisotropic $\delta\epsilon$, which introduces a finite eccentricity ϵ_n. Evidently, in free-streaming, the isotropic and anisotropic components of the phase-space distribution f evolve independently of each other and the anisotropic perturbation can be computed exactly. However, when computing the induced changes of the phase-space distribution $f^{(1)}$, one is required to perform the Landau matching at the level of the full energy-momentum tensor emerging from $f^{(0)}$, which introduces a non-trivial coupling of the isotropic and anisotropic components. Hence, for simplicity, we will solve the corresponding eigenvalue equation only to linear order in the anisotropic perturbations, which formally corresponds to a leading order expansion in ϵ_n. In the following, we will denote the linearized corrections to observables X due to the anisotropic perturbation as δX.

5.2.2 Observables

Since we want to examine momentum anisotropies, all observables of interest will be derived from the momentum distribution $\frac{\mathrm{d}N}{\mathrm{d}^2 p_\perp \mathrm{d}y}$, which can be obtained from the phase space density f by integrating over coordinate space variables. Specifically in Milne coordinates, the four-volume transformation entails an extra functional determinant for the 3d hypersurface integration at fixed proper time τ, such that

$$\frac{\mathrm{d}N}{\mathrm{d}^2\mathbf{p}_\perp \mathrm{d}y} = \frac{\nu_{\mathrm{eff}}}{(2\pi)^3} \int_{\mathbf{x}_\perp} \int \mathrm{d}\eta \; p_\perp \tau \cosh(y-\eta) \, f \,. \tag{5.30}$$

Based on the momentum distribution $\frac{\mathrm{d}N}{\mathrm{d}^2p_\perp \mathrm{d}y}$ we will extract the following moments [4]

$$V_{mn} = \int_{\mathbf{p}_\perp} e^{in\phi_{\mathbf{p}_\perp}} p_\perp^m \frac{\mathrm{d}N}{\mathrm{d}^2\mathbf{p}_\perp \mathrm{d}y} = \int_{\mathbf{x}_\perp} \left\langle p^\tau p_\perp^m e^{in\phi_p} \right\rangle \,. \tag{5.31}$$

that can be directly related to the observables that are of interest to us. Specifically, one has $\frac{\mathrm{d}E_\perp}{\mathrm{d}\eta} = V_{10}$ and $v_n^E = \frac{V_{1n}}{V_{10}}$.

5.2.3 Free streaming solution

The free-streaming solution of (5.27) can be computed e.g. via the method of characteristics to be

$$f^{(0)}(\tau, \mathbf{x}_\perp, \mathbf{p}_\perp, y-\eta) = f^{(0)}\left(\tau_0, \mathbf{x}_\perp - \mathbf{v}_\perp t(\tau, \tau_0, y-\eta), \mathbf{p}_\perp, \operatorname{arsinh}\left(\frac{\tau}{\tau_0}\sinh(y-\eta)\right)\right), \tag{5.32}$$

where $\mathbf{v}_\perp = \mathbf{p}_\perp/|\mathbf{p}_\perp|$ and

$$t(\tau, \tau_0, y-\eta) = \tau\cosh(y-\eta) - \sqrt{\tau_0^2 + \tau^2\sinh^2(y-\eta)}\,. \tag{5.33}$$

We note that the free-streaming result simplifies significantly for $f^{(0)}(\tau_0, \mathbf{x}_\perp, \mathbf{p}_\perp, y-\eta) \propto \delta(y-\eta)$, as in this case

$$\delta\left(\operatorname{arsinh}\left(\frac{\tau}{\tau_0}\sinh(y-\eta)\right)\right) = \frac{\tau_0}{\tau}\delta(y-\eta) \tag{5.34}$$

and

$$t(\tau, \tau_0, 0) = \tau - \tau_0 = \Delta\tau\,. \tag{5.35}$$

By applying this simplification to our initial condition in Eq. (5.3), we obtain

$$f^{(0)}(\tau, \mathbf{x}_\perp, \mathbf{p}_\perp, y-\eta) = \frac{(2\pi)^3}{\nu_{\mathrm{eff}}}\frac{\delta(y-\eta)}{\tau p_\perp} F\left(\frac{Q_s(\mathbf{x}_\perp - \mathbf{v}_\perp\Delta\tau)}{p_\perp}\right)\,. \tag{5.36}$$

Evidently, the free-streaming evolution will not change the momentum distribution $\frac{\mathrm{d}N}{\mathrm{d}^2p_\perp \mathrm{d}y}$ since there are no scatterings and therefore also the moments $V_{mn}^{(0)}$ will remain constant

$$V_{m,n=0}^{(0)}(\tau) = V_{m,n=0}^{(0)}(\tau_0), \qquad V_{m,n>0}^{(0)}(\tau) = 0, \tag{5.37}$$

where the last equality follows by noting that the initial condition is isotropic in momentum space. Subsequently, all v_n^Es with $n \neq 0$ vanish identically at all times τ, while the energy per unit rapidity remains constant

$$v_n^{E,(0)} = 0, \qquad \frac{dE_\perp^{(0)}}{d\eta}(\tau) = \frac{dE_\perp}{d\eta}(\tau_0). \tag{5.38}$$

[4] Note that, in contrast to the different treatments described in the other sections, the analytical treatment allows to describe more than just the energy-weighted version of the flow harmonics. Nevertheless, there are two important reasons for extracting moments of the distributions, rater than differential observables such as $\frac{\mathrm{d}N}{\mathrm{d}^2p_\perp \mathrm{d}y}$ or $v_n(p_\perp)$. The first is that the integral over $p_\perp$ will be crucial in facilitating further analytical integrations later on. But perhaps the more convincing reason is the aforementioned simplification of the problem when restricting it to the case of $m = 1$ for energy weighted observable.

5.2.4 Landau matching

Next, the free-streaming result can be used to compute the energy momentum tensor of the isotropic background $T^{(0)\mu\nu}$ and its anisotropic perturbations $\delta T^{(0)\mu\nu}$, which will be needed to obtain the local thermodynamic variables that enter the collision integral $C[f]$. Defining

$$v_\perp^\mu = p^\mu/p_\perp|_{y-\eta=0} = (1, \mathbf{v}_\perp, 0) \tag{5.39}$$

the isotropic part $T^{(0)\mu\nu}$ of the energy momentum tensor is given by

$$T^{(0)\mu\nu} = \frac{\tau_0}{\tau}\int \frac{\mathrm{d}\phi_p}{2\pi}\, v_\perp^\mu v_\perp^\nu\, \bar{\epsilon}(\tau_0, \mathbf{x}_\perp - \Delta\tau \mathbf{v}_\perp)\,. \tag{5.40}$$

Due to isotropy, it has only four independent entries and can be written as

$$T^{(0)\mu\nu} = \begin{pmatrix} T^{(0)\tau\tau} & T^{(0)\tau\perp}\hat{\mathbf{x}}_\perp^t & 0 \\ T^{(0)\tau\perp}\hat{\mathbf{x}}_\perp & T^{(0)\mathbb{1}}\mathbb{1} + T^{(0)\perp\perp}\hat{\mathbf{x}}_\perp\hat{\mathbf{x}}_\perp^t & 0 \\ 0 & 0 & 0 \end{pmatrix}. \tag{5.41}$$

where we denote $\hat{\mathbf{x}}_\perp = \mathbf{x}_\perp/|\mathbf{x}_\perp|$. Based on the symmetries of $T^{(0)\mu\nu}$, the corresponding eigenvectors satisfying the relations

$$u_\mu T^{(0)\mu\nu} = \epsilon u^\nu\,, \tag{5.42}$$
$$t_\mu T^{(0)\mu\nu} = p_t t^\nu\,, \tag{5.43}$$
$$s_\mu T^{(0)\mu\nu} = p_s s^\nu \tag{5.44}$$

can be parametrized as

$$u^\mu = \gamma(1, \beta\hat{\mathbf{x}}_\perp, 0)\,, \tag{5.45}$$
$$t^\mu = \gamma(\beta, \hat{\mathbf{x}}_\perp, 0)\,, \tag{5.46}$$
$$s^\mu = (0, i\sigma_2\hat{\mathbf{x}}_\perp, 0)\,, \tag{5.47}$$

where

$$\beta = \frac{3T^{(0)\tau\tau}+T^{(0)\perp\perp}}{4T^{(0)\tau\perp}} - \sqrt{\left(\frac{3T^{(0)\tau\tau}+T^{(0)\perp\perp}}{4T^{(0)\tau\perp}}\right)^2 - 1} \tag{5.48}$$

is the local rest frame velocity, $\gamma = (1-\beta^2)^{-1/2}$ and $i\sigma_2 = \begin{pmatrix} 0 & 1 \\ -1 & 0 \end{pmatrix}$; the corresponding eigenvalues are given by

$$\epsilon = T^{(0)\tau\tau} - \beta T^{(0)\tau\perp}\,, \tag{5.49}$$
$$p_t = \beta T^{(0)\tau\perp} - T^{(0)\perp\perp} - T^{(0)\mathbb{1}}\,, \tag{5.50}$$
$$p_s = -T^{(0)\mathbb{1}}\,, \tag{5.51}$$

Now, similarly to the isotropic background in Eq. (5.40), the anisotropic part of the energy-momentum tensor can be computed as

$$\delta T^{(0)\mu\nu} = \frac{\tau_0}{\tau}\int \frac{\mathrm{d}\phi_p}{2\pi}\, v_\perp^\mu v_\perp^\nu\, \delta\epsilon(\tau_0, \mathbf{x}_\perp - \Delta\tau \mathbf{v}_\perp), \tag{5.52}$$

which – due to the absence of isotropy – features six independent entries and its

eigenvalues and eigenvectors will be a complicated function of all of them. Obtaining their exact result would be cumbersome and ultimately pointless, as it would be too complex to perform further calculations with them, so instead we will linearize the Landau matching condition in the perturbation, meaning that the corrections $\delta\epsilon$ and δu^μ are computed from

$$\delta u_\mu T^{(0)\mu\nu} + u_\mu \delta T^{(0)\mu\nu} = \delta\epsilon u^\mu + \epsilon \delta u^\mu \,, \tag{5.53}$$

$$u_\mu \delta u^\mu = 0 \,. \tag{5.54}$$

The second condition ensures that the perturbation preserves the correct normalization of u^μ to linear order. In order to solve this system of equations, we can expand

$$\delta u^\mu = \delta u_t t^\mu + \delta u_s s^\mu \tag{5.55}$$

and use the orthogonality of the eigenbasis of $T^{(0)\mu\nu}$ to obtain via contraction with the eigenvectors from (5.53) the following results:

$$\delta\epsilon = u_\mu \delta T^{(0)\mu\nu} u_\nu \quad , \tag{5.56}$$

$$\delta u_t = \frac{u_\mu \delta T^{(0)\mu\nu} t_\nu}{p_t - \epsilon} \,, \tag{5.57}$$

$$\delta u_s = \frac{u_\mu \delta T^{(0)\mu\nu} s_\nu}{p_s - \epsilon} \quad . \tag{5.58}$$

While Eqns. (5.49-5.51,5.56-5.58) provide schematic expressions for the $\epsilon, \delta\epsilon, u^\mu$ and δu^μ, the exact forms of $T^{(0)\mu\nu}$ and $\delta T^{(0)\mu\nu}$ that determine these quantities consist of lengthy expressions which are provided in Appendix B.

5.2.5 First order corrections in $\hat{\gamma}$

Now that we have obtained the local energy densities and flow velocities, computing the corrections $\delta f^{(1)}$ due to the first scatterings according to

$$\frac{p^\mu}{p^\tau}\partial_\mu f^{(1)} = \frac{C[f^{(0)}]}{p^\tau} \tag{5.59}$$

is comparetively straightforward after realizing that this is just the inhomogeneous case of the PDE we already solved for free streaming. The solution (5.32) allows to read off the Green's function for propagation in time and compute $f^{(1)}$ via

$$f^{(1)}(\tau, \mathbf{x}_\perp, \mathbf{p}_\perp, y-\eta) = \int_{\tau_0}^{\tau} \mathrm{d}\tau' \, \frac{C[f^{(0)}]}{p^\tau}\Big(\tau', \mathbf{x}_\perp - \mathbf{v}_\perp t(\tau, \tau', y-\eta), \mathbf{p}_\perp, \operatorname{arsinh}\left(\frac{\tau}{\tau'}\sinh(y-\eta)\right)\Big) \tag{5.60}$$

Since we will integrate over space to compute $\frac{\mathrm{d}N^{(1)}}{\mathrm{d}^2p_\perp \mathrm{d}y}$ according to (5.30), we can simplify this expression by performing the following substitutions

$$\begin{aligned} \mathbf{x}_\perp{}' &= \mathbf{x}_\perp - \mathbf{v}_\perp t(\tau, \tau', y-\eta), \\ \eta' &= y - \operatorname{arsinh}\left(\frac{\tau}{\tau'}\sinh(y-\eta)\right), \end{aligned} \tag{5.61}$$

such that

$$\mathrm{d}^2\mathbf{x}_\perp{}' = \mathrm{d}^2\mathbf{x}_\perp, \qquad \mathrm{d}\eta' = \frac{\tau}{\tau'}\frac{\cosh(y-\eta)}{\cosh(y-\eta')}\mathrm{d}\eta, \tag{5.62}$$

yielding the following result for the changes in the momentum space distribution $\frac{\mathrm{d}N^{(1)}}{\mathrm{d}^2p_\perp \mathrm{d}y}$

$$\frac{\mathrm{d}N^{(1)}}{\mathrm{d}^2p_\perp \mathrm{d}y}(\tau, \mathbf{p}_\perp) = \int_{\tau_0}^{\tau}\mathrm{d}\tau' \int_{\mathbf{x}_\perp{}'}\int \mathrm{d}\eta'\ \tau'\frac{\nu_{\mathrm{eff}}}{(2\pi)^3}C[f^{(0)}]\left(\tau', \mathbf{x}_\perp{}', \mathbf{p}_\perp, y-\eta'\right) \quad , \tag{5.63}$$

where in the following, we will drop the primes on all integration variables except for τ'. Since, as stated in section 5.2.2, the final observables we want to compute correspond to $\mathrm{d}^2p_\perp$-integrated moments of $\frac{\mathrm{d}N}{\mathrm{d}^2p_\perp \mathrm{d}y}$, one is then left with the calculation of the following six dimensional integral

$$V_{mk}^{(1)}(\tau) = \int_{\mathbf{p}_\perp} e^{in\phi_p}p_\perp^m \int_{\tau_0}^{\tau}\mathrm{d}\tau' \int_{\mathbf{x}_\perp}\int \mathrm{d}\eta\ \tau'\frac{\nu_{\mathrm{eff}}}{(2\pi)^3}C[f^{(0)}]\left(\tau', \mathbf{x}_\perp, \mathbf{p}_\perp, y-\eta\right) \ . \tag{5.64}$$

We find that four of these integrals can be carried out analytically, while the remaining two integrals over $\mathrm{d}\tau'$ and $\mathrm{d}x_\perp$ require numerical methods. Below we provide a brief outline of the four analytical integrations and explain how different terms can be categorized. Explicit expressions and further details of the analytic calculation can be found in Appendix C.

The integration over $p_\perp$ is performed first to obtain moments of F and f_{eq}, which will facilitate the other integrations. Since the integrand depends mostly on $u \cdot v$, we substitute integration over the position space azimuthal angle ϕ_x for integration over $\phi_{\mathbf{x}_\perp\mathbf{p}_\perp} = \phi_x - \phi_p$. The integral over η is straightforward for the term containing a Dirac-Delta but for other terms it is of similar complexity to the integral over $\phi_{\mathbf{x}_\perp\mathbf{p}_\perp}$ and both are performed together. After these integrations, the only remaining dependence on the azimuthal momentum angle takes the form $e^{ik\phi_p}\cos(n\phi_{\mathbf{p}_\perp\mathbf{n}_\perp})$ ($\phi_{\mathbf{p}_\perp\mathbf{n}_\perp} = \phi_p - \Psi_n$) and the last integral becomes a trigonometric orthogonality relation, which signifies that eccentricities do not mix, as is to be expected due to the linearization.

Due to the fact that we consider an isotropic background with a purely anisotropic perturbation, the leading order expansion of the flow harmonics is given by

$$v_n^{(m)} = \frac{V_{mn}}{V_{m0}} = \frac{\delta V_{mn}^{(1)}}{V_{m0}^{(0)}} + \text{nonlinear terms} \tag{5.65}$$

Due to this symmetry, one also finds that the leading order opacity contributions to the observables V_{mn} conveniently separate into the first order isotropic corrections $V_{m0}^{(1)} \propto \hat{\gamma}$ for $n = 0$ on one hand and the first order anisotropic corrections $\delta V_{mn}^{(1)} \propto \hat{\gamma}\delta_n$ to only moments with $n \neq 0$ on the other hand. While the former ($V_{m0}^{(1)}$) represent opacity corrections to the evolution of the isotropic background, the latter ($\delta V_{mn}^{(1)}$)

describe the systems response to the anisotropic energy perturbations.

Besides, another important mathematical as well as physical distinction is that between terms $V_{mn}^{(1,0)}$ coming from the decay of $f^{(0)}$ and terms $V_{mn}^{(1,eq)}$ coming from the buildup of f_{eq}. In our calculation we treat these terms separately and then sum them to find the total observable. However, it is important to point out that in many cases the two terms turn out to have different parametric dependencies. By construction of the expansion scheme, all of them are proportional to $\hat{\gamma}$. However due to the different functional forms of $f^{(0)}$ and f_{eq} we obtain that the isotropic ($n = 0$) corrections are given by

$$V_{m0}^{(1,0)} = -\hat{\gamma} V_{m0}^{(0)} \, \mathcal{P}_m(\tilde{\tau}) \, , \tag{5.66}$$

$$V_{m0}^{(1,eq)} = +\hat{\gamma} \nu_{\text{eff}} R^{-m} \left(\nu_{\text{eff}}^{-1} \frac{\mathrm{d}E_\perp^{(0)}}{\mathrm{d}\eta} R \right)^{\frac{m+3}{4}} \mathcal{Q}_m(\tilde{\tau}) \, , \tag{5.67}$$

and similarly for the anistropic corrections ($n \neq 0$)

$$V_{mn}^{(1,0)} = -\hat{\gamma} \delta_n V_{m0}^{(0)} \, \mathcal{P}_{mn}(\tilde{\tau}) \, , \tag{5.68}$$

$$V_{mn}^{(1,eq)} = +\hat{\gamma} \delta_n \nu_{\text{eff}} R^{-m} \left(\nu_{\text{eff}}^{-1} \frac{\mathrm{d}E_\perp^{(0)}}{\mathrm{d}\eta} R \right)^{\frac{m+3}{4}} \mathcal{Q}_{mn}(\tilde{\tau}) \, . \tag{5.69}$$

Detailed expressions of the functions $\mathcal{P}_m(\tilde{\tau}), \mathcal{Q}_m(\tilde{\tau}), \mathcal{P}_{mn}(\tilde{\tau}), \mathcal{Q}_{mn}(\tilde{\tau})$ are given in Eqns. (C.16,C.20,C.41,C.60). Of course, the appearance of a different parametric behavior is not too surprising, as f^0 depends on the entire momentum distribution, whereas f_{eq} only depends on the local energy density. Generally, to fix the relative size of decay and buildup for $V_{mn}^{(1)}$, we need an input for $\frac{\mathrm{d}E_\perp^{(0)}}{\mathrm{d}\eta}$ and $V_{m0}^{(0)}$, which means specifying the related moments of the initial momentum distribution F in Eq. (5.26). Clearly, the only exception to this rule is the case $m = 1$ of energy weighted observables, where $V_{10}^{(0)} = \frac{\mathrm{d}E_\perp^{(0)}}{\mathrm{d}\eta}$ and the calculation of $V_{1n}^{(1)}/V_{10}^{(0)}$ does not require any further specification of the initial momentum distribution F.

By restricting our attention to energy weighted observables, we can then perform the residual integrals numerically, to obtain the leading order changes in the initial energy per unit rapidity

$$\frac{\mathrm{d}E_\perp^{(1)}}{d\eta}(\tau \to \infty) \Big/ \left(\hat{\gamma} \frac{\mathrm{d}E_\perp^{(0)}}{\mathrm{d}\eta} \right) = -0.210 \tag{5.70}$$

and the flow response

$$v_2^E(\tau \to \infty) / \left(\hat{\gamma}\epsilon_2\right) = 0.212 \tag{5.71}$$

$$v_3^E(\tau \to \infty) / \left(\hat{\gamma}\epsilon_3\right) = 0.0665 \tag{5.72}$$

$$v_4^E(\tau \to \infty) / \left(\hat{\gamma}\epsilon_4\right) = -0.00914 \, , \tag{5.73}$$

which we will compare to full numerical solutions of the RTA Boltzmann equation in the following. Beyond the results in Eqns. (5.70-5.73), which provide the asymptotic ($\tau \to \infty$) values of the transverse energy and flow coefficients, it is clear that Eq. (5.64) also gives access to the time evolution of these quantities which we will further investigate in Sec. 5.4.

We note that the above result are obtained for the initial condition in Eqs. (5.5-5.7) with $\alpha = 1/2$, which is different than the case $\alpha = 0$ considered in [78]. If we choose $\alpha = 0$ instead, we find

$$v_2^E(\tau \to \infty)/\left(\hat{\gamma}\epsilon_2\right) = 0.213 \tag{5.74}$$

$$v_3^E(\tau \to \infty)/\left(\hat{\gamma}\epsilon_3\right) = 0.0621 \tag{5.75}$$

$$v_4^E(\tau \to \infty)/\left(\hat{\gamma}\epsilon_4\right) = -0.00483\,, \tag{5.76}$$

in agreement with [78].[5] By comparing the results for different v_ns in Eq. (5.71-5.73,5.74-5.76), one finds that v_2 appears to be rather insensitive to α, whereas the higher order v_ns are more sensitive to α, as we will further discuss in Sec. 5.4.2. Especially v_4 changes by approximately a factor of two between the two cases, and can even turn out to have different signs for different values of α, indicating a strong dependence on the initial profile in the low opacity regime.

5.3 Numerical procedure for non-linear solution

We will now discuss two different schemes to obtain numerical solutions of the RTA Boltzmann equation, which are based on a momentum moment expansion discussed in subsec. 5.3.1 and the relativistic Lattice Boltzmann method discussed in subsec. 5.3.2.

5.3.1 Expansion in spherical harmonic moments

Within our first approach, we follow previous works [144], where instead of describing the evolution of the phase space density f, the numerical algorithm solves time evolution equations only for some energy weighted momentum moments on a two-dimensional lattice in transverse space. Specifically, we consider the following energy weighted moments C_l^m of the phase-space distribution

$$C_l^m := \tau \int \frac{\mathrm{d}^3p}{(2\pi)^3}\, Y_l^m(\theta_p,\phi_p)\, p^\tau\, f = \int \frac{\mathrm{d}^2p_\perp}{(2\pi)^2} \int \frac{\mathrm{d}p_\eta}{2\pi}\, Y_l^m(\theta_p,\phi_p) \sqrt{p_\perp^2 + \frac{p_\eta^2}{\tau^2}}\, f\,.$$

where Y_l^m denote the spherical harmonics, which are given in terms of the associated Legendre polynomials P_l^m as

$$Y_l^m(\theta,\phi) = y_l^m\, P_l^m(\cos\theta)\, e^{im\phi} \tag{5.77}$$

with normalization

$$y_l^m = \sqrt{\frac{2l+1}{4\pi}\frac{(l-m)!}{(l+m)!}} \tag{5.78}$$

and the momentum space angles in Eq. (5.77) are parametrized by the polar and azimuthal angles θ_p and ϕ_p defined as

$$\cos\theta_p = \frac{p_\eta/\tau}{p^\tau}\,, \quad \tan\phi_p = \frac{p^2}{p^1}\,. \tag{5.79}$$

[5] Note that for comparison with [78], one also need to account for the factor of ϵ_n/δ_n in Eq. (5.9).

Since only a finite number of moments can be described numerically, the algorithm only keeps track of the moments with $l < l_{max}$ for an adjustable large enough value of l_{max} to achieve apparent convergence.

Initial conditions & Evolution equation for moments

By taking the corresponding moments of the initial conditions in Eq. (5.3), one obtains the initial conditions for the spherical harmonic moments as

$$C_l^m(\tau_0) = \tau_0\, \epsilon(\tau_0, \mathbf{x}_\perp)\, y_l^0\, P_l^0(0)\, \delta^{m0}\ . \tag{5.80}$$

This expression contains as a factor the Legendre polynomial evaluation $P_l^0(0)$, which vanishes for odd l and is otherwise given by

$$P_l^0(0) = (-1)^{l/2}\pi^{-1/2}\frac{\Gamma\left(\frac{l+1}{2}\right)}{\Gamma\left(\frac{l}{2}+1\right)}\ . \tag{5.81}$$

Simlarly, denoting the local rest-frame velocity as $u^\mu = \gamma\,(1, \beta_1, \beta_2, 0)$ and taking the corresponding moments of the Boltzmann equation (5.1) then yields the following equation of motion for the spherical harmonic moments

$$\begin{aligned}
\partial_\tau C_l^m = {}& \frac{1}{\tau}(b_{l,+2}^m C_{l+2}^m + b_{l,0}^m C_l^m + b_{l,-2}^m C_{l-2}^m) \\
& + \frac{1}{2}\left(\frac{\gamma\beta_1}{\tau_R} - \partial_1\right)[u_{l,+}^m C_{l+1}^{m+1} + u_{l,-}^m C_{l-1}^{m+1} + d_{l,+}^m C_{l+1}^{m-1} + d_{l,-}^m C_{l-1}^{m-1}] \\
& + \frac{1}{2i}\left(\frac{\gamma\beta_2}{\tau_R} - \partial_2\right)[u_{l,+}^m C_{l+1}^{m+1} + u_{l,-}^m C_{l-1}^{m+1} - d_{l,+}^m C_{l+1}^{m-1} - d_{l,-}^m C_{l-1}^{m-1}] \\
& + \frac{1}{\tau_R}E_l^m(u^\mu, T) - \frac{\gamma}{\tau_R}C_l^m\ ,
\end{aligned} \tag{5.82}$$

where the terms with spatial derivatives proportional to the coefficients u, d describe free-streaming while the terms proportional to the coefficients b are related to the longitudinal expansion. The corresponding coefficients are given by [144][6]

$$u_{l,-}^m = \sqrt{\frac{(l-m)(l-m-1)}{4l^2-1}}\ , \qquad u_{l,+}^m = -\sqrt{\frac{(l+m+1)(l+m+2)}{4l(l+2)+3}}\ , \tag{5.83}$$

$$d_{l,-}^m = -\sqrt{\frac{(l+m)(l+m-1)}{(4l^2-1)}}\ , \qquad d_{l,+}^m = \sqrt{\frac{(l-m+1)(l-m+2)}{4l(l+2)+3}}\ , \tag{5.84}$$

[6] Note that here $b_{l,0}^m$ is smaller by $\frac{1}{3}$ compared to [144] because the C_l^m are weighted with τ instead of $\tau^{4/3}$.

$$
\begin{aligned}
b^m_{l,-2} &= -\frac{l+2}{2l-1}\sqrt{\frac{(l-m)(l-m-1)(l+m)(l+m-1)}{(2l-3)(2l+1)}}\,, \\
b^m_{l,0} &= \frac{1-3(l^2-l)+5m^2}{4l(l+1)-3}\,, \\
b^m_{l,+2} &= \frac{l-1}{2l+3}\sqrt{\frac{(l-m+1)(l-m+2)(l+m+2)(l+m+1)}{(2l+5)(2l+1)}}\,,
\end{aligned} \tag{5.85}
$$

Finally all terms that are inversely proportionals to the relaxation time τ_R result from the collision kernel and describe the relaxation of the system towards local equilibrium, with the equilibrium moments E^l_m given by

$$
\begin{aligned}
E^m_l &= \int \frac{\mathrm{d}^2 p_\perp}{(2\pi)^2}\int \frac{\mathrm{d}p_\eta}{2\pi}\, Y^m_l(\theta_p,\phi_p)\, p^\mu u_\mu\, f_{eq} \\
&= 2^{-l-2}\pi^{1/2}\tau\epsilon\, Y^m_l\left(\frac{\pi}{2},\phi_u\right)\gamma^{-3}\beta^l\frac{\Gamma(l+3)}{\Gamma\left(l+\frac{3}{2}\right)}\,{}_2F_1\left(\frac{l+3}{2},\frac{l+4}{2};l+\frac{3}{2};\beta^2\right)
\end{aligned} \tag{5.86}
$$

where we denote $\tan\phi_u = \beta_1/\beta_2$ and $\beta^2 = \beta_1^2+\beta_2^2$ and refer to Appendix D for further details of the calculation. We also note for later convenience, that by separately keeping track of the free-streaming, long. expansion and collisional contributions in Eq. (5.82), we can compute the respective contributions to the rate of change of any observables.

Evaluation of Eq. (5.82) also requires an input for the local energy density ϵ and flow velocity u^μ, which have to be computed via Landau matching. In practice, we first compute the various components of the energy momentum tensor from the following linear combintations of spherical harmonic moments

$$\tau T^{\tau\tau} = \sqrt{4\pi}C^0_0 \tag{5.87}$$

$$\tau T^{\tau 1} = \sqrt{\frac{2\pi}{3}}(C^{-1}_1 - C^1_1) \tag{5.88}$$

$$\tau T^{\tau 2} = \sqrt{\frac{2\pi}{3}}i(C^{-1}_1 + C^1_1) \tag{5.89}$$

$$\tau T^{11} = \sqrt{\frac{4\pi}{9}}\left(C^0_0 - \sqrt{\frac{1}{5}}C^0_2\right) + \sqrt{\frac{2\pi}{15}}(C^2_2 + C^{-2}_2) \tag{5.90}$$

$$\tau T^{22} = \sqrt{\frac{4\pi}{9}}\left(C^0_0 - \sqrt{\frac{1}{5}}C^0_2\right) - \sqrt{\frac{2\pi}{15}}(C^2_2 + C^{-2}_2) \tag{5.91}$$

$$\tau T^{12} = \sqrt{\frac{2\pi}{15}}i(C^{-2}_2 - C^2_2) \tag{5.92}$$

and subsequently perform a numerical diagonalization of T^μ_ν using the Eigen C++ library [169], to obtain the rest-frame velocity u^μ and local energy density ϵ as the timelike eigenvector and eigenvalue.

With regards to the numerical implementation of Eq. (5.82), we also note that the terms containing spatial derivatives can be efficiently computed in Fourier space, and we employ an $\mathcal{O}(a_S^2)$ improved five-point stencil derivative. Concerning the discretization of the time step, we employ a fourth order Runge-Kutta scheme with adaptive time step of typically $\delta\tau = 0.01\min(\tau, R/10)$.

Observables

Since the numerical setup is restricted to energy weighted moments of the phase-space distribution, all observables that can be computed are necessarily weighted with energy as well. Evidently, to compute an observable, it has to be expressed as a linear combination of the moments C_l^m, meaning that it has to be expanded in spherical harmonics. By making use of their orthogonality relation, one can then express observables of the form

$$\tau \left\langle (p^\tau)^2 \, \mathcal{O} \right\rangle = \int \frac{\mathrm{d}^2 p_\perp}{(2\pi)^2} \int \frac{\mathrm{d}p_\eta}{2\pi} \, p^\tau \, \mathcal{O}(\theta_p, \phi_p) \, f \tag{5.93}$$

as a linear combination of the coefficients

$$\tau \left\langle (p^\tau)^2 \, \mathcal{O} \right\rangle = \sum_{(l,m)} \alpha^{\mathcal{O}}_{m,l} \, C_l^m \ , \tag{5.94}$$

where the expansion coefficients $\alpha^{\mathcal{O}}_{m,l}$ are determined as

$$\alpha^{\mathcal{O}}_{m,l} = \int \mathrm{d}\Omega_p \, \mathcal{O}(\theta_p, \phi_p) \, Y_l^{m*}(\theta_p, \phi_p) \ . \tag{5.95}$$

Specifically, for calculating the observables $dE_\perp/dy$ and v_n^E that are of interest to us, we need to consider integrals of expressions of the form

$$\mathcal{O}_n(\theta_p, \phi_p) = e^{in\phi_p} \sin(\theta_p) \ . \tag{5.96}$$

Since the ϕ_p-dependence of Y_l^{m*} is simply given by $e^{-im\phi_p}$, it is already obvious that $\alpha^{\mathcal{O}_n}_{m,l}$ vanishes for all $m \neq n$. Additionally, for increasing l the spherical harmonics Y_l^{n*} alternate between being symmetric and antisymmetric w.r.t. θ_p, such that $\alpha^{\mathcal{O}_n}_{n,l} = 0$ for $l - n$ odd, while for $l - n$ even, the coefficients can be computed as

$$\alpha^{\mathcal{O}_n}_{n,l} \ = \ 2\pi 2^{-l} y_l^n \sum_{k=0}^{\frac{l-n}{2}} (-1)^{k+n} \binom{l}{n} \binom{2l-2k}{l} \frac{(l-2k)!}{(l-2k-n)!} \frac{\Gamma\left(\frac{n+3}{2}\right) \Gamma\left(\frac{l-2k-n+1}{2}\right)}{\Gamma\left(\frac{l-2k+4}{2}\right)} \ . \tag{5.97}$$

In the special case $n = 1$, only one coefficient is nonvanishing, but otherwise there are infinitely many. However, their values are decreasing with l quickly enough so that cutting off the expansion at l_{max} yields a reasonable approximation.

5.3.2 Relativistic Lattice Boltzmann solver

Within our second approach, we employ a relativistic lattice Boltzmann solver inspired by the finite difference Relativistic Lattice Boltzmann (RLB) algorithm discussed in Refs. [170–174]. The strategy for devising the numerical method is split into three main parts, that are described in this subsection. The structure of the kinetic equation is presented in Sec. 5.3.2 in two forms. The first form is based on the standard Bjorken coordinates $(\tau, \mathbf{x}_\perp, \eta)$, while the second relies on a set of hybrid free-streaming coordinates, inspired by the approach in Ref. [80]. The momentum space discretization is discussed in Sec. 5.3.2. The spatial and temporal discretization, as well as the numerical schemes employed for the advection and time stepping, are briefly summarized in Sec. 5.3.2.

Boltzmann equation for the RLB approach

In the RLB method, we employ the factorization of the momentum space with respect to the coordinates $(p,\ v_z,\ \phi_p)$ introduced in Eq. (5.10). Starting from Eq. (5.11), we apply the LB algorithm at the level of the function $\mathcal{F}_{\rm RLB} = \frac{\tau_0}{\tau}\mathcal{F}$, where $\mathcal{F}$ is introduced in Eq. (5.12). Specifically,

$$\mathcal{F}_{\rm RLB} = \frac{\pi \nu_{\rm eff} R^2 \tau_0}{(2\pi)^3} \left(\frac{{\rm d}E_\perp^{(0)}}{{\rm d}\eta}\right)^{-1} \int_0^\infty {\rm d}p^\tau\, (p^\tau)^3 f. \tag{5.98}$$

Dimensionless versions of the coordinates τ and $\mathbf{x}_\perp$ are defined by normalization to $R^{3/4}\tau_0^{1/4}$ [175], i.e.

$$\begin{aligned} \bar{\tau} =& \frac{\tau}{\tau_0^{1/4} R^{3/4}} = \left(\frac{R}{\tau_0}\right)^{1/4} \tilde{\tau}, \\ \bar{\mathbf{x}}_\perp =& \frac{\mathbf{x}_\perp}{\tau_0^{1/4} R^{3/4}} = \left(\frac{R}{\tau_0}\right)^{1/4} \tilde{\mathbf{x}_\perp}, \end{aligned} \tag{5.99}$$

while the energy density and temperature are non-dimensionalized with respect to constant quantities:

$$\begin{aligned} \bar{\epsilon} =& \frac{\tau_0 \pi R^2 \epsilon}{dE_\perp^{(0)}/d\eta} = \frac{\tau_0}{\tau}\tilde{\epsilon}, \\ \overline{T} =& \left(\frac{\tau_0 \pi R^2 \frac{\pi^2}{30}\nu_{\rm eff}}{dE_\perp^{(0)}/d\eta}\right)^{1/4} T = \left(\frac{\tau_0}{\tau}\right)^{1/4} \tilde{T}, \end{aligned} \tag{5.100}$$

such that $\bar{\epsilon} = \overline{T}^4$. In this section, we use an overhead bar $\bar{}$ to denote dimensionless quantities obtained using the above convention, in contrast to the overhead tilde $\tilde{}$ employed in Sec. 5.1 (note that $\overline{T}$ and $\bar{\epsilon}$ are related to T and ϵ through constant factors). The Boltzmann equation (5.11) written for $\mathcal{F}_{\rm RLB}$ introduced above reads [175]:

$$\begin{aligned} \left(\frac{\partial}{\partial\bar{\tau}} + \mathbf{v}_\perp \cdot \overline{\nabla} + \frac{1+v_z^2}{\tau}\right)\mathcal{F}_{\rm RLB} - \frac{1}{\bar{\tau}}\frac{\partial[v_z(1-v_z^2)\mathcal{F}_{\rm RLB}]}{\partial v_z} \\ = -\hat{\gamma}(v^\mu u_\mu)\overline{T}(\mathcal{F}_{\rm RLB} - \mathcal{F}_{\rm RLB}^{eq}). \end{aligned} \tag{5.101}$$

The components of the stress-energy tensor can be non-dimensionalized in the same way as the energy density, being related to $\mathcal{F}_{\rm RLB}$ through

$$\overline{T}^{\mu\nu} = \int d\Omega_p\, v^\mu v^\nu \mathcal{F}_{\rm RLB}. \tag{5.102}$$

The energy-weighted flow harmonics (3.41) can be obtained via

$$v_n^E = \frac{\int_{\mathbf{x}_\perp}\int d\Omega_p \sqrt{1-v_z^2}\, e^{in\phi_p}\mathcal{F}_{\rm RLB}}{\int_{\mathbf{x}_\perp}\int d\Omega_p \sqrt{1-v_z^2}\,\mathcal{F}_{\rm RLB}}. \tag{5.103}$$

The Boltzmann equation in the form given in Eq. (5.101) serves as the basis of the algorithm employed for large values of the opacity $\hat{\gamma}$. At small values of the opacity, we find the form in Eq. (5.101) unsuitable and instead employ free-streaming coordinates

in momentum space. This approach is inspired from Ref. [175] but differs from the aforementioned approach because the spatial coordinates are left unchanged. Defining

$$\begin{aligned} p^{\tau}_{\rm fs} =& p^{\tau}\Delta, & v^{\rm fs}_z =& \frac{\tau v_z}{\tau_0 \Delta}, \\ p^{\tau} =& p^{\tau}_{\rm fs}\Delta_{\rm fs}, & v_z =& \frac{\tau_0 v^{\rm fs}_z}{\tau \Delta_{\rm fs}}, \end{aligned} \tag{5.104}$$

where

$$\begin{aligned} \Delta =& \sqrt{1+\left(\frac{\tau^2}{\tau_0^2}-1\right)v_z^2}, \\ \Delta_{\rm fs} = \frac{1}{\Delta} =& \sqrt{1-\left(1-\frac{\tau_0^2}{\tau^2}\right)v_{z;{\rm fs}}^2}. \end{aligned} \tag{5.105}$$

the Boltzmann equation (5.11) becomes

$$\frac{\partial f}{\partial \bar{\tau}} + \frac{1}{\Delta_{\rm fs}}\mathbf{v}_{\perp;{\rm fs}}\cdot\overline{\nabla}_{\perp} f = -\hat{\gamma}(v^{\mu}u_{\mu})\overline{T}(f-f_{eq}), \tag{5.106}$$

where $\mathbf{v}_{\perp;{\rm fs}} = \sqrt{1-v^2_{z;{\rm fs}}}(\cos\phi_p, \sin\phi_p)$, while $v_\mu u^\mu = u^\tau - \frac{1}{\Delta_{\rm fs}}\mathbf{v}_{\perp;{\rm fs}}\cdot\mathbf{u}_\perp$. We now introduce the function $\mathcal{F}_{\rm fs}$, defined in analogy to Eq. (5.98) using integration with respect to $p^\tau_{\rm fs}$:

$$\mathcal{F}_{\rm fs} = \frac{\pi\nu_{\rm eff}R^2\tau_0}{(2\pi)^3}\left(\frac{{\rm d}E^{(0)}_{\perp}}{{\rm d}\eta}\right)^{-1}\int_0^{\infty}{\rm d}p^{\tau}_{\rm fs}\,(p^{\tau}_{\rm fs})^3 f, \tag{5.107}$$

such that Eq. (5.106) becomes

$$\frac{\partial \mathcal{F}_{\rm fs}}{\partial \bar{\tau}} + \frac{1}{\Delta_{\rm fs}}\boldsymbol{v}_{\perp;{\rm fs}}\cdot\overline{\nabla}_{\perp}\mathcal{F}_{\rm fs} = -\hat{\gamma}(v^{\mu}u_{\mu})\overline{T}(\mathcal{F}_{\rm fs}-\mathcal{F}^{eq}_{\rm fs}). \tag{5.108}$$

Due to the changes to the momentum space degrees of freedom, the computation of the components of the stress-energy tensor becomes more involved. Taking into account the transformation of the measure $dp^\tau\,(p^\tau)^2 d\Omega_p = (\tau_0/\tau)dp^\tau_{\rm fs}(p^\tau_{\rm fs})^2 d\Omega_{p;{\rm fs}}$, the dimensionless components $\overline{T}^{\mu\nu}$ can be computed as

$$\begin{aligned} \overline{T}^{\tau\tau} =& \frac{\tau_0}{\tau}\int d\Omega_{p;{\rm fs}}\,\Delta_{\rm fs}\,\mathcal{F}_{\rm fs}, \\ \overline{T}^{\tau i} =& \frac{\tau_0}{\tau}\int d\Omega_{p;{\rm fs}} v^i_{\perp;{\rm fs}}\mathcal{F}_{\rm fs}, \\ \overline{T}^{ij} =& \frac{\tau_0}{\tau}\int d\Omega_{p;{\rm fs}}\frac{v^i_{\perp;{\rm fs}}v^j_{\perp;{\rm fs}}}{\Delta_{\rm fs}}\mathcal{F}_{\rm fs}, \\ \tau^2\overline{T}^{\eta\eta} =& \frac{\tau_0^3}{\tau^3}\int d\Omega_{p;{\rm fs}}\frac{v^2_{z;{\rm fs}}}{\Delta_{\rm fs}}\,\mathcal{F}_{\rm fs}, \end{aligned} \tag{5.109}$$

where $v^i_{\perp;{\rm fs}} = v_{\perp;{\rm fs}}(\cos\phi_p, \sin\phi_p)$ and $v_{\perp;{\rm fs}} = \sqrt{1-v^2_{z;{\rm fs}}}$. Based on the the equilibrium Bose-Einstein distribution at vanishing chemical potential

$$f_{\rm eq} = \left(e^{p_\mu u^\mu/T}-1\right)^{-1}. \tag{5.110}$$

the functions $\mathcal{F}^{eq}_{\rm RLB}$ and $\mathcal{F}^{eq}_{\rm fs}$ in Eq. (5.98), are readily obtained as

$$\begin{aligned}\mathcal{F}^{eq}_{\rm RLB} =& \frac{1}{4\pi}\frac{\bar{\epsilon}}{(u^0 - \mathbf{v}_\perp\cdot\boldsymbol{u}_\perp)^4},\\ \mathcal{F}^{eq}_{\rm fs} =& \frac{1}{4\pi}\frac{\bar{\epsilon}}{(u^0\Delta_{\rm fs} - \boldsymbol{v}_{\perp;\rm fs}\cdot\boldsymbol{u}_\perp)^4},\end{aligned} \tag{5.111}$$

where $\bar{\epsilon} = \overline{T}^4$.

The system is initialized using the Romatschke-Strickland distribution [176] for Bose-Einstein statistics [177]

$$f_{\rm RS} = \left\{\exp\left[\frac{1}{\Lambda}\sqrt{(p\cdot u)^2 + \xi_0(p\cdot\hat{\eta})^2}\right] - 1\right\}^{-1}, \tag{5.112}$$

where $\hat{\eta}^\mu$ is the unit-vector along the rapidity coordinate. Simplifying to the initial state considered in this Chapter, Eq. (5.112) reduces to

$$f_{\rm RS} = \left[\exp\left(\frac{p^\tau}{\Lambda}\sqrt{1+\xi_0 v_z^2}\right) - 1\right]^{-1}. \tag{5.113}$$

The function $\Lambda \equiv \Lambda(\mathbf{x}_\perp)$ is determined from

$$\Lambda^4(\mathbf{x}_\perp) = 2T^4(\tau_0,\mathbf{x}_\perp)\left(\frac{\arctan\sqrt{\xi_0}}{\sqrt{\xi_0}} + \frac{1}{1+\xi_0}\right)^{-1}, \tag{5.114}$$

where $T(\tau_0,\mathbf{x}_\perp)$ is obtained from the initial energy density $\epsilon(\tau_0,\mathbf{x}_\perp)$ via the equation $\epsilon = aT^4$, where $a = \frac{\pi^2\nu_{\rm eff}}{30}$ for Bose-Einstein statistics. The anisotropy parameter ξ_0 can be used to set the ratio of longitudinal and transverse pressures $\mathcal{P}_{L;0}/\mathcal{P}_{T;0}$ via

$$\frac{\mathcal{P}_{L;0}}{\mathcal{P}_{T;0}} = \frac{2}{1+\xi_0}\frac{(1+\xi_0)\frac{\arctan\sqrt{\xi_0}}{\sqrt{\xi_0}} - 1}{1+(\xi_0-1)\frac{\arctan\sqrt{\xi_0}}{\sqrt{\xi_0}}}. \tag{5.115}$$

The case $\mathcal{P}_{L;0}/\mathcal{P}_{T;0} = 0$ implied by the initial conditions in Eq. (5.3) can be reached only as the limit $\xi_0 \to \infty$. In our simulations, we consider finite (large) values of ξ_0 and, for simplicity, we employ the same value of ξ_0 throughout the whole transverse plane. Since at initial time $\tau = \tau_0$ $p^\tau_{\rm fs} = p^\tau$ and $v_{z;\rm fs} = v_z$, it can be seen that the initial conditions $\mathcal{F}^{\rm RS}_{\rm RLB}$ and $\mathcal{F}^{\rm RS}_{\rm fs}$ are equal and given by

$$\mathcal{F}^{\rm RS}_{\rm RLB} = \mathcal{F}^{\rm RS}_{\rm fs} = \frac{\bar{\epsilon}/2\pi}{(1+\xi_0 v_z^2)^2}\left(\frac{\arctan\sqrt{\xi_0}}{\sqrt{\xi_0}} + \frac{1}{1+\xi_0}\right)^{-1}. \tag{5.116}$$

Momentum space discretization

In this work, we employ the discretization of the momentum space discussed in Ref. [171]. In this scheme, we employ $Q_{\phi_p}\times Q_z$ discrete values for ϕ_p and v_z ($v_{z;\rm fs}$ in the case of the free-streaming variables), such that (ϕ_p, v_z) or $(\phi_p, v_{z;\rm fs})$ are replaced by $(\phi_{p;i}, v_{z;j})$ and $(\phi_{p;i}, v^{\rm fs}_{z;j})$, respectively. The discrete set of distributions $\mathcal{F}^*_{ij}$ (with $*\in\{\rm RLB, fs\}$) are related to the original distribution function $\mathcal{F}_*$, via [171]

$$\begin{pmatrix}\mathcal{F}^{\rm RLB}_{ij}\\ \mathcal{F}^{\rm fs}_{ij}\end{pmatrix} = \frac{2\pi}{Q_{\phi_p}} w_j \begin{pmatrix}\mathcal{F}_{\rm RLB}(\phi_{p;i}, v_{z;j})\\ \mathcal{F}_{\rm fs}(\phi_{p;i}, v^{\rm fs}_{z;j}).\end{pmatrix}. \tag{5.117}$$

The weight $2\pi/Q_{\phi_p}$ is computed in both RLB and fs cases following the prescription of the Mysovskikh (trigonometric) [178] quadrature, by which the trigonometric circle is discretized equidistantly, $\phi_{p;j} = \phi_0 + \frac{2\pi}{Q_{\phi_p}}\left(j - \frac{1}{2}\right)$, with $1 \leq j \leq Q_{\phi_p}$. For definiteness, we set the arbitrary offset ϕ_0 to 0. For the discretization of v_z (RLB) and $v_{z;\mathrm{fs}}$ (FS), we employ two different strategies as discussed below.

RLB case. In the case of large values of $\hat{\gamma}$, when Eq. (5.101) is considered, we employ the Gauss-Legendre quadrature, such that w_j represent the Gauss-Legendre weights and $v_{z;j}$ are the roots of the Legendre polynomial of order Q_z, i.e. $P_{Q_z}(v_{z;j}) = 0$. Their values up to quadrature orders $Q_z = 1000$ can be found in the supplementary material of Ref. [171]. In this approach, the term $\partial[v_z(1-v_z^2)\mathcal{F}_{\mathrm{RLB}}]/\partial v_z$ is computed by projection onto the space of Legendre polynomials,

$$\left[\frac{\partial[v_z(1-v_z^2)\mathcal{F}_{\mathrm{RLB}}]}{\partial v_z}\right]_{ji} = \sum_{j'=1}^{Q_z} \mathcal{K}^P_{j,j'}\mathcal{F}^{\mathrm{RLB}}_{j'i}. \tag{5.118}$$

The matrix elements $\mathcal{K}^P_{j,j'}$, given in Eq. (3.54) of Ref. [171], are

$$\begin{aligned}\mathcal{K}^P_{j,j'} = w_j \sum_{m=1}^{Q_z-3} \frac{m(m+1)(m+2)}{2(2m+3)} P_m(v_{z;j})P_{m+2}(v_{z;j'}) \\ - w_j \sum_{m=1}^{Q_z-1} \frac{m(m+1)}{2} P_m(v_{z;j}) \left[\frac{(2m+1)P_m(v_{z;j'})}{(2m-1)(2m+3)}\right. \\ \left. + \frac{m-1}{2m-1} P_{m-2}(v_{z;j'})\right].\end{aligned} \tag{5.119}$$

The components of the stress-energy tensor are obtained by replacing the integration with respect to $\mathrm{d}\Omega_p$ with a double sum over i and j:

$$\overline{T}^{\mu\nu} = \sum_{i=1}^{Q_{\phi_p}} \sum_{j=1}^{Q_z} \mathcal{F}^{\mathrm{RLB}}_{ij} v^\mu_{ij} v^\nu_{ij}, \tag{5.120}$$

where $v^\tau_{ij} = 1$, $(v^1_{ij}, v^2_{ij}) = \sqrt{1-v^2_{z;j}}(\cos\phi_{p;i}, \sin\phi_{p;j})$ and $v^\eta_{ij} = \tau^{-1}v_{z;j}$. A similar prescription is employed for the computation of the $\mathrm{d}\Omega_p$ integral in the energy-weighted flow harmonics v^E_n (5.103).

FS case. For small values of $\hat{\gamma}$, the free-streaming coordinate $v_{z;\mathrm{fs}}$ is discretized in a logarithmic scale. Inspired from Eq. (A61) of Ref. [80], we first perform the change of coordinate to

$$v_{z;\mathrm{fs}} = \frac{1}{A}\tanh\chi, \tag{5.121}$$

where $0 < A < 1$ and χ takes values between $\pm\mathrm{artanh}\, A$. In order to increase the accuracy of the momentum space integration, we consider the rectangle method and take the discrete values χ_j at the center of the Q_z equidistant intervals, such that

$$\chi_j = \left(\frac{2j-1}{Q_z} - 1\right)\mathrm{artanh} A, \qquad v^{\mathrm{fs}}_{z;j} = \frac{1}{A}\tanh\chi_j. \tag{5.122}$$

The quadrature weights w_j are then computed based on the Jacobian due to the change of integration variable from $v_{z;\mathrm{fs}}$ to χ,

$$w_j = \frac{2\mathrm{artanh}A}{AQ_z \cosh^2 \chi_j}. \tag{5.123}$$

Since the discretization of $v_{z;\mathrm{fs}}$ presented above is no longer given by a Gauss quadrature prescription, we note that the FS approach gives rise to a numerical scheme which is more similar to the Discrete Velocity Method (DVM) approach [179, 180]. As before, the components of the stress-energy tensor can be obtained by replacing the integral with respect to $\mathrm{d}\Omega_p$ in Eq. (5.109) with quadrature sums:

$$\begin{aligned}
\overline{T}^{\tau\tau} =& \frac{\tau_0}{\tau} \sum_{i,j} \Delta_j^{\mathrm{fs}} \mathcal{F}_{ij}^{\mathrm{fs}}, \\
\begin{pmatrix} \overline{T}^{\tau 1} \\ \overline{T}^{\tau 2} \end{pmatrix} =& \frac{\tau_0}{\tau} \sum_{i,j} v_{\perp;j}^{\mathrm{fs}} \begin{pmatrix} \cos\phi_{p;i} \\ \sin\phi_{p;i} \end{pmatrix} \mathcal{F}_{ij}^{\mathrm{fs}}, \\
\begin{pmatrix} \overline{T}^{11} \\ \overline{T}^{12} \\ \overline{T}^{22} \end{pmatrix} =& \frac{\tau_0}{\tau} \sum_{i,j} \frac{(v_{\perp;j}^{\mathrm{fs}})^2}{\Delta_j^{\mathrm{fs}}} \begin{pmatrix} \cos^2\phi_{p,i} \\ \sin\phi_{p,i}\cos\phi_{p,i} \\ \sin^2\phi_{p,i} \end{pmatrix} \mathcal{F}_{ij}^{\mathrm{fs}}, \\
\tau^2 \overline{T}^{\eta\eta} =& \frac{\tau_0^3}{\tau^3} \sum_{i,j} \frac{(v_{z;j}^{\mathrm{fs}})^2}{\Delta_j^{\mathrm{fs}}} \mathcal{F}_{ij}^{\mathrm{fs}},
\end{aligned} \tag{5.124}$$

where $\Delta_j^{\mathrm{fs}} = [1-(1-\tau_0^2/\tau^2)(v_{z;j}^{\mathrm{fs}})^2]^{1/2}$ and $v_{\perp;j}^{\mathrm{fs}} = \sqrt{1-(v_{z;j}^{\mathrm{fs}})^2}$. A similar procedure is employed for the computation of v_n^E (5.103).

Finite difference schemes

In order to obtain the numerical solution of Eqs. (5.101) and (5.108), we consider an equidistant discretization of the temporal and spatial variables. Setting the time step as $\delta\tau$, the time coordinate is discretized according to $\tau_n = \tau_0 + n\delta\tau$. Writing the Boltzmann equation as

$$\frac{\partial \mathcal{F}}{\partial \tau} = L[\mathcal{F}], \tag{5.125}$$

where $L[\mathcal{F}]$ can be found from Eqs. (5.101) or (5.108), we employ the third-order total variation diminishing (TVD) Runge-Kutta method proposed in Ref. [181, 182]. This algorithm allows the values $\mathcal{F}_{n+1}$ of the distribution functions at the new time step to be obtained from the old ones using two intermediate stages.

The advection along the transverse directions is performed using the flux-based upwind-biased fifth order weighted essentially non-oscillatory (WENO-5) scheme [183, 184]. Considering that the spatial domain of extent $L_1 \times L_2$ is discretized using $N_1 \times N_2$ equidistant nodes, the coordinates of the discrete points are

$$\begin{aligned}
x_{1,s} =& x_{1,\mathrm{left}} + \frac{L_1}{N_1}\left(s - \frac{1}{2}\right), \\
x_{2,r} =& x_{2,\mathrm{bot}} + \frac{L_2}{N_2}\left(r - \frac{1}{2}\right),
\end{aligned} \tag{5.126}$$

with $1 \leq s \leq N_1$ and $1 \leq r \leq N_2$. Focusing without loss of generality on the derivative with respect to x_1, the algorithm entails

$$c_1 \left(\frac{\partial \mathcal{F}}{\partial x_1} \right)_{s,r} = \frac{\mathbb{F}_{s+\frac{1}{2},r} - \mathbb{F}_{s-\frac{1}{2},r}}{\delta x_1}, \tag{5.127}$$

where $\delta x_1 = L_1/N_1$. The velocity c_1 is given in the case when $\hat{\gamma}$ is large, when Eq. (5.101) is solved, by $c_1 = \sqrt{1 - v_z^2} \cos\phi_p$, being independent of position and space. In the case of small values of $\hat{\gamma}$, Eq. (5.108) shows that the advection velocity $c_1 = \frac{1}{\Delta}\sqrt{1 - \tilde{v}_z^2} \cos\phi_p$ depends on the Bjorken time τ, however it remains constant throughout the entire transverse plane. The stencils required to compute the fluxes $\mathbb{F}_{s\pm\frac{1}{2},r}$ are chosen in an upwind-biased manner based on the sign of c_1. Since the algorithm to compute these stencils is rather lengthy, we do not repeat it here and instead refer the interested reader to Refs. [171, 183–185] for details.

5.4 Results

We will now analyze the space-time evolution of the system and the development of transverse flow as a function of the opacity parameter $\hat{\gamma}$ (c.f. Eq. (5.23)). We focus on the range of opacities $0.01 \leq \hat{\gamma} \leq 400$ and consider different initial eccentricities $\epsilon_n \in \{0.01, 0.05, 0.1, 0.2, 0.32, 0.36\}$ (c.f. Eqns. (5.6,5.7)).

If not stated otherwise, open symbols/dashed lines correspond to results obtained using the expansion in spherical harmonic moments in Sec. 5.3.1, where we typically use $l_{\max} = 32$,$N_S = 256$, $a_S = 0.0625\ R$.[7] Conversely, results obtained with the relativistic lattice Boltzmann (RLB) method are represented by solid symbols/solid lines. The RLB simulations are divided in two batches. The first batch includes systems with $\hat{\gamma} \geq 2$. For these simulations, we used the RLB algorithm for large $\hat{\gamma}$ described in Sec. 5.3.2 with $Q_z = 40$ and $Q_{\phi_p} = 80$, while the number of nodes on each semiaxis is taken to be $X = 100$ for $\epsilon_n \geq 0.05$ and $X = 200$ for $\epsilon_n < 0.05$. The anisotropy parameter in the initial state is set to $\xi_0 = 20$, corresponding to an initial ratio $\mathcal{P}_L/\mathcal{P}_T \simeq 0.08$. The second batch comprises the systems with $\hat{\gamma} \leq 2$ for which we employ the hybrid free-streaming algorithm described in Sec. 5.3.2 with $Q_z = 500$ and $Q_{\phi_p} = 80$. In this case, the anisotropy parameter is set to $\xi_0 = 100$, corresponding to $\mathcal{P}_L/\mathcal{P}_T \simeq 0.02$ and the spatial resolution is $X = 100$ nodes per semiaxis.

5.4.1 Cooling due to longitudinal expansion ($dE_\perp/d\eta$)

Before we discuss the development of transverse flow, we first investigate the cooling of the system due to work performed against the longitudinal expansion, which is quantified by the decrease of the transverse energy per rapidity $\mathrm{d}E_\perp/\mathrm{d}\eta$. We first note that for a free-streaming system $\mathrm{d}E_\perp/\mathrm{d}\eta$ is constant. Increasing the opacity will initially only have a small effect, which can be quantified in terms of the linear decrease in $\hat{\gamma}$ calculated in Sec. 5.2.5. However, for large opacities $\hat{\gamma} \gg 1$, the system has sufficient time to undergo pressure isotropization at early times, leading to an extended phase of longitudinal cooling, which results in a significant decrease of $\mathrm{d}E_\perp/\mathrm{d}\eta$. Hence, when presenting our results for $\mathrm{d}E_\perp/\mathrm{d}y(\tau)$ in Fig. 5.1, we have grouped them into two plots for large opacities in the upper panel and small opacities in the lower panel. While for large opacities, the curves are normalized by the initial value $\mathrm{d}E_\perp^{(0)}/\mathrm{d}\eta$ and

[7] We note that results for $\hat{\gamma} \leq 1$ require a larger accuracy, and we use $l_{\max} = 48$,$N_S = 320$, $a_S = 0.05\ R$. Similarly, for accurate calculations of $\mathrm{d}E_\perp/\mathrm{d}y$ we need a larger value of $l_{\max}$ and we employ $l_{\max} = 96$,$N_S = 160$, $a_S = 0.06\ R$ in this case.

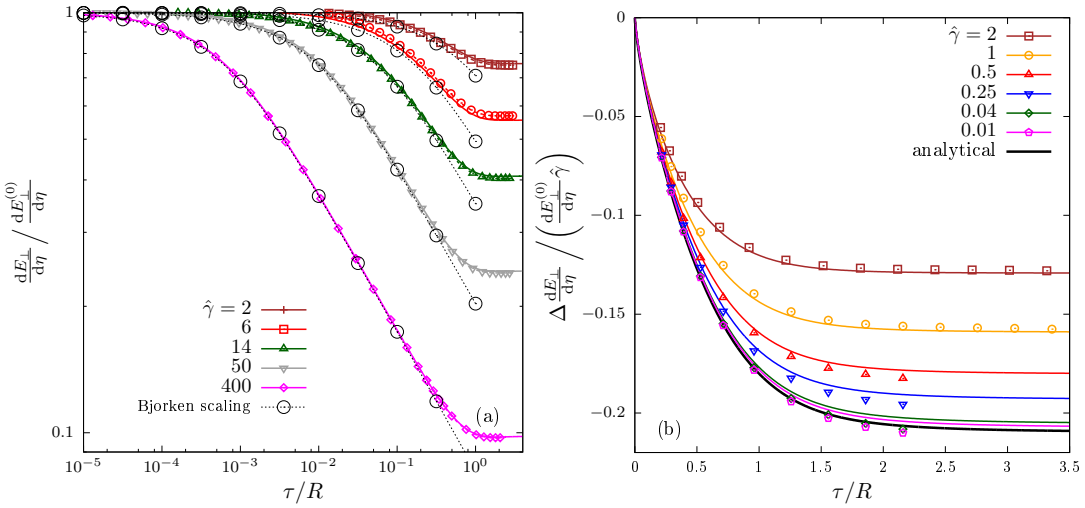

FIGURE 5.1: Evolution of $dE_\perp/d\eta$ (left) and $\Delta dE_\perp/d\eta = dE_\perp/d\eta - dE_\perp^{(0)}/d\eta$ (right) normalized with respect to the initial value $dE_\perp^{(0)}/d\eta$ for various large (left) and small opacities (right). Colored solid lines were obtained with the RLB method, while open symbols denote results from the moment method. The solid black line shows the first order result in opacity expansion. Dashed black lines with black circles corresponds to the Bjorken flow prediction derived in Eq. (4.36), and the curves in the top are presented on double logarithmic scale. All results are obtained for initial eccentricity $\epsilon_2 = 0.05$.

plotted on a doubly logarithmic scale to visualize the power law decay of $\mathrm{d}E_\perp/\mathrm{d}\eta$ at intermediate times, for small opacities we show the difference of $\mathrm{d}E_\perp/\mathrm{d}\eta - \mathrm{d}E_\perp^{(0)}/\mathrm{d}\eta$, normalized by the initial value and $\hat{\gamma}$ to account for the linear behaviour in opacity. We also show a comparison with the analytical result from Section 5.2.5, which provides a good description of the curves for $\hat{\gamma} \lesssim 1$.

Qualitatively, all curves exhibit a similar behavior starting out from the early time fixed point of kinetic theory, where longitudinal pressure vanishes and energy per rapidity stays almost constant. Subsequently, as longitudinal pressure develops due to interactions work is being performed, which starts to happen earlier and earlier the larger the opacity. Eventually, at late times $\tau/R \gtrsim 1$, the transverse expansion becomes dominant and the system rapidly cools down, resulting in a late time plateau of the $\mathrm{d}E_\perp/\mathrm{d}\eta(\tau)$-curves.

We find that for large opacities $\hat{\gamma} \gtrsim 10$, the pressure isotropization at early times and the onset of the transverse expansion at later times are sufficiently well separated to observes an intermediate $\tau^{-1/3}$-scaling of $\mathrm{d}E/\mathrm{d}\eta$, which is due to the early time Bjorken flow behaviour discussed in Section 4.1.1. The local Bjorken flow attractor scaling scheme can be applied to this setup. Specifically, the behaviour of $\mathrm{d}E_\perp/d\eta$ can be predicted using the formula given in Eq. (4.36), which is indicated by black circles in the upper panel of Fig. 5.1 and agrees remarkably well with numerical results for the large opacities up to times $\tau/R \lesssim 0.1$.

Local Bjorken flow scaling predicts that $dE_\perp/d\eta$ decreases as $\tau^{-1/3}$ at intermediate times, before the transverse expansion becomes dominant. By comparing the results in Fig. 5.1, one finds that for sufficiently large opacities the power law behavior in Eq. (4.37) is indeed realized at intermediate times, and discontinues once $\tau/R \simeq 1$, when the transverse expansion becomes dominant, such that the estimate (4.37) is no longer applicable and $\frac{dE_\perp/d\eta}{dE_\perp^0/d\eta}$ attains a constant asymptotic value.

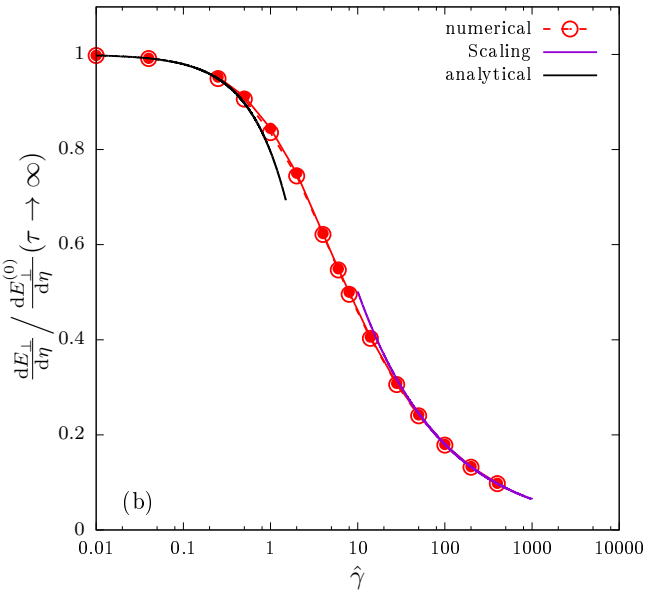

FIGURE 5.2: Opacity ($\hat{\gamma}$) dependence of the ratio of final to initial (transverse) energy per-unit rapidity $\frac{dE_\perp}{d\eta} \Big/ \frac{dE_\perp^{(0)}}{d\eta}$. The red solid line with filled circles denotes results from the RLB method, while the red dotted line with open circles was obtained in the moment method. Numerical results are compared to analytical results obtained in leading order opacity expansion (black solid curve), and a power-law scaling fit $\frac{dE_\perp}{d\eta} \Big/ \frac{dE_\perp^{(0)}}{d\eta} \approx 1.4\,\hat{\gamma}^{-4/9}$ at large opacities (purple solid line)

.

We note that our estimate in Eq. (4.37) also shows that for sufficiently large opacities, where longitudinal cooling occurs predominantly before the transverse expansion sets in, the final value of $\frac{dE_\perp/d\eta}{dE_\perp^0/d\eta}$ is propotional to $\hat{\gamma}^{-4/9}$, as previously argued in [80]. Numerical results for the asymptotic values of $\frac{dE_\perp/d\eta}{dE_\perp^0/d\eta}$, extracted by performing extrapolations of the curves of the form $a+b\tilde{\tau}^{-c}$, where a, b and c are fitting parameters, are shown in Fig. 5.2 as a function of the opacity parameter $\hat{\gamma}$. We find that at low $\hat{\gamma}$, the analytical result to leading order in opacity (c.f. Eq. (5.70)), represented with a solid black line, provide an accurate description up to $\hat{\gamma} \lesssim 1$. Conversely, for large opacities $\hat{\gamma}$, the decrease of the energy per unit rapidity $\frac{dE_\perp/d\eta}{dE_\perp^0/d\eta}$ exhibits the expected scaling behavior, with $\frac{dE_\perp/d\eta}{dE_\perp^0/d\eta} \approx 1.4\ \hat{\gamma}^{-4/9}$ for $\hat{\gamma} \gtrsim 10$, as indicated by the purple line. By comparing the numerical coefficient with Eq. (4.37), this result seems to indicate that cooling stops at a time $\tau_{\rm stop} \simeq 0.6R$, which is consistent with the trend seen for the high $\hat{\gamma}$ curves in Fig. 5.1(a).

5.4.2 Development & opacity dependence of transverse flow harmonics (v_n)

Next, we will analyze the development of anisotropic flow in terms of the time dependence of the harmonic transverse flow coefficients v_n^E for different opacities. We recall, that the initial anisotropies are modeled using a single harmonic (n) perturbation and first look at the time dependence of v_2^E, v_3^E and v_4^E for different opacities, where in each case the eccentricities are fixed to $\epsilon_n = 0.05$, which serves as a good approximation to the small eccentricity limit. We measure the magnitude of the linear response

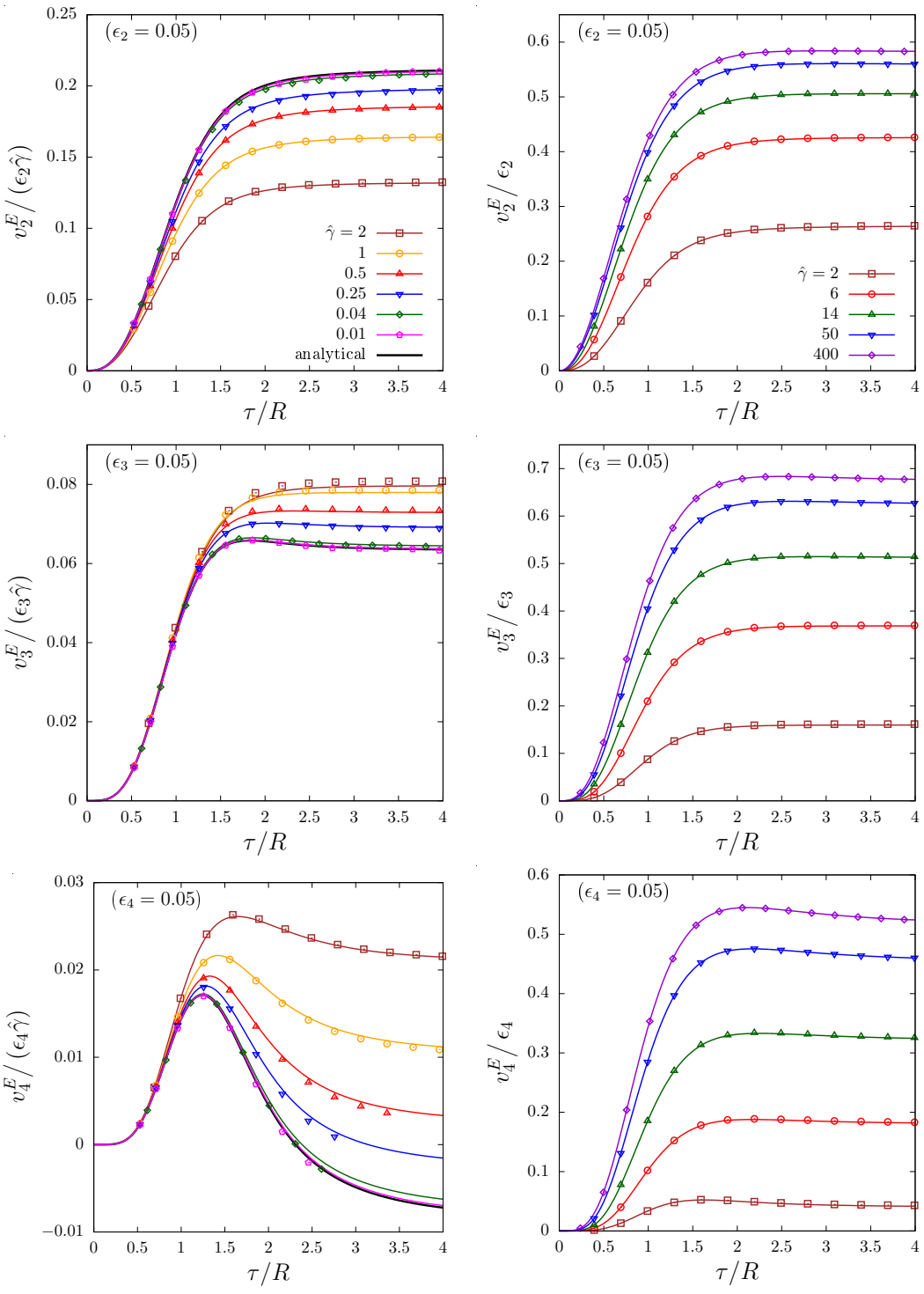

FIGURE 5.3: Evolution of the linear flow response $v_n^E/\epsilon_n\hat{\gamma}$ at small opacities $\hat{\gamma}$ (left) and v_n^E/ϵ_n at large opacities $\hat{\gamma}$ (right). Different rows correspond to elliptic flow $n = 2$ (top), triangular flow $n = 3$ (middle) and quadrangular flow $n = 4$ (botom). Colored solid lines were obtained in the RLB method, while open symbols denote results from the moments method. Analytical results are plotted as solid black lines. All results were obtained for an initial eccentricity $\epsilon_n = 0.05$.

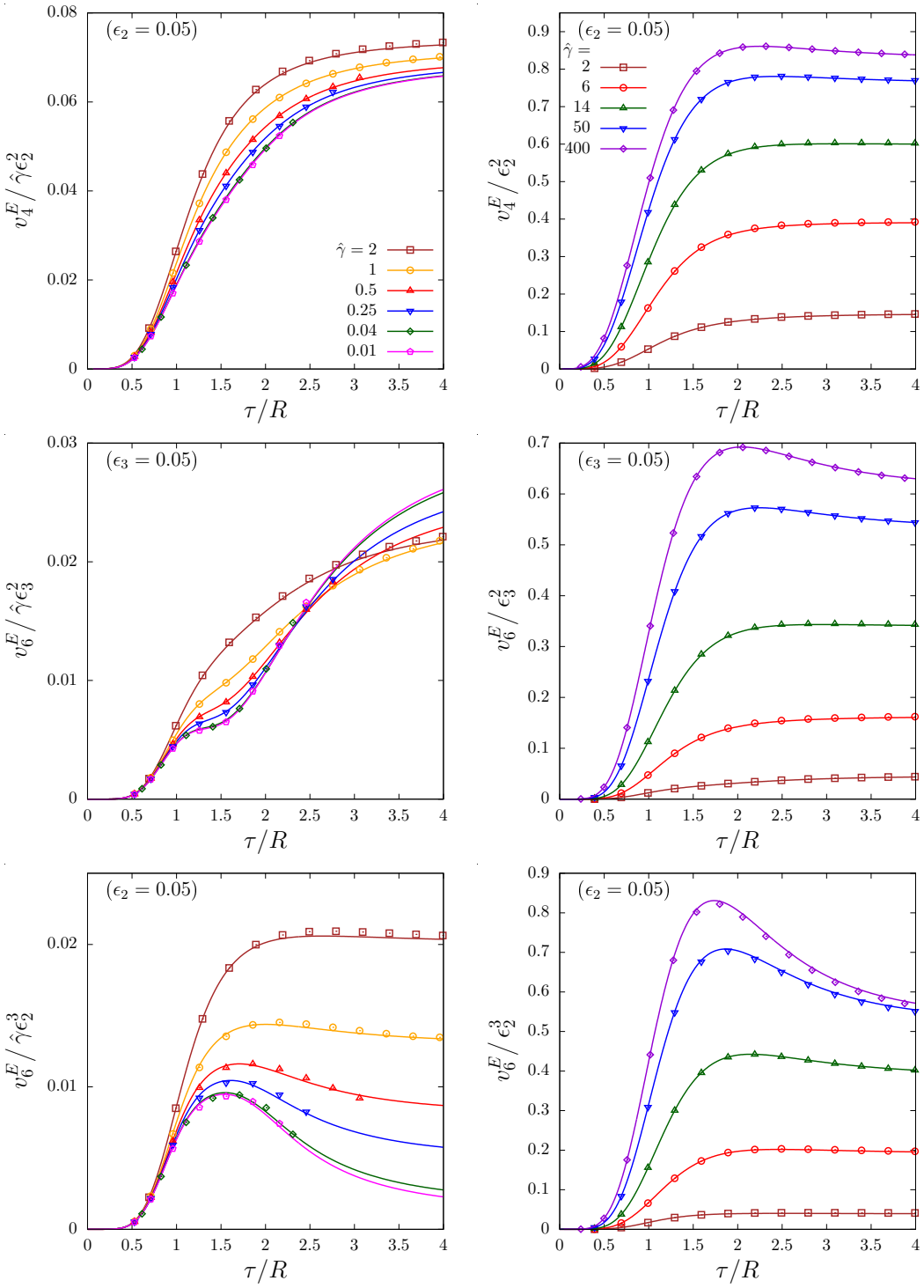

FIGURE 5.4: (top line) Evolution at low opacities of the non-linear flow response coefficients $v_4^E/\epsilon_2^2\hat{\gamma}$ (left), $v_6^E/\epsilon_3^2\hat{\gamma}$ (middle), and $v_6^E/\epsilon_2^3\hat{\gamma}$ (right). (bottom line) Evolution at large opacities of v_4^E/ϵ_2^2, v_6^E/ϵ_3^2 (middle), and v_6^E/ϵ_2^3 (right). Colored solid lines were obtained in the RLB method, while open symbols denote results from the moments method. All results were obtained for an initial eccentricity $\epsilon_n = 0.05$.

ratio v_n/ϵ_n for each harmonic; in addition we also extract the non-linear response of the fourth and sixth order harmonics via the ratios v_4/ϵ_2^2, v_6/ϵ_3^2 and v_6/ϵ_2^3.

Since the qualitative behaviour of v_n is somewhat different in the regimes of small and large opacities $\hat{\gamma}$, we again divide our results into two categories corresponding to $\hat{\gamma} \geq 2$ and $\hat{\gamma} \leq 2$, as in Fig. 5.1. Since the analytical calculation in Sec. 5.2 indicates that at small $\hat{\gamma}$, all response coefficients increase linearly with $\hat{\gamma}$, we will further normalize our low opacity results ($\hat{\gamma} \leq 2$) by division with respect to $\hat{\gamma}$.

Our results are compactly summarized in Figs. 5.3 and 5.4, where we present numerical results for the linear $(v_2/\epsilon_2, v_3/\epsilon_3, v_4/\epsilon_4)$ and non-linear $(v_4/\epsilon_2^2, v_6/\epsilon_3^2, v_6/\epsilon_2^3)$ response coefficients obtained for small (top panels) and large (bottom panels) values of $\hat{\gamma}$. We find that for small values of $\hat{\gamma} \lesssim 0.04$, the leading order linear dependence of v_n/ϵ_n on $\hat{\gamma}$ computed in Eq. (5.71-5.73) is nicely confirmed by the asymptotic approach of our numerical results to the analytical results, represented by a solid black line. Similarly, a linear dependence with respect to $\hat{\gamma}$ is also found for the non-linear response coefficients $v_4/\epsilon_2^2, v_6/\epsilon_3^2, v_6/\epsilon_2^3$, which for v_4/ϵ_2^2 is in line with the result obtained in Ref. [78] for a slightly different initial setup. While for $\hat{\gamma} \gtrsim 0.25$, all linear flow coefficients exhibit a positive response with respect to the initial eccentricities, the quadrangular flow $v_4/\epsilon_4\hat{\gamma}$ in Fig. 5.3 shows a negative response for $\hat{\gamma} \lesssim 0.25$.

Based on a closer inspection, one finds that the curves of $v_4/(\epsilon_4\hat{\gamma})$ exhibit an early time increase similar to the behavior seen for the other harmonic flow coefficients, however in contrast to v_2, v_3 the initial rise of v_4 peaks around $\tau \simeq 1.5R$, followed by a decrease due to negative contributions received at large times. When increasing the opacity, non-linear effects cause the elliptic flow response $v_2/(\epsilon_2\hat{\gamma})$ to decrease, while $v_3/(\epsilon_3\hat{\gamma})$, $v_4/(\epsilon_4\hat{\gamma})$ as well as the non-linear $v_4/(\epsilon_2^2\hat{\gamma})$ and $v_2/(\epsilon_2^3\hat{\gamma})$ exhibit an increasing trend; due to the rather complicated time dependence, the behavior of $v_6/(\epsilon_3^2\hat{\gamma})$ appears non-monotonic. Clearly, the largest effect is seen in the case of the v_4/ϵ_4-response which changes sign as the late time contributions become less and less prominent.

When considering large opacities $\hat{\gamma} \gtrsim 2$ shown in the bottom panels of Figs. 5.3 and 5.4, the curves for linear $(v_2/\epsilon_2, v_3/\epsilon_3, v_4/\epsilon_4)$ and non-linear $(v_4/\epsilon_2^2, v_6/\epsilon_3^2, v_6/\epsilon_2^3)$ response coefficients retain the same qualitative time dependence and monotonically increase as a function of $\hat{\gamma}$, seemingly approaching a finite large opacity limit, which we will further examine in the following. Generally, we find that the linear anisotropic flow response develops pre-dominantly in the regime $0.5 \lesssim \tau/R \lesssim 2$ and then stay almost constant, with the exception of the aforementioned late time decrease of linear v_4. In the case of the non-linear coefficients $v_4/\epsilon_2^2, v_6/\epsilon_3^2$ and v_6/ϵ_2^3 the response takes a little longer to develop, but nevertheless the asymptotic late time value is reached on similar timescales $0.5 \lesssim \tau/R \lesssim 4$.

Beyond the time evolution of the different flow harmonics, additional insights into the development of anisotropic flow can be gained from their production rates $p(v_n)$, which correspond the local rate of change of these quantities. Since free-streaming and longitudinal expansion do not change the (transverse) momentum distribution of particles, the build up of anisotropic flow is solely due to interactions. We can thus determine the production rate $p(O)$ of a flow observable $O = \int d^2x_\perp \int \frac{\mathrm{d}^3p}{(2\pi)^3}\, \mathcal{O}\, f$ as

$$p(O) = \left.\frac{\mathrm{d}O}{\mathrm{d}x_\perp \mathrm{d}\tau}\right|_{\mathrm{coll}} = \int \mathrm{d}\phi_{x_\perp}\, x_\perp \int \frac{\mathrm{d}^3p}{(2\pi)^3}\, \mathcal{O}\, \left.\frac{\mathrm{d}}{\mathrm{d}\tau} f\right|_{\mathrm{coll}}, \tag{5.128}$$

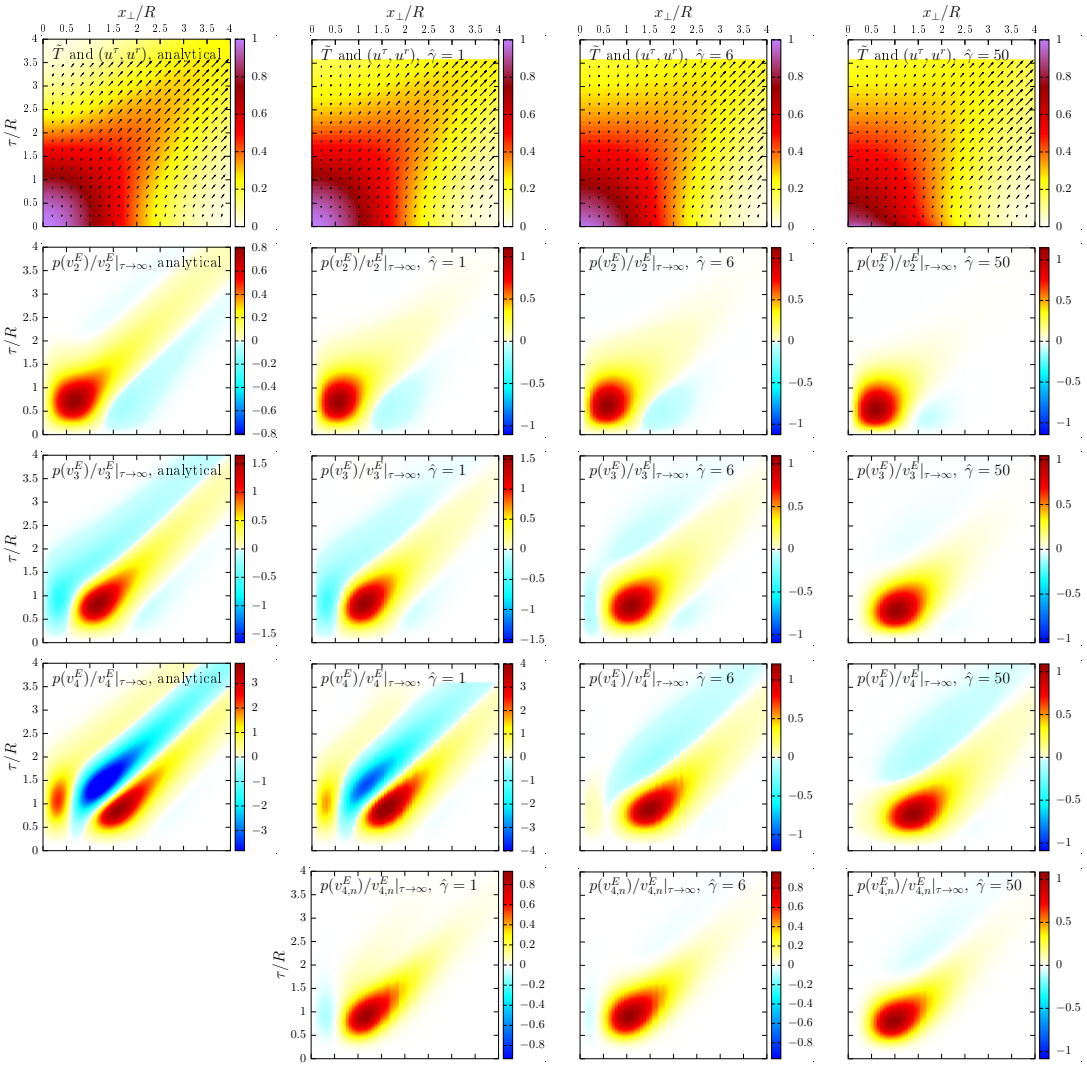

FIGURE 5.5: (top row) Space-time profiles of the effective temperature $\tilde{T}$ along with the temporal and radial components of the vector field u^μ, presented in the $x_\perp$-τ-plane for $\epsilon_n = 0.05$. (bottom rows) Space-time profiles of the production rates of linear v_2^E, v_3^E and v_4^E response (second to fourth row) as well as nonlinear v_4^E response (fifth row) . Numerical results were obtained in the moment method.

where the rate of change of the phase-space distribution f due to collisions is given by

$$\left.\frac{\mathrm{d}}{\mathrm{d}\tau}f\right|_{\mathrm{coll}} = \frac{v^\mu u_\mu}{\tau_R}(f_{eq} - f)\,. \tag{5.129}$$

Specifically, the observables v_n^E are defined according to Eq. (3.41) as quotients of two such terms, such that the production rate $p(O)$ receives two contributions coming from the numerator and denominator according to the quotient rule for differentiation.

Fig. 5.5 features heat maps in the $x_\perp$-τ-plane for $p(v_2)$, $p(v_3)$ and $p(v_4)$ as well as $p(v_{4,n})$ referring to the nonlinear response, normalized by the respective late time asymptotic values of v_n for several different opacities ranging from the analytical results for small opactites $\hat{\gamma} \ll 1$ all the way to $\hat{\gamma} = 50$. Besides the production rates of different v_n, the top panel of Fig. 5.5, also shows a heat-map of the dimensionless temperature $\tilde{T}$ and the flow components u^τ and u^r to allow for a comparison with the spatial distribution and expansion of the system. The latter showcase how with increasing opacity, the system cools more rapidly in the center and the transverse expansion proceeds much slower, resulting in a longer lifetime of the central fireball. Strong correlations of the temperature profile in τ and $x_\perp$ only develop at much later times when compared to the free streaming limit, which exhibits a prominent diagonal line in the $\tilde{T}$-heatmap. Inspection of the $p(v_n)$-heatmaps reveals that different regions in the $x_\perp$-τ-plane contribute with different signs to the development of anisotropic flow v_n. By comparing the results for v_2, v_3 and v_4, one also observes that for larger n the relevant regions extend more towards larger $x_\perp$, while at the same time more of these regions appear, causing large cancellations between the different contributions. Specifically for small opacitites, the structure of the heatmaps of the v_n production rates can be related to the weight

$$\begin{aligned}
&|\mathbf{x}_\perp - \mathbf{v}_\perp \Delta\tau|^n \cos(n\phi_{\mathbf{x}_\perp - \mathbf{v}_\perp\Delta\tau, \mathbf{n}_\perp}) \\
&= \sum_{j=0}^{n} (-1)^j \binom{n}{j} x_\perp^n \left(\frac{\Delta\tau}{x_T}\right)^j \Big[\cos(n\phi_{\mathbf{x}_\perp\mathbf{n}_\perp})\cos(j\phi_{\mathbf{x}_\perp\mathbf{p}_\perp}) - \sin(n\phi_{\mathbf{x}_\perp\mathbf{n}_\perp})\sin(j\phi_{\mathbf{x}_\perp\mathbf{p}_\perp})\Big]
\end{aligned} \tag{5.130}$$

with which the anisotropic perturbations of the initial phase-space distribution propagate in free streaming. Since the evolution of the perturbation is expressed as a sum of $n+1$ terms containing different powers of $\Delta\tau/x_\perp$ with alternating signs, it will divide the $x_\perp$-τ-plane into $n+1$ regions of alternating signs depending on which one of these terms dominates. In addition, the production of the anisotropic flow v_ns will be weighted with the local effective temperature $\tilde{T}$ of the system, such that for small opacities most of the contributions originate from the $\tau \sim x_\perp$ diagonal, so only $\Delta\tau/x_\perp$-terms that dominate close to that region will have a significant impact on the total $v_n(\tau)$. Specifically, for $n = 2$, there is only one dominant term, which explains the monotonic increase of v_2 as a function of time seen in Fig. 5.3. Conversely, for $n = 3$, one positive and one negative contribution are competing, with the positive one being slightly larger than the negative one, which is why for small opacities v_3/e_3 is significantly smaller than v_2/e_2 and features a slight negative trend at late times. Finally, in the case of $n = 4$, there are three relevant terms. At early times, the two positive contribution from the inner and outer border of the system win and v_4 increases, but the one negative contribution surrounded by them in the $x_\perp$-τ-plane is closest to the diagonal and dominates at late times, resulting in a sign change for v_4

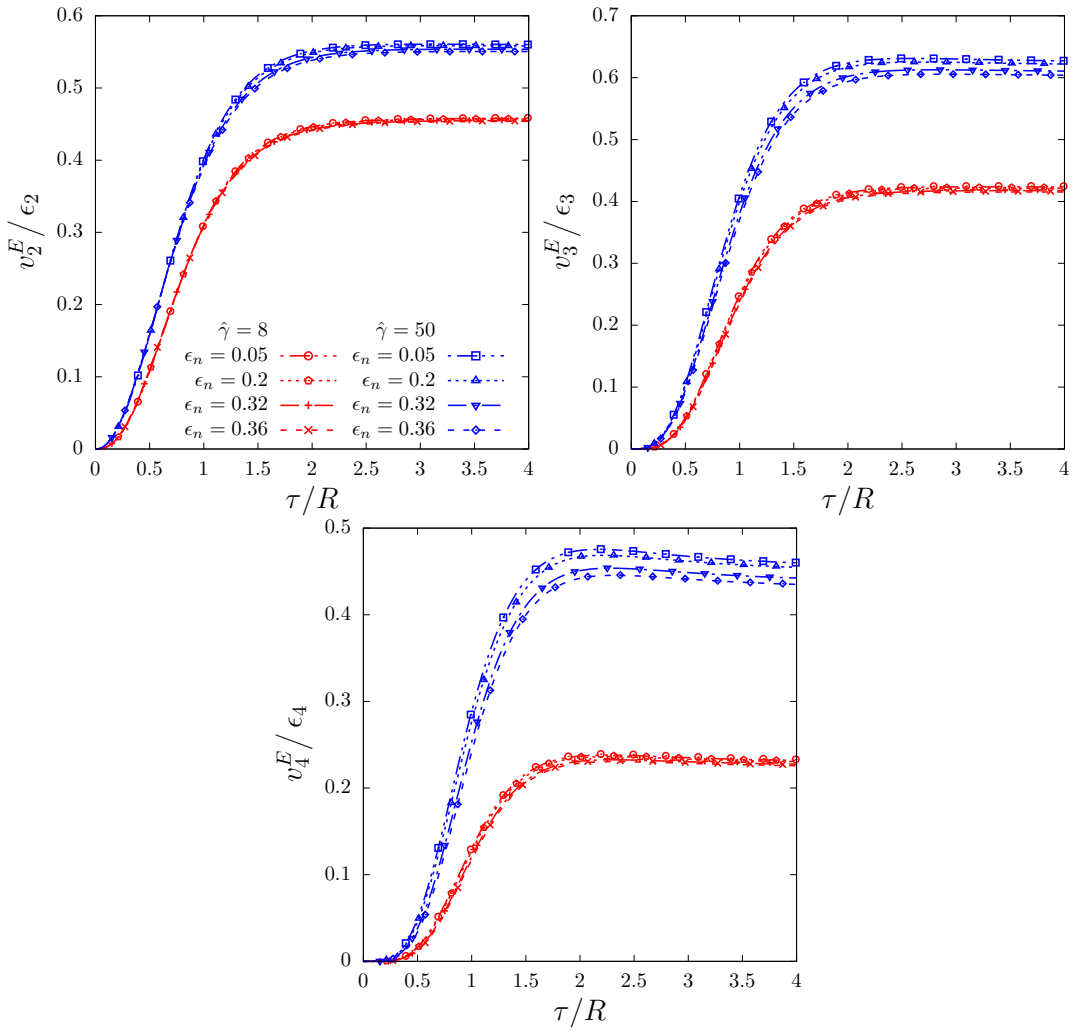

FIGURE 5.6: Linear response coefficients v_n^E/ϵ_n for elliptic flow $n = 2$ (top left), triangular flow $n = 3$ (top right) and quadrangular flow $n = 4$ (bottom) as a function of τ/R for different opacities $\hat{\gamma} = 8$ and $\hat{\gamma} = 50$ and various different eccentricities ϵ_n. Lines denote results from the RLB method and symbols show results from the moment method.

observed for the smallest opacities in Fig. 5.3.

With increasing opacity one observes a clear change in the shapes of the regions, resulting in a shift of v_n production towards earlier τ and smaller $x_\perp$ in Fig. 5.5. However, more strikingly the increase of opacity also leads to a change of the relative weights of different regions, developing towards a scenario with only one dominant positive contribution for all the v_ns at large opacity.

We finally note that the weighting with the effective temperature $\tilde{T}$ plays an important role in this mechanism, such that a different initial condition could result in different relative weights of the regions with different sign of the production rates, which can have notable effects on the buildup of the different flow harmonics. Clearly, one should expect that the higher order flow harmonics, where more cancellations appear are more sensitive to changes of the initial conditions, and indeed we find that varying the parameter α that controls the radial profile (c.f. Sec. 5.1.1) will have a notable influence on the $v_3(\tau)$ and $v_4(\tau)$-curves at small opacities.

Beyond the opacity dependence, one may also examine how the development of

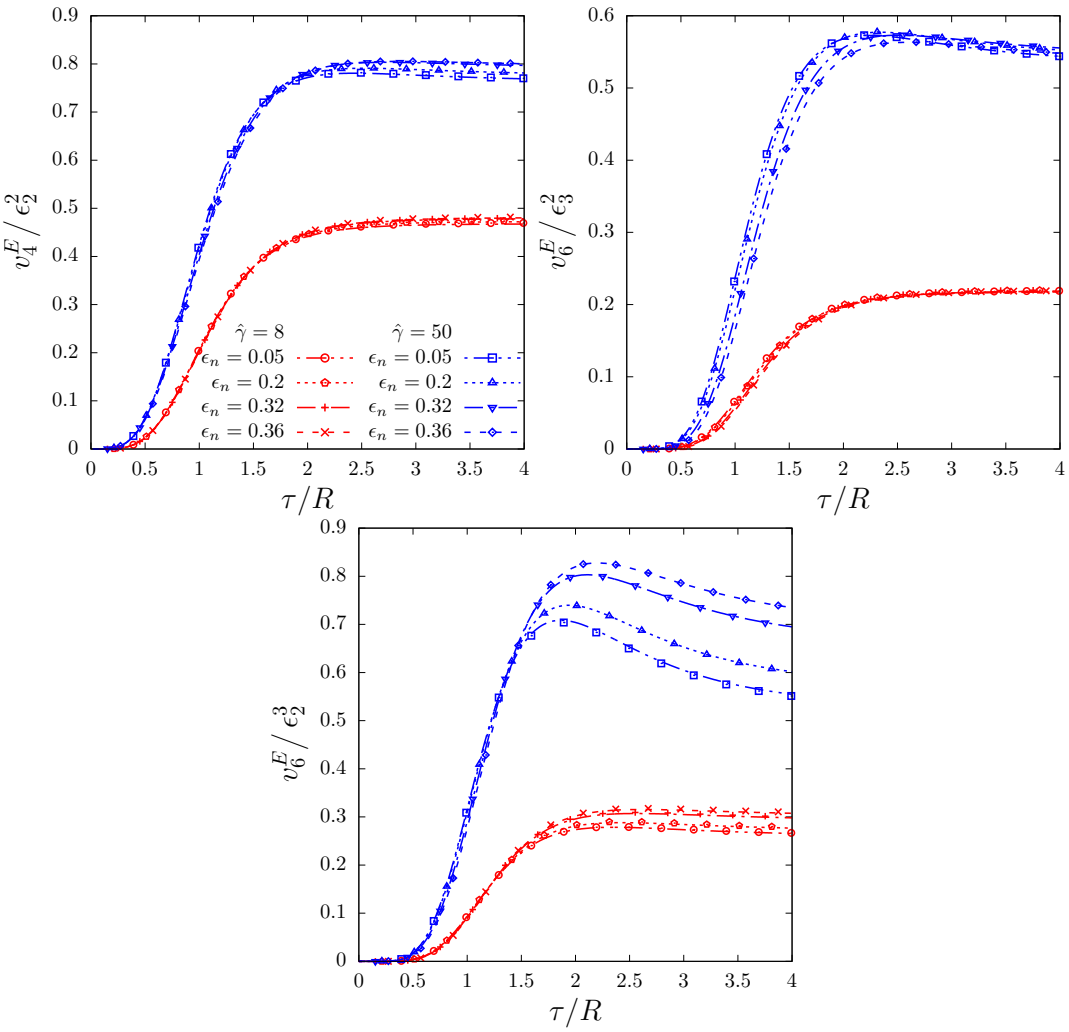

FIGURE 5.7: Non-linear response coefficients v_4^E/ϵ_2^2 (top right), v_6^E/ϵ_3^2 (top left) and v_6^E/ϵ_2^3 (bottom) as a function of τ/R for different opacities $\hat{\gamma} = 8$ and $\hat{\gamma} = 50$ and various different eccentricities ϵ_n. Lines denote results from the RLB method and symbols show results from the moment method.

anisotropic flow $v_n(\tau)$ changes with the amplitude ϵ_n of the respective initial eccentricity. Fig. 5.6 and 5.7 showcase how the curves of normalized flow spread with eccentricity for two representative fixed values of $\hat{\gamma}$. Somewhat surprisingly, we find that the curves exhibit only very small deviations from an entirely linear (quadratic) dependence on eccentricity in the linear v_2, v_3 and v_4 (quadratic v_4 and v_6) flow response, even for rather large eccentricities. The only response featuring a significant dependence on eccentricity is the cubic v_6 response to ϵ_2. While this holds true not only for the final values but also for the entire build up and evolution as a function of τ/R, we remark however, that these findings are probably specific to the particularly simple geometry considered in our setup, and it will therefore be important to extend such systematic studies of the opacity dependence of the flow response towards more realistic profiles of the transverse geometry.

Next, in order to further scrutinize the eccentricity dependence, we extract the extrapolated final values of v_n/ϵ_n resp. nonlinear v_4/ϵ_2^2, v_6/ϵ_3^2 and v_6/ϵ_2^3 at late times and plot them as a function of the square of the relevant eccentricity for several different opacities. Our results shown in Fig. 5.8 and 5.9 again confirm the surprisingly small deviations from perfect linear (quadratic) scaling of the flow response, with only

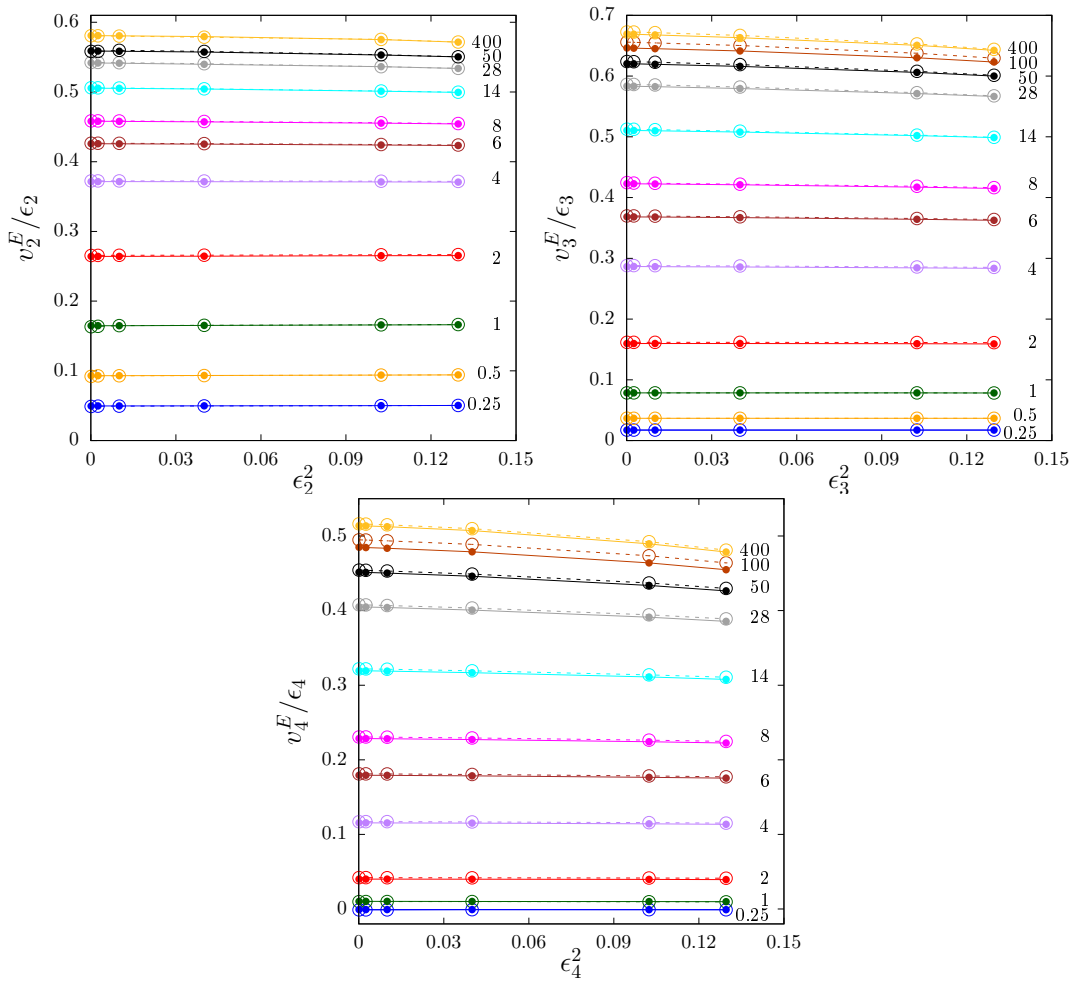

FIGURE 5.8: Eccentricity ϵ_n-dependence of the linear response coefficients $\kappa_{n,n} = v_n^E(\tau \to \infty)/\epsilon_n$ for elliptic flow $n = 2$ (top left), triangular flow $n = 3$ (top right) and quadrangular flow $n = 4$ (bottom). Solid lines with filled circles denote results from the RLB method, while dotted lines with open circles were obtained in the moment method.

very slight negative (positive) trends at large opacity and eccentricity. Our results in Fig. 5.8 appear to be in conflict with results previously obtained by Kurkela et al. [15] in the same setup. We note once again, that although the absence of significant non-linearity in the eccentricities may seem in conflict with conventional knowledge (see e.g. [86, 163, 164]), we attribute this to the specific initial conditions considered within our setup, and we have explicitly checked that hydrodynamic simulations of the same initial conditions also lead to similar results for v_2/ϵ_2. Vice versa, the absence non-linearities within our setup also indicates that the significant non-linearity observed for more realistic initial state models should be attributed to other features of the initial states considered in hydrodynamic simulations of heavy-ion collisions, which are not solely characterized in terms of the usual eccentricties.

Since the flow response to the initial eccentricity is essentially linear within our setup, our findings for the development of transverse flow can be compactly summarized in Fig. 5.10, where we present results for the $\hat{\gamma}$-dependence of the response coefficients $\kappa_{n,n} = \lim_{\epsilon_n \to 0} v_n/\epsilon_n$ as well as $\kappa_{4,22} = \lim_{\epsilon_2 \to 0} v_4/\epsilon_2^2$, $\kappa_{6,33} = \lim_{\epsilon_3 \to 0} v_6/\epsilon_3^2$ and $\kappa_{6,222} = \lim_{\epsilon_2 \to 0} v_6/\epsilon_2^3$ estimated from our data at $\epsilon = 0.05$. Besides the numerical results, we also indicate the linearized analytical approximation in Eqns. (5.71-5.73)

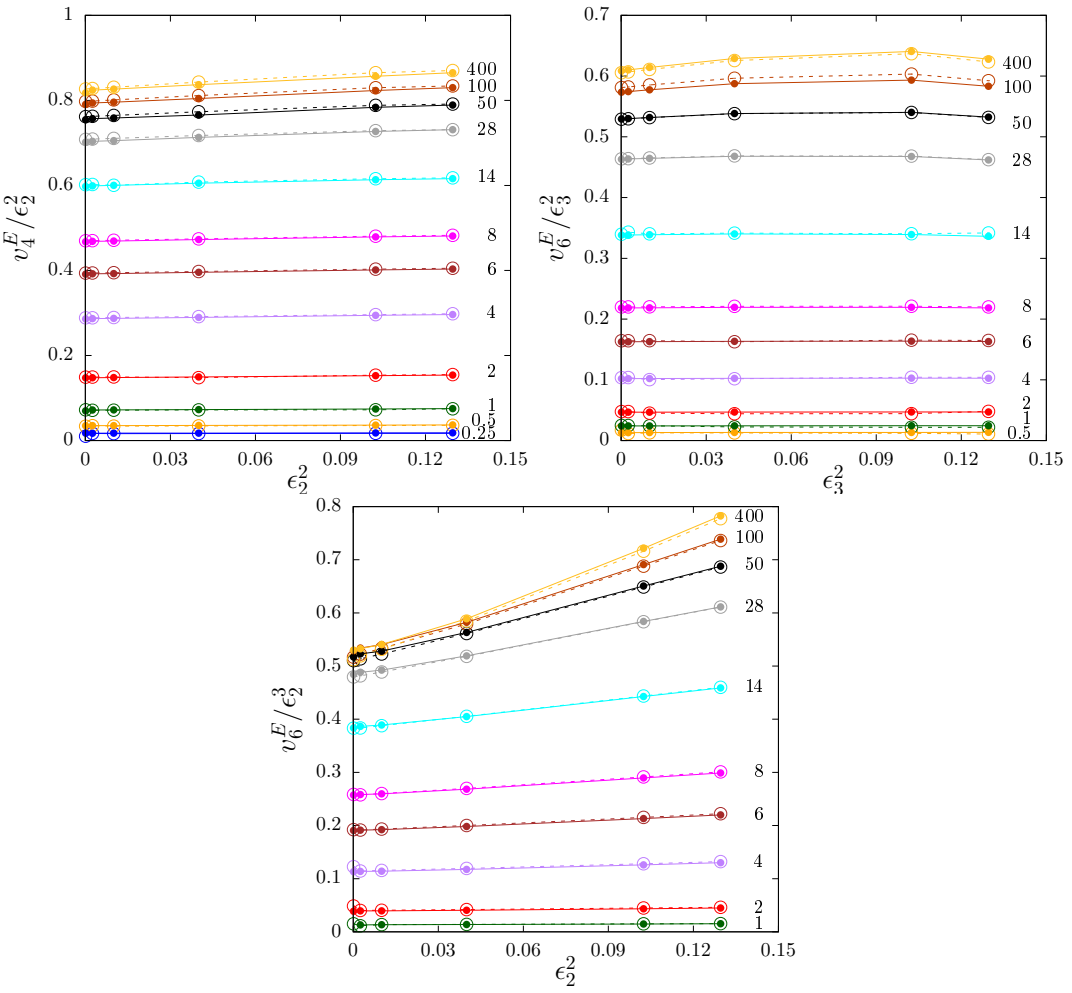

FIGURE 5.9: Eccentricity (ϵ_n) dependence of the non-linear response coefficients $\kappa_{4,22} = v_4^E(\tau \to \infty)/\epsilon_2^2$ (top left), $\kappa_{6,33} = v_6^E(\tau \to \infty)/\epsilon_3^2$ (top right) and $\kappa_{6,222} = v_6^E(\tau \to \infty)/\epsilon_2^3$ (bottom). Solid lines with filled circles denote results from the RLB method, while dotted lines with open circles were obtained in the moment method.

and the numerical results of Kurkela et al. [15]. Despite the discrepancy in the results for the eccentricity dependence, we generally find good agreement with Kurkela et al. in the linear response at low opacities ($\hat{\gamma} \lesssim 10$), which only starts to deviate slightly at larger opacities.

Concerning the opacity dependence, one finds that at low opacities up to $\hat{\gamma} \lesssim 1$, the linear response coefficients are reasonably well described by the leading order opacity expansion $\kappa_{n,n} \sim \hat{\gamma}$ in Eqns. (5.71-5.73). However, one should note that, due to the intricate space-time structure of v_n production, the higher harmonic coefficents are increasingly sensitive to changes in the underlying dynamics, such that e.g. $\kappa_{4,4}$, starts to deviate from the leading order opacity expansion already at smaller values of $\hat{\gamma}$. When increasing the opacity further, one observes a sizeable change in the linear and non-linear flow response coefficients for $1 \lesssim \hat{\gamma} \lesssim 100$, which is no longer captured by the leading order opacity expansion. Eventually, for very large opacities $\hat{\gamma} \gtrsim 100$, the opacity dependence of the linear and nonlinear response coefficients becomes weaker and weaker, indicating a saturation towards a finite large opacity limit. Empirically, we find that in this regime, the opacity dependence of the response coefficients can be well approximated by a constant asymtptotic value and a power law correction, with the asymptotic values $\kappa(\hat{\gamma} \to \infty)$ indicated by horizontal arrows in Fig. 5.10.

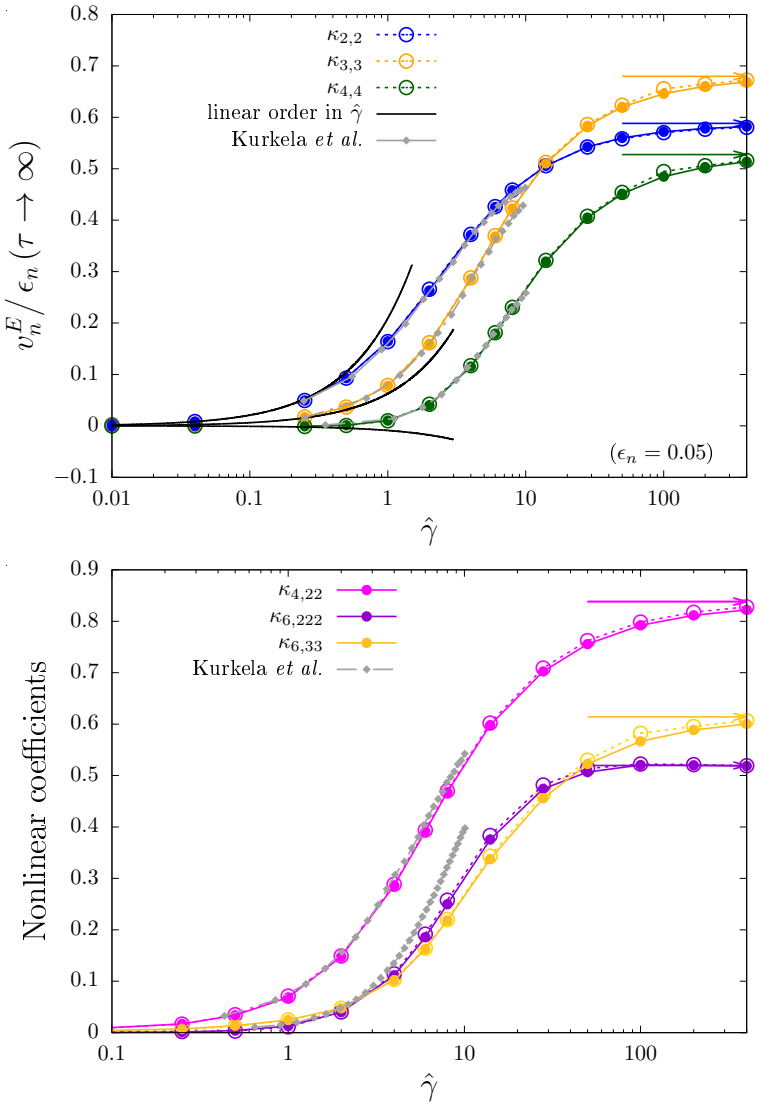

FIGURE 5.10: Opacity ($\hat{\gamma}$) dependence of (top) the linear $\kappa_{n,n} = \lim_{\epsilon_n \to 0} v_n^E(\tau \to \infty)/\epsilon_n$ and (bottom) the non-linear $\kappa_{n,mm} = \lim_{\epsilon_m \to 0} v_n^E(\tau \to \infty)/\epsilon_m^2$, $\kappa_{n,mmm} = \lim_{\epsilon_m \to 0} v_n^E(\tau \to \infty)/\epsilon_m^3$ response coefficients. Colored solid lines with filled circles denote results from the RLB method, while colored dotted lines with open circles were obtained in the moment method. The black solid lines show the results obtained to leading order in opacity expansion for the linear coefficients (top). Gray lines represent the results of Kurkela et al. in [15] (no such results are available for $\kappa_{6,33}$ in the bottom panel). Horizontal arrows indicate asymptotic values extracted from a fit to the numerical data at large opacities (see text).

5.4.3 Energy flow & hydrodynamic limit

So far we have employed an effective kinetic description to study longitudinal cooling and the development of transverse flow as a function of the opacity parameter $\hat{\gamma}$. While at small opacities $\hat{\gamma} \ll 1$ the results from numerical simulations are well described by the first interaction correction to free-streaming, one generally expects that in the opposite limit of large opacities $\hat{\gamma} \gg 1$, the effective kinetic description approaches the limit of dissipative and eventually ideal hydrodynamics. Hence in order to investigate, to what extent this expectation holds true, we will now compare our results from

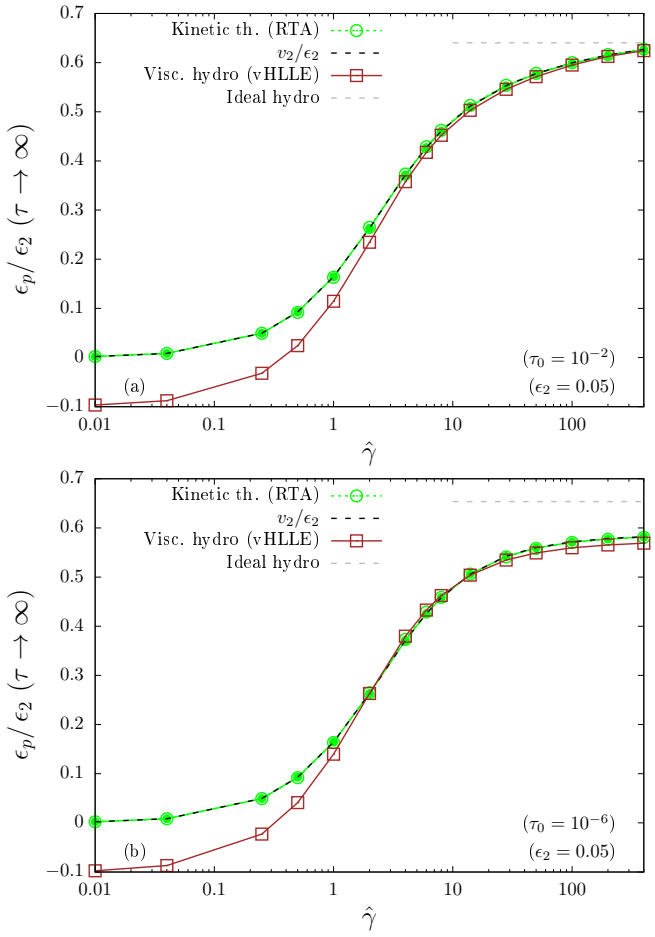

FIGURE 5.11: Opacity ($\hat{\gamma}$) dependence of the energy-flow response ϵ_p/ϵ_2 for two different initialization times $\tau_0/R = 10^{-2}$ (top) and $\tau_0/R = 10^{-6}$ (bottom). Two results are plotted for kinetic theory: those from the RLB method are plotted as a green solid line with filled circles and those from the moments method are plotted as a green dashed line with open circles. All results are for $\epsilon_2 = 0.05$.

kinetic theory with numerical simulations in Mueller-Israel-Stewart type second order relativistic viscous hydrodynamics.

We employ the publicly available vHLLE code originally introduced in Ref. [153], and extend the latest GitHub branch[8] to include the initial conditions considered in this Chapter. Apart from the conservation equation for the stress-energy tensor, $\nabla_\nu T^{\mu\nu} = 0$, the code implements the Müller-Israel-Stewart equations for the evolution of the pressure deviator $\pi^{\mu\nu}$, which for the case of a conformal fluid reduce to [186]

$$\dot{\pi}^{\langle\mu\nu\rangle} = \frac{2\eta\sigma^{\mu\nu} - \pi^{\mu\nu}}{\tau_\pi} - \frac{\delta_{\pi\pi}}{\tau_\pi}\pi^{\mu\nu}\theta + \frac{\phi_7}{\tau_\pi}\pi_\alpha^{\langle\mu}\pi^{\nu\rangle\alpha} - \frac{\tau_{\pi\pi}}{\tau_\pi}\pi_\alpha^{\langle\mu}\sigma^{\nu\rangle\alpha}, \tag{5.131}$$

where $\sigma_{\mu\nu} = 2\nabla_{\langle\mu}u_{\nu\rangle}$ is the shear tensor, $\theta = \nabla_\mu u^\mu$ is the expansion scalar, while the transport coefficients appearing above satisfy [187]

$$\tau_\pi = \frac{5\eta}{sT}, \qquad \frac{\delta_{\pi\pi}}{\tau_\pi} = \frac{4}{3}, \qquad \phi_7 = \frac{9}{70p}, \qquad \frac{\tau_{\pi\pi}}{\tau_\pi} = \frac{10}{7}. \tag{5.132}$$

We note already at this stage, that the early time behavior in ideal and viscous hydrodynamics does not agree with the early time free-streaming limit of kinetic theory, which as pointed in [15, 26] leads to an unphysical behavior of $dE_\perp/d\eta$ at early times, that makes the scaling variable $\hat{\gamma}$ ill-defined in the limit $\tau_0 \to 0$. While in [15], this problem was addressed by modifying the initial conditions and matching the energy per unit rapidity at a later time $\tau/R = 1$ of the evolution, we follow the more common procedure, and choose a finite initial time τ_0, where we initialize the energy density as in Eqns. (5.6) and (5.7), and set the components of the shear stress tensor, $\pi^{\mu\nu}$, to[9]

$$\tau_0^{-2}\pi^{\eta\eta} = -2\pi^{xx} = -2\pi^{yy} = -p, \tag{5.133}$$

which ensures vanishing longitudinal pressure, to comply with the initial conditions for kinetic theory in Eq. (5.3). [10] Similarly, we fix the value of the shear viscosity to entropy density ratio η/s for a given value of $\hat{\gamma}$ in the same way as for RTA, via Eq. (5.23), evaluated at initial time τ_0. By comparing kinetic theory and hydrodynamic simulations with the same finite τ_0, we can then achieve a direct comparison and in addition investigate the dependence on the initialization time τ_0 in the two different theories.

Evaluating the energy-weighted flow harmonics v_n^E considered in this work, a Cooper-Frye-like mechanism should be considered to reconstruct the phase-space distribution function from the hydrodynamic fields e, u^μ and $\pi^{\mu\nu}$. We circumvent this ambiguity by instead referring to the stress-energy anisotropy ϵ_p, which according to Eq. (3.44), can be defined directly in terms of the components of the energy-momentum tensor. Since $T^{\mu\nu}$ is fundamentally accessible in both kinetic theory and hydrodynamics, a comparison between the two theories can be made unambiguously at the level of ϵ_p. While the quantity ϵ_p measures the second harmonic modulation of the energy flow, and in our kinetic theory simulations exhibits almost identical behavior to v_2^E, we are not aware of generalizations of ϵ_p to higher order flow harmonics, and will therefore restrict our attention to $n = 2$ perturbations, with initial eccentricity

[8] Commit number `efa9e28d24d5115a8d813485232fb342b38380f0`.

[9] We employ a conformal equation of state $e = 3p$.

[10] Since at very early times, the evolution in viscous hydrodynamics and kinetic theory does not agree, another conceivable option is to initialize the hydrodnamic simulation on the hydrodynamic attractor for Bjorken flow [15, 26]. We have also performed such simulations, and find no significant differences regarding the development of transverse flow.

$\epsilon_2 = 0.05$.[11]

Our results for the elliptic energy-flow response are compactly summarized in Fig. 5.11, where we compare the opacity dependence of ϵ_p/ϵ_2 in kinetic theory (RTA) and hydrodynamics (vHLLE) for two different initialization times $\tau_0/R = 10^{-2}, 10^{-6}$ in the top and bottom panels. When considering the larger initialization time $\tau_0/R = 10^{-2}$, one finds that viscous hydrodynamics provides a reasonable description of kinetic theory for $\hat{\gamma} \gtrsim 5$, with both curves smoothly approaching the ideal hydrodynamic limit for large opacities, as indicated by the gray dashed line. When considering a much smaller initialization time, $\tau_0/R = 10^{-6}$, we find small deviations between kinetic theory and hydrodynamics in the same opacity range. While these deviations might not be very sizeable, they notably do not steadily decrease with increasing opacity, as one would naively expect. Moreover, a perhaps more evident observation is that neither of the two curves appears to approach the ideal hydrodynamics result, such that even when extrapolated to infinite opacity the RTA value ($\simeq 0.59$) slightly differs from the vHLLE value ($\simeq 0.57$) and both fall about 10% short of the ideal hydrodynamic limit ($\simeq 0.64$).

Even though this behavior may appear counterintuitive at first sight, it can ultimately be traced back to the non-commutativity of the limits $\tau_0 \to 0$, where the system is subject to a rapid longitudinal expansion, and $\hat{\gamma} \to \infty$, where hydrodynamics emerges from kinetic theory as the system undergoes rapid equilibration. Starting from kinetic theory, it is clear that for any finite opacity $\hat{\gamma}$ the system is initially far-from equilibrium and behaves as approximately free-streaming, until on time scales $\tau_{\rm eq}/R \sim \hat{\gamma}^{-4/3}$ the system undergoes equilibration, and the subsequent evolution can be approximately described by viscous or even ideal fluid dynamics. While in the limit $\hat{\gamma} \to \infty$, the equilibration time $\tau_{\rm eq}/R \to 0$ and fluid dynamics becomes applicable at earlier and earlier times, the early time free-streaming and initial approach towards equilibrium is never correctly described by fluid dynamics. The results in Fig. 5.11, thus provide a clear illustration of the fact that at very early times, the system is necessarily out-of-equilibrium and the two limits $\hat{\gamma} \to \infty$ and $\tau_0 \to 0$ are in general not commutative.

Even though at large opacities the mismatch between kinetic theory and hydrodynamics occurs only at very early times, this affects e.g. the longitudinal cooling and can still have a notable effect on the development of anisotropic flow at later times, which is seen in Fig. 5.11. We are thus lead to conclude that a non-equilibrium description of the early time dynamics is inevitable to accurately describe the development of anisotropic flow, even at relatively large opacities.

As a final remark to the comparison of opacity dependencies in the different descriptions, we note that for any finite τ_0 kinetic theory and viscous hydrodynamics will approach ideal hydrodynamics for sufficiently large opacities where the equilibration time $\tau_{\rm eq}$ becomes smaller than the initialization time τ_0. While the results shown in Fig. 5.12 provide an explicit illustration of this behavior, the convergence towards ideal hydrodynamics at large opacities corresponds to the incorrect order of limits, as physically one needs to account for the entire space-time evolution of the system, i.e. the limit $\tau_0 \to 0$ has to be taken before $\hat{\gamma} \to \infty$.

One may wonder, how the increasingly short period of non-equilibrium evolution at early times can have such a significant impact on the transverse flow, which only develops on much later times scales $\tau/R \gtrsim 0.1$. While it is true that at very early times, the system does not develop a significant amount of transverse expansion and

[11] We have checked that, similar to the kinetic theory results in Fig. 5.8, non-linear contributions $\epsilon_p \sim e_2^3$ are sufficiently small to be neglected for the linear response analysis of ϵ_p/e_2.

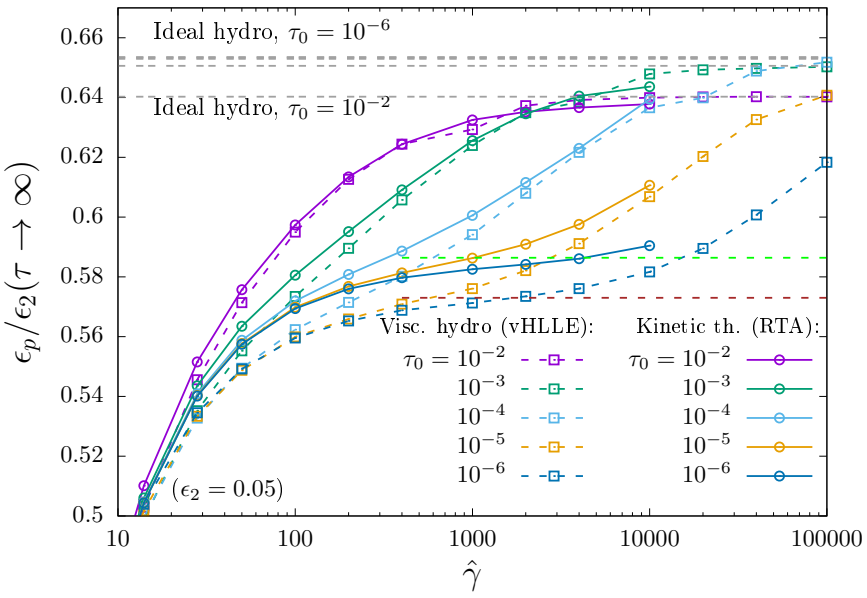

FIGURE 5.12: Opacity ($\hat{\gamma}$) dependence of the response coefficient ϵ_p/ϵ_2 in kinetic theory (RTA, obtained using the RLB method), viscous (vHLLE) and ideal hydrodynamics for different initialization times $\tau_0/R = 10^{-2} - 10^{-6}$. Convergence towards ideal hydrodynamics is only observed when the initialization time becomes smaller than the equilibration time of the system.

can locally be described by Bjorken flow as discussed in Section 5.4.1, it is equally important to realize that the early-time dynamics is nevertheless inhomogeneous in the transverse plane. Due to the fact that the initial energy density locally sets the scale for the Bjorken evolution, some regions will experience a faster cooling relative to others, thereby changing the shape of the energy density distribution in transverse space. Due to this phenomenon of inhomogenous longitudinal cooling, the geometric eccentricities will be modified even before the transverse expansion sets in. Since the anisotropic flow is built up solely due to transverse expansion, its magnitude is determined by the value of the eccentricity at the onset of transverse expansion. We therefore conclude that differences in the longitudinal cooling at early times are ultimately responsible for the observed differences in the transverse flow.

We illustrate this behavior in Fig. 5.13, where we present the evolution of the coordinate space eccentricity ϵ_2 as a function of time τ/R. Different colored curves in the top panel show the evolution of ϵ_2 in kinetic theory for different opacities. Similarly, the bottom panel shows the corresponding results obtained in viscous hydrodynamics (vHLLE). The ideal hydrodynamics result is shown for comparison as a solid black line in both panels. Starting around $\tau \sim 0.1R$ all curves exhibit a significant drop due to the onset of transverse expansion. However, in kinetic theory and viscous hydrodynamics, the eccentricity decreases even before that due to the previously discussed phenomenon of inhomogeneous longitudinal cooling. Strikingly, this effect can also be described (semi-) analytically by approximating the dynamics as a collection of local Bjorken flows as discussed in Section 4.1.1, which yields results for the decrease of ϵ_2 that we plotted as dashed black lines. We note that the limiting behavior for this decrease can be obtained as

$$\lim_{\tau\to\infty} \frac{\epsilon_2(\tau)}{\epsilon_{2;0}} = \frac{(1-\gamma/4)^3}{(1-\gamma/6)^3}, \tag{5.134}$$

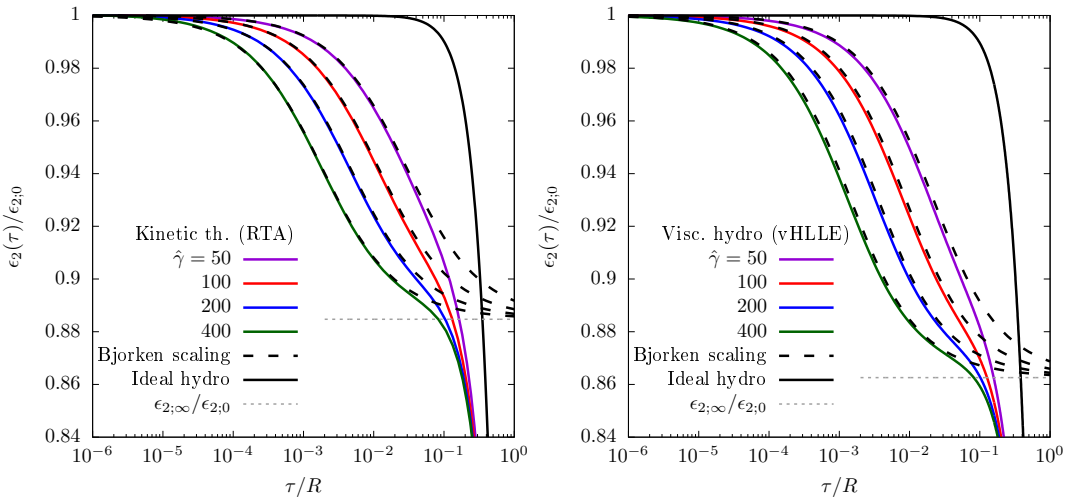

FIGURE 5.13: Comparison of the evolution of ϵ_2 normalized to its initial value $\epsilon_{2;0}$ on a logarithmic timescale for kinetic theory obtained using the moments method (left) and viscous hydrodynamics (right). Also shown are the corresponding results in Bjorken flow scaling approximation (dashed black lines) and ideal hydrodynamics (solid black lines). Gray dashed lines show the limit in Eq. (5.134) in the absence of transverse expansion.

where γ is related to the behaviour of the universal function $\mathcal{E}(\tilde{w}) \sim \tilde{w}^{\gamma}$ at small $\tilde{w}$, such that in kinetic theory $\gamma = 4/9$, whereas for the hydrodynamic theory in Eq. (5.131), one has $\gamma = (\sqrt{505} - 13)/18 \simeq 0.526$. Evaluating Eq. (5.134) for the above values of γ, one obtains a $\sim 11.5\%$ (RTA) and 13.7% (VHLLE) decrease of ϵ_2 solely due to the longitudinal expansion, as indicated by the gray dashed lines in Fig. 5.13. Hence, this effect indeed takes on the correct magnitude to be able to describe the difference of $\sim 10\%$ in the large opacity limits of kinetic theory and viscous hydro compared to ideal hydrodynamics.

5.5 Discussion

We employed the Boltzmann equation in the conformal relaxation time approximation as a simple model to study the space-time dynamics of small and large systems created in high-energy hadronic collisions. Within the simple effective kinetic description described in Sec. 5.1, the evolution of the system depends on a single dimensionless opacity parameter $\hat{\gamma}$ that combines the system size and energy dependences, and we estimate $\hat{\gamma}$ to range from values $\lesssim 1$ in p+Pb collisions to ≈ 10 in Pb+Pb collisions at LHC energies (c.f. Eq. (5.24) and (5.25)). We considered in this chapter an analytical form of the initial condition that might not necessarily be realistic, but it does reproduce for our purposes the relevant features of the initial state.

We performed (semi-)analytic calculations at leading order in opacity $\hat{\gamma}$ (c.f. Sec. 5.2) and developed first principles numerical simulations (c.f. Sec. 5.3) to investigate the longitudinal cooling of the transverse energy per unit rapidity, $\mathrm{d}E_{\perp}/d\eta$, and the development of transverse flow quantified by the (energy weighted) flow harmonics v_n^E for a large range of opacities.

We find that with increasing opacities, pressure isotropization takes place at earlier and earlier times, such that for large opacities $\hat{\gamma} \gtrsim 1$ the onset of longitudinal cooling of the system is well described by one dimensional Bjorken dynamics, until at later times $\tau/R \gtrsim 0.1$ the effects of the transverse expansion can no longer be ignored.

By studying the response to anisotropic perturbations of the initial energy density, we investigated the development of transverse flow from low to high opacities. While for small opacities, $\hat{\gamma} \lesssim 1$, the development of transvserse flow is reasonably well described by the leading order opacity corrections to free-streaming, we find that for $1 \lesssim \hat{\gamma} \lesssim 100$ the linear and non-linear flow response exhibits a strong opacity dependence, and eventually saturates for large opacities $\hat{\gamma} \gtrsim 100$. In contrast to large opacities, at small opacities the time evolution of linear quartic and several non-linear flow responses exhibit non-monotonic behaviour. In the case of the linear quartic flow, we were able to explain this behaviour via the "flow production rates" as a radial density and rate in time. It stands to reason that a similar explanation could be found also for the non-linear flow responses.

Even though one naively expects the results for large opacities $\hat{\gamma} \gg 1$ to approach the hydrodynamic limit, it turns out that subtleties of the limits $\hat{\gamma} \to \infty$ and $\tau_0 \to 0$ provide a restriction on the accuracy of hydrodynamic descriptions. Since the early time pre-equilibrium dynamics of the system cannot be accurately described by ordinary viscous or ideal hydrodynamics, deviations between all approaches persists even at very large opacities. With respect to RTA results, we found discrepancies of the viscous and ideal hydro results of the order of $\sim 2.5\%$ and $\sim 12\%$, respectively. However, as these discrepancies can be mostly attributed to the phenomenon of inhomogeneous longitudinal cooling, we believe that the inclusion of a more appropriate pre-equilibrium description as in KøMPøST [141, 188] may significantly improve the agreement between microscopic and macroscopic descriptions (see also [175]). Similarly, it is also conceivable that setups of hydrodynamic simulations could be modified in order to alleviate discrepancies with kinetic theory, which we will investigate further in the next chapter.

Chapter 6

Opacity dependence of pre-equilibrium and applicability of hydro

In Chapter 5, we found that for final state observables related to transverse flow, results from purely hydrodynamic simulations are in disagreement with results from kinetic theory even at very large opacities due to differences of the dynamics in these two theories during the pre-equilibrium phase.

We now want to examine how in practice simulations of heavy ion collisions based on hydrodynamics can be brought into agreement with kinetic theory simulations. Therefore, we will use a more realistic initial condition that was obtained as the average of Monte-Carlo-generated collision events, which is introduced in Sec. 6.1. The time evolution is again modeled in simplified RTA of kinetic theory. Within this model, we perform an analysis of the circumstances under which hydrodynamics becomes applicable as a function of opacity and time, as determined by comparing results for cooling and transverse flow to kinetic theory. The different evolution schemes we used are discussed in Section 6.2. The insights from Chapter 4 about the early time attractor can be applied to this setup as described in Section 6.3. Based on our results for the differences of kinetic theory and hydrodynamics in this phase, we introduce a scaling scheme for the initial condition of hydro that can counteract these differences. This scheme relies on a timescale separation of equilibration and the onset of transverse expansion. In Section 6.4, we discuss the time evolution of the system at three example opacities. On the basis of transverse profiles, we indicate how the picture changes from a close-to-free-streaming to an almost fully equilibrated system in kinetic theory. We compare the time evolution in kinetic theory and viscous hydrodynamics as well as in hybrid schemes. Within these hybrid schemes, the first part of the system's evolution is modelled using kinetic theory. Afterwards, we switch to hydrodynamics to model the remainder of the evolution. For sufficiently large opacities, our proposed scaling scheme indeed brings hydrodynamics into agreement with kinetic theory after pre-equilibrium. Based on the system's equilibration, we present a useful criterion for the applicability of hydrodynamics, which can be used to define the switching times for hybrid schemes. This criterion is reached at later evolution times for smaller opacities and in some cases is never fulfilled. We find that when switching sufficiently late, hybrid schemes are also in good agreement with kinetic theory. KøMPøST + viscous hydro simulations yield similar results as simulations with full kinetic theory + viscous hydrodynamics.

The range of applicability of the different schemes can best be assessed by studying the opacity dependence of final state observables. In Section 6.5, we compare first naive and scaled hydrodynamics to kinetic theory and establish $4\pi\eta/s \lesssim 3$ as the opacity range where the scaling scheme brings agreement. We then show results from

the two hybrid simulation schemes, which can improve on scaled hydro results in the intermediate opacity range around $4\pi\eta/s \sim 3$.

In Sec. 6.6, we provide a brief discussion of the results of this Chapter. Appendices E and F provide further details on how the linearized results in opacity expansion were obtained, while in Appendices G and H we discuss some additional results for the time evolution of the system.

6.1 Initial state

We will use a realistic average initial condition for the $30-40\%$ most central Pb-Pb collisions at $\sqrt{s_{NN}} = 5.02\,\text{TeV}$. This initial condition was generated numerically on a transverse grid of size 512×512 in the following way . A saturation model based initial state generator was used to generate 8 million events with aligned directions of the impact parameter, which were then divided into centrality classes. Then the pointwise average of all events in each centrality class was taken. We made sure that in the resulting event averages statistical fluctuations are sufficiently suppressed by checking that they feature no local peaks above an energy density level of 10^{-6} times its maximum. More details on this event generation procedure can be found in [189].

In terms of the observables introduced in Sec. 3.6, some of the characteristic properties for the initial condition we use are summarized in Table 6.1. As we use a fixed profile, the parameters R and $\frac{dE_\perp^{(0)}}{d\eta}$ are also fixed and we vary the opacity $\hat{\gamma}$ via η/s. Hence, throughout this Chapter, whenever discussing opacity dependencies, we will characterize the opacity via the value of the shear viscosity to entropy density ratio η/s. Note, however, that these two quantities are inversely proportional.

$dE_\perp^{(0)}/d\eta$ [GeV]	R [fm]	$\hat{\gamma} \times 4\pi\eta/s$	ϵ_2	ϵ_4	ϵ_6
1280	2.78	11.3	0.416	0.210	0.0895

TABLE 6.1: Characteristic properties of the initial condition for the energy density used in this work.

6.2 Evolution Models

We want compare the dynamics of several different time evolution frameworks, which were all introduced in Chapter 3. Specifically, we will employ RTA kinetic theory in the numerical implementation as introduced in Sec. 5.3.2 as well as a corresponding opacity expansion and treatment in KøMPøST. We will also employ ideal and viscous hydrodynamics as implemented in the vHLLE code [153][1] with RTA transport coefficients.

6.2.1 Validation of KøMPøST

Before employing KøMPøST to describe pre-equilibrium, we first checked to what extend results from modified RTA-KøMPøST are in agreement with results from full kinetic theory in RTA for our specific initial condition. This comparison was done on the basis of the time evolution of the observables that we consider in this Chapter but also for crosssections through profiles of the energy-momentum tensor after some evolution time. All KøMPøST results presented here were obtained using an initial time of $\tau_0 = 10^{-6}\,R$.

[1] Commit number `efa9e28d24d5115a8d8134852-32fb342b38380f0`.

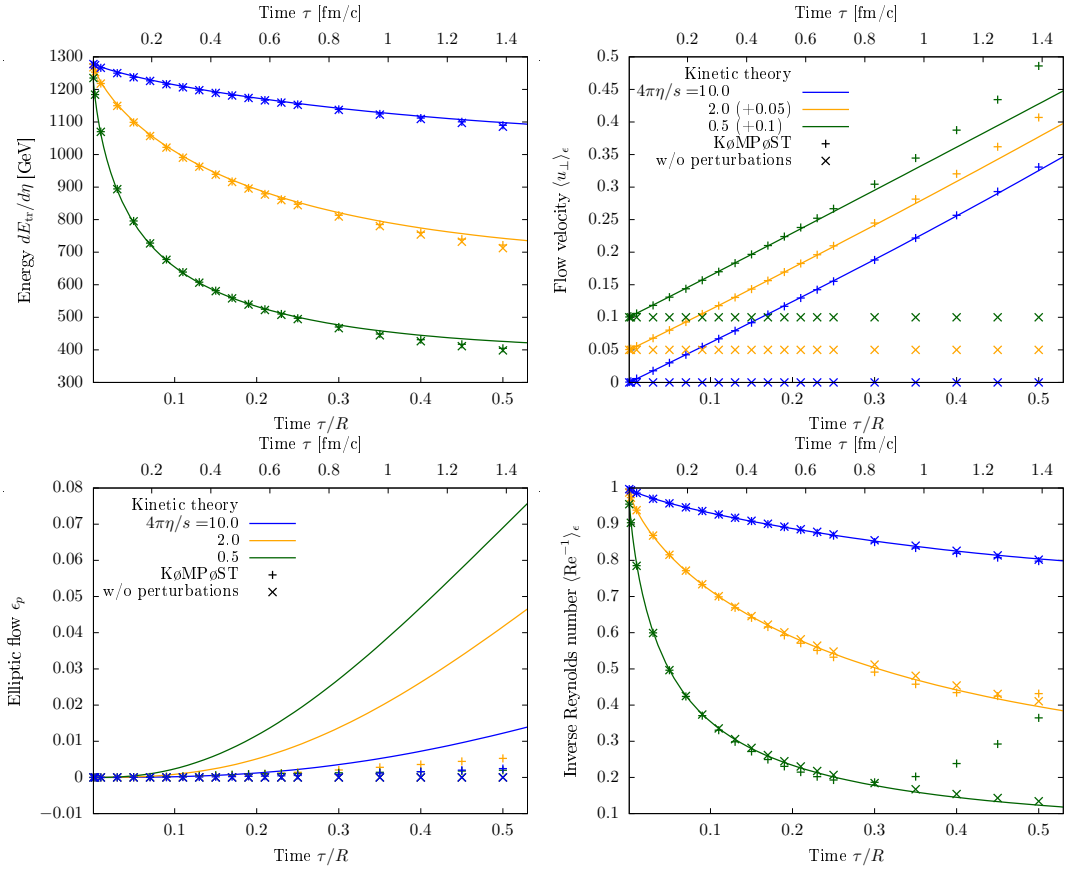

FIGURE 6.1: Time evolution of transverse energy $dE_{\mathrm{tr}}/d\eta$ (top left, cf. Eq. 3.43), transverse flow velocity $\langle u_\perp \rangle_\epsilon$ (top right, cf. Eq. 3.53), elliptic flow ϵ_p (bottom left, cf. Eq. 3.44) and inverse Reynolds number $\langle \mathrm{Re}^{-1} \rangle_\epsilon$ (bottom right, cf. Eq. 3.52). Plotted are results from KøMPøST (RTA) with (+ symbols) and without (× symbols) energy perturbations compared to full kinetic theory results (solid lines) at three different opacities $4\pi\eta/s = 0.5$ (green), 2 (yellow) and 10 (blue). In the plot of transverse flow velocity, results at different opacities are shifted in value in order to be distinguishable.

Fig. 6.1 shows a comparison of the time evolution of four different transverse space integrated observables at three different values of the shear viscousity, namely $4\pi\eta/s = 0.5, 2, 10$. The results from KøMPøST are plotted with symbols "+" for the mode with and "×" for the mode without energy perturbations and are benchmarked for times up to $\tau = 0.5R$ against the results obtained using a full kinetic theory description plotted with lines.

The decrease of transverse energy $dE_{\mathrm{tr}}/d\eta$ is described very well in both modes. As without energy perturbations, the energy-momentum tensor is propagated as if there were no local gradients, it predicts zero transverse flow velocity $\langle u_\perp \rangle_\epsilon$ and elliptic flow ϵ_p. The mode with energy perturbations can describe the buildup of $\langle u_\perp \rangle_\epsilon$ correctly. On the other hand, while giving nonzero results, it still vastly underestimates the buildup of anisotropic flow ϵ_p. The inverse Reynolds number $\langle \mathrm{Re}^{-1} \rangle_\epsilon$ is well described by both modes at early times, but results from the mode with energy perturbations deviate at very late times.

Generally, the comparison suggest that for certain observables, KøMPøST results can be accurate even slightly beyond the timeframe it was intended for, which is on the order of 1 fm. Other observables, in particular those related to anisotropies, are not described correctly.

In a further comparison of KøMPøST to full kinetic theory data, we also investigated profiles of certain components of $T^{\mu\nu}$ at fixed shear viscosity $4\pi\eta/s = 2$ and three different fixed times $\tau = 0.1R$, $0.3R$ and $0.5R$. The same comparisons were also performed in the local rest frame with analogous quantities that are defined via the variables ϵ, u^μ and $\pi^{\mu\nu}$. Fig. 6.2 illustrates our findings. This time, KøMPøST results are plotted with lines and full kinetic theory results with symbols.

The results confirm that for energy or energy flow observables like $T^{\tau\tau}$, $T^{\tau y}$ and $T^{xx}+T^{yy}$, KøMPøST works well even on a local level and in the outskirts of the system for all evolution times that we examined. The only part of the energy-momentum tensor for which KøMPøST results shows significant deviations are anisotropies in the shear stress, as measured by $T^{xx} - T^{yy}$. While this observable is still correctly reproduced in the central part of the system, it exhibits sizeable deviations of up to a factor of five at a radial distance of $r \gtrsim R$. These deviations also explain the errors in elliptic flow ϵ_p.

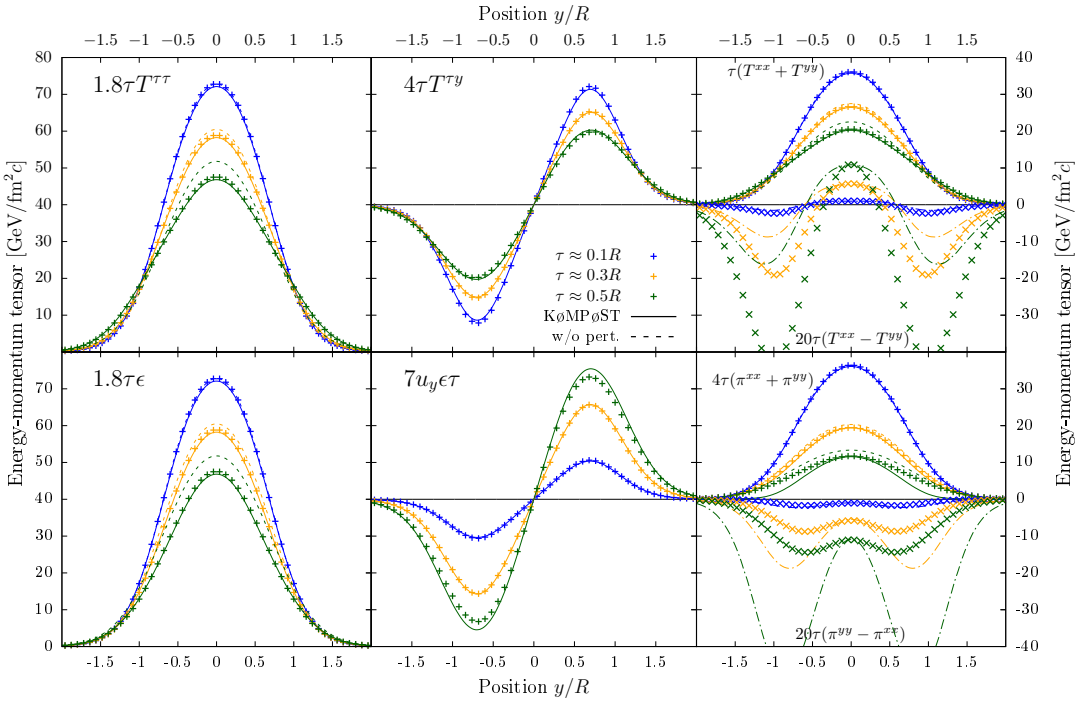

FIGURE 6.2: Comparison of KøMPøST (RTA) and full kinetic theory via results for the energy-momentum tensor on the line $x = 0$, represented at fixed times $\tau/R \simeq 0.1$ in blue, 0.3 in yellow and 0.5 in green. The full kinetic theory results are plotted with points (+,×), while the KøMPøST ones obtained with and without energy perturbations are plotted with solid and dashed lines, respectively. Anisotropic observables are nonzero only with energy perturbations and are plotted with point-dashed lines. The upper row shows, from left to right, the following components of the energy-momentum tensor: $T^{\tau\tau}$ (left), $T^{\tau y}$ (middle), as well as $T^{xx} + T^{yy}$ and $T^{xx} - T^{yy}$ (right). The lower row shows analogous local rest-frame quantities, namely ϵ (left), ϵu^y (middle), as well as $\pi^{xx} + \pi^{yy}$ and $\pi^{yy} - \pi^{xx}$ (right). Notice the change in sign for the latter when compared to the upper panel. All observables were multiplied with τ and rescaled with a constant factor to adjust their magnitudes such that they can be plotted on the same total range of 80 GeV/fm^{2}c.

	Kinetic theory	Naive hydro		Scaled hydro	
		Ideal	Viscous	Ideal	Viscous
γ	4/9	0	0.526	0	0.526
α	1	2/3	1.071	2/3	1.071
$\frac{R}{\tau}\frac{\langle u_\perp\rangle_{\epsilon,\text{early}}}{1-(\tau_0/\tau)^{\alpha}}$	0.614	0.691	0.600	0.658	0.606
$\frac{R}{\tau}\frac{\langle u_\perp\rangle_{\epsilon,\text{late}}}{1-(\tau_0/\tau)^{2/3}}$	0.658	0.691	0.652	0.658	0.658

TABLE 6.2: Estimates for the pre-flow generated in kinetic theory, ideal hydrodynamics and viscous hydrodynamics (see Sec. 6.3.2 for details regarding the naive and scaled hydrodynamics setups).

6.3 Early-time dynamics of different models

We will now discuss what we can learn from applying the insights about the early time attractor in systems with transverse expansion described in Chapter 4 to the setup used in this Chapter.

6.3.1 Pre-flow estimation

The pre-flow estimates obtained in Section 4.1.2 - specifically the Eqs. (4.50) and (4.52) - can be evaluated numerically for the $30-40\%$ centrality profile that we are considering in this Chapter. The results for the different theories (kinetic theory, ideal hydrodynamics and viscous hydrodynamics) are shown in Table 6.2. Here, we contrast the "naive" and "scaled" initial conditions for hydrodynamics, which will be discussed in detail in the following subsection. In the early-time regime, it can be seen that kinetic theory leads to more flow than viscous hydrodynamics (2% and 1% more for the naive and scaled initialization, respectively), while ideal hydrodynamics leads to more flow than kinetic theory (13% and 7% more for the naive and scaled initializations, respectively). In the late-time limit, both ideal and viscous hydrodynamics are brought in agreement with kinetic theory when the scaled initialization is employed. In the case of the naive initialization, ideal hydrodynamics gives about 5% more flow, while viscous hydrodynamics underestimates the flow by less than 1%.

6.3.2 Setting initial conditions

From the discussion in Section 4.1.1, it becomes clear that the pre-equilibrium evolution of the fluid depends on the theory employed to describe it. We take as the "correct" evolution that described by kinetic theory, when $\mathrm{d}E_{\mathrm{tr}}/\mathrm{d}\eta$ remains constant during the free-streaming stage of pre-equilibrium. This can be seen by setting $\gamma = 4/9$ in Eq. (4.30). Since in viscous hydrodynamics, $\gamma \simeq 0.526 > 4/9$, $\mathrm{d}E_{\mathrm{tr}}/\mathrm{d}\eta$ will actually increase during pre-equilibrium, thus leading for the same initial energy profile to an unphysically higher transverse plane energy at late times, as illustrated in Fig. 4.2. Similarly, the change in eccentricity due to the pre-equilibrium evolution will be different compared to kinetic theory. We will now discuss how these phenomena specifically affect the pre-equilibrium evolution of our initial state as given in Sec. 6.1 and how they are counteracted by locally scaling the initial condition. We will then give the quantitative details of the scaling prescription.

Fig. 6.3 illustrates the size of the effect on transverse energy $\mathrm{d}E_{\mathrm{tr}}/\mathrm{d}\eta$ in the top panel and ellipticity ϵ_2 in the bottom panel. In naive hydrodynamics using the same initial condition as kinetic theory, $\mathrm{d}E_{\mathrm{tr}}/\mathrm{d}\eta$ rises to a value about $1.5\times$ bigger than in

kinetic theory at the onset of equilibration and will remain in disagreement throughout the rest of the evolution. The dashed lines show predictions of the behaviour in the local Bjorken flow scaling approximation according to Eq. (4.29). In our proposed scheme the initial value of $\mathrm{d}E_{\mathrm{tr}}/\mathrm{d}\eta$ is scaled down in such a way that it dynamically reaches agreement with kinetic theory. Similarly, we find that the ellipticity decreases in both kinetic theory and in hydro, but more so in the latter case. This means that in naive hydro the eccentricity will have a smaller value at the onset of the buildup of transverse flow than kinetic theory, which will result in smaller final values of elliptic flow. With the scaling scheme, the initial ellipticity is scaled up in hydrodynamics and will come into agreement with kinetic theory.

As the local scaling factor for the hydrodynamic initial condition is computed in the local Bjorken flow approximation, it assumes that the system will fully equilibrate before the onset of transverse expansion. How well this works in practice will be discussed in Sec. 6.4.2.

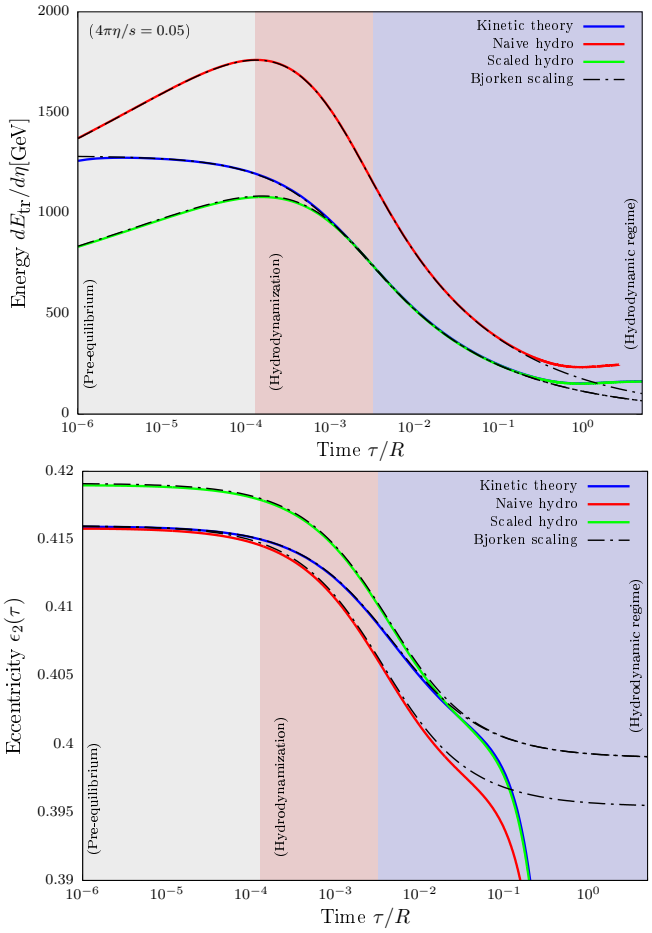

FIGURE 6.3: Early time evolution of transverse energy $\frac{dE_{\mathrm{tr}}}{d\eta}$ (top, cf. Eq. 3.43) and ellipticity ϵ_2 (bottom, cf. Eq. 3.49) in kinetic theory (blue), naive hydrodynamics (red) and scaled hydrodynamics (green). Hydrodynamics behaves differently in pre-equilibrium, such that differences to a kinetic theory description build up. This can be counteracted by scaling the initial condition.

We now move to the quantitative analysis of the pre-equilibrium behaviour in the two hydro schemes. In the first one, dubbed "naive hydrodynamics", we will impose the same energy density ϵ_0 at initial time τ_0 as in kinetic theory. We first note that the precise RTA initial conditions described in Sec. 3.7 are not compatible

with the hydrodynamic attractor due to the vanishing longitudinal pressure. Indeed, noting the relations $P_T = \epsilon(\frac{1}{3} - \frac{f_\pi}{2})$ and $P_L = \epsilon(\frac{1}{3} + f_\pi)$, as well as the relation $f_{\pi;0} = -\frac{2\gamma}{3}/(1-\gamma/4)$ implied by Eq. (4.19), the early-time expression for $T^{\mu\nu}$ reads

$$T_0^{\mu\nu} = \frac{\epsilon_0}{1-\gamma/4} \times \mathrm{diag}\left(1-\frac{\gamma}{4}, \frac{1}{3}+\frac{\gamma}{4}, \frac{1}{3}+\frac{\gamma}{4}, \frac{1}{3}-\frac{3\gamma}{4}\right), \tag{6.1}$$

which reduces to $T_0^{\mu\nu} = \mathrm{diag}\,(\epsilon_0, \epsilon_0/2, \epsilon_0/2, 0)$ for RTA, when $\gamma = 4/9$. Since in hydrodynamics, $\gamma > 4/9$, the initial transverse-plane energy will be larger than in RTA:

$$\frac{\mathrm{d}E^0_{\mathrm{tr};\gamma}}{\mathrm{d}\eta} = \frac{2}{3}\frac{1+3\gamma/4}{1-\gamma/4}\frac{\mathrm{d}E^0_{\mathrm{tr;RTA}}}{\mathrm{d}\eta}. \tag{6.2}$$

This explains why even at initial time the naive hydro curve in Fig. 6.3 already starts above the kinetic theory one.

Acknowledging that viscous hydrodynamics does not capture correctly the pre-equilibrium evolution of the fluid, we propose to change the initialization of hydrodynamics in such a way that the energy density ϵ locally agrees with the kinetic theory prediction at late times. In principle, this works only when the pre-equilibrium evolution ends before the onset of transverse expansion. Taking a and η/s to be identical in the two theories and demanding that they both reach the same $(\tau^{4/3}\epsilon)_\infty$ value when $\tau \to \infty$, Eq. (4.24) shows that the local modification of the initial energy density in hydrodynamics (denoted $\epsilon_{0,\gamma}$) is

$$\epsilon_{0,\gamma} = \left[\left(\frac{4\pi\eta/s}{\tau_0}a^{1/4}\right)^{\frac{1}{2}-\frac{9\gamma}{8}}\left(\frac{C_\infty^{\mathrm{RTA}}}{C_\infty^{\gamma}}\right)^{9/8}\epsilon_{0,\mathrm{RTA}}\right]^{\frac{8/9}{1-\gamma/4}}, \tag{6.3}$$

where the specific shear viscosity η/s is considered to have the same value in viscous hydrodynamics and in kinetic theory. Using the above energy profile in Eqs. (4.31), (4.33) and (4.52) shows that after pre-equilibrium (i.e., at large $\tilde{w}$), $\mathrm{d}E_{\mathrm{tr}}/\mathrm{d}\eta$, the eccentricities ϵ_n and the average flow velocity $\langle u_\perp \rangle_\epsilon$ will reach the corresponding RTA limits, irrespective of the value of γ. We note, however, that the pre-equilibrium behaviour of all of the above observables will still be different from that in RTA.

Before ending this Section, we emphasize that the rescaling of the initial conditions shown in Eq. (6.3) is not only possible, but also mandatory for ideal hydrodynamics simulations, when $\gamma = 0$ and $C_\infty = 1$. While when applying the scaling procedure to viscous hydrodynamics, η/s was considered as an invariant physical parameter, in ideal hydrodynamics (when $\eta = 0$), this is no longer the case. Instead, the factor η/s helps rescale the initial energy density such that at late times, $\tau^{4/3}\epsilon$ obtained in ideal hydrodynamics would match the one in a hypothetical RTA system with that given value of η/s. The agreement between ideal hydro and RTA can be expected of course only in the limit $\eta/s \to 0$. Specifically, Eq. (6.3) reduces in the case of ideal hydro to

$$\epsilon_{0,\mathrm{id}} = \left(\frac{4\pi\eta}{s}\right)^{4/9}_{\mathrm{RTA}} C_\infty^{\mathrm{RTA}}\frac{a^{1/9}}{\tau_0^{4/9}}\epsilon_{0,\mathrm{RTA}}^{8/9}. \tag{6.4}$$

For definiteness, we perform the ideal hydro simulation at $4\pi\eta/s = 1$, rescaling the results appropriately when comparing to kinetic theory at other values of $4\pi\eta/s$.

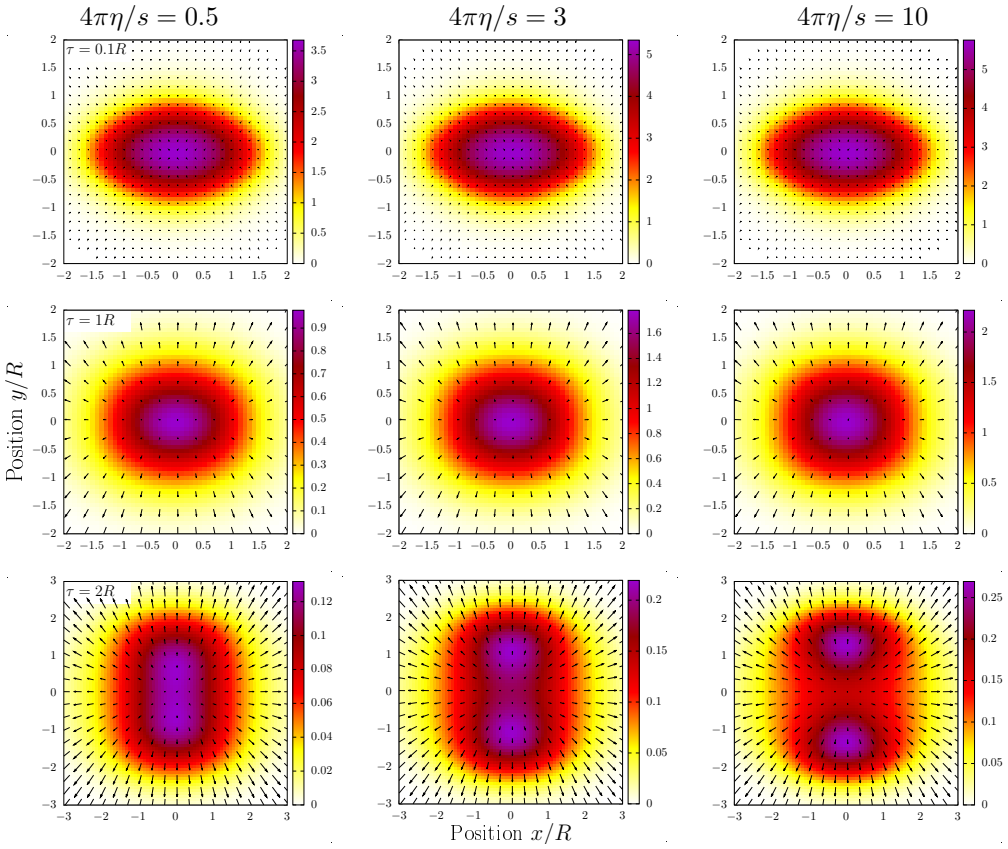

FIGURE 6.4: Time evolution of transverse profiles of the restframe energy density $\tau\epsilon$ in a heatmap plot together with transverse components of the flow velocity (u^x, u^y) as a vector field plot for the averaged initial condition used in this work at different opacities $4\pi\eta/s = 0.5$ (left), 3 (middle) and 10 (right). The snapshot times $\tau = 0.1R$ (top), $\tau = 1R$ (middle) and $\tau = 2R$ (bottom) were chosen as the beginning, peak and end of the buildup of elliptic flow ε_p.

6.4 Space-time evolution at different opacities and in different setups

The different behaviour of hydrodynamics compared to kinetic theory in pre-equilibrium can best be assessed via the time dependence of the studied observables. This also allows to study the behaviour during different stages of the collision. In Section 6.4.1, we discuss the time evolution of transverse profiles of the system in kinetic theory. Subsection 6.4.2 compares the time evolution of the tracked observables in kinetic theory and scaled viscous hydrodynamics. These are then used as the basis for a discussion of the time evolution in hybrid simulation schemes in Sec. 6.4.3.

6.4.1 Evolution of transverse profiles in kinetic theory

We now want to discuss the system's time evolution at different opacities resolved in transverse space. This is illustrated in Fig. 6.4 via heatmap plots of the time scaled local rest frame energy density $\tau\epsilon$ together with a vector plot of the transverse components of the flow velocity u^μ at three different values of the shear viscosity, $4\pi\eta/s = 0.5, 3, 10$, which are representative of the regimes of hydrodynamic behaviour, close-to-free-streaming behaviour and the intermediate transitioning regime. The time evolution of these profiles is sampled at three different times, $\tau = 0.1R$, $1R$ and $2R$,

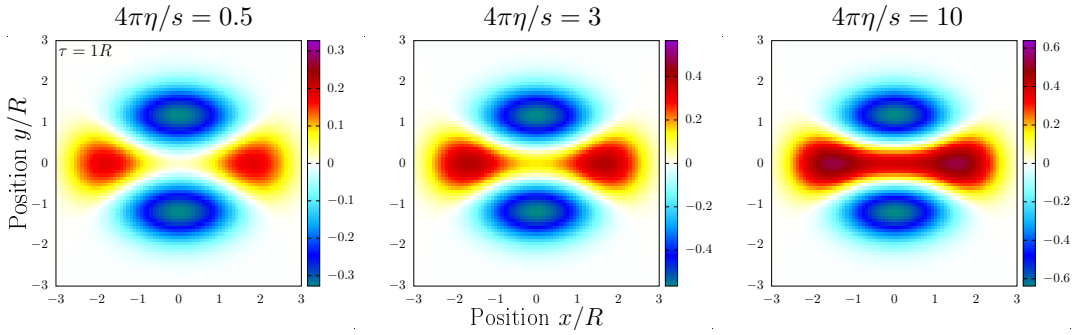

FIGURE 6.5: Transverse profiles of the transverse anisotropy $\tau(T^{xx} - T^{yy})$ of diagonal components of the energy-momentum tensor in kinetic theory at time $\tau = 1R$ for different opacities $4\pi\eta/s = 0.5$ (left), 3 (middle), 10 (right).

which mark the beginning, peak and end of the buildup of elliptic flow ε_p, as discussed in Section 6.4.2.

At the earliest time, $\tau = 0.1R$, transverse dynamics have not had a large effect yet: flow velocities are negligible and the main geometric properties of the profile remain unchanged. The only obvious difference is the overall scale. At smaller η/s, the system starts cooling sooner, performing more work against the longitudinal expansion, resulting in significantly smaller energy densities when compared to larger η/s.

$\tau = 1R$ marks the characteristic time where transverse expansion effects become significant. Here, we see the profile taking on a more circular shape. We also see significant flow velocities, which rise in magnitude with the distance from the center. For smaller shear viscosity η/s, meaning larger interaction rates, the system tends to lump together more, resulting in a smaller spatial extent and smaller flow velocities compared to larger η/s.

At the largest selected time, $\tau = 2R$, the interaction rate in the system has significantly decreased due to the dilution caused by the transverse expansion. Over time, the dynamics will approach a free-streaming expansion in all directions. It is apparent in all three cases that the system has expanded mainly in the directions of larger gradients in the initial state. For small shear viscosity η/s, the system's energy density is still peaked in the center due to stronger collective behaviour. On the other hand, at large η/s, the system evolution is closer to a free-streaming propagation of the initial state, resulting in two high-density areas at distances $r \approx \tau$ from the center. Though the difference is barely visible, the built-up flow velocities are larger for larger η/s.

We can discern additional spatially resolved information on the opacity dependence of the system's evolution by also comparing profile plots of the anisotropic stress, $T^{xx} - T^{yy}$, which are presented in Fig. 6.5. Per definition in Eq. (3.44), the transverse integral of this quantity is proportional to elliptic flow ε_p, which builds up more at smaller opacities. Note that the symmetry phase factor takes the value $e^{2i\phi_p} = -1$ in this case, such that a negative integral results in positive ε_p. The plots show that the transverse plane separates into regions with different sign of the anisotropic stress. The behaviour in the outskirts is dictated by transverse expansion, resulting in positive values in $\pm x$-direction and negative values in $\pm y$-direction. The buildup of elliptic flow seems to proceed mainly via the positive parts decaying more than negative ones. At small opacities in the right panel, particles propagate with few interactions. Due to the initial almond shape, most of the particles in the center propagate in $\pm x$-direction, resulting in a larger T^{xx} than T^{yy}. At large opacities in the left panel, the system is hydrodynamized and the anisotropic stress comes mostly from the direction of flow.

Since the flow components u_x and u_y are zero in the center of the system, anisotropic stress vanishes.

6.4.2 Time evolution of observables in kinetic theory and hydrodynamics

We will now examine the time evolution of certain characteristic transverse space integrated observables in both kinetic theory and the scaled hydrodynamics scheme that was proposed in Section 6.3.2 as a countermeasure to the unphysical pre-equilibrium behaviour of hydrodynamics discussed in Section 4.1.1. This will provide additional insights into the system's behaviour but also reveal how well the scaled hydro scheme works at different opacities. Fig. 6.6 shows comparisons of the time evolution of transverse energy $\mathrm{d}E_{\mathrm{tr}}/\mathrm{d}\eta$, elliptic flow ε_p, average transverse flow velocity $\langle u_\perp \rangle_\epsilon$ and average inverse Reynolds number $\langle \mathrm{Re}^{-1} \rangle_\epsilon$ in both models at three different opacities. Since we are using a fixed initial profile, we plot ε_p without normalization to the initial state eccentricity ϵ_2. As an illustration of the motivation for the scaling scheme in hydrodynamics, for $\mathrm{d}E_{\mathrm{tr}}/\mathrm{d}\eta$ and $\langle \mathrm{Re}^{-1} \rangle_\epsilon$ we also compare with the time evolution in the absence of transverse expansion, where we describe the system as a collection of local Bjorken flows.

The time evolution of transverse energy $\mathrm{d}E_{\mathrm{tr}}/\mathrm{d}\eta$ closely follows results from Bjorken flow scaling at early times, as predicted in section 4.1.1. In Bjorken flow scaling, this observable starts out being constant in the free-streaming period of kinetic theory, while in hydrodynamics, it follows a positive power law, cf. Eq. (4.30). From there, in both cases the time evolution smoothly transitions to a late time equilibrium power law $\mathrm{d}E_{\mathrm{tr}}/\mathrm{d}\eta \sim \tau^{-1/3}$. The timescale of this transition depends on the opacity and is smaller at smaller η/s. In RTA[2], it scales as $\tau_{\mathrm{eq}} \sim (\eta/s)^{4/3}$ [1]. By construction, results from scaled hydrodynamics agree with kinetic theory results in the late time limit of Bjorken flow scaling. The time evolution in full simulations follows this behaviour up to times $\tau \sim R$, when effects of transverse expansion become significant. The rapid dilution due to transverse expansion decreases interaction rates and causes $\mathrm{d}E_{\mathrm{tr}}/\mathrm{d}\eta$ to approach a constant value. For large opacities like $4\pi\eta/s = 0.1$, the Bjorken flow equilibrium where both models agree sets in long before transverse expansion and even afterwards the results will stay in agreement. Intermediate opacities around $4\pi\eta/s = 1$ mark the transition region where results for $\mathrm{d}E_{\mathrm{tr}}/\mathrm{d}\eta$ from both models just barely come into agreement before approaching a constant value. At small opacities like in the case of $4\pi\eta/s = 10$, the onset of transverse expansion interrupts the Bjorken flow scaling period before the two model descriptions have come into agreement. The residual discrepancy then persists throughout the evolution of the system and leads to a mismatch of final state observables,which becomes worse as η/s is increased.

The second line of Fig. 6.6 shows the time evolution of the elliptic flow coefficient ε_p. Again, like in the case of $\mathrm{d}E_{\mathrm{tr}}/\mathrm{d}\eta$, the decrease of interaction rates due to the dilution caused by transverse expansion, ε_p reaches a late-time plateau. Thus, at all opacities, ε_p builds up in a timeframe of $\tau \lesssim 2R$. Contributions from early times are negligible, such that effectively the buildup starts at $\tau \gtrsim 0.1R$. As indicated in the log-log insets, the kinetic theory curves exhibit at early times an approximate power-law increase, $\varepsilon_p \propto \tau^{8/3}$. In contrast, the scaled hydro curve for ε_p first dips to negative values. For $4\pi\eta/s = 0.5$, when equilibration is achieved before the onset of transverse expansion, the scaled hydro curve merges into the RTA one as implied

[2] In general, the equilibration timescale scales with $(\eta/s)^{3(1-\gamma/4)/2}$, with γ as defined in Eq. (4.19). Numerically, the exponent 1.30 for viscous hydrodynamics is close to the one for RTA.

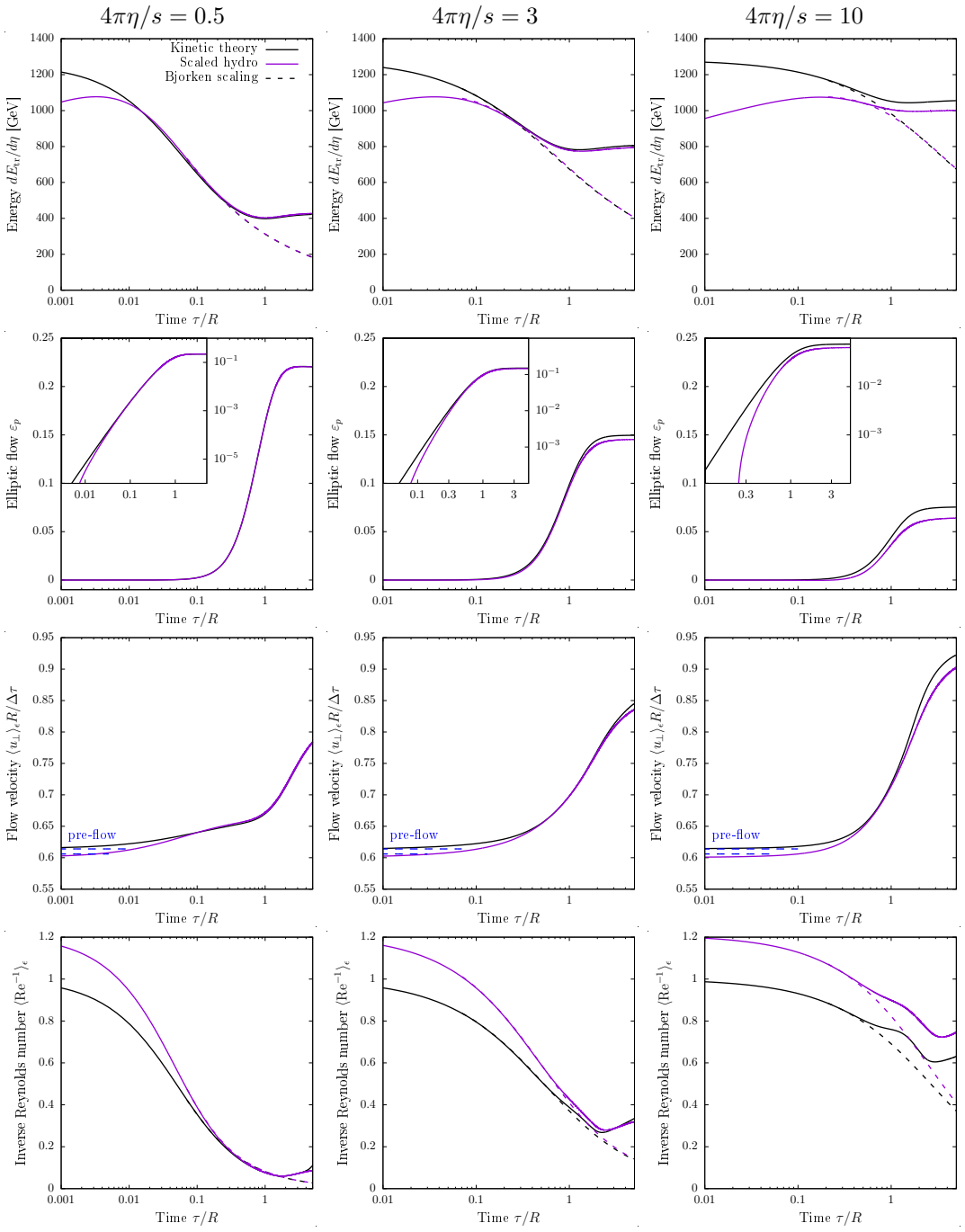

FIGURE 6.6: Time evolution of (from top to bottom) transverse energy $\mathrm{d}E_{\mathrm{tr}}/\mathrm{d}\eta$ [cf. Eq. (3.43)], elliptic flow ε_p [cf. Eq. (3.44)], transverse flow velocity $\langle u_\perp \rangle_\epsilon$ [cf. Eq. (3.53)] and inverse Reynolds number $\left\langle \mathrm{Re}^{-1} \right\rangle_\epsilon$ [cf. Eq. (3.52)] in kinetic theory (black) and scaled viscous hydrodynamics (purple). The time axis is scaled logarithmically in all plots. The plots showing elliptic flow ε_p feature an inset plot of the same quantity plotted in log-log scale. The plots of flow velocity also show the pre-flow result from Table. (6.2) for the early-time limit for $\langle u_\perp \rangle_\epsilon / (\Delta\tau/R)$ (0.614 for kinetic theory and 0.606 for scaled hydrodynamics).

by the discussion in Sec. 6.3.2. At small opacity ($4\pi\eta/s = 10$), the merging process is interrupted by transverse expansion. The scaled hydro result for ε_p is in perfect agreement with kinetic theory at large opacities and stays in good agreement at intermediate opacities. Due to a smaller overall interaction rate, the ε_p-response decreases with decreasing opacity. For small opacities, a negative trend in the early time behaviour of hydrodynamics causes discrepancies with kinetic theory. This trend will become dominant at even smaller opacities, resulting in negative values of the late time plateaus.

As discussed in Section 4.1.2, at early times $\langle u_\perp \rangle_\epsilon$ builds up linearly with the elapsed time $\Delta\tau = \tau - \tau_0$ in kinetic theory. For finite initialization time τ_0, the detailed behaviour in hydrodynamics is slightly different, but almost indistinguishable from linearity in $\Delta\tau$. Hence, we plot the ratio $\frac{\langle u_\perp \rangle_\epsilon}{\Delta\tau/R}$and indicate the early time limit via constant lines. The plots confirm that there are slight differences in the early time behaviour of the flow velocities in hydrodynamics and kinetic theory, however they come into agreement on similar timescales as $\mathrm{d}E_{\mathrm{tr}}/\mathrm{d}\eta$. This is partly owing to the fact that early time contributions to the total $\langle u_\perp \rangle_\epsilon$ are negligible. $\langle u_\perp \rangle_\epsilon$ enters a period of superlinear rise during transverse expansion. While this period ends earlier at larger opacities due to dilution of the system and transition to free-streaming, the total rise of $\frac{\langle u_\perp \rangle_\epsilon}{\Delta\tau/R}$ is nevertheless larger. Comparing hydrodynamic results to kinetic theory results, the late time free-streaming does not seem to be accurately reproduced, as hydrodynamics underestimates $\langle u_\perp \rangle_\epsilon$. Problems in the late time behaviour are less relevant for the other observables we discuss, as they tend to plateau at late times. This late time discrepancy between hydrodynamics and kinetic theory is thus a phenomenon that mainly affects $\langle u_\perp \rangle_\epsilon$ among the observables that were tracked in this work, and is not related to pre-equilibrium.

Finally, we look at the time evolution of the average inverse Reynolds number, which is a measure of the size of non-equilibrium effects in the system. We normalized this in such a way that in RTA, its initial value is equal to one (note that in scaled hydro, $\mathrm{Re}^{-1} \sim 1.212$ when $\tau_0 \to 0$). Like for $\mathrm{d}E_{\mathrm{tr}}/\mathrm{d}\eta$, the two model descriptions will come into agreement in the late time limit of Bjorken flow scaling, on timescales that are larger for smaller opacities. Due to equilibration, in this period $\langle \mathrm{Re}^{-1} \rangle_\epsilon$ experiences a phase of rapid decay towards 0, as expected since Re^{-1} measures non-equilibrium effects. The effect of transverse expansion on this observable is not straightforwardly understood, except for the fact that due to the additional dilution, $\langle \mathrm{Re}^{-1} \rangle_\epsilon$ must be larger in full simulations than in Bjorken flow scaling. For large opacities, transverse expansion seems to only slow down the approach to equilibrium. However, at intermediate opacities we see a significant rise in $\langle \mathrm{Re}^{-1} \rangle_\epsilon$. We also computed results for the limit of vanishing opacity. Here, the inverse Reynolds number remains constant at early times, but later increases due to transverse expansion, e.g. at $\tau = 4R$ to a value of $\langle \mathrm{Re}^{-1} \rangle_\epsilon(\tau = 4R) = 1.322$. However, an increase due to transverse expansion cannot be the only late time effect, as we can see from the results at $4\pi\eta/s = 10$, where even after its first departure thereof, the average inverse Reynolds number goes back to dropping at similar speeds as the Bjorken flow scaling result, before starting to rise at late times. But what we can say with certainty is that $\langle \mathrm{Re}^{-1} \rangle_\epsilon$ will have a minimum value that is larger for smaller opacities. For very small opacities, it will not drop significantly below its initial value of 1 before starting to rise.

For a more detailed examination of the opacity dependence of the time evolution in kinetic theory ranging from very small ($4\pi\eta/s = 1000$) to very large opacities ($4\pi\eta/s = 0.01$), please see App. G.

After examining the time evolution of these observables and establishing some

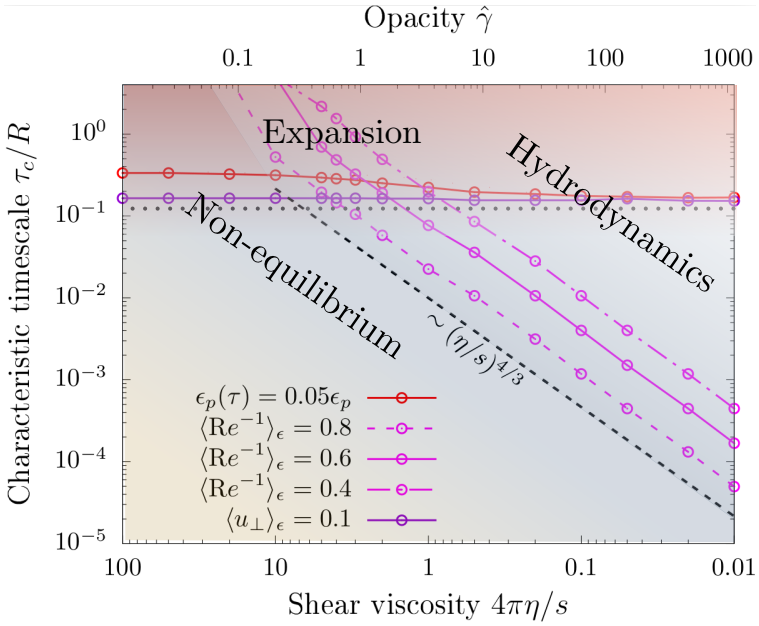

FIGURE 6.7: Opacity ($\hat{\gamma} = \frac{11.3}{4\pi\eta/s}$) dependence of the characteristic times where the elliptic flow ε_p [cf. Eq. (3.44)] reaches 5% of its late time ($\tau = 4R$) value (red), the transverse flow velocity [cf. Eq. (3.53)] builds up to a value of $\langle u_\perp \rangle_\epsilon = 0.1$ (purple), or the inverse Reynolds number [cf. Eq. (3.52)] drops to a value of $\langle \mathrm{Re}^{-1} \rangle_\epsilon = 0.8$ (pink, dashed), 0.6 (pink, solid) or 0.4 (pink, long-short dashed). The buildup in transverse flow velocity marks the transition from the Bjorken flow scaling regime to the regime of transverse expansion, while the drop in inverse Reynolds number marks the region where hydrodynamics is applicable.

understanding about the implications of their buildup, we now want to invert this logic. As the change in these observables carries information on the state of the system, e.g. the progress of its equilibration or the onset of transverse expansion, we want to track the first times these observables reach a specific milestone of their time evolution as a function of opacity. Fig. 6.7 shows plots of kinetic theory results for these curves for five different milestone criteria. Specifically, we tracked when the average transverse flow velocity reaches a value of 0.1 as a criterion for the onset of transverse expansion, the time when the elliptic flow response builds up to 5% of its maximum value at the given opacity as a criterion for the beginning of the buildup of flow, and the time when the average inverse Reynolds number reaches values of 0.4, 0.6 and 0.8, which tells us to what degree hydrodynamization has progressed. As it turns out, the curve for the flow velocity criterion is almost perfectly flat at a value of $\tau_c \approx 0.15R$, meaning that the early time buildup of $\langle u_\perp \rangle_\epsilon$ is mostly independent of the opacity. The elliptic flow criterion is met at similar times as the flow velocity criterion at large opacities, but at slightly later times $\tau_c \approx 0.3R$ for small opacities. Despite the general timeframe of ε_p-buildup being independent of opacity, it seems to start slightly earlier at larger opacities. The most interesting criterion curves are those for the average inverse Reynolds number. The systems adherence to early time Bjorken flow scaling leads to a power law behaviour $\tau_c \propto (\eta/s)^{4/3}$ for all three of these curves at large opacities. The curves deviate from this power law when the criterion is not reached before transverse expansion sets in at times $\tau \sim R$. For small opacities, the criteria are never met, as the average inverse Reynolds number reaches a minimum value larger than the criterion value, as already stated in the discussion of Fig. 6.6. The behaviour of $\mathrm{d}E_{\mathrm{tr}}/\mathrm{d}\eta$ resembles that of $\mathrm{d}E_\perp/\mathrm{d}\eta$, which we already discussed in

the previous Chapter. Similarly to $\langle \mathrm{Re}^{-1} \rangle_\epsilon$, it follows Bjorken flow scaling at early times, resulting in a similar power law behaviour.

6.4.3 Time evolution in hybrid schemes

Another way to alleviate discrepancies due to the behaviour of hydrodynamics in the pre-equilibrium phase as discussed in Section 4.1.1 is to model the time evolution via a hybrid scheme, switching from a kinetic theory based description at early times to hydrodynamics at later times, i.e. initializing the hydrodynamic simulation with the energy-momentum tensor computed from the kinetic theory based time evolution. This requires to fix a criterion for when to switch descriptions.

As we argue that hydrodynamics becomes viable only after some timescale related to equilibration, we also expect the accuracy of hybrid scheme results to depend on the switching times. Due to the opacity dependence of equilibration, it might be beneficial to choose switching times as a function of opacity. Hence we tested both a hybrid scheme with fixed switching times at two different times $\tau = 0.4\,\mathrm{fm}$ and $\tau = 1\,\mathrm{fm}$, which are in the range of switching times typically used in phenomenological descriptions, and with dynamically determined switching times.

In order to tie this definition to the phenomenon of equilibration, we determine the dynamical switching times on the basis of the dropoff the average inverse Reynolds number $\langle \mathrm{Re}^{-1} \rangle_\epsilon$, i.e. we switch as soon as this quantity first reaches a specific value. Specifically, we chose the values $\langle \mathrm{Re}^{-1} \rangle_\epsilon = 0.8$, 0.6 and 0.4 (sometimes we will consider switching also when $\langle \mathrm{Re}^{-1} \rangle_\epsilon$ drops below 0.2). In the case of a transversally homogeneous system, Fig. 4.1 shows that these values for the inverse Reynolds number correspond to various degrees of hydrodynamization of the system. Speicifically, $\mathrm{Re}^{-1} = 0.8$ ($\tilde{w} \simeq 0.2$) corresponds to the onset of hydrodynamization. When $\mathrm{Re}^{-1} = 0.6$ ($\tilde{w} \simeq 0.6$), the system significantly progressed through the hydrodynamization process, while when $\mathrm{Re}^{-1} = 0.4$ (($\tilde{w} \simeq 1$), the system has hydrodynamized and the kinetic theory and hydrodynamics attractor curves are almost merged. Due to the relation (4.7) between $\tilde{w}$ and the Bjorken time τ, the characteristic times τ_c when Re^{-1} drops below a certain threshold increase with $4\pi\eta/s$ (see Sec. 6.4.2 for a detailed discussion).

The results are illustrated by the time evolution of transverse energy $\mathrm{d}E_{\mathrm{tr}}/\mathrm{d}\eta$, elliptic flow ε_p and average transverse flow velocity $\langle u_\perp \rangle_\epsilon$ compared for different choices of the switching times, as plotted in Fig. 6.8 at three different opacities. The early time evolution was computed with the RLB method of simulating kinetic theory. The plots also compare to results from a pure kinetic theory simulation as well as from our scaled viscous hydro scheme. Here we plot all results including the ones for elliptic flow ε_p on a logarithmic scale of the time axis so that the different switching times are discernible. The ε_p plots also feature an inset plot on log-log scale. It can be seen that the curves corresponding to the hybrid setups tend to detach from the RTA curve towards lower values of ε_p. Since in viscous hydro, the equilibration process leads to a decrease of spatial eccentricity ϵ_2 (see lower panel of Fig. 6.3), the hybrid simulations with early switching times will lead to lower late-time values of ε_p (see the discussion in the next section).

At a small shear viscosity of $4\pi\eta/s = 0.1$, all switching schemes yield accurate results for all three observables. Since the equilibration timescale is small for this opacity, it has equilibrated by the time we switch descriptions such that kinetic theory and hydrodynamics are in agreement. The $\langle \mathrm{Re}^{-1} \rangle_\epsilon$-based criteria are fulfilled early on in the system's evolution such that the dynamically chosen switching times are significantly smaller than the fixed ones. However, when comparing results from pure

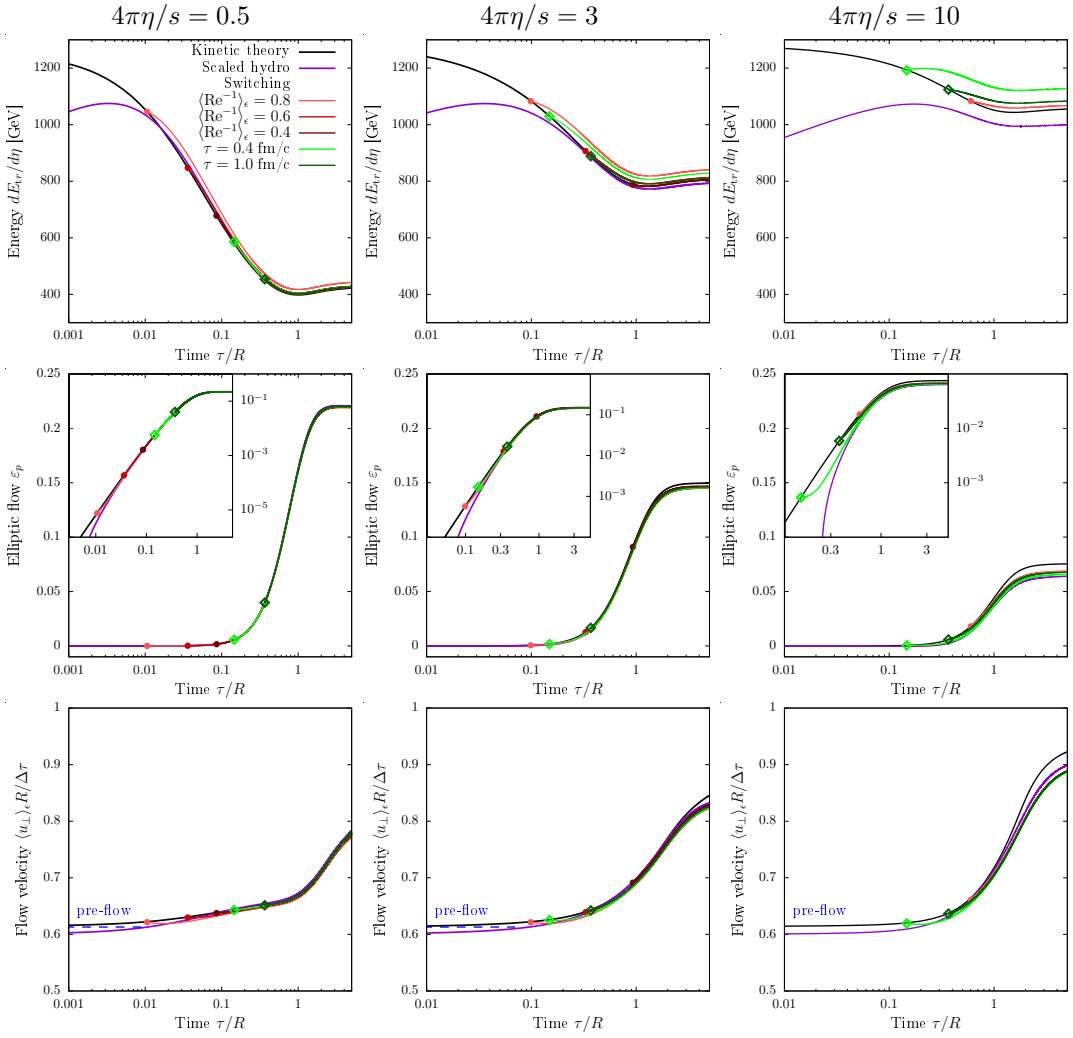

FIGURE 6.8: Time evolution of transverse energy $\mathrm{d}E_{\mathrm{tr}}/\mathrm{d}\eta$ [top, cf. Eq. (3.43)], elliptic flow ε_p [middle, cf. Eq. (3.44)] and transverse flow velocity $\langle u_\perp \rangle_\epsilon$ [bottom, cf. Eq. (3.53)] in hybrid kinetic theory + viscous hydro simulations at opacities $4\pi\eta/s = 0.5$ (left), 3 (middle) and 10 (right) when switching at different values of the inverse Reynolds number [cf. Eq. (3.52)] $\left\langle \mathrm{Re}^{-1} \right\rangle_\epsilon = 0.8$ (light red), 0.6 (red) and 0.4 (dark red) or fixed time $\tau = 0.4\,\mathrm{fm}$ (light green) and $\tau = 1\,\mathrm{fm}$ (dark-green). The switching points are marked with filled symbols. The time axis is scaled logarithmically. The plots showing elliptic flow ε_p feature an inset plot of the same quantity plotted in log-log scale. In the flow velocity plots, we also show the estimate $\langle u_\perp \rangle_{\epsilon,\mathrm{RTA}} = 0.614\Delta\tau/R$ for the early-time build-up of pre-flow in kinetic theory (see Table 6.2).

kinetic theory or viscous hydrodynamics, they are within the timeframe where both descriptions are in accaptable agreement. The only curve where a deviation from kinetic theory is clearly visible is the one for $\mathrm{Re} = 0.8$, where hydrodynamization has only partly progressed before the onset of transverse expansion.

The results at $4\pi\eta/s = 3$ now show that it is indeed necessary to give the choice of switching times some thought, as here we see a significant increase in accuracy of results for $\mathrm{d}E_{\mathrm{tr}}/\mathrm{d}\eta$ and $\langle u_\perp \rangle_\epsilon$ with later switching times. For this opacity, the dynamically chosen switching times are on a similar scale as the fixed ones. We also see that the nature of any discrepancies with pure kinetic theory results is the same as in the case of hydrodynamics. As soon as we switch, the curves of these observables follow a trajectory that is qualitatively similar to the pure hydrodynamics result, meaning that $\mathrm{d}E_{\mathrm{tr}}/\mathrm{d}\eta$ is increased, while $\langle u_\perp \rangle_\epsilon$ and ε_p are decreased relative to the kinetic theory result.

The strength of the dynamically chosen switching times is well displayed for results at $4\pi\eta/s = 10$. In this case, the system is still far from hydrodynamized at the two fixed switching times, leading to sizeable inaccuracies in the corresponding hybrid scheme results for all three observables, but especially for $\mathrm{d}E_{\mathrm{tr}}/\mathrm{d}\eta$. As $\left\langle \mathrm{Re}^{-1} \right\rangle_\epsilon$ does not drop low enough, two of the three criteria for the dynamical switching were not reached. However, the result for switching at the largest of the three values of $\left\langle \mathrm{Re}^{-1} \right\rangle_\epsilon$ retains a similar level of accuracy as at smaller shear viscosity and is a significant improvement to fixed time switching results.

Overall, we find that while switching at fixed time is conceptionally straightforward and always possible, the accuracy of this scheme strongly depends on the opacity and results at large opacity show large deviations from full kinetic theory. They can be far away from kinetic theory results at small opacities. On the other hand, switching based on $\left\langle \mathrm{Re}^{-1} \right\rangle_\epsilon$ is not always possible because this quantity does not drop to the desired values at small opacities, but whenever it is possible, the accuracy of the result can be estimated beforehand and depends only little on opacity. In other words, the dynamical definition yields the earliest possible switching time for a desired accuracy, and whenever $\left\langle \mathrm{Re}^{-1} \right\rangle_\epsilon$ does not drop enough for it to be determined, hydrodynamics is not viable in the first place.

Finally, we also tested hybrid schemes with the same switching times but with an early time evolution computed in KøMPøST. We found that due to its limited range of applicability, some of the later switching times could not be viably reached with this description. But whenever we were able to obtain results, they were in good agreement with the results from the previously discussed scheme, except for some systematic errors in ε_p and $\langle u_\perp \rangle_\epsilon$. These results are presented in more detail in Appendix H, together with analogous time dependence plots to those presented in Fig. 6.8.

6.5 Opacity dependence of final state observables in kinetic theory and beyond

The previous Section's comparison of the time evolution in different models has provided insights into the nature of different sources of discrepancies and at what opacities to expect them. For a detailed opacity-resolved analysis, it is convenient to study the dependence of final state observables on a wide range in opacity from the free-streaming regime to ideal fluid behaviour. In Sec. 6.5.1, we present opacity dependencies in kinetic theory, naive viscous hydrodynamics and scaled viscous hydrodynamics. Section 6.5.2 discusses results for hybrid simulation schemes.

6.5.1 Scaled and naive hydrodynamics compared to kinetic theory

First, we assess the performance of scaled hydrodynamics as described in Sec. 6.3.2 when compared to a common naive initialization scheme of hydrodynamics, where the simulation is started at a time τ_0 where hydrodynamization is likely to have set in, with the same initial condition for $\tau_0\epsilon(\tau_0, \mathbf{x}_\perp)$ as we are using for kinetic theory simulations initialized in the early time free-streaming limit. Fig 6.9 shows the opacity dependences of transverse energy $\mathrm{d}E_{\mathrm{tr}}/\mathrm{d}\eta$, elliptic flow ε_p and average transverse flow velocity $\langle u_\perp \rangle_\epsilon$ in kinetic theory, scaled hydrodynamics and naive hydrodynamics at two different initialization times $\tau_0 = 0.4\,\mathrm{fm}$ and $\tau_0 = 1\,\mathrm{fm}$, which are in the range of values typically used in phenomenological descriptions.

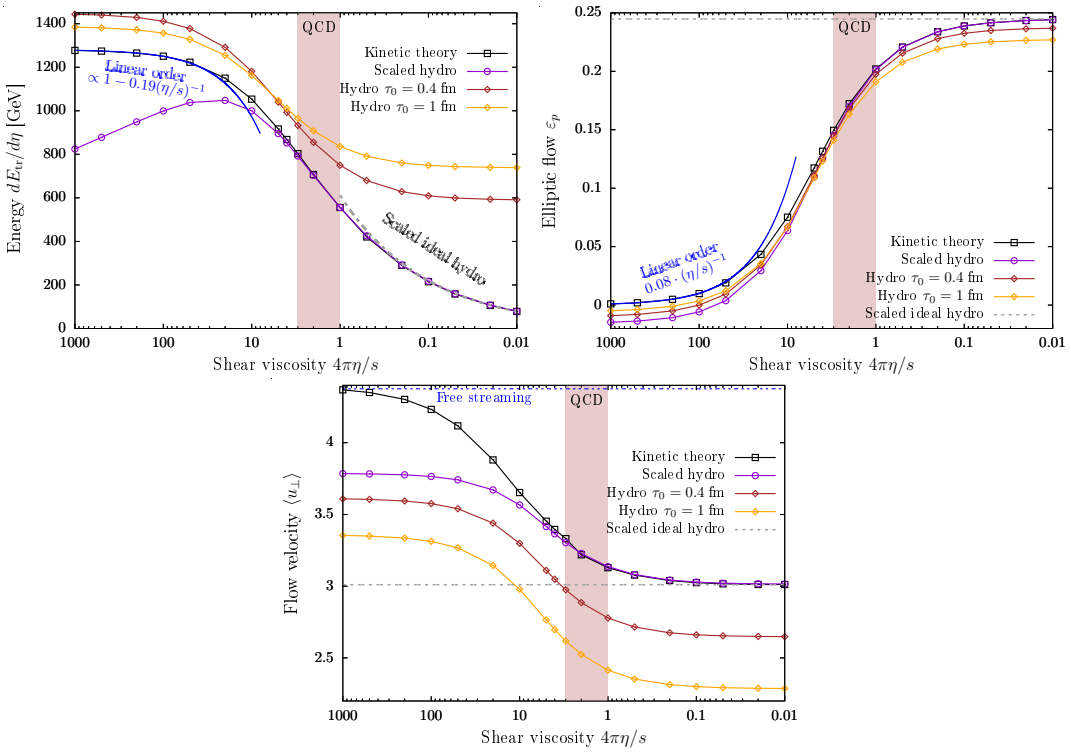

FIGURE 6.9: Opacity- (η/s-) dependence of the final ($\tau = 4R$) values of transverse energy $\mathrm{d}E_{\mathrm{tr}}/\mathrm{d}\eta$ [top, cf. Eq. (3.43)], elliptic flow ε_p [middle, cf. Eq. (3.44)] and transverse flow velocity $\langle u_\perp \rangle$ [bottom, cf. Eq. (3.53)] for kinetic theory (black), scaled hydro (purple) and naive hydro at two different initialization times $\tau_0 = 0.4\,\mathrm{fm}$ (brown) and 1 fm (yellow). Also plotted are the small opacity limits of an opacity-linearized result (blue) in the top two plots, the free-streaming result (blue, dashed) in the bottom plot as well as the opacity-scaled ideal hydrodynamics results (grey, dashed). The latter follows a $(\eta/s)^{4/9}$ scaling law for $\mathrm{d}E_{\mathrm{tr}}/d\eta$ as per the intialization scheme in Eq. (6.4). The ideal hydro results are 611 GeV$\cdot(\eta/s)^{4/9}$ for $\mathrm{d}E_{\mathrm{tr}}/d\eta$, 0.244 for ε_p and 3.01 for $\langle u_\perp \rangle_\epsilon$. The red shaded region shows the realistic values for QCD according to Bayesian estimates.

For all three observables, the kinetic theory results smoothly interpolate between limiting cases of small and large opacities. For $\mathrm{d}E_{\mathrm{tr}}/\mathrm{d}\eta$ and ε_p, we compare at small opacities to results from the linear order opacity expansion that is introduced in Sec. 3.2.2. Results from full kinetic theory are in excellent agreement with these approximations for $4\pi\eta/s \gtrsim 20$. In the case of $\langle u_\perp \rangle_\epsilon$, we present results for the free-streaming limit $\hat{\gamma} \to 0$, which the full kinetic theory results converge to at small opacities.

On the other end of the opacity spectrum, the results from both kinetic theory and scaled viscous hydrodynamics converge to those of scaled ideal hydrodynamics in the limit $\eta/s \to 0$. Even though $\eta/s = 0$ by definition in ideal hydrodynamics, we represent the scaled ideal hydro results as a function of $4\pi\eta/s$ in the equivalent RTA simulation [see discussion around Eq. (6.4)], leading to a power-law dependence $\mathrm{d}E_{\mathrm{tr}}/\mathrm{d}\eta \propto (4\pi\eta/s)^{4/9}$, which is confirmed by the scaled viscous hydrodynamics and kinetic theory results (this result was derived from early-time Bjorken scaling in [1]). The curves for ε_p and $\langle u_\perp \rangle_\epsilon$ converge at large opacities to the ideal hydrodynamics limit that was obtained with a scaled initial condition. This is not a priori obvious but rather an achievement of our proposed scheme. Ideal hydrodynamics is the large opacity limit of kinetic theory only after hydrodynamization. At any finite opacity, kinetic theory simulations feature a pre-equilibrium period which is absent in ideal hydro. In this period, the ellipticity ϵ_2 decreases in kinetic theory, such that with the same initial condition, it would result in a smaller elliptic flow ε_p than in ideal hydro. The agreement is only reached after scaling the hydro initial condition as discussed in Section 6.1.

Comparing now to hydrodynamic results, for all three obserables, the large opacity limits of scaled hydrodynamics and kinetic theory are in excellent agreement. Going to small opacities, all observables are underestimated in hydro, which will be further discussed in the following. Agreement holds for $4\pi\eta/s \lesssim 3$. On the other hand, for naive hydrodynamics, the opacity dependence curves show qualitatively similar behaviour but are in quantitative disagreement for all opacities.

This is obvious in the case of $\mathrm{d}E_{\mathrm{tr}}/\mathrm{d}\eta$, which is significantly overestimated. We find that that the large opacity power law is not captured. There are different reasons for this in the two limiting cases of large and small opacity. For small opacities $4\pi\eta/s \gtrsim 10$, despite the initialization time being large, it is still smaller than the equilibration timescale and the simulation will partly undergo a hydrodynamic pre-equilibrium phase. As we have seen, in this phase $\mathrm{d}E_{\mathrm{tr}}/\mathrm{d}\eta$ increases in hydrodynamic simulations before the onset of transverse expansion, while staying constant in kinetic theory, so it is overestimated in hydro. For the smaller initialization time $\tau_0 = 0.4\,\mathrm{fm}$, the system is in pre-equilibrium for a longer time compared to $\tau_0 = 1\,\mathrm{fm}$. This is why results for $\tau_0 = 0.4\,\mathrm{fm}$ yield a larger final value of $\mathrm{d}E_{\mathrm{tr}}/\mathrm{d}\eta$ at small opacities. On the other hand, for large opacities $4\pi\eta/s \lesssim 3$, the system would have been in equilibrium for a significant amount of time if it had been initialized at an earlier time. In the equilibrated phase before transverse expansion, $\mathrm{d}E_{\mathrm{tr}}/\mathrm{d}\eta$ drops proportionally to $\tau^{-1/3}$. The larger the initialization time, the more of this period is cut out of the simulation, resulting in a larger final value. This is why the curve for initialization at $\tau_0 = 1\,\mathrm{fm}$ is above the one for $\tau_0 = 0.4\,\mathrm{fm}$ at large opacities, resulting in a crossing of the two at intermediate opacities $4\pi\eta/s \sim 5$. The equilibration timescale becomes smaller and smaller at larger and larger opacities, meaning that for fixed initialization time more and more of the $\tau^{-1/3}$-scaling period is cut out. This is why the large opacity power law is not reproduced in naive hydrodynamics.

These problems are cured in scaled hydrodynamics. It is initialized at very early times, so no part of the time evolution is lost. The discrepancies due to hydrodynamic pre-equilibrium behaviour are cured via scaling the initial energy density as discussed in Sec. 6.1 such that agreement with kinetic theory is reached only after equilibration. However, for small opacities $4\pi\eta/s \gtrsim 3$, the underlying assumption of a timescale separation of equilibration and transverse expansion no longer holds. In this case, scaled hydrodynamics underestimates $\mathrm{d}E_{\mathrm{tr}}/\mathrm{d}\eta$, as transverse expansion interrupts its approach to kinetic theory behaviour before agreement is reached.

Of the three presented observables, ε_p in naive hydrodynamics shows the weakest

deviations from kinetic theory results. This is in alignment with our expectations, as we know that hydro has been very successfull in phenomenological descriptions of anisotropic flow. The reasons might be that ε_p builds up on timescales that are fully captured by simulations at initialization times of ~ 1 fm and depends very little on the overall energy scale. But certainly, this level of agreement was not to be expected a priori and should be regarded as a concidence. The influence of the initialization time is as follows. At small opacities $4\pi\eta/s \gtrsim 10$, a part of the early time negative trend in hydrodynamics is cut out, resulting in larger results for later initialization times. For large opacities $4\pi\eta/s \lesssim 1$, ε_p already has positive contributions at early times which might be cut out, resulting in smaller final values for later initialization times. But very early initialization times cannot bring hydro into agreement with kinetic theory. As discussed in section 4.1.1, hydrodynamics initialized at very early times exhibits a larger decrease of the eccentricity during pre-equilibrium, resulting in lower final values of ε_p than in kinetic theory. However, the scaling procedure counteracts this phenomenon by increasing the eccentricity in the initial state of hydrodynamic simulations, such that scaled hydrodynamics is in perfect agreement with kinetic theory at large opacities $4\pi\eta/s \lesssim 3$. For small opacities $4\pi\eta/s \gtrsim 10$, on the other hand, due to the early initialization scaled hydrodynamics features a longer period of the aforementioned early time negative buildup of ε_p, resulting in final values which are lower than in the case of the naive hydro initializations discussed above.

The flow velocity results from naive hydrodynamics again show two effects. One of them is straightforward: as this observable rises monotonically with time, for larger initialization times, there is less time for $\langle u_\perp \rangle_\epsilon$ to build up, resulting in an underestimate. This effect is cured in scaled hydrodynamics due to the early initialization. At small opacities $4\pi\eta/s \gtrsim 10$, we see an additional decrease of hydrodynamic results compared to kinetic theory due to its inability to describe the late-time free-streaming behaviour. This is an effect that both hydro schemes (based on naive and scaled initial conditions) have in common.

6.5.2 Hybrid simulations

As described in Section 6.4.3, another way to bring hydrodynamic results into agreement with kinetic theory is to use hybrid schemes switching from a kinetic theory based early time description to hydrodynamics at later times. We tried switching both at fixed times as well as at the first times equilibration has proceeded to a given extent, which we quantified by the inverse Reynolds number dropping to a specific value. We also tested two different model descriptions for early times: full kinetic theory and KøMPøST. As described in the previous Section, the time evolution curves of all observables instantaneously change behaviour when the models are switched, such that switching too early will be affected by the inaccurate description of pre-equilibrium in hydrodynamics. We now want to quantitatively assess the accuracy of various switching schemes as a function of opacity.

We first discuss results for the opacity dependence in hybrid simulations with $\langle \mathrm{Re}^{-1} \rangle_\epsilon$-based switching, which are plotted in Fig. 6.10. For early switching times on the timescale of equilibration, hybrid results may reflect the inaccurate pre-equilibrium behaviour in hydrodynamics. Of course, in this case, there is no scaling of the initial condition to counteract this behaviour. However, this also means that these schemes do not suffer from discrepancies due to an incomplete approach of a scaled initial condition to kinetic theory behaviour before the onset of transverse expansion, and therefore tend to be more accurate than scaled hydrodynamics at intermediate opacities, i.e. for $4\pi\eta/s \sim 3$. However, results plotted with smaller crosses and dashed

lines were obtained in simulations with switching times larger than $0.5R$, so in this case it is questionable whether these schemes could be considered hybrid results, as the crucial parts of the time evolution were actually described in kinetic theory.

Going into more detail, hybrid results typically overestimate $\mathrm{d}E_{\mathrm{tr}}/\mathrm{d}\eta$ because of the hydrodynamic pre-equilibrium increase after switching. ε_p is underestimated, however, the hydrodynamic negative early time trend is alleviated, such that results from kinetic theory + viscous hydro are typically larger than scaled hydro results. Hybrid results show a consistent underestimation of $\langle u_\perp \rangle_\epsilon$, but on a relative scale this error is negligible. This could be due to hydrodynamic flow velocities typically being smaller than those in kinetic theory at early times, causing a dip in $\langle u_\perp \rangle_\epsilon$ relative to kinetic theory after switching.

Comparing kinetic theory + viscous hydrodynamics in the left column of the figure to KøMPøST + viscous hydrodynamics in the right column, one obvious difference is that in the latter, some of the results for smaller opacities are missing, because there the $\langle \mathrm{Re}^{-1} \rangle_\epsilon$-based switching times were too late to be reached with KøMPøST [3]. Where it does work, it produces almost the same results for $\mathrm{d}E_{\mathrm{tr}}/\mathrm{d}\eta$ as kinetic theory. The underestimation of $\langle u_\perp \rangle_\epsilon$ is slightly more severe in KøMPøST. It does seem to have a systematic component on top of the one related to switching early. But the total deviation is still negligible. The largest difference is seen in ε_p, which is not built up at all in KøMPøST simulations, thus there is a significantly larger underestimation at smaller opacities, where a larger part of the time evolution is described in KøMPøST.

Next, we shift our attention to results from hybrid schemes at fixed switching times $\tau_s = 0.4\,\mathrm{fm}$ and $\tau_s = 1\,\mathrm{fm}$, which are presented in Fig. 6.11. As expected from the discussion of the time evolution in Sec. 6.4.3, again kinetic theory + viscous hydrodynamics yields perfectly accurate results at large opacities $4\pi\eta/s \lesssim 1$ and improves on scaled hydrodynamics at intermediate opacities $4\pi\eta/s \sim 3$, but less so than for dynamically chosen switching times. The upshot is that hybrid schemes with fixed switching times are applicable for arbitrarily small opacities. However, here the results for the three tracked observables show similar problems to those obtained in naive hydrodynamics simulations discussed earlier in this section. Due to incomplete equilibration at early switching times, $\mathrm{d}E_{\mathrm{tr}}/\mathrm{d}\eta$ increases after switching. ε_p suffers from the early time negative trend in hydrodynamics, but slightly less than scaled hydrodynamics. $\langle u_\perp \rangle_\epsilon$ is again only slightly underestimated in hybrid schemes when compared to scaled hydrodynamics due to the different pre-equilibrium. This is an improvement over naive hydrodynamics, as instead of starting at late times with no flow velocity, the early time buildup is described in kinetic theory. Both schemes suffer equally from the inability of hydrodynamics to describe flow velocities in the late time free-streaming limit.

Also for fixed switching times, KøMPøST + viscous hydrodynamics results for $\mathrm{d}E_{\mathrm{tr}}/\mathrm{d}\eta$ and $\langle u_\perp \rangle_\epsilon$ are in good agreement with those obtained in kinetic theory + viscous hydrodynamics simulations. We again see the effect of the absence of ε_p-buildup in KøMPøST. Since we do not increase the duration of time evolution in KøMPøST, the effect is not larger at small opacities $4\pi\eta/s \gtrsim 10$. In fact, here we see agreement with results from kinetic theory + viscous hydrodynamics, as there is no significant buildup of ε_p at early times. However, at large opacities $4\pi\eta/s \lesssim 5$,

[3] For large evolution times, KøMPøST crashes in the setup stage when computing the Green's functions. This is because they are only implemented for a finite number of points in momentum space and have to be convolved with a Gaussian smearing kernel $\exp(-\sigma^2|\mathbf{k}|/2)$. But the Green's functions scale in $|\mathbf{k}|(\tau - \tau_0)$ such that for too large of an evolution time this smearing is no longer sufficient.

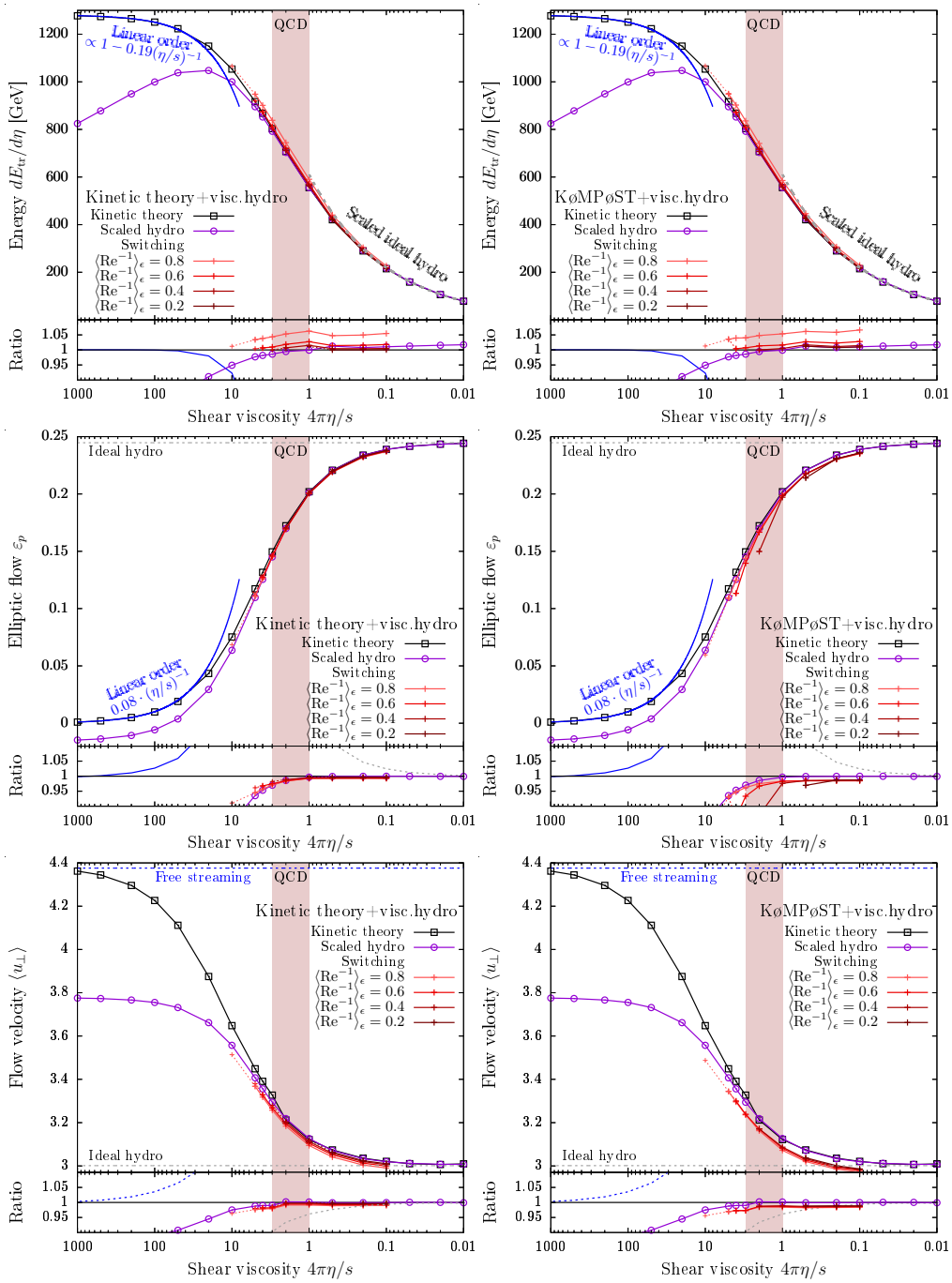

FIGURE 6.10: Opacity- (η/s-) dependence of the final ($\tau = 4R$) values of transverse energy $dE_{\rm tr}/dy$ (top, cf. Eq. 3.43), elliptic flow ϵ_p (middle, cf. Eq. 3.44) and transverse flow velocity $\langle u_\perp \rangle$ (bottom, cf. Eq. 3.53) in hybrid kinetic theory + viscous hydro (left) resp. KøMPøST + viscous hydro simulations (right) when switching at different values of the inverse Reynolds number (c.f. Eq. 3.52) $\left\langle \mathrm{Re}^{-1} \right\rangle_\epsilon = 0.8$, 0.6, 0.4 and 0.2 plotted in different shades of red from light to dark. Results from simulations with switching times after $\tau = 0.5R$ are plotted with smaller points (+) and dashed lines. The results are compared to kinetic theory (black), scaled hydro (purple) and the small opacity limits of an opacity-linearized result (blue) in the top two plots resp. the free-streaming result (blue, dashed) in the bottom plot as well as the large opacity limit of ideal hydro (grey, dashed) in the bottom two plots as well as a $(\eta/s)^{4/9}$ scaling law (green) in the top plot. The red shaded region shows the realistic values for QCD according to Bayesian estimates. The bottom part of the plot shows the ratios of all results to those from kinetic theory.

this buildup starts earlier, which is why KøMPøST + viscous hydrodynamics results underestimate the final values in these cases.

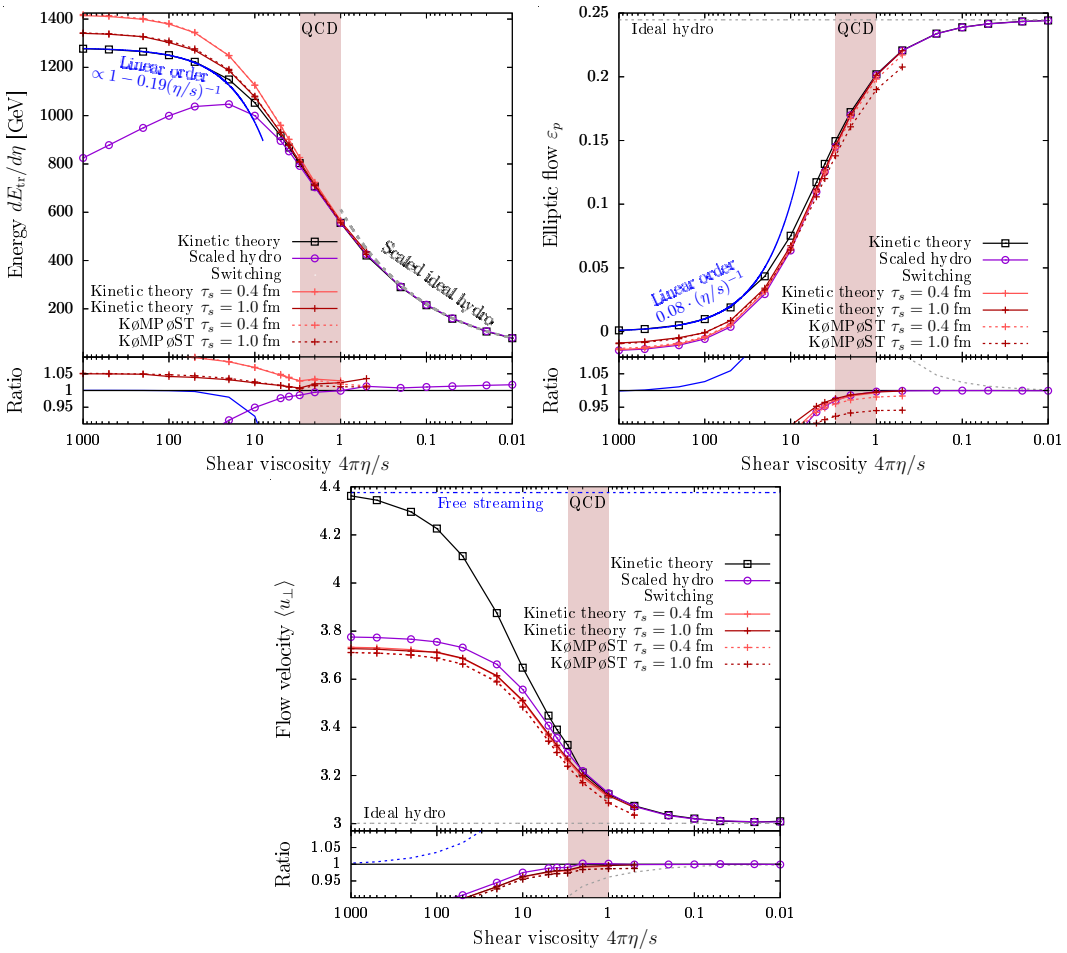

FIGURE 6.11: Opacity- (η/s-) dependence of the final ($\tau = 4R$) values of transverse energy $\mathrm{d}E_{\rm tr}/\mathrm{d}\eta$ [top, cf. Eq. (3.43)], elliptic flow ε_p [middle, cf. Eq. (3.44)] and transverse flow velocity $\langle u_\perp \rangle$ [bottom, cf. Eq. (3.53)] in hybrid kinetic theory + viscous hydro (solid lines) resp. KøMPøST + viscous hydro simulations (dashed lines) when switching at fixed times $\tau = 0.4\,\mathrm{fm}$ (light red) and $\tau = 1\,\mathrm{fm}$ (dark red). The results are compared to kinetic theory (black), scaled hydro (purple) and the small opacity limits of an opacity-linearized result (blue) in the top two plots resp. the free-streaming result (blue, dashed) in the bottom plot as well as the large opacity limit of scaled ideal hydro (grey, dashed), which scales as $(\eta/s)^{4/9}$ in the top plot. The red shaded region shows the realistic values for QCD according to Bayesian estimates. The bottom part of the plot shows the ratios of all results to those from kinetic theory.

6.6 Discussion

In this chapter, we examined hydrodynamic and kinetic theory simulations of hadronic collisions. Within a simplified model setup based on RTA and using a fixed initial profile that was obtained as an average of events in the 30-40% centrality class of PbPb collisions, we scanned the dynamical behaviour on the whole range in interaction rates as parametrized by the opacity $\hat{\gamma}$ defined in Eq. (3.13), which for the fixed profile is inversely proportional to shear viscosity, $\hat{\gamma} = 11.3/(4\pi\eta/s)$. This study was based

on results for the transverse energy $\mathrm{d}E_{\mathrm{tr}}/\mathrm{d}\eta$, elliptic flow ε_p, radial flow $\langle u_\perp \rangle_\epsilon$ and shear stress as measured via the inverse Reynolds number $\langle \mathrm{Re}^{-1} \rangle_\epsilon$. At small opacities $4\pi\eta/s \gtrsim 20$, kinetic theory agrees with results from a linearization in opacity. Here, the system is too dilute for hydrodynamics to be applicable, which was confirmed quantitatively in Section 6.5.1: the time evolution of transverse energy, radial flow and shear stress is in significant disagreement in hydrodynamic simulations compared to kinetic theory. For large opacities $4\pi\eta/s \sim 0.1$, in the limit of high interaction rates, kinetic theory is expected to converge to hydrodynamics. Our results confirm that the two descriptions are in agreement after pre-equilibrium. Going down to intermediate opacities, we found that for suitable setups of hydrodynamics, results for final state transverse energy, elliptic flow and radial flow are in good agreement with kinetic theory up to shear viscosities $4\pi\eta/s \lesssim 3$ for the examined profile, which translates to opacity values $\hat{\gamma} \gtrsim 4$.

However, hydrodynamics is not suitable for describing out-of-equilibrium behaviour in the early pre-equilibrium stage and the late time period where the microscopic description of kinetic theory approaches a free-streaming behaviour. In both of these regimes, hydrodynamic results are in quantitative disagreement with kinetic theory, which can be seen at the level of final state observables, as discussed in Section 4.1.1. Omitting the pre-equilibrium period or naively employing hydrodynamics to describe it will yield inaccurate results. On the other hand, at late times where interactions die out, these observables no longer build up and approach constant values, such that hydrodynamic descriptions yield similar results to kinetic theory. However, the late time free-streaming stage does have an effect on radial flow, which is underestimated in hydrodynamics.

We examined two different modified setups of hydrodynamic simulations that can alleviate problems with the pre-equilibrium evolution. The first setup follows the idea of an early initialization of hydrodynamics with a scaled initial condition relative to kinetic theory to counteract the differences in the pre-equilibrium evolution. These differences are predicted locally based on insights from Bjorken flow, which is accurate in systems with a timescale separation of equilibration and the onset of Bjorken flow. By construction, this setup yields accurate results at large opacities $4\pi\eta/s \lesssim 3$, but fails at smaller opacities, where equilibration takes longer and is interrupted by transverse expansion. The results obtained in this setup are presented in Sections 6.4.2 and 6.5.1.

The second setup is a hybrid simulation switching from kinetic theory based descriptions at early times to hydrodynamics for later times. In these schemes, as described in Section 6.4.3, we saw an immediate change of the time evolution behaviour at the moment that we switch the dynamical descriptions. Thus, the accuracy of hybrid simulations depends on the extent to which the kinetic theory and hydrodynamic descriptions of the system's time evolution have come into agreement by the time we switch. This approach to agreement between the two descriptions is what we call hydrodynamization. We found that this criterion can in practice be quantified via the inverse Reynolds number. Fig. 4.1 shows that the system is partly hydrodynamized when $\mathrm{Re}^{-1} = 0.8$, significantly hydrodynamized when $\mathrm{Re}^{-1} = 0.6$ and has reached almost perfect agreement of the two descriptions at $\mathrm{Re}^{-1} = 0.4$. The accuracy of hybrid simulations when switching at a fixed value of $\langle \mathrm{Re}^{-1} \rangle_\epsilon$ can be estimated beforehand and is almost independent of the opacity. As detailed in Section 6.5.2, results from simulations with late switching times are accurate at high opacities $4\pi\eta/s \lesssim 1$ and can slightly improve on our first setup at intermediate opacities $4\pi\eta/s \sim 3$. At small opacities $4\pi\eta/s \gtrsim 20$, $\langle \mathrm{Re}^{-1} \rangle_\epsilon$ does not drop below 0.8, meaning the system does not equilibrate enough for hydrodynamics to become applicable at any point during the

system's evolution.

For the early time kinetic theory description in hybrid models, we used both full kinetic theory and the compact KøMPøST code. The latter uses a linearization scheme in perturbations around local homogeneity to propagate the energy-momentum tensor according to the Boltzmann equation under the relaxation time approximation (the original version [141, 145] is based on the QCD effective kinetic theory [142]). We first tested the performance of KøMPøST as detailed in Section 6.2.1 and found that it can accurately reproduce full kinetic theory results for transverse energy, radial flow and isotropic shear stress, but due to the linearization it significantly underestimates elliptic flow. It is by construction limited to times on the order of $0.5R$. In hybrid simulations with switching times in this regime, transverse energy and radial flow results reach similar accuracy as when employing full kinetic theory. However, the underestimation of elliptic flow causes discrepancies when the switching time is non-negligible compared to the timescale of transverse expansion.

Chapter 7

Conclusions

We will now conclude with a general summary of the main results presented in this work and outline possible future research endeavors that might build on it. For a more detailed discussion of the results of Chapters 5 and 6, we refer to their respective "Discussion"-Sections.

The main point of this work was to study the cooling due to longitudinal expansion and the dynamics of transverse flow in hadronic collisions, i.e. the buildup of azimuthal anisotropies in the momentum distribution of produced particles, based on kinetic theory descriptions and to probe where conventional simulations based on hydrodynamics might have shortcomings due to the fact that they can not describe non-equilibrium behaviour.

We started in Chapter 4 with a detailed discussion of the mathematical description of the Bjorken flow attractor. When describing the collision system as conformal, boost-invariant and homogeneous in the transverse plane in a large variety of dynamical models, the time evolution of different initial conditions quickly collapses onto a universal attractor curve, which has a different early time behaviour in different models. We motivated its use for a local description of the early time dynamics in systems with transverse expansion that can be applied to each point in transverse space. This collection of local Bjorken flows then allows to approximate the dynamics before transverse expansion at times $\tau/R \lesssim 0.1$. This allows to quantify in a straightforward way how different the early time evolution of the energy density is in hydrodynamics when compared to kinetic theory. The insights gained from this scaling scheme were used in the following two chapters for early time comparisons but also to motivate a modified initial condition for hydrodynamics. For future research of attractor behaviour in simulations of heavy ion collisions, it would be interesting to study whether a variation of this type of behaviour exists in systems with transverse expansion also more globally, beyond an approximation to Bjorken flow dynamics.

In Chapter 5 we studied transverse flow in conformal RTA kinetic theory. We corroborated the result that the opacity $\hat{\gamma}$ is the single model parameter that quantifies the time evolution in this model and examined cooling in terms of the decrease of transverse energy $\mathrm{d}E_\perp/\mathrm{d}\eta$ as well as linear and non-linear anisotropic flow responses as quantified by the flow harmonics v_n to spatial anisotropies in the initial state on the full parametric range in opacity $\hat{\gamma}$ and eccentricities ϵ_n on the basis of a simplified analytical initial condition. We found that numerical results for cooling and flow at small opacities are in good agreement with semi-analytical results from a linearization in opacity, which descibes the limiting case of very dilute systems where only few particles undergo scatterings. For large opacities, we detailed how insights from the Bjorken flow attractor can be used to describe the early time cooling behaviour in simulations with transverse dynamics. Our numerical results for flow responses show saturation behaviour at large opacities, indicating convergence to a large-opacity limit.

As hydrodynamics is defined as an effective description of the dynamics close to equilibrium and equilibration proceeds faster at larger opacities, kinetic theory is expected to converge to hydrodynamics in the large opacity limit. However, when we tested to what extend results for final state elliptic flow within the two descriptions agree with each other, we found discrepancies even at very large opacities. We were able to attribute them to a decrease of eccentricities in pre-equilibrium due to inhomogeneous cooling, which was confirmed also in the Bjorken flow attractor scaling scheme.

While our current study provides a detailed assessment of the development of transverse flow from very small to very large opacities, some of the shortcomings should be addressed prior to inferring phenomenological conclusions for proton-proton, proton-nucleus and nucleus-nucleus collisions. Evidently, it would be important to perform event-by-event studies with a more realistic transverse collision geometry, which would allow to study also the system size dependence of probability distributions and correlations of observables. This would require additional algorithmic improvements and significantly larger computation time. To reduce the computational cost, it might be worthwhile to explore the possibility of a simplified event-by-event simulation framework based on opacity expansion, which would allow to perform these types of statistical studies for the case of small systems. The end goal would be to push simulation tools for small systems to a state where they could be used for Bayesian analyses. Beyond such straightforward extensions, it would also be interesting to consider more realistic collision kernels [81] and investigate the effects of a non-conformal equation of state, which however will require additional theoretical developments.

In Chapter 6 we performed a more thorough investigation of the range of applicability of hydrodynamics by comparing to conformal RTA kinetic theory on the basis of several observables, specifically elliptic flow ϵ_p, transverse energy $\mathrm{d}E_{\mathrm{tr}}/d\eta$, transverse flow velocity $\langle u_\perp \rangle_\epsilon$ and shear stress as measured by the inverse Reynolds number $\left\langle \mathrm{Re}^{-1} \right\rangle_\epsilon$, which quantifies the relative size of non-equilibrium effects in the system. This time, the study was based on an average initial energy density profile of Pb-Pb collisions at $\sqrt{s_{NN}} = 5.02\,\mathrm{TeV}$ - i.e. at LHC energies - in the 30-40% centrality class. We were able to confirm more generally that pre-equilibrium dynamics cause problems in hydrodynamics. Not including it in the simulation has a significant effects even on final state observables. But hydrodynamic descriptions of pre-equilibrium are inaccurate and lead to similar effects.

Based on insights from the Bjorken flow attractor, we propose a local scaling scheme of the initial condition of hydrodynamics according to the differences in pre-equilibrium behaviour of the two theories. We find that within this scheme, agreement of the theories can be restored for large opacities. Specifically, the scheme succeeds in cases where equilibration proceeds to a sufficient degree in order to bring kinetic theory and hydrodynamics into agreement before the onset of transverse expansion. In other cases, on top of problems with applying hydrodynamics to a non-equilibrated system, remnants of the scaling scheme persist throughout the evolution. The results, together with comparisons to Bjorken flow attractor curves, also allow to identify the inverse Reynolds number as a criterion for equilibration. This results in an evolution time and opacity dependent regime of applicability for hydrodynamics.

We also studied hybrid simulation schemes switching from kinetic theory based descriptions to hydrodynamic ones. By studying the dependence of the results on the switching time, we confirm that it should be chosen on the basis of the drop in inverse Reynolds number. Switching too early results in discrepancies due to the inaccurate description of pre-equilibrium in hydrodynamics. We conclude that in systems showing no significant decrease of the inverse Reynolds number, hydrodynamics never

becomes applicable. Hybrid simulations can improve on results from our proposed scaling scheme for hydrodynamics at intermediate opacities.

For the early-time kinetic theory results, we used an RTA kinetic theory code as well as the linearized response framework KøMPøST in RTA mode. We confirmed that KøMPøST can produce results at a similar level of accuracy within its realm of applicability, i.e. for evolution times $\tau \lesssim 0.5R$, except for anisotropic flow, which does not build up in KøMPøST. This conclusion is corroborated by comparisons of the time evolution and profiles of the energy-momentum tensor to RTA kinetic theory, but also by comparing final state results of hybrid schemes.

This work provides the baseline for analyses of hadronic collisions in frameworks based on the microscopic dynamics of kinetic theory. It is part of a series of recent efforts [1, 15, 80, 81, 86] to push the practical applicability of these dynamics in theoretical simulations. One important goal that has yet to be reached is to improve the codes that implement them in order to be able to also run event-by-event simulations. At the moment, the tool that is closest to fulfilling this goal is KøMPøST, which we confirmed to function properly for its intended use, but it is confined to the pre-equilibrium phase of heavy-ion collisions.

Broadly speaking, our results confirm that in principle hydrodynamics is the proper tool for describing mid-central collisions, if and only if the pre-equilibrium is described correctly. Issues with this phase in hydrodynamic descriptions can be alleviated by changing the interpretation of the initial state in the way discussed in Section 6.3.2. As alluded to in Section 4.1 as well as in previous works [31], appropriate changes to the evolution equations might achieve similar improvements. This also includes resummed hydrodynamic approaches such as anisotropic hydroynamics (aHydro) [190–194], which can accurately describe the inhomogeneous longitudinal cooling and it will be interesting to further investigate this in the future.

Modern Bayesian Inference frameworks typically model pre-equilibrium dynamics by free-streaming [2, 4]. As we have seen, the dynamics in this phase can have a noticeable effect on final state observables. We thus advocate to modify these frameworks to employ a more accurate description of pre-equilibrium. This would increase the accuracy of extracted properties of the QGP, but also make it feasible to extract information about model parameters related to this stage - e.g. the equilibration time - from experimental data.

Appendix A

Free-streaming the anisotropies

In linear order of the opacity expansion, the dynamics of the anisotropies is naturally dominated by the free-streaming limit, as will also be more evident from the calculations in the following sections. It is therefore pivotal to examine how the anisotropic factors of $x_\perp^n \cos(n\phi_{\mathbf{x}_\perp\mathbf{n}_\perp})$ that are part of the initial condition in Eqs. (5.6,5.7) behave under free-streaming according to the propagation as given in Eq. (5.36). The notation $\phi_{\mathbf{x}_\perp\mathbf{n}_\perp} = \phi_x - \Psi_n$ was introduced in Eq. (5.8). For this purpose, it is convenient to rewrite the $\cos(n\phi)$ and $\sin(n\phi)$ in terms of the Chebyshev polynomials of the first and second kind [154, Ch. 18]:

$$\cos(n\phi) = T_n(\cos(\phi)), \qquad \sin(n\phi) = \sin(\phi)\, U_{n-1}(\cos(\phi)). \tag{A.1}$$

The explicit form of the Chebyshev polynomials,

$$\begin{aligned} T_n(z) =& \frac{n}{2}\sum_{k=0}^{\lfloor \frac{n}{2} \rfloor}(-1)^k \frac{(n-k-1)!}{(n-2k)!k!}(2z)^{n-2k}, \\ U_n(z) =& \sum_{k=0}^{\lfloor \frac{n}{2} \rfloor}(-1)^k \binom{n-k}{k}(2z)^{n-2k}, \end{aligned} \tag{A.2}$$

can be used to express $\cos(n\phi)$ and $\sin(n\phi)$ in terms of powers of $\cos\phi$. Under free-streaming (5.32), the factor $x_\perp^n \cos(n\phi^{(n)}_{\mathbf{x}_\perp\mathbf{n}_\perp})$ evolves according to

$$|\mathbf{x}_\perp - \mathbf{v}_\perp\Delta\tau|^n \cos(n\phi_{\mathbf{x}_\perp-\mathbf{v}_\perp\Delta\tau,\mathbf{n}_\perp}) = |\mathbf{x}_\perp - \mathbf{v}_\perp\Delta\tau|^n T_n\left(\frac{(\mathbf{x}_\perp - \mathbf{v}_\perp\Delta\tau)\cdot\mathbf{n}_\perp}{|\mathbf{x}_\perp - \mathbf{v}_\perp\Delta\tau|}\right), \tag{A.3}$$

where Eq. (A.1) was employed on the right hand side. In the above, the time lapse $t(\tau, \tau_0, y-\eta)$ was replaced by $\Delta\tau = \tau - \tau_0$ by virtue of Eq. (5.35).

The Chebyshev polynomials obey the identity

$$z^n = |z|^n T_n\left(\frac{a}{|z|}\right) + ib|z|^{n-1}U_{n-1}\left(\frac{a}{|z|}\right), \tag{A.4}$$

where a and b are real numbers and $z = a + ib$ is a complex number. Denoting $\phi_{\mathbf{p}_\perp\mathbf{n}_\perp} = \phi_p - \Psi_n$, we set

$$\begin{aligned} a &\to x_\perp \cos(\phi_{\mathbf{x}_\perp\mathbf{n}_\perp}) - \Delta\tau \cos(\phi_{\mathbf{p}_\perp\mathbf{n}_\perp}), \\ b &\to x_\perp \sin(\phi_{\mathbf{x}_\perp\mathbf{n}_\perp}) - \Delta\tau \sin(\phi_{\mathbf{p}_\perp\mathbf{n}_\perp}), \\ z &\to x_\perp e^{i\phi_{\mathbf{x}_\perp\mathbf{n}_\perp}} - \Delta\tau\, e^{i\phi_{\mathbf{p}_\perp\mathbf{n}_\perp}}, \end{aligned} \tag{A.5}$$

such that $\mathrm{Re}(z^n)$ is just the expression on the left hand side of Eq. (A.3), an expression with a very simple dependence on $\phi_{\mathbf{x}_\perp \mathbf{p}_\perp} = \phi_x - \phi_p$ can be derived:

$$\begin{aligned}
&|\mathbf{x}_\perp - \mathbf{v}_\perp \Delta\tau|^n \cos(n\phi_{\mathbf{x}_\perp - \mathbf{v}_\perp \Delta\tau, \mathbf{n}_\perp}) \\
&\quad = \sum_{j=0}^{n} \binom{n}{j} x_T^{n-j} (-\Delta\tau)^j [\cos(n\phi_{\mathbf{x}_\perp \mathbf{n}_\perp}) \cos(j\phi_{\mathbf{x}_\perp \mathbf{p}_\perp}) - \sin(n\phi_{\mathbf{x}_\perp \mathbf{n}_\perp}) \sin(j\phi_{\mathbf{x}_\perp \mathbf{p}_\perp})].
\end{aligned} \tag{A.6}$$

Appendix B

Solving integrals in Landau matching

In order to be able to perform the necessary integrals of the kernel according to Eq. 5.64, we will need specific expressions for ϵ and u^μ, meaning that we need to compute the exact form of $T^{(0)\mu\nu}$ and $\delta T^{(0)\mu\nu}$ by solving the integrals given in Section 5.2.4.

As we will discuss below, we can break the integration down to solving integrals of an exponential of $\cos(\phi)$ multiplied with powers of trigonometric functions. These can be expressed in terms of modified Bessel functions of the first kind.

$$\int \mathrm{d}\phi\, e^{a\cos(\phi)}\, \cos(n\phi) = 2\pi I_n(a) \quad , \tag{B.1}$$

$$\int \mathrm{d}\phi\, e^{a\cos(\phi)}\, \cos(n\phi)\, \cos^m(\phi) = 2\pi I_n^{(m)}(a) \quad , \tag{B.2}$$

$$\int \mathrm{d}\phi\, e^{a\cos(\phi)}\, \sin(n\phi) = 0 \quad , \tag{B.3}$$

$$\int \mathrm{d}\phi\, e^{a\cos(\phi)}\, \sin(n\phi)\, \sin(\phi) = 2\pi I_n'(a) - 2\pi I_{n+1}(a) \quad , \tag{B.4}$$

$$\int \mathrm{d}\phi\, e^{a\cos(\phi)}\, \sin(n\phi)\, \cos(\phi)\, \sin(\phi) = 2\pi I_n''(a) - 2\pi I_{n+1}'(a) \quad . \tag{B.5}$$

It is straightforward to see that $T^{(0)\mu\nu}$ is indeed of this form as

$$T^{(0)\mu\nu} = \frac{\tau_0}{\tau} \int \frac{\mathrm{d}\phi_p}{2\pi}\, v_\perp^\mu v_\perp^\nu\, \bar{\epsilon}(\tau_0, \mathbf{x}_\perp - \Delta\tau \mathbf{v}_\perp), \tag{B.6}$$

where $v_\perp^\mu = (1, \cos\phi_p, \sin\phi_p, 0)$ has no longitudinal component under free-streaming due to the $\delta(y-\eta)$ function in Eq. (5.36). The integral with respect to $p_\perp$ was performed according to Eq. (5.4). At zeroth order, we took into account only the isotropic part of the initial energy density profile $\bar{\epsilon}$, introduced in Eq. (5.6), which is evaluated at shifted coordinates according to

$$\bar{\epsilon}(\tau_0, \mathbf{x}_\perp - \Delta\tau \mathbf{v}_\perp) = \frac{1}{\pi R^2 \tau_0} \frac{\mathrm{d}E_\perp^{(0)}}{\mathrm{d}\eta} \exp\left(-\frac{x_\perp^2 + \Delta\tau^2 - 2x_\perp \Delta\tau\, \cos(\phi_x - \phi_p)}{R^2} \right). \tag{B.7}$$

Using the integral formulae given in Eq. (B.5), the components of the stress-energy tensor introduced in Eq. (5.41) can be computed to be

$$T^{(0)\tau\tau} = \frac{1}{\tau}\frac{1}{\pi R^2}\frac{\mathrm{d}E_\perp^{(0)}}{\mathrm{d}\eta}\exp\left(-\frac{x_\perp^2+\Delta\tau^2}{R^2}\right) I_0(2b) \quad , \tag{B.8}$$

$$T^{(0)\tau\perp} = \frac{1}{\tau}\frac{1}{\pi R^2}\frac{\mathrm{d}E_\perp^{(0)}}{\mathrm{d}\eta}\exp\left(-\frac{x_\perp^2+\Delta\tau^2}{R^2}\right) I_1(2b) \quad , \tag{B.9}$$

$$T^{(0)\perp\perp} = \frac{1}{\tau}\frac{1}{\pi R^2}\frac{\mathrm{d}E_\perp^{(0)}}{\mathrm{d}\eta}\exp\left(-\frac{x_\perp^2+\Delta\tau^2}{R^2}\right) I_2(2b) \quad , \tag{B.10}$$

$$T^{(0)\mathbb{1}} = \frac{1}{\tau}\frac{1}{\pi R^2}\frac{\mathrm{d}E_\perp^{(0)}}{\mathrm{d}\eta}\exp\left(-\frac{x_\perp^2+\Delta\tau^2}{R^2}\right) [I_0(2b) - I_0''(2b)] \quad , \tag{B.11}$$

where we defined $b = \frac{x_\perp \Delta\tau}{R^2}$.

The anisotropic part $\delta T^{(0)\mu\nu}$,

$$\delta T^{(0)\mu\nu} = \frac{\tau_0}{\tau}\int \frac{\mathrm{d}\phi_{\mathbf{x}_\perp\mathbf{p}_\perp}}{2\pi}\, v_\perp^\mu v_\perp^\nu\, \delta\epsilon(\tau_0, \mathbf{x}_\perp - \Delta\tau\mathbf{v}_\perp), \tag{B.12}$$

exhibits a dependence on the angle $\phi_{\mathbf{x}_\perp\mathbf{n}_\perp}$ due to the form (5.7) of the anisotropic part of the initial energy profile, which is evaluated at shifted coordinates according to:

$$\begin{aligned}&\delta\epsilon(\tau_0, \mathbf{x}_\perp - \Delta\tau\mathbf{v}_\perp)\\ &\quad= \frac{1}{\pi R^2\tau_0}\frac{\mathrm{d}E_\perp^{(0)}}{\mathrm{d}\eta}\exp\left[-\bar{\alpha}\frac{|\mathbf{x}_\perp - \Delta\tau\mathbf{v}_\perp|^2}{R^2}\right]\delta_n\left(\frac{|\mathbf{x}_\perp - \Delta\tau\mathbf{v}_\perp|}{R}\right)^n \cos(n\phi_{\mathbf{x}_\perp\mathbf{n}_\perp}) \quad .\end{aligned} \tag{B.13}$$

Solving the integrals in Eq. (B.12) is a bit more difficult, requiring the computation of an angular integral of the free-streamed anisotropies. We have already seen in App. A how we can rewrite them into a term with a straightforward $\phi_{\mathbf{x}_\perp\mathbf{p}_\perp}$-dependence. An additional $\phi_{\mathbf{x}_\perp\mathbf{p}_\perp}$-dependence comes from the velocity vectors v^μ. In the computation of $\delta\epsilon$, δu_t and δu_s they will be contracted with the eigenvectors u^μ, t^μ and s^μ in the following ways:

$$\begin{aligned}u_\mu v^\mu v^\nu u_\nu &= \gamma^2[1 - 2\beta\cos(\phi_{\mathbf{x}_\perp\mathbf{p}_\perp}) + \beta^2\cos^2(\phi_{\mathbf{x}_\perp\mathbf{p}_\perp})] \quad ,\\ u_\mu v^\mu v^\nu t_\nu &= \gamma^2[\beta - \cos(\phi_{\mathbf{x}_\perp\mathbf{p}_\perp}) - \beta^2\cos(\phi_{\mathbf{x}_\perp\mathbf{p}_\perp}) + \beta\cos^2(\phi_{\mathbf{x}_\perp\mathbf{p}_\perp})] \quad ,\\ u_\mu v^\mu v^\nu s_\nu &= -\gamma[\sin(\phi_{\mathbf{x}_\perp\mathbf{p}_\perp}) - \beta\cos(\phi_{\mathbf{x}_\perp\mathbf{p}_\perp})\sin(\phi_{\mathbf{x}_\perp\mathbf{p}_\perp})] \quad .\end{aligned} \tag{B.14}$$

Taking into account all of the ingredients presented above, we indeed find that we can decompose all terms into integrals of the form in Eq. (B.5). We can plug the results into Eqs. (5.56-5.58) to obtain explicit expressions for the anisotropic corrections $\delta\epsilon$,

δu_t and δu_s:

$$\begin{aligned}\delta\epsilon = u_\mu \delta T^{(0)\mu\nu} u_\nu &= \delta_n \frac{1}{\tau}\frac{\mathrm{d}E_\perp^{(0)}}{\mathrm{d}\eta}\frac{1}{2\pi R^{n+2}} e^{-\bar{\alpha}\frac{x_\perp^2+\Delta\tau^2}{R^2}} \int \frac{d\phi_{\mathbf{x}_\perp\mathbf{p}_\perp}}{2\pi} e^{2\bar{\alpha}b\cos(\phi_{\mathbf{x}_\perp\mathbf{p}_\perp})}\gamma^2 \\ &\times [1 - 2\beta\cos(\phi_{\mathbf{x}_\perp\mathbf{p}_\perp}) + \beta^2\cos^2(\phi_{\mathbf{x}_\perp\mathbf{p}_\perp})] \\ &\times \sum_{j=0}^{n}\binom{n}{j} x_\perp^{n-j}(-\Delta\tau)^j \cos(n\phi_{\mathbf{x}_\perp\mathbf{n}_\perp} + j\phi_{\mathbf{x}_\perp\mathbf{p}_\perp}) \qquad \text{(B.15)} \\ &= \cos(n\phi_{\mathbf{x}_\perp\mathbf{n}_\perp})\delta_n \frac{1}{\tau}\frac{\mathrm{d}E_\perp^{(0)}}{\mathrm{d}\eta}\frac{1}{\pi R^{n+2}} e^{-\bar{\alpha}\frac{x_\perp^2+\Delta\tau^2}{R^2}}\gamma^2 \\ &\times \sum_{j=0}^{n}\binom{n}{j} x_\perp^{n-j}(-\Delta\tau)^j [I_j(2\bar{\alpha}b) - 2\beta I_j'(2\bar{\alpha}b) + \beta^2 I_j''(2\bar{\alpha}b)] \qquad \text{(B.16)}\end{aligned}$$

$$\begin{aligned}\delta u_t = \frac{u_\mu \delta T^{(0)\mu\nu} t_\nu}{p_t - \epsilon} &= \delta_n \frac{1}{\tau}\frac{\mathrm{d}E_\perp^{(0)}}{\mathrm{d}\eta}\frac{1}{\pi R^{n+2}} e^{-\bar{\alpha}\frac{x_\perp^2+\Delta\tau^2}{R^2}} \int \frac{d\phi_{\mathbf{x}_\perp\mathbf{p}_\perp}}{2\pi} e^{2\bar{\alpha}b\cos(\phi_{\mathbf{x}_\perp\mathbf{p}_\perp})}\gamma^2 \\ &\times [\beta - \cos(\phi_{\mathbf{x}_\perp\mathbf{p}_\perp}) - \beta^2\cos(\phi_{\mathbf{x}_\perp\mathbf{p}_\perp}) + \beta\cos^2(\phi_{\mathbf{x}_\perp\mathbf{p}_\perp})] \\ &\times \sum_{j=0}^{n}\binom{n}{j} x_\perp^{n-j}(-\Delta\tau)^j \cos(n\phi_{\mathbf{x}_\perp\mathbf{n}_\perp} + j\phi_{\mathbf{x}_\perp\mathbf{p}_\perp}) \qquad \text{(B.17)} \\ &= \cos(n\phi_{\mathbf{x}_\perp\mathbf{n}_\perp})\delta_n \frac{1}{p_t - \epsilon}\frac{1}{\tau}\frac{\mathrm{d}E_\perp^{(0)}}{\mathrm{d}\eta}\frac{1}{\pi R^{n+2}} e^{-\bar{\alpha}\frac{x_\perp^2+\Delta\tau^2}{R^2}}\gamma^2 \\ &\times \sum_{j=0}^{n}\binom{n}{j} x_\perp^{n-j}(-\Delta\tau)^j [\beta I_j(2\bar{\alpha}b) - (1+\beta^2) I_j'(2\bar{\alpha}b) + \beta I_j''(2\bar{\alpha}b)]] \qquad \text{(B.18)}\end{aligned}$$

$$\begin{aligned}\delta u_s = \frac{u_\mu \delta T^{(0)\mu\nu} s_\nu}{p_s - \epsilon} &= \delta_n \frac{1}{\tau}\frac{\mathrm{d}E_\perp^{(0)}}{\mathrm{d}\eta}\frac{1}{\pi R^{n+2}} e^{-\bar{\alpha}\frac{x_\perp^2+\Delta\tau^2}{R^2}} \int \frac{d\phi_{\mathbf{x}_\perp\mathbf{p}_\perp}}{2\pi} e^{2\bar{\alpha}b\cos(\phi_{\mathbf{x}_\perp\mathbf{p}_\perp})}\gamma \\ &\times [\sin(\phi_{\mathbf{x}_\perp\mathbf{p}_\perp}) - \beta\cos(\phi_{\mathbf{x}_\perp\mathbf{p}_\perp})\sin\phi_{\mathbf{x}_\perp\mathbf{p}_\perp}] \\ &\times \sum_{j=0}^{n}\binom{n}{j} x_\perp^{n-j}(-\Delta\tau)^j \cos(n\phi_{\mathbf{x}_\perp\mathbf{n}_\perp} + j\phi_{\mathbf{x}_\perp\mathbf{p}_\perp}) \qquad \text{(B.19)} \\ &= -\sin(n\phi_{\mathbf{x}_\perp\mathbf{n}_\perp})\delta_n \frac{1}{p_s - \epsilon}\frac{1}{\tau}\frac{\mathrm{d}E_\perp^{(0)}}{\mathrm{d}\eta}\frac{1}{\pi R^{n+2}} e^{-\bar{\alpha}\frac{x_\perp^2+\Delta\tau^2}{R^2}}\gamma \\ &\times \sum_{j=0}^{n}\binom{n}{j} x_\perp^{n-j}(-\Delta\tau)^j [I_j'(2\bar{\alpha}b) - I_{j+1}(2\bar{\alpha}b) - \beta I_j''(2\bar{\alpha}b) + \beta I_{j+1}'(2\bar{\alpha}b)] \qquad \text{(B.20)}\end{aligned}$$

Appendix C

Details of linearized calculation

As stated in Section 5.2.5, the linear order corrections to the observables V_{mn} can be computed as a six-dimensional integral of the kernel:

$$V_{mn}^{(1)}(\tau) = \int \mathrm{d}^2 p_\perp \; e^{in\phi_p} p_\perp^m \int_{\tau_0}^{\tau} \mathrm{d}\tau' \int \mathrm{d}^2 x_\perp \int \mathrm{d}\eta \; \tau' \frac{\nu_{\mathrm{eff}}}{(2\pi)^3} C[f^{(0)}] \left(\tau', \mathbf{x}_\perp, \mathbf{p}_\perp, y-\eta\right) \quad , \tag{C.1}$$

$$C[f^{(0)}] = -p^\mu u_\mu \left(5\frac{\eta}{s}\right)^{-1} T \left(f^{(0)} - f_{eq}\right) \quad . \tag{C.2}$$

We already outlined in that section how this problem can be split into different terms. The moments V_{m0} depend only on the isotropic part, while the moments V_{mn} with $n \neq 0$ vanish in the isotropic case and have to be computed to linear order in the anisotropic perturbations. Additionally, the linear order corrections to the moments split into buildup of equilibrium $V_{mn}^{(1,eq)}$ and decay of the initial condition $V_{mn}^{(1,0)}$ as computed from the corresponding parts of the kernel:

$$C_{eq}[f^{(0)}] = p^\mu u_\mu \left(5\frac{\eta}{s}\right)^{-1} T \; f_{eq} \quad , \tag{C.3}$$

$$C_0[f^{(0)}] = -p^\mu u_\mu \left(5\frac{\eta}{s}\right)^{-1} T \; f^{(0)} \quad . \tag{C.4}$$

This section discusses how four of the integrals can be computed analytically for each of these terms. Many of the angular integrations will again take the forms of the integral formulae given in the beginning of Appendix B. We will start with the moments V_{m0} as they are independent of the anisotropic perturbation.

Exact expressions for the local theormodynamic quantities T, u^μ can be computed from the components of $T^{\mu\nu}$ that are discussed in Appendix B according to the formulae derived in Section 5.2.4. In terms of $b = \frac{x_\perp \Delta\tau}{R^2}$, they read

$$T = R^{-1} \left(\frac{1}{\pi} \frac{30}{\nu_{\mathrm{eff}} \pi^2} \frac{\mathrm{d}E_\perp^{(0)}}{\mathrm{d}\eta} R\right)^{1/4} \left(\frac{R}{\tau}\right)^{1/4} \exp\left(-\frac{x_\perp^2 + \Delta\tau^2}{4R^2}\right) \left[I_0(b) - \beta I_0'(b)\right]^{1/4} \quad , \tag{C.5}$$

$$u^\mu = \gamma(1, \beta\hat{\mathbf{x}}_\perp, 0) \; , \quad \gamma = (1-\beta^2)^{-1/2} \; , \quad \beta = \frac{I_0(b)}{I_1(b)} - \frac{1}{2b} - \sqrt{\left[\frac{I_0(b)}{I_1(b)} - \frac{1}{2b}\right]^2 - 1} \; . \tag{C.6}$$

Looking at the expression for T, it is immediately apparent that its dimensionless constant prefactor together with $\left(5\frac{\eta}{s}\right)^{-1}$ constitutes a factor of $\hat{\gamma}$ in $C[f^{(0)}]$, as we

have predicted in Section 5.1.2. We can immediately also compute

$$p^\mu u_\mu = \gamma p_\perp \left[\cosh(y-\eta) - \beta\, \cos(\phi_{\mathbf{x}_\perp \mathbf{p}_\perp})\right] \quad . \tag{C.7}$$

Reminding also of the form of $f^{(0)}$

$$f^{(0)}(\tau, \mathbf{x}_\perp, \mathbf{p}_\perp, y-\eta) = \frac{(2\pi)^3}{\nu_{\text{eff}}} \frac{\delta(y-\eta)}{\tau p_\perp} F\left(\frac{Q_s(\mathbf{x}_\perp - \mathbf{v}_\perp \Delta\tau)}{p_\perp}\right) \quad , \tag{C.8}$$

where Q_s is fixed by the isotropic energy density according to (5.4,5.6,5.26) to be of the form

$$Q_s(\mathbf{x}_\perp) = Q_{s,0} \exp\left(-\frac{x_\perp^2}{3R^2}\right) \quad , \tag{C.9}$$

we can compute $V_{mn}^{(1,0)}$ by plugging the above expressions into the integral formula (C.1) for the part of the kernel given in (C.4). Due to the fact that in both cases we integrate $f^{(0)}$, the integral over $p_\perp$ is analogous to the computation of the zeroth-order moments $V_{m0}^{(0)}$, where

$$V_{m0}^{(0)} = \int \mathrm{d}^2 p_\perp p_\perp^m \frac{\mathrm{d}N^{(0)}}{\mathrm{d}^2 p_\perp \mathrm{d}y} \tag{C.10}$$

$$= 2\pi \int \mathrm{d}^2 x_\perp \int \mathrm{d}\eta \int_0^\infty \mathrm{d}p_\perp p_\perp^{m+1} \delta(y-\eta) F\left(\frac{Q_s(\mathbf{x}_\perp - \mathbf{v}_\perp \Delta\tau)}{p_\perp}\right) \tag{C.11}$$

$$= 2\pi \int \mathrm{d}^2 x_\perp Q_s^{m+2}(\mathbf{x}_\perp) \int_0^\infty \mathrm{d}k\, k^{m+1} F\left(\frac{1}{k}\right) \tag{C.12}$$

$$= 4\pi^2 \frac{3R^2}{m+2} Q_{s,0}^{m+2} \int_0^\infty \mathrm{d}k\, k^{m+1} F\left(\frac{1}{k}\right) \quad . \tag{C.13}$$

We can therefore express our result for $V_{m0}^{(1,0)}$ in terms of these zeroth-order moments and find

$$V_{m0}^{(1,0)}(\tau) = -V_{m0}^{(0)} \left(5\frac{\eta}{s}\right)^{-1} \frac{m+2}{3R^2} \int_{\tau_0}^\tau \mathrm{d}\tau' \int_0^\infty \mathrm{d}x_\perp\; x_\perp T\, \gamma \exp\left[-\frac{(m+2)(\Delta\tau'^2 + x_\perp^2)}{3R^2}\right]$$
$$\times \int_0^{2\pi} \frac{\mathrm{d}\phi_{\mathbf{x}_\perp \mathbf{p}_\perp}}{2\pi} \left[1 - \beta \cos(\phi_{\mathbf{x}_\perp \mathbf{p}_\perp})\right] \exp\left(\frac{2(m+2) b\, \cos(\phi_{\mathbf{x}_\perp \mathbf{p}_\perp})}{3}\right) \tag{C.14}$$

$$= -V_{m0}^{(0)}\, \hat{\gamma}\, \mathcal{P}_m(\tilde{\tau}) \quad , \tag{C.15}$$

$$\mathcal{P}_m(\tilde{\tau}) = \frac{(m+2)}{3} \int_{\tilde{\tau}_0}^{\tilde{\tau}} \mathrm{d}\tilde{\tau}' \int_0^\infty \mathrm{d}\tilde{x}_\perp\; \tilde{x}_\perp \tilde{T}\, \gamma \exp\left[-\frac{(m+2)}{3}(\Delta\tilde{\tau}'^2 + \tilde{x}_\perp^2)\right]$$
$$\times \left[I_0\left(\frac{2m+4}{3} b\right) - \beta I_0'\left(\frac{2m+4}{3} b\right)\right] \quad . \tag{C.16}$$

where one has to keep in mind that in the integrand b, β, γ and T are to be understood as functions of τ' instead of τ. In the last step, the result was rewritten into the tilded coordinates introduced in Section 5.1.2 to make the parametric dependences more apparent.

For $V_{mn}^{(1,eq)}$ given by Eq. (C.1) with the partial kernel (C.3), computing the moments of f_{eq} via the $p_\perp$-integration yields

$$V_{m0}^{(1,eq)}(\tau) = \left(5\frac{\eta}{s}\right)^{-1} \frac{\nu_{\text{eff}}}{(2\pi)^2}\Gamma(m+3)\,\zeta(m+3)\int_{\tau_0}^{\tau}\mathrm{d}\tau'\int_0^\infty \mathrm{d}x_\perp\; x_\perp \tau' T^{m+4}$$
$$\times \int_0^{2\pi}\mathrm{d}\phi_{\mathbf{x}_\perp\mathbf{p}_\perp}\int \mathrm{d}\eta\,\left\{\gamma\left[\cosh(y-\eta)-\beta\cos(\phi_{\mathbf{x}_\perp\mathbf{p}_\perp})\right]\right\}^{-m-2} \tag{C.17}$$

$$= \left(5\frac{\eta}{s}\right)^{-1} \frac{\nu_{\text{eff}}}{2\pi^{1/2}}\,\Gamma(m+3)\,\zeta(m+3)\,\frac{\Gamma\left(\frac{m+2}{2}\right)}{\Gamma\left(\frac{m+3}{2}\right)}\int_{\tau_0}^{\tau}\mathrm{d}\tau'\int_0^\infty \mathrm{d}x_\perp\; x_\perp\tau'$$
$$\times T^{m+4}\gamma^{-m-2}\;{}_2F_1\left(\frac{m+2}{2},\frac{m+2}{2};1;\beta^2\right) \tag{C.18}$$

$$= \hat{\gamma}\nu_{\text{eff}}R^{-m}\left(\frac{1}{\pi}\nu_{\text{eff}}^{-1}\frac{\mathrm{d}E_\perp^{(0)}}{\mathrm{d}\eta}R\right)^{(m+3)/4}\quad \mathcal{Q}_m(\tilde{\tau})\quad , \tag{C.19}$$

$$\mathcal{Q}_m(\tilde{\tau}) = \left(\frac{\pi^2}{30}\right)^{-(m+3)/4}\frac{1}{2\pi^{1/2}}\,\Gamma(m+3)\,\zeta(m+3)\,\frac{\Gamma\left(\frac{m+2}{2}\right)}{\Gamma\left(\frac{m+3}{2}\right)}\int_{\tilde{\tau}_0}^{\tilde{\tau}}\mathrm{d}\tilde{\tau}'\int_0^\infty \mathrm{d}\tilde{x}_\perp\;\tilde{x}_\perp\tilde{\tau}'$$
$$\times \tilde{T}^{m+4}\gamma^{-m-2}\;{}_2F_1\left(\frac{m+2}{2},\frac{m+2}{2};1;\beta^2\right). \tag{C.20}$$

After absorbing one of the T-prefactors into $\hat{\gamma}$, the parametric dependence of this term given by (C.19). As the basic structure of the integrands is the same, moments with $n \neq 0$ will have the same parametric dependences except for the additional anisotropy parameter δ_n.

Now to compute the anisotropic corrections $\delta V_{mn}^{(1)}$ for $n \neq 0$, we first need to derive the change $\delta C[f^{(0)}]$ in the kernel

$$C[f^{(0)}] = -p^\mu u_\mu\left(5\frac{\eta}{s}\right)^{-1} T\left(f_{eq}-f^{(0)}\right) \tag{C.21}$$

due to the anisotropies, so we can plug it into (C.1). $C[f^{(0)}]$ depends on three quantities that receive anisotropic corrections: $f^{(0)}$, T and u^μ. Linearization in the corrections will yield three different contributions. Separating the terms proportional to $f^{(0)}$ from those proportional to f_{eq}, we can split the kernel into the following two parts:

$$\delta C_0[f^{(0)}] = -\left(5\frac{\eta}{s}\right)^{-1} p_\mu\left(u^\mu T\,\delta f^{(0)} + u^\mu\delta T f^{(0)} + \delta u^\mu T f^{(0)}\right) \tag{C.22}$$

$$\delta C_{eq}[f^{(0)}] = \left(5\frac{\eta}{s}\right)^{-1} p_\mu\left[\left(u^\mu\delta T + \delta u^\mu T\right) f_{eq}\left(\frac{p_\nu u^\nu}{T}\right)\right.$$
$$\left. + \left(-u^\mu\delta T + \delta u^\mu T\right)\frac{p_\rho u^\rho}{T} f'_{eq}\left(\frac{p_\nu u^\nu}{T}\right)\right] \tag{C.23}$$

We can compute the anisotropic contributions to thermodynamic quantities that show up in the kernel from the results for $\delta\epsilon$, δu_t and δu_s given in Eq.s (B.16,B.18,B.20). The change in temperature δT can be computed by linearizing the equation of state $T = \left(\frac{\pi^2}{30}\nu_{\text{eff}}\right)^{-1/4}\epsilon^{-1/4}$ in $\delta\epsilon$, and the contraction $\delta u_\mu p^\mu$ can be expressed in terms of

δu_t and δu_s.

$$\delta T = \frac{1}{4}\left(\frac{\pi^2}{30}\nu_{\text{eff}}\right)^{-1/4}\epsilon^{-3/4}\delta\epsilon = \frac{1}{4}\left(\frac{\pi^2}{30}\nu_{\text{eff}}\right)^{-1}T^{-3}\delta\epsilon\,, \tag{C.24}$$

$$\begin{aligned} p^\mu\delta u_\mu = p^\mu(\delta u_t t_\mu + \delta u_s s_\mu) &= \delta u_t p_\perp\gamma[\beta\cosh(y-\eta) - \cos(\phi_{\mathbf{x}_\perp\mathbf{p}_\perp})] \\ &\quad - \delta u_s p_\perp \sin(\phi_{\mathbf{x}_\perp\mathbf{p}_\perp})\,. \end{aligned} \tag{C.25}$$

The only anisotropic quantity that we still need to derive is the form of the perturbation $\delta f^{(0)}$ due to the energy density perturbation $\delta\epsilon$. Given that

$$f^{(0)}(\tau,\mathbf{x}_\perp,\mathbf{p}_\perp,y-\eta) = \frac{(2\pi)^3}{\nu_{\text{eff}}}\frac{\delta(y-\eta)}{\tau p_\perp}F\left(\frac{Q_s(\mathbf{x}_\perp-\Delta\tau)}{p_\perp}\right)\,, \tag{C.26}$$

the change in f is due to the change in Q_s which is directly related to ϵ. More specifically,

$$\delta f(\tau,\mathbf{x}_\perp,\mathbf{p}_\perp,y-\eta) = \frac{(2\pi)^3}{\nu_{\text{eff}}}\frac{\delta(y-\eta)}{\tau p_\perp}\frac{\delta Q_s(\mathbf{x}_\perp-\Delta\tau\mathbf{v}_\perp)}{p_\perp}F'\left(\frac{Q_s(\mathbf{x}_\perp-\Delta\tau\mathbf{v}_\perp)}{p_\perp}\right) \tag{C.27}$$

where

$$\delta Q_s(\mathbf{x}_\perp) = \frac{1}{3}Q_s(\mathbf{x}_\perp)\frac{\delta\epsilon(\tau_0,\mathbf{x}_\perp)}{\epsilon(\tau_0,x_\perp)} = \frac{1}{3}Q_s(\mathbf{x}_\perp)\,\delta_n\exp\left(-\alpha\frac{x_\perp^2}{R^2}\right)\left(\frac{x_\perp}{R}\right)^n\cos(n\phi_{\mathbf{x}_\perp\mathbf{n}_\perp})\,. \tag{C.28}$$

Evaluating δQ_s at $\mathbf{x}_\perp-\Delta\tau\mathbf{v}_\perp$ will thus yield as a factor the free-streamed version of $x_\perp^n\cos(n\phi_{\mathbf{x}_\perp\mathbf{n}_\perp})$ that was computed in appendix A.

We now want to compute the moments $V_{mn}^{(1,0)}$ for $n\neq 0$ by computing the integrals in Eq. (C.1) for the part of the kernel perturbation given in Eq. (C.22). As in the isotropic case, we can simplify the integral expression by identifying $V_{m0}^{(0)}$. This holds true also for the term containing $\delta f^{(0)}$ instead of $f^{(0)}$, since

$$\begin{aligned} &\int \mathrm{d}p_\perp p_\perp^m\,Q_s(\mathbf{x}_\perp-\mathbf{v}_\perp\Delta\tau)\,F'\left(\frac{Q_s(\mathbf{x}_\perp-\mathbf{v}_\perp\Delta\tau)}{p_\perp}\right) \\ &\qquad = (m+2)\int \mathrm{d}p_\perp p_\perp^{m+1}\,F\left(\frac{Q_s(\mathbf{x}_\perp-\mathbf{v}_\perp\Delta\tau)}{p_\perp}\right)\,. \end{aligned} \tag{C.29}$$

The angular integrals are of the same type as the ones in Appendix B, however each of the three perturbations has a slightly different angular dependence, so we will

discuss them one by one. The δf-term is proportional to

$$\int \mathrm{d}\phi_{\mathbf{p}_\perp\mathbf{n}_\perp} \int \mathrm{d}\phi_{\mathbf{x}_\perp\mathbf{p}_\perp} e^{in\phi_{\mathbf{p}_\perp\mathbf{n}_\perp}} e^{2\left(\frac{m+2}{3}+\alpha\right)b\,\cos(\phi_{\mathbf{x}_\perp\mathbf{p}_\perp})}(1-\beta\cos(\phi_{\mathbf{x}_\perp\mathbf{p}_\perp}))$$
$$\times \sum_{j=0}^{n}\binom{n}{j} x_\perp^{n-j}(-\Delta\tau)^j\,\cos(n\phi_{\mathbf{x}_\perp\mathbf{n}_\perp}+j\phi_{\mathbf{x}_\perp\mathbf{p}_\perp}) \tag{C.30}$$
$$= 2\pi \int \mathrm{d}\phi_{\mathbf{p}_\perp\mathbf{n}_\perp} e^{in\phi_{\mathbf{x}_\perp\mathbf{p}_\perp}}\cos(n\phi_{\mathbf{p}_\perp\mathbf{n}_\perp})$$
$$\times \sum_{j=0}^{n}\binom{n}{j} x_\perp^{n-j}(-\Delta\tau)^j\,\left[I_j\left(\left(\frac{m+2}{3}+\alpha\right)b\right)-\beta I_j'\left(\left(\frac{m+2}{3}+\alpha\right)b\right)\right] \tag{C.31}$$
$$= 2\pi^2 \sum_{j=0}^{n}\binom{n}{j} x_\perp^{n-j}(-\Delta\tau)^j\,\left[I_j\left(\left(\frac{m+2}{3}+\alpha\right)b\right)-\beta I_j'\left(\left(\frac{m+2}{3}+\alpha\right)b\right)\right]\,. \tag{C.32}$$

The δT-perturbation contains via $\delta\epsilon$ a factor of $\cos(n\phi_{\mathbf{x}_\perp\mathbf{n}_\perp}) = \cos(n\phi_{\mathbf{p}_\perp\mathbf{n}_\perp})\cos(n\phi_{\mathbf{x}_\perp\mathbf{p}_\perp}) - \sin(n\phi_{\mathbf{p}_\perp\mathbf{n}_\perp})\sin(n\phi_{\mathbf{x}_\perp\mathbf{p}_\perp})$. The term that is odd in $\phi_{\mathbf{x}_\perp\mathbf{p}_\perp}$ will vanish, while the other integrates to

$$\int \mathrm{d}\phi_{\mathbf{p}_\perp\mathbf{n}_\perp} \int \mathrm{d}\phi_{\mathbf{x}_\perp\mathbf{p}_\perp} e^{in\phi_{\mathbf{p}_\perp\mathbf{n}_\perp}} e^{2\frac{m+2}{3}b\,\cos(\phi_{\mathbf{x}_\perp\mathbf{p}_\perp})}[1-\beta\,\cos(\phi_{\mathbf{x}_\perp\mathbf{p}_\perp})]\,\cos(n\phi_{\mathbf{x}_\perp\mathbf{n}_\perp}) \tag{C.33}$$
$$= 2\pi \int \mathrm{d}\phi_{\mathbf{p}_\perp\mathbf{n}_\perp} e^{in\phi_{\mathbf{x}_\perp\mathbf{p}_\perp}}\cos(n\phi_{\mathbf{p}_\perp\mathbf{n}_\perp})\left[I_n\left(\frac{m+2}{3}b\right)-\beta I_n'\left(\frac{m+2}{3}b\right)\right] \tag{C.34}$$
$$= 2\pi^2\left[I_n\left(\frac{m+2}{3}b\right)-\beta I_n'\left(\frac{m+2}{3}b\right)\right]\,. \tag{C.35}$$

Lastly, the δu^μ-perturbation is of the form $\delta u_t\gamma[\beta-\cos(\phi_{\mathbf{x}_\perp\mathbf{p}_\perp})] - \delta u_s\sin(\phi_{\mathbf{x}_\perp\mathbf{p}_\perp})$. The term containing $\delta u_t \propto \cos(n\phi_{\mathbf{x}_\perp\mathbf{n}_\perp})$ behaves exactly like before:

$$\int \mathrm{d}\phi_{\mathbf{p}_\perp\mathbf{n}_\perp} e^{in\phi_{\mathbf{p}_\perp\mathbf{n}_\perp}} \int \mathrm{d}\phi_{\mathbf{x}_\perp\mathbf{p}_\perp} e^{2\frac{m+2}{3}b\,\cos(\phi_{\mathbf{x}_\perp\mathbf{p}_\perp})}[\beta-\cos(\phi_{\mathbf{x}_\perp\mathbf{p}_\perp})]\cos(n\phi_{\mathbf{x}_\perp\mathbf{n}_\perp}) \tag{C.36}$$
$$= 2\pi^2\left[\beta I_n\left(\frac{m+2}{3}b\right)-I_n'\left(\frac{m+2}{3}b\right)\right]\,, \tag{C.37}$$

while the other term contains a factor of $-\sin(\phi_{\mathbf{x}_\perp\mathbf{p}_\perp})\,\delta u_s$ which has the total angular dependence $-\sin(\phi_{\mathbf{x}_\perp\mathbf{p}_\perp})\sin(n\phi_{\mathbf{x}_\perp\mathbf{n}_\perp}) = -\sin(\phi_{\mathbf{x}_\perp\mathbf{p}_\perp})[\cos(n\phi_{\mathbf{p}_\perp\mathbf{n}_\perp})\sin(n\phi_{\mathbf{x}_\perp\mathbf{p}_\perp}) + \sin(n\phi_{\mathbf{p}_\perp\mathbf{n}_\perp})\cos(n\phi_{\mathbf{x}_\perp\mathbf{p}_\perp})]$, so in angular integration, the $\phi_{\mathbf{x}_\perp\mathbf{p}_\perp}$-even part becomes

$$\int \mathrm{d}\phi_{\mathbf{p}_\perp\mathbf{n}_\perp} e^{in\phi_{\mathbf{p}_\perp\mathbf{n}_\perp}} \int \mathrm{d}\phi_{\mathbf{x}_\perp\mathbf{p}_\perp} e^{2\frac{m+2}{3}\,b\,\cos(\phi_{\mathbf{x}_\perp\mathbf{p}_\perp})}(-\sin(\phi_{\mathbf{x}_\perp\mathbf{p}_\perp}))\sin(n\phi_{\mathbf{x}_\perp\mathbf{n}_\perp}) \tag{C.38}$$
$$= -2\pi^2\left[\beta I_n'\left(\frac{m+2}{3}b\right)-I_{n+1}\left(\frac{m+2}{3}b\right)\right]\,. \tag{C.39}$$

Putting all of this together, we can find the 2d integral expression for $\delta V_{mn}^{(1,0)}$:

$$\delta V_{mn}^{(1,0)} = -V_{m0}^{(0)}\,\delta_n\,\hat{\gamma}\,\mathcal{P}_{mn}(\tilde{\tau}) \quad , \tag{C.40}$$

$$\begin{aligned}
\mathcal{P}_{mn}(\tilde{\tau}) = {} & \frac{m+3}{6}\int_{\tilde{\tau}_0}^{\tilde{\tau}} \mathrm{d}\tilde{\tau}' \int_0^{\infty} \mathrm{d}\tilde{x}_\perp \tilde{x}_\perp \gamma \tilde{T} \exp\left[-\left(\frac{m+2}{3}+\alpha\right)(\tilde{x}_\perp^2 + \Delta\tilde{\tau}'^2)\right] \\
& \times \sum_{j=0}^{n} \binom{n}{j} \tilde{x}_\perp^{n-j} (-\Delta\tilde{\tau}')^j \Bigg\{ \frac{m+2}{3}\left[I_j\left(\left(\frac{m+2}{3}+\alpha\right)b\right)\right. \\
& \left. -\beta I_j'\left(\left(\frac{m+2}{3}+\alpha\right)b\right)\right] + \frac{1}{4}\frac{1}{\tilde{\tau}'}\gamma^2\tilde{T}^{-4}\left[I_n\left(\frac{m+2}{3}b\right) - \beta I_n'\left(\frac{m+2}{3}b\right)\right] \\
& \times \left[I_j(2\bar{\alpha}b) - 2\beta I_j'(2\bar{\alpha}b) + \beta^2 I_j''(2\bar{\alpha}b)\right] + \Bigg\{ \gamma^2 \Bigg[\left(2\beta + \frac{1}{2b}\right) I_1(2b) \\
& \left. - 2I_0(2b)\right]^{-1} \left[\beta I_j(2\bar{\alpha}b) - (1+\beta^2) I_j'(2\bar{\alpha}b) + \beta I_j''(2\bar{\alpha}b)\right] \\
& \times \left[\beta I_n\left(\frac{m+2}{3}b\right) - I_n'\left(\frac{m+2}{3}b\right)\right] - \left[\left(\beta - \frac{1}{2b}\right) I_1(2b) - I_0(2b)\right]^{-1} \\
& \times \left[I_j'(2\bar{\alpha}b) - I_{j+1}(2\bar{\alpha}b) - \beta I_j''(2\bar{\alpha}b) + \beta I_{j+1}'(2\bar{\alpha}b)\right] \\
& \times \left[\beta I_n'\left(\frac{m+2}{3}b\right) - I_{n+1}\left(\frac{m+2}{3}b\right)\right] \Bigg\} \Bigg\}
\end{aligned} \tag{C.41}$$

Next, we will compute $\delta V_{mn}^{(1,eq)}$ by plugging (C.23) into (C.1). Again, the most straightforward integration is the one over $p_\perp$, which equates to taking moments of f_{eq}. Terms containing f_{eq}' can be cast into the same form as the others by partial integration, which yields

$$\int \mathrm{d}p_\perp\, p_\perp^{m+2} \frac{p_\mu u^\mu}{T} f_{eq}'\left(\frac{p_\nu u^\nu}{T}\right) = -(m+3)\int \mathrm{d}p_\perp\, p_\perp^{m+2} f_{eq}\left(\frac{p_\nu u^\nu}{T}\right) \quad . \tag{C.42}$$

To compute the angular integrals, as in the computation of $\delta V_{mn}^{(1,0)}$ we can rewrite the $\phi_{\mathbf{x}_\perp\mathbf{n}_\perp}$-dependence of $\delta\epsilon$, δu_t and δu_s into a dependence on $\phi_{\mathbf{p}_\perp\mathbf{n}_\perp}$ and $\phi_{\mathbf{x}_\perp\mathbf{p}_\perp}$, which makes the $\phi_{\mathbf{p}_\perp\mathbf{n}_\perp}$-integration trivial. However, the next step will be the trickiest one of this entire section, as the integrals over $\phi_{\mathbf{x}_\perp\mathbf{p}_\perp}$ and η are highly non-trivial. The integrals that need to be computed for the different anisotropic correction terms are:

$$\int \mathrm{d}\eta \int \mathrm{d}\phi_{\mathbf{x}_\perp\mathbf{p}_\perp} \left(\frac{p_\mu u^\mu}{p_\perp}\right)^{-m-2} \delta\epsilon \quad , \tag{C.43}$$

$$\int \mathrm{d}\eta \int \mathrm{d}\phi_{\mathbf{x}_\perp\mathbf{p}_\perp} \left(\frac{p_\mu u^\mu}{p_\perp}\right)^{-m-3} \delta u_t \left[\beta\cosh(y-\eta) - \cos(\phi_{\mathbf{x}_\perp\mathbf{p}_\perp})\right] \quad , \tag{C.44}$$

$$\int \mathrm{d}\eta \int \mathrm{d}\phi_{\mathbf{x}_\perp\mathbf{p}_\perp} \left(\frac{p_\mu u^\mu}{p_\perp}\right)^{-m-3} \delta u_s \sin(\phi_{\mathbf{x}_\perp\mathbf{p}_\perp}) \quad . \tag{C.45}$$

Getting rid of all prefactors that do not depend on the integration variables, this amounts to computing the following integrals:

$$G_\epsilon(n,m,\beta) = \int \mathrm{d}\eta \int \mathrm{d}\phi_{\mathbf{x}_\perp\mathbf{p}_\perp} \left[\cosh(y-\eta) - \beta\cos(\phi_{\mathbf{x}_\perp\mathbf{p}_\perp})\right]^{-m-2} \cos(n\phi_{\mathbf{x}_\perp\mathbf{p}_\perp}) \quad , \tag{C.46}$$

$$\begin{aligned} G_{u_t}(n,m,\beta) = &\int \mathrm{d}\eta \int \mathrm{d}\phi_{\mathbf{x}_\perp\mathbf{p}_\perp} \left[\cosh(y-\eta) - \beta\cos(\phi_{\mathbf{x}_\perp\mathbf{p}_\perp})\right]^{-m-3} \\ &\times \left[\beta\cosh(y-\eta) - \cos(\phi_{\mathbf{x}_\perp\mathbf{p}_\perp})\right] \cos(n\phi_{\mathbf{x}_\perp\mathbf{p}_\perp}) \quad , \end{aligned} \tag{C.47}$$

$$\begin{aligned} G_{u_s}(n,m,\beta) = &\int \mathrm{d}\eta \int \mathrm{d}\phi_{\mathbf{x}_\perp\mathbf{p}_\perp}, \left[\cosh(y-\eta) - \beta\cos(\phi_{\mathbf{x}_\perp\mathbf{p}_\perp})\right]^{-m-3} \\ &\times \sin(\phi_{\mathbf{x}_\perp\mathbf{p}_\perp}) \sin(n\phi_{\mathbf{x}_\perp\mathbf{p}_\perp}) \quad . \end{aligned} \tag{C.48}$$

We have defined these integrals as the functions $G_X(n,m,\beta)$ to abbreviate the notation of our results. To compute them, we rewrite again $\sin(n\phi_{\mathbf{x}_\perp\mathbf{p}_\perp})$ and $\cos(n\phi_{\mathbf{x}_\perp\mathbf{p}_\perp})$ into Chebyshev polynomials as we did in Appendix A. Since the polynomial expression for $\sin(n\phi_{\mathbf{x}_\perp\mathbf{p}_\perp})$ also contains a factor of $\sin(\phi_{\mathbf{x}_\perp\mathbf{p}_\perp})$ which together with the in (C.48) already present sine combines to $1-\cos^2(\phi_{\mathbf{x}_\perp\mathbf{p}_\perp})$, now only different powers of $\cos(\phi_{\mathbf{x}_\perp\mathbf{p}_\perp})$ without any sines occur in the integrand, which can be integrated analytically as follows:

$$\int \mathrm{d}\eta \int \mathrm{d}\phi_{\mathbf{x}_\perp\mathbf{p}_\perp} [\cosh(y-\eta) - \beta\cos(\phi_{\mathbf{x}_\perp\mathbf{p}_\perp})]^{-m-2} \cos^l(\phi_{\mathbf{x}_\perp\mathbf{p}_\perp}) \tag{C.49}$$

$$= 4\int_1^\infty \mathrm{d}x \int_{-1}^1 \mathrm{d}y \frac{[x-\beta y)]^{-m-2} y^l}{\sqrt{1+x^2}\sqrt{1-y^2}} \tag{C.50}$$

$$= \begin{cases} \frac{2\pi\Gamma\left(\frac{m+2}{2}\right)\Gamma\left(\frac{l+1}{2}\right)}{\Gamma\left(\frac{m+3}{2}\right)\Gamma\left(\frac{l+2}{2}\right)} \, {}_3F_2\left(\frac{m+2}{2}, \frac{m+2}{2}, \frac{l+1}{2}; \frac{1}{2}, \frac{l+2}{2}; \beta^2\right) & , \text{ l even} \\ \frac{4\pi\beta\Gamma\left(\frac{m+3}{2}\right)\Gamma\left(\frac{l+2}{2}\right)}{\Gamma\left(\frac{m+2}{2}\right)\Gamma\left(\frac{l+3}{2}\right)} \, {}_3F_2\left(\frac{m+3}{2}, \frac{m+3}{2}, \frac{l+2}{2}; \frac{3}{2}, \frac{l+3}{2}; \beta^2\right) & , \text{ l odd} \end{cases} , \tag{C.51}$$

$$\int \mathrm{d}\eta \int \mathrm{d}\phi_{\mathbf{x}_\perp\mathbf{p}_\perp} [\cosh(y-\eta) - \beta\cos(\phi_{\mathbf{x}_\perp\mathbf{p}_\perp})]^{-m-3} \cos^l(\phi_{\mathbf{x}_\perp\mathbf{p}_\perp}) \cosh(y-\eta) \tag{C.52}$$

$$= 4\int_1^\infty \mathrm{d}x \int_{-1}^1 \mathrm{d}y \frac{[x-\beta y)]^{-m-3} y^l x}{\sqrt{1+x^2}\sqrt{1-y^2}} \tag{C.53}$$

$$= \begin{cases} \frac{2\pi\Gamma\left(\frac{m+2}{2}\right)\Gamma\left(\frac{l+1}{2}\right)}{\Gamma\left(\frac{m+3}{2}\right)\Gamma\left(\frac{l+2}{2}\right)} \, {}_3F_2\left(\frac{m+2}{2}, \frac{m+4}{2}, \frac{l+1}{2}; \frac{1}{2}, \frac{l+2}{2}; \beta^2\right) & , \text{ l even} \\ \frac{4\pi\beta\Gamma\left(\frac{m+5}{2}\right)\Gamma\left(\frac{l+2}{2}\right)}{\Gamma\left(\frac{m+4}{2}\right)\Gamma\left(\frac{l+3}{2}\right)} \, {}_3F_2\left(\frac{m+3}{2}, \frac{m+5}{2}, \frac{l+2}{2}; \frac{3}{2}, \frac{l+3}{2}; \beta^2\right) & , \text{ l odd} \end{cases} . \tag{C.54}$$

To simplify these expressions, we can make use of the following property of the Γ-function:

$$\frac{\Gamma\left(n+\frac{1}{2}\right)}{\Gamma\left(n+1\right)} = \frac{(2n)!}{4^n(n!)^2}\sqrt{\pi} \tag{C.55}$$

Then one finds the following expressions for the integrals (C.46)-(C.48).

$$
\begin{aligned}
&G_\epsilon(n,m,\beta) \\
&= \int \mathrm{d}\eta \int \mathrm{d}\phi[\cosh(y-\eta)-\beta\cos(\phi)]^{-m-2}\frac{n}{2}\sum_{k=0}^{\lfloor\frac{n}{2}\rfloor}(-1)^k\frac{(n-k-1)!}{(n-2k)!k!}\,2^{n-2k}\,\cos^{n-2k}(\phi) \\
&= \pi^{3/2}n\begin{cases}
\frac{\Gamma\left(\frac{m+2}{2}\right)}{\Gamma\left(\frac{m+3}{2}\right)}\sum_{k=0}^{\lfloor\frac{n}{2}\rfloor}(-1)^k\frac{(n-k-1)!}{\left(\frac{n-2k}{2}!\right)^2k!}\;{}_3F_2\left(\frac{m+2}{2},\frac{m+2}{2},\frac{n-2k+1}{2};\frac{1}{2},\frac{n-2k+2}{2};\beta^2\right)\;, & \text{n even}\\
\beta\frac{\Gamma\left(\frac{m+2}{2}\right)}{\Gamma\left(\frac{m+3}{2}\right)}\sum_{k=0}^{\lfloor\frac{n}{2}\rfloor}(-1)^k\frac{(n-k-1)!}{\left(\frac{n-2k-1}{2}!\right)^2k!}\;{}_3F_2\left(\frac{m+3}{2},\frac{m+3}{2},\frac{n-2k+2}{2};\frac{3}{2},\frac{n-2k+3}{2};\beta^2\right)\;, & \text{n odd}
\end{cases}
\end{aligned}
\tag{C.56}
$$

$$
\begin{aligned}
&G_{u_t}(n,m,\beta) = \int \mathrm{d}\eta \int \mathrm{d}\phi[\cosh(y-\eta)-\beta\cos(\phi)]^{-m-3} \\
&\quad\times\sum_{k=0}^{\lfloor\frac{n-1}{2}\rfloor}(-1)^k\binom{n-k-1}{k}2^{n-2k-1}\left[\cos^{n-2k-1}(\phi)-\cos^{n-2k+1}(\phi)\right] \\
&= 2\pi^{3/2}\begin{cases}
\frac{\Gamma\left(\frac{m+3}{2}\right)}{\Gamma\left(\frac{m+4}{2}\right)}\sum_{k=0}^{\lfloor\frac{n-1}{2}\rfloor}(-1)^k\frac{(n-k-1)!}{\left(\frac{n-2k-1}{2}!\right)^2k!}\Big[\;{}_3F_2\left(\frac{m+3}{2},\frac{m+3}{2},\frac{n-2k}{2};\frac{1}{2},\frac{n-2k+1}{2};\beta^2\right) \\
\qquad+\frac{n-2k}{n-2k+1}\;{}_3F_2\left(\frac{m+3}{2},\frac{m+3}{2},\frac{n-2k+2}{2};\frac{1}{2},\frac{n-2k+3}{2};\beta^2\right)\Big]\;, & \text{n odd}\\
\beta\frac{\Gamma\left(\frac{m+4}{2}\right)}{\Gamma\left(\frac{m+3}{2}\right)}\sum_{k=0}^{\lfloor\frac{n-1}{2}\rfloor}(-1)^k\frac{(n-k-1)!}{\left(\frac{n-2k-2}{2}!\right)^2k!}\Big[\;{}_3F_2\left(\frac{m+4}{2},\frac{m+4}{2},\frac{n-2k+1}{2};\frac{3}{2},\frac{n-2k+2}{2};\beta^2\right) \\
\qquad+\frac{n-2k+1}{n-2k+2}\;{}_3F_2\left(\frac{m+4}{2},\frac{m+4}{2},\frac{n-2k+3}{2};\frac{3}{2},\frac{n-2k+4}{2};\beta^2\right)\Big]\;, & \text{n even}
\end{cases}
\end{aligned}
\tag{C.57}
$$

$$
\begin{aligned}
&G_{u_s}(n,m,\beta) = \int \mathrm{d}\eta \int \mathrm{d}\phi[\cosh(y-\eta)-\beta\cos(\phi)]^{-m-3} \\
&\quad\times\frac{n}{2}\sum_{k=0}^{\lfloor\frac{n}{2}\rfloor}(-1)^k\frac{(n-k-1)!}{(n-2k)!k!}\,2^{n-2k}\left[\beta\cos^{n-2k}(\phi)\cosh(y-\eta)-\cos^{n-2k+1}(\phi)\right] \\
&= \pi^{3/2}n\begin{cases}
\sum_{k=0}^{\lfloor\frac{n}{2}\rfloor}(-1)^k\frac{(n-k-1)!}{\left(\frac{n-2k}{2}!\right)^2k!}\left[\beta\frac{\Gamma\left(\frac{m+2}{2}\right)}{\Gamma\left(\frac{m+3}{2}\right)}\;{}_3F_2\left(\frac{m+2}{2},\frac{m+4}{2},\frac{n-2k+1}{2};\frac{1}{2},\frac{n-2k+2}{2};\beta^2\right)\right. \\
\qquad\left.-2\beta\frac{\Gamma\left(\frac{m+4}{2}\right)}{\Gamma\left(\frac{m+3}{2}\right)}\frac{n-2k+1}{n-2k+2}\;{}_3F_2\left(\frac{m+4}{2},\frac{m+4}{2},\frac{n-2k+3}{2};\frac{3}{2},\frac{n-2k+4}{2};\beta^2\right)\right]\;, & \text{n even}\\
\sum_{k=0}^{\lfloor\frac{n}{2}\rfloor}(-1)^k\frac{(n-k-1)!}{\left(\frac{n-2k}{2}!\right)^2k!}\left[\beta^2\frac{\Gamma\left(\frac{m+5}{2}\right)}{\Gamma\left(\frac{m+4}{2}\right)}\;{}_3F_2\left(\frac{m+3}{2},\frac{m+5}{2},\frac{n-2k+2}{2};\frac{3}{2},\frac{n-2k+3}{2};\beta^2\right)\right. \\
\qquad\left.-\beta\frac{\Gamma\left(\frac{m+3}{2}\right)}{2\Gamma\left(\frac{m+4}{2}\right)}\;{}_3F_2\left(\frac{m+3}{2},\frac{m+3}{2},\frac{n-2k+2}{2};\frac{1}{2},\frac{n-2k+3}{2};\beta^2\right)\right]\;, & \text{n odd}
\end{cases}
\end{aligned}
\tag{C.58}
$$

The final step to computing the total expression for $\delta V_{mn}^{(1,eq)}$ is a bookkeeping task of combining all the above integration steps, at the end of which one acquires

$$\delta V_{mn}^{(1,eq)} = \hat{\gamma}\delta_n \nu_{\rm eff} R^{-m} \left(\frac{1}{\pi}\nu_{\rm eff}^{-1}\frac{{\rm d}E_\perp^{(0)}}{{\rm d}\eta}R\right)^{(m+3)/4} \mathcal{Q}_{mn}(\tilde{\tau}) \quad , \tag{C.59}$$

$$\begin{aligned}
\mathcal{Q}_{mn}(\tilde{\tau}) = {} & \left(\frac{\pi^2}{30}\right)^{-(m+3)/4} \frac{1}{8\pi^2}\zeta(m+3)\int_{\tilde{\tau}_0}^{\tilde{\tau}} {\rm d}\tilde{\tau}' \int_0^\infty {\rm d}\tilde{x}_\perp \tilde{x}_\perp \exp\left[-\bar{\alpha}\left(\tilde{x}_\perp^2 + \Delta\tilde{\tau}'^2\right)\right] \\
& \times \gamma^{-m-2}\,\tilde{T}^m \sum_{j=0}^{n}\binom{n}{j}\tilde{x}_\perp^{n-j}(-\Delta\tilde{\tau}')^j \left\{\frac{1}{4}[\Gamma(m+3)+\Gamma(m+4)]\,\gamma^2\,[I_j(2\bar{\alpha}b)\right. \\
& - 2\beta I_j'(2\bar{\alpha}b) + \beta^2 I_j''(2\bar{\alpha}b)]\,G_\epsilon(n,m,\beta) + [\Gamma(m+3)-\Gamma(m+4)]\,\tilde{\tau}'\,\tilde{T}^4 \\
& \times \left\{\gamma^2\left[\left(2\beta+\frac{1}{2b}\right)I_1(2b) - 2I_0(2b)\right]^{-1}[\beta I_j(2\bar{\alpha}b) - (1+\beta^2)I_j'(2\bar{\alpha}b)\right. \\
& + \beta I_j''(2\bar{\alpha}b)]\,G_{u_t}(n,m,\beta) - \left[\left(\beta-\frac{1}{2b}\right)I_1(2b) - I_0(2b)\right]^{-1} \\
& \left.\left.\times\,[I_j'(2\bar{\alpha}b) - I_{j+1}(2\bar{\alpha}b) - \beta I_j''(2\bar{\alpha}b) + \beta I_{j+1}'(2\bar{\alpha}b)]\,G_{u_s}(n,m,\beta)\right\}\right\}
\end{aligned} \tag{C.60}$$

Appendix D

Equilibrium moments of the numerical setup

In this appendix, the equilibrium moments E_l^m emerging in the time evolution equations for the moments C_l^m as derived in Section 5.3.1 are computed. Since taking the integral $\int \mathrm{d}p^\tau (p^\tau)^3$ of the equilibrium distribution will yield the energy density, the expression simplifies in spherical coordinates.

$$E_l^m = \int \frac{\mathrm{d}^2 p_\perp}{(2\pi)^2} \int \frac{\mathrm{d}p_\eta}{2\pi} Y_l^m(\theta_p, \phi_p)\, p^\mu u_\mu\, f_{eq} \tag{D.1}$$

$$= \tau \int_0^\infty \mathrm{d}p^\tau (p^\tau)^3 \int_0^{2\pi} \frac{\mathrm{d}\phi_p}{2\pi} \int \frac{\mathrm{d}\cos\theta_p}{2} Y_l^m(\theta_p, \phi_p) \frac{1}{2\pi^2} v^\mu u_\mu f_{eq}\left(\frac{p^\mu u_\mu}{T}\right) \tag{D.2}$$

$$= \tau\epsilon \int_0^{2\pi} \frac{\mathrm{d}\phi_p}{2\pi} \int \frac{\mathrm{d}\cos\theta_p}{2} Y_l^m(\theta_p, \phi_p)\, (v^\mu u_\mu)^{-3} \tag{D.3}$$

In this calculation, we have defined $v^\mu = p^\mu / p^\tau$. To compute the angular integral, we write

$$v^\mu u_\mu = \gamma\,(1 - \vec{\beta}\cdot\vec{v}) = \gamma\,(1 - \beta\cos\theta_{up}) \tag{D.4}$$

and express the spherical harmonics in a rotated coordinate system, thus writing

$$Y_l^m(\theta_p, \phi_p) = \sum_{m'=-l}^{l} \left(D_{mm'}^l\right)^* Y_l^{m'}(\theta_{up}, \phi_{up}) \quad , \tag{D.5}$$

where the Wigner D-matrix depends on the angles involved in the rotation from (θ_{up}, ϕ_{up}) to (θ_p, ϕ_p). In these coordinates, the ϕ_{up}-integral becomes trivial, thus only an integral of the Legendre polynomials remains to be computed.

$$\int_0^{2\pi} \frac{\mathrm{d}\phi_{up}}{2\pi} \int \frac{\mathrm{d}\cos\theta_{up}}{2} Y_l^{m'}(\theta_{up}, \phi_{up})\, \gamma^{-3}\,(1 - \beta\,\cos\theta_{up})^{-3} = \delta^{m'0} y_l^0 \int \mathrm{d}x \frac{P_l(x)}{2\gamma^3(1-\beta x)^3} \tag{D.6}$$

For the case $m' = 0$, the Wigner D-matrix simplifies to

$$\left(D_{m0}^l\right)^* = \sqrt{\frac{4\pi}{2l+1}} Y_l^m(\theta_{rot}, \phi_{rot}) \quad . \tag{D.7}$$

Since $\vec{u}$ lies in the transverse plane, where its orientation is given by ϕ_u, we can identify the rotation angles to be $\theta_{rot} = \frac{\pi}{2}$ and $\phi_{rot} = \phi_u$, which yields

$$E_l^m = \tau\epsilon\, Y_l^m\left(\frac{\pi}{2}, \phi_u\right) \int_{-1}^{1} \mathrm{d}x\, \frac{P_l(x)}{2\gamma^3(1-\beta x)^3} \quad . \tag{D.8}$$

Finally, the remaining integral can be solved analytically:

$$\int_{-1}^{1} \mathrm{d}x \frac{P_l(x)}{2\gamma^3(1-\beta x)^3} = 2^{-l-2}\pi^{1/2}\frac{\Gamma\left(l+3\right)}{\Gamma\left(l+\frac{3}{2}\right)}\gamma^{-3}\beta^l\ {}_2F_1\left(\frac{l+4}{2}, \frac{l+3}{2}; l+\frac{3}{2}; \beta^2\right) \quad . \tag{D.9}$$

Appendix E

Setup of the numerical code computing linear order results

In this Appendix, we explain the setup of of the numerical code needed for obtaining the linear order results presented in Chapter 6 according to the expansion scheme discussed in Sec. 3.2.2.

The code is set up to compute the zeroth and first order contributions to the energy-momentum tensor, which is given in terms of the phase space density as

$$T^{\mu\nu} = \frac{\nu_{\text{eff}}}{(2\pi)^3} \int \mathrm{d}^2 p_\perp \int \mathrm{d}y \; p^\mu p^\nu f \; . \tag{E.1}$$

For simplicity, observables that are nonlinear in $T^{\mu\nu}$ with contributions from both zeroth and first order in the opacity expansion were computed only to zeroth order.

The code is set up as follows. For an arbitrary initial energy density distribution $\epsilon_0(\tau_0, \mathbf{x}_\perp)$, the free-streaming energy momentum tensor is given as

$$T^{(0)\mu\nu} = \frac{\tau_0}{\tau} \int \frac{\mathrm{d}\phi_v}{2\pi} \, v_\perp^\mu v_\perp^\nu \, \epsilon_0(\tau_0, \mathbf{x}_\perp - \Delta\tau \mathbf{v}_\perp) \quad . \tag{E.2}$$

The integral over ϕ_v is performed numerically, using the same stencils for all entries to prevent errors later on. Now, to go to first order in the opacity expansion, we first have to compute the zeroth order results for the restframe energy density $\epsilon(\tau, \mathbf{x}_\perp)$ and the flow velocity $u^\mu(\tau, \mathbf{x}_\perp)$, as they are required for evaluating the RTA collision kernel. This is achieved by numerical diagonalization of $T^{(0)\mu\nu}$.

As computed before, the first order correction to the phase space distribution is given as an integral of the zeroth order collision kernel.

$$f^{(1)}(\tau, \mathbf{x}_\perp, \mathbf{p}_\perp, y - \eta) = \int_{\tau_0}^{\tau} \mathrm{d}\tau' \, \frac{C[f^{(0)}]}{p^\tau} \left(\tau', \mathbf{x}_\perp{}', \mathbf{p}_\perp, y' - \eta\right) \tag{E.3}$$

The primes on the variables indicate the use of free-streaming coordinates. From this, the first order correction to the energy-momentum tensor is obtained as

$$T^{(1)\mu\nu} = \int d^2\mathbf{p}_\perp \int dy \; p^\mu p^\nu \int_{\tau_0}^{\tau} d\tau' \, \frac{C[f^{(0)}](\tau', \mathbf{x}_\perp{}', \mathbf{p}_\perp, y' - \eta)}{p^\tau(\mathbf{p}_\perp, y' - \eta)} \; . \tag{E.4}$$

As it turns out, the observables that are to be computed to first order in opacity depend only on transverse integrals of the components of T^{ij}. Thus, we need to perform a 6D integral, which can be done in part analytically, reducing the complexity of the numerical integration. For further details of the analytical preparatory groundwork for the numerical implementation, see Appendix F.

The observables are now computed from these results in the following way. As a substitute for $dE_\perp/dy$, we extract

$$\frac{dE_{\mathrm{tr}}}{dy} = \tau \int_{\mathbf{x}_\perp} T^{11} + T^{22} \tag{E.5}$$

$$= \tau \int_{\mathbf{x}_\perp} T^{(0)11} + T^{(0)22} + T^{(1)11} + T^{(1)22} \,. \tag{E.6}$$

As elliptic flow is given as a quotient of two transverse integrals of components of $T^{\mu\nu}$ where the denominator vanishes at zeroth order, the first order result is given as

$$\epsilon_p = \frac{\int_{\mathbf{x}_\perp} T^{11} - T^{22} + 2iT^{12}}{\int_{\mathbf{x}_\perp} T^{11} + T^{22}} \tag{E.7}$$

$$= \frac{\int_{\mathbf{x}_\perp} T^{(1)11} - T^{(1)22} + 2iT^{(1)12}}{\int_{\mathbf{x}_\perp} T^{(0)11} + T^{(0)22}} \,. \tag{E.8}$$

Both of these observables depend on the transverse integral of $T^{(0)11} + T^{(0)22}$, which using E.2 can be straightforwardly evaluated to

$$\int_{\mathbf{x}_\perp} T^{(0)11} + T^{(0)22} = \frac{1}{\tau} \frac{\mathrm{d}E_\perp^{(0)}}{\mathrm{d}\eta} \,. \tag{E.9}$$

In particular, the quantity $dE_{\mathrm{tr}}/d\eta$, which we introduced as the analogue of $dE_\perp/dy$, is in fact identical to $dE_\perp/dy$ to zeroth order. Furthermore it is constant in time, so only the first order correction has to be computed. We furthermore compute zeroth order results for the average transverse flow velocity and the average inverse Reynolds number as

$$\langle u_\perp \rangle = \frac{\int_{\mathbf{x}_\perp} \epsilon^{(0)} \sqrt{\left(u_1^{(0)}\right)^2 + \left(u_2^{(0)}\right)^2}}{\int_{\mathbf{x}_\perp} \epsilon^{(0)}} \,, \tag{E.10}$$

$$\langle \mathrm{Re}^{-1} \rangle = \frac{\int_{\mathbf{x}_\perp} \sqrt{6\pi^{(0)\mu\nu}\pi^{(0)}_{\mu\nu}}}{\int_{\mathbf{x}_\perp} \epsilon^{(0)}} \tag{E.11}$$

$$= \frac{\int_{\mathbf{x}_\perp} \sqrt{6T^{(0)\mu\nu}T^{(0)}_{\mu\nu} - \frac{24}{3}\left(\epsilon^{(0)}\right)^2}}{\int_{\mathbf{x}_\perp} \epsilon^{(0)}} \,. \tag{E.12}$$

Appendix F

Analytical and numerical integration in the computation of linear order results

As discussed in the previous Appendix, obtaining numerical results for the linear order term in the energy momentum tensor requires the computation of a 6D integral. In this Appendix, we explain what part of this integral is performed analytically and give the specific form of the remaining integral which the code computes numerically.

We start from the expression in Eq. E.4 for the purely spatial components of the energy momentum tensor. Stating now the free-streaming coordinates in explicit form, the integral that has to be computed for each component of $T^{(1)ij}$ is

$$\int_{\mathbf{x}_\perp} T^{(1)ij} = -\frac{\nu_{\text{eff}}}{(2\pi)^3}\int_{\mathbf{x}_\perp}\int_{\mathbf{p}_\perp}\int \mathrm{d}y\; p^i p^j \int_{\tau_0}^{\tau} \mathrm{d}\tau' \frac{C[f^{(0)}]}{p^\tau}\Big(\tau', \mathbf{x}_\perp{}' = \mathbf{x}_\perp - \mathbf{v}_\perp \Delta\tau \\ , \mathbf{p}_\perp, y' - \eta = \operatorname{arcsinh}\left(\frac{\tau}{\tau'}\sinh(y-\eta)\right)\Big)\ . \quad \text{(F.1)}$$

For more information on where they come from, one may consult our previous paper [1]. When substituting to these coordinates, the Jacobian for the $\mathbf{x}_\perp$-integration is trivial, but the one for y involves

$$\mathrm{d}y' = \frac{\tau}{\tau'}\frac{\cosh(y-\eta)}{\cosh(y'-\eta)}\mathrm{d}y \quad \text{(F.2)}$$

$$= \frac{\tau}{\tau'}\frac{\sqrt{1+\left(\frac{\tau'}{\tau}\right)^2\sinh^2(y'-\eta)}}{\cosh(y'-\eta)}\mathrm{d}y\ . \quad \text{(F.3)}$$

Right away and from this point on, we will drop the primes on all coordinates except τ' for convenience. Also plugging in the specific form of the RTA kernel

$$C[f] = -\frac{p^\mu u_\mu}{\tau_R}(f - f_{\text{eq}}) \quad \text{(F.4)}$$

we arrive at

$$\int_{\mathbf{x}_\perp} T^{(1)ij} = -\frac{\nu_{\text{eff}}}{(2\pi)^3}\int_{\mathbf{p}_\perp}\int_{\mathbf{x}_\perp}\int dy \int_{\tau_0}^{\tau} d\tau' \mathbf{p}_\perp^i \mathbf{p}_\perp^j \frac{\tau'}{\tau}\frac{1}{\sqrt{1+\left(\frac{\tau'}{\tau}\right)^2\sinh^2(y-\eta)}}\frac{v^\mu u_\mu^{(0)}}{\tau_R} \\ \times (f^{(0)} - f_{\text{eq}})(\tau', \mathbf{x}_\perp, \mathbf{p}_\perp, y-\eta)\ , \quad \text{(F.5)}$$

where we defined $v^\mu = p^\mu/p_\perp$, such that

$$v^\mu u_\mu = \gamma[\cosh(y-\eta) - \mathbf{v}_\perp \cdot \boldsymbol{\beta}] \,. \tag{F.6}$$

The relaxation time is given as

$$\tau_R = 5\frac{\eta}{s}[T^{(0)}]^{-1} \,, \tag{F.7}$$

where the zeroth order Temperature is computed from the zeroth order restframe energy density $e^{(0)}$ via the equation of state. For compactness we will stick to denoting it simply as τ_R.

It is convenient to consider separately the contributions coming from the decay of $f^{(0)}$ and from the buildup of f_{eq}, which we will call $T^{(1,0)ij}$ and $T^{(1,eq)ij}$. In the case of the former, we plug in

$$f^{(0)}(\tau, \mathbf{x}_\perp, \mathbf{p}_\perp, y-\eta) = \frac{(2\pi)^3}{\nu_{\text{eff}}}\frac{\delta(y-\eta)}{\tau p_\perp}\frac{\mathrm{d}N_0}{\mathrm{d}^2\mathbf{x}_\perp \mathrm{d}^2\mathbf{p}_\perp \mathrm{d}y}(\mathbf{x}_\perp - \mathbf{v}_\perp\Delta\tau, \mathbf{p}_\perp) \,. \tag{F.8}$$

Due to the Dirac-Delta, the integration over y is trivial for this term, while integrating over $p_\perp = |\mathbf{p}_\perp|$ will yield

$$\epsilon(\tau_0, \mathbf{x}_\perp - \mathbf{v}_\perp\Delta\tau) = \frac{2\pi}{\tau_0}\int \mathrm{d}p_\perp \; p_\perp^2 \; \frac{\mathrm{d}N_0}{\mathrm{d}^2\mathbf{x}_\perp \mathrm{d}^2\mathbf{p}_\perp \mathrm{d}y}(\mathbf{x}_\perp - \mathbf{v}_\perp\Delta\tau, \mathbf{p}_\perp) \,. \tag{F.9}$$

The other integrals cannot be computed analytically. We thus arrive at

$$T^{(1,0)ij} = -\int_{\tau_0}^{\tau}\mathrm{d}\tau' \int \frac{\mathrm{d}\phi_v}{2\pi}\mathbf{v}_\perp^i\mathbf{v}_\perp^j \frac{v^\mu u_\mu^{(0)}}{\tau_R}\frac{\tau_0}{\tau}\; \epsilon(\tau_0, \mathbf{x}_\perp - \mathbf{v}_\perp\Delta\tau') \,. \tag{F.10}$$

For the equilibrium buildup contribution, we can use the moment properties of the equilibrium distribution to perform the integral over $p_\perp$.

$$\frac{\nu_{\text{eff}}}{(2\pi^3}\int_0^\infty \mathrm{d}p_\perp \, p_\perp^3 f_{\text{eq}}\left(\frac{p^\mu u_\mu}{T}\right) = \frac{1}{4\pi}\frac{\epsilon}{(v^\mu u_\mu)^4} \tag{F.11}$$

$$T_{\text{eq}}^{(1)ij} = \int_{\tau_0}^{\tau}\mathrm{d}\tau'\frac{\tau'}{\tau}\frac{\epsilon^{(0)}}{\tau_R}\int\frac{\mathrm{d}y}{2}\int\frac{\mathrm{d}\varphi_v}{2\pi}\frac{1}{\sqrt{1+\left(\frac{\tau'}{\tau}\right)^2\sinh^2(y-\eta)}}\frac{\mathbf{v}_\perp^i\mathbf{v}_\perp^j}{(v^\mu u_\mu^{(0)})^3} \tag{F.12}$$

We now define for notational convenience the auxiliary quantity F_{eq}^{ij} as the remaining 2D momentum integral.

$$F_{\text{eq}}^{ij} = \int\frac{\mathrm{d}y}{2}\frac{\mathrm{d}\varphi_v}{2\pi}\frac{1}{\sqrt{1+\left(\frac{\tau'}{\tau}\right)^2\sinh^2(y-\eta)}}\frac{\mathbf{v}_\perp^i\mathbf{v}_\perp^j}{(v^\mu u_\mu^{(0)})^3} \tag{F.13}$$

This is a transverse tensor depending only on one transverse vector, specifically is $\boldsymbol{\beta}$. We can thus decompose it as

$$F_{\text{eq}}^{ij} = A\delta^{ij} + B\beta^{-2}\boldsymbol{\beta}^i\boldsymbol{\beta}^j \,, \tag{F.14}$$

where for the coefficients A and B we can derive expressions via projection. The integrals over ϕ_v can then be computed analytically.

$$\delta^{ij}F^{ij}_{eq} = 2A + B = \int \frac{dy}{2} \frac{1}{\sqrt{1+\frac{\tau'^2}{\tau^2}\sinh^2(y-\eta)}} \int \frac{d\phi_v}{2\pi} \frac{1}{\gamma^3[\cosh(y-\eta)-\beta\cos(\phi_{uv})]^3} \tag{F.15}$$

$$= \int \frac{dy}{2} \frac{2\cosh^2 y - \eta + \beta^2}{2\gamma^3\sqrt{1+\frac{\tau'^2}{\tau^2}\sinh^2(y-\eta)^2}\left(\cosh^2(y-\eta)-\beta^2\right)^{5/2}} \tag{F.16}$$

$$= \int \frac{dy}{2} \frac{1}{\gamma^3\sqrt{1+\frac{\tau'^2}{\tau^2}\sinh^2(y-\eta)^2}\left(\cosh^2(y-\eta)-\beta^2\right)^{3/2}}$$

$$+ \int \frac{dy}{2} \frac{3\beta^2}{2\gamma^3\sqrt{1+\frac{\tau'^2}{\tau^2}\sinh^2(y-\eta)^2}\left(\cosh^2(y-\eta)-\beta^2\right)^{5/2}} \tag{F.17}$$

$$= I_1 + \frac{3}{2}I_2 \tag{F.18}$$

$$\beta^{-2}\boldsymbol{\beta}^i\boldsymbol{\beta}^j F^{ij}_{eq} = A + B$$

$$= \int \frac{dy}{2} \frac{1}{\gamma^3\sqrt{1+\frac{\tau'^2}{\tau^2}\sinh^2(y-\eta)}} \int \frac{d\phi_v}{2\pi} \frac{\cos^2(\phi_{uv})}{[\cosh(y-\eta)-\beta\cos(\phi_{uv})]^3} \tag{F.19}$$

$$= \int \frac{dy}{2} \frac{\cosh^2 y - \eta + 2\beta^2}{2\gamma^3\sqrt{1+\frac{\tau'^2}{\tau^2}\sinh^2(y-\eta)^2}\left(\cosh^2(y-\eta)-\beta^2\right)^{5/2}} \tag{F.20}$$

$$= \frac{1}{2}I_1 + \frac{3}{2}I_2 \tag{F.21}$$

This means that A and B are given by the integrals I_1 and I_2 via

$$A = \frac{1}{2}I_1 \ , \quad B = \frac{3}{2}I_2 \ . \tag{F.22}$$

Since we weren't able to find analytical solutions to the integrals over y, in the numerical implementation we instead interpolate them from a set of numerically integrated values. I_1 and I_2 depend on the two parameters τ'^2/τ^2 and β^2. When performing the integration over τ' via a Riemann sum, the first of these parameters is constant in each integration step, so the interpolation has to be set up only in β^2 within this step.

With F^{ij}_{eq} given in this way, in total the integrals of $T^{(1)ij}$ over transverse space can be computed as

$$\int_{\mathbf{x}_\perp} T^{(1)ij} = \int_{\tau_0}^{\tau} d\tau' \int_{\mathbf{x}_\perp} \frac{1}{\tau_R} \int \frac{d\phi_v}{2\pi} \Big(\frac{\tau'}{\tau}\epsilon^{(0)}F^{ij}_{\mathrm{eq}} - \mathbf{v}_\perp{}^i\mathbf{v}_\perp{}^j v^\mu u^{(0)}_\mu \ \frac{\tau_0}{\tau} \ \epsilon(\tau_0, \mathbf{x}_\perp - \mathbf{v}_\perp\Delta\tau') \Big) \ . \tag{F.23}$$

Note that the zeroth order results for the flow velocity $u^{(0)}_\mu$ and the restframe energy density $e^{(0)}$ which also enters τ_R via the temperature have been computed in the first step of diagonalizing $T^{(0)\mu\nu}$. Thus, all quantities appearing in this integrand are known and the 4D integral can be performed numerically.

Appendix G

Overview of time evolution at different opacities

In Section 6.4.2 we compared the time evolution of the tracked observables in kinetic theory and scaled viscous hydro and pointed out some qualitative differences for results at three different opacities. To get a better overview of the opacity dependence in the time evolution, we can also compare results coming exclusively from kinetic theory on a wide range in opacity. This comparison for the time evolution of transverse energy $dE_{\mathrm{tr}}/d\eta$, elliptic flow ϵ_p, transverse flow velocity $\langle u_\perp \rangle_\epsilon$ and inverse Reynolds number $\left\langle \mathrm{Re}^{-1} \right\rangle_\epsilon$ is presented in Fig. G.1 for opacities ranging from $4\pi\eta/s = 0.01$ to 1000.

For very small opacities $4\pi\eta/s \sim 1000$, the system is close to free-streaming and transverse energy $dE_{\mathrm{tr}}/d\eta$ is almost constant. At larger opacities, due to more work being performed in the longitudinal expansion, $dE_{\mathrm{tr}}/d\eta$ increases by a larger total amount. The opacity also sets the timescale for this cooling, as it sets in earlier for larger opacities.

Elliptic flow ϵ_p stays close to zero at small opacities $4\pi\eta/s \sim 1000$ and rises monotonically with opacity at each point in time. Qualitatively, the curves look the same at all opacities, with a buildup period at times $0.1R \lesssim \tau \lesssim 2R$ and almost constant behaviour afterwards. The onset of this buildup is slightly earlier at larger opacities, but this difference is negligible.

As expected, the transverse flow velocity $\langle u_\perp \rangle_\epsilon$ starts with the same early-time linear behaviour for all opacities. The proportionality constant with elapsed time $\Delta\tau = \tau - \tau_0$ can be computed according to Eq. 4.50 and evaluates to $\langle u_\perp \rangle_\epsilon = 0.61\Delta\tau/R$. The larger the opacity, the earlier the system starts to deviate from this behaviour. For the largest opacities $4\pi\eta/s \lesssim 0.1$, the system is in its local Bjorken flow equilibrium state long enough for early time contributions to become negligible, such that it transitions to the late time pre-flow proportionality law. According to Eq. 4.52, in this regime, the flow velocity is given by $\langle u_\perp \rangle_\epsilon = 0.66\Delta\tau/R$. All curves exhibit their strongest rise on the timescale of transverse expansion, $\tau \sim R$. The rise is stronger at smaller opacities and in all cases contributes the most to the buildup, such that the final ($\tau = 4R$) values of transverse flow velocity are also larger at smaller opacities.

The inverse Reynolds number $\left\langle \mathrm{Re}^{-1} \right\rangle_\epsilon$ stays almost constant at early times for small opacities $4\pi\eta/s \sim 1000$, but then slightly increases due to transverse expansion. At large enough opacities $4\pi\eta/s \lesssim 10$, interactions equilibrate the system and decrease its value. This process sets in earlier at larger opacities and brings the value of the inverse Reynolds number down to almost zero for the largest opacities $4\pi\eta/s \lesssim 0.05$. In these cases, the value stays close to zero even during transverse expansion. At slightly smaller opacities $0.05 \lesssim 4\pi\eta/s \lesssim 1$, there is a small rise in inverse Reynolds number due to transverse expansion. However, this sets in later than in the case of the smallest opacities. The curves for intermediate to small opacities $1 \lesssim 4\pi\eta/s \lesssim 100$ exhibit a bumpy behaviour during transverse expansion.

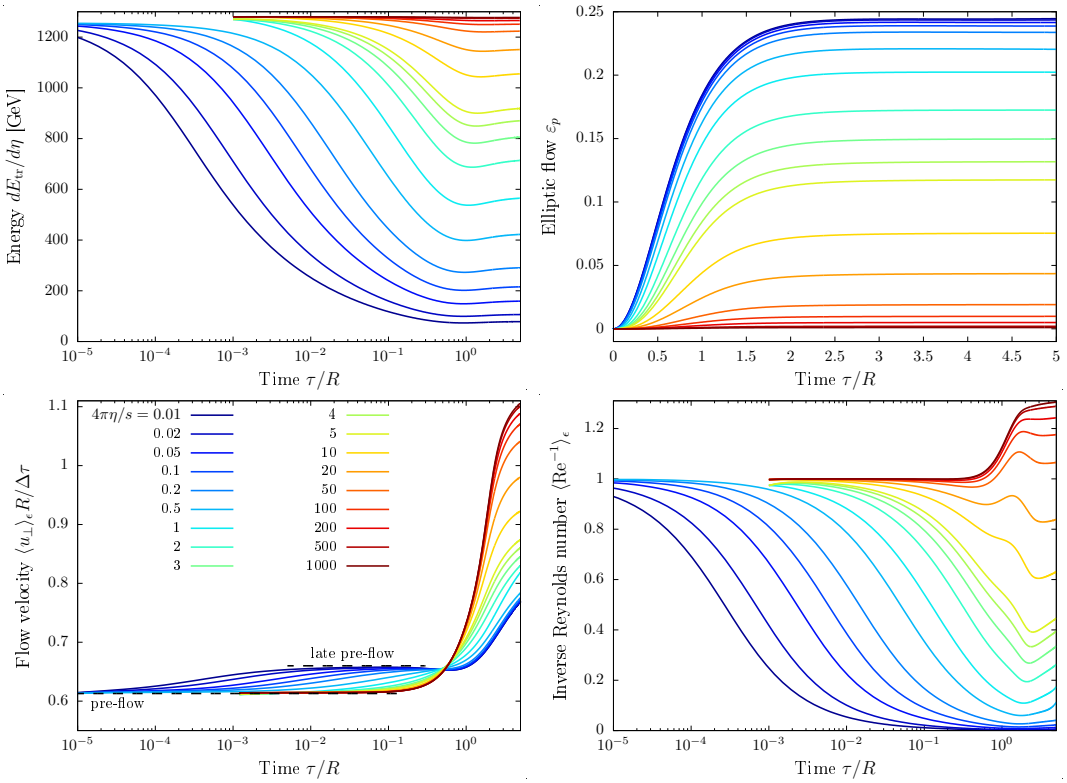

FIGURE G.1: Time evolution of transverse energy $\frac{dE_{\rm tr}}{d\eta}$ (top left, cf. Eq. 3.43), elliptic flow ε_p (top right, cf. Eq. 3.44), transverse flow velocity $\langle u_\perp \rangle_\epsilon$ (bottom left, cf. Eq. 3.53) and inverse Reynolds number $\langle {\rm Re}^{-1} \rangle_\epsilon$ (bottom right, cf. Eq. 3.52) in kinetic theory for a wide range of opacities (η/s) plotted in different colors. The plot of transverse flow velocity $\langle u_\perp \rangle_\epsilon$ also shows the pre-flow result $\langle u_\perp \rangle_{\epsilon,\rm early} = 0.61\Delta\tau/R$ according to Eq. 4.50 and the late pre-flow result $\langle u_\perp \rangle_{\epsilon,\rm late} = 0.66\Delta\tau/R$ according to Eq. 4.52.

Appendix H

Time evolution in KøMPøST + viscous hydro simulations

In Section 6.4.3 we named hybrid simulation frameworks as a solution for alleviating problems with pre-equilibrium in hydrodynamic simulations and discussed the time evolution mainly in hybrid kinetic theory + viscous hydro simulations. The alternative hybrid framework using KøMPøST instead of full kinetic theory for the pre-equilibrium evolution has some limitations, but when applicable, yields results of similar accuracy. The time evolution of transverse energy $dE_{\mathrm{tr}}/d\eta$, elliptic flow ϵ_p and transverse flow velocity $\langle u_\perp \rangle_\epsilon$ in KøMPøST + viscous hydro simulations switching at fixed time τ_s or fixed value of the inverse Reynolds number $\left\langle \mathrm{Re}^{-1} \right\rangle_\epsilon$ is shown in Fig. H.1 for three different opacities $4\pi\eta/s = 0.5$, 3 and 10.

The values of $dE_{\mathrm{tr}}/d\eta$ at the time of switching are reproduced by KøMPøST almost perfectly. As one would expect, the time evolution afterwards follows a very similar behaviour to kinetic theory + viscous hydrodynamics, including the inaccuracies of hydrodynamic pre-equilibrium when switching too early.

As KøMPøST produces almost no elliptic flow, its value at switching time is close to zero. But the buildup during the hydro part of the simulation proceeds similarly to other simulation schemes, such that the discrepancy to kinetic theory in the final state ($\tau = 4R$) is of similar size to the one at switching time. It is therefore larger at larger switching times.

The values of transverse flow velocity $\langle u_\perp \rangle_\epsilon$ are in KøMPøST slightly underestimated for small switching times and slightly overestimated for large switching times. After switching, the curves seem to bend towards the hydrodynamic curve. This bending is mainly due to the division by $\Delta\tau$. $\langle u_\perp \rangle_\epsilon$ in the hydro phase of hybrid simulations builds up similarly than in pure hydrodynamic simulations. The contributions from later times are much larger than those at early times, such that the discrepancy from early times becomes negligible. At late times, results from all switchting times underestimate $\langle u_\perp \rangle_\epsilon$ by almost the same amount, similarly to hybrid kinetic theory + viscous hydro simulations.

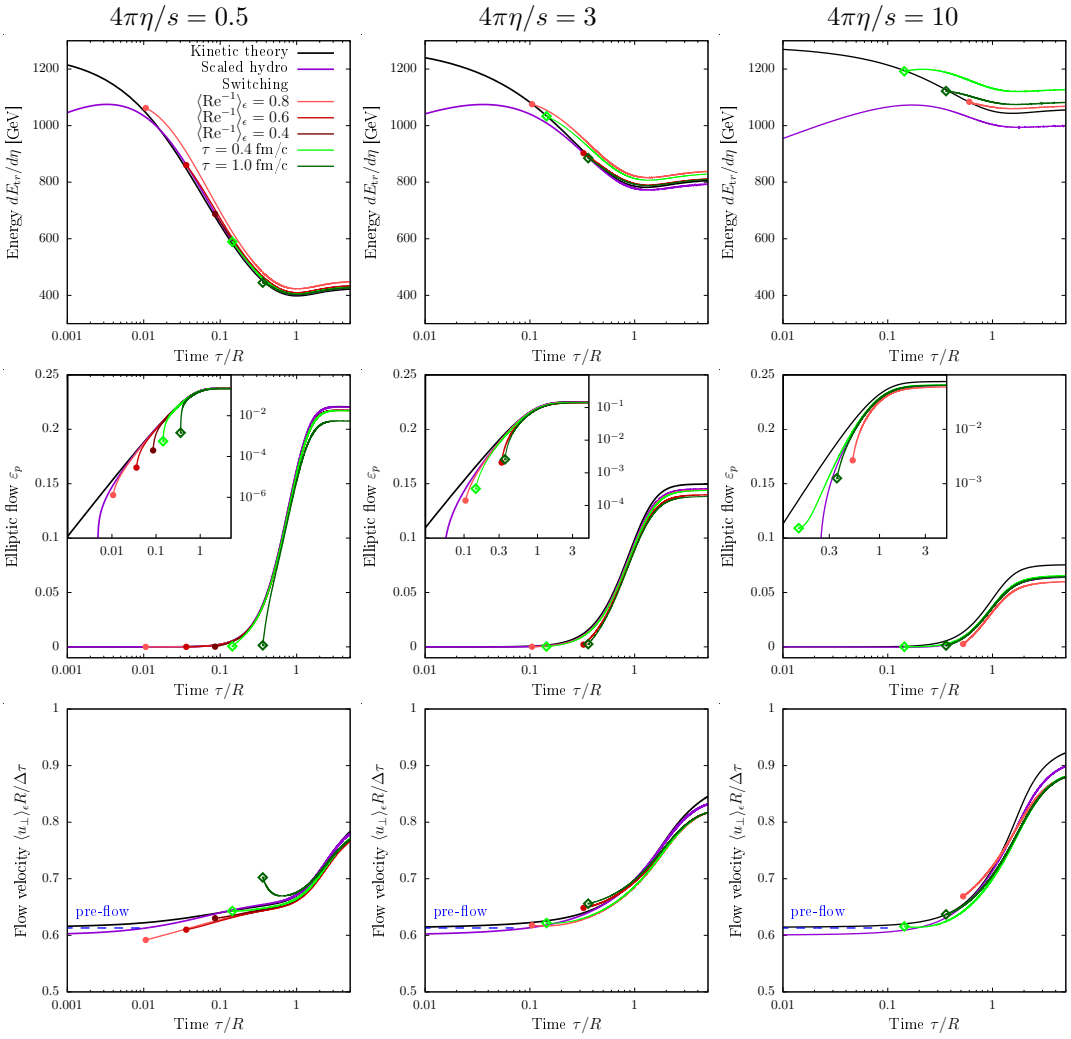

FIGURE H.1: Time evolution of transverse energy $dE_{\mathrm{tr}}/d\eta$ (top, cf. Eq. 3.43), elliptic flow ε_p (middle, cf. Eq. 3.44) and transverse flow velocity $\langle u_\perp\rangle_\epsilon$ (bottom, cf. Eq. 3.53) in hybrid KøMPøST + viscous hydro simulations at opacities $4\pi\eta/s = 0.5$ (left), 3 (middle) and 10 (right) when switching at different values of the inverse Reynolds number (c.f. Eq. 3.52) $\left\langle \mathrm{Re}^{-1}\right\rangle_\epsilon = 0.8$ (light red), 0.6 (red) and 0.4 (dark red) or fixed time $\tau = 0.4\,\mathrm{fm}$ (light green) and $\tau = 1\,\mathrm{fm}$ (dark-green). The switching points are marked with filled symbols. The time axis is scaled logarithmically. The plots showing elliptic flow ϵ_p feature an inset plot of the same quantity plotted in log-log scale. Again, the flow velocity plots also show the pre-flow result $\langle u_\perp\rangle_\epsilon = 0.61\Delta\tau/R$ according to Eq. 4.50.

Bibliography

[1] V. E. Ambrus, S. Schlichting, and C. Werthmann, "Development of transverse flow at small and large opacities in conformal kinetic theory," *Phys. Rev. D*, vol. 105, no. 1, p. 014 031, 2022. DOI: 10.1103/PhysRevD.105.014031. arXiv: 2109.03290 [hep-ph].

[2] J. H. Putschke *et al.*, "The JETSCAPE framework," Mar. 2019. arXiv: 1903.07706 [nucl-th].

[3] D. Everett *et al.*, "Multisystem Bayesian constraints on the transport coefficients of QCD matter," *Phys. Rev. C*, vol. 103, no. 5, p. 054 904, 2021. DOI: 10.1103/PhysRevC.103.054904. arXiv: 2011.01430 [hep-ph].

[4] G. Nijs, W. van der Schee, U. Gürsoy, and R. Snellings, "Bayesian analysis of heavy ion collisions with the heavy ion computational framework Trajectum," *Phys. Rev. C*, vol. 103, no. 5, p. 054 909, 2021. DOI: 10.1103/PhysRevC.103.054909. arXiv: 2010.15134 [nucl-th].

[5] F. G. Gardim, G. Giacalone, M. Luzum, and J.-Y. Ollitrault, "Thermodynamics of hot strong-interaction matter from ultrarelativistic nuclear collisions," *Nature Phys.*, vol. 16, no. 6, pp. 615–619, 2020. DOI: 10.1038/s41567-020-0846-4. arXiv: 1908.09728 [nucl-th].

[6] B. Schenke, C. Shen, and P. Tribedy, "Running the gamut of high energy nuclear collisions," *Phys. Rev. C*, vol. 102, no. 4, p. 044 905, 2020. DOI: 10.1103/PhysRevC.102.044905. arXiv: 2005.14682 [nucl-th].

[7] D. A. Teaney, *Viscous Hydrodynamics and the Quark Gluon Plasma*, R. C. Hwa and X.-N. Wang, Eds., 2010. DOI: 10.1142/9789814293297_0004. arXiv: 0905.2433 [nucl-th].

[8] H. Song, S. A. Bass, U. Heinz, T. Hirano, and C. Shen, "200 A GeV Au+Au collisions serve a nearly perfect quark-gluon liquid," *Phys. Rev. Lett.*, vol. 106, p. 192 301, 2011. DOI: 10.1103/PhysRevLett.106.192301.

[9] C. Gale, S. Jeon, and B. Schenke, "Hydrodynamic Modeling of Heavy-Ion Collisions," *Int. J. Mod. Phys. A*, vol. 28, p. 1 340 011, 2013. DOI: 10.1142/S0217751X13400113. arXiv: 1301.5893 [nucl-th].

[10] U. Heinz and R. Snellings, "Collective flow and viscosity in relativistic heavy-ion collisions," *Ann. Rev. Nucl. Part. Sci.*, vol. 63, pp. 123–151, 2013. DOI: 10.1146/annurev-nucl-102212-170540. arXiv: 1301.2826 [nucl-th].

[11] M. Luzum and H. Petersen, "Initial State Fluctuations and Final State Correlations in Relativistic Heavy-Ion Collisions," *J. Phys. G*, vol. 41, p. 063 102, 2014. DOI: 10.1088/0954-3899/41/6/063102. arXiv: 1312.5503 [nucl-th].

[12] S. Jeon and U. Heinz, "Introduction to Hydrodynamics," *Int. J. Mod. Phys. E*, vol. 24, no. 10, p. 1 530 010, 2015. DOI: 10.1142/S0218301315300106. arXiv: 1503.03931 [hep-ph].

[13] A. Kurkela and Y. Zhu, "Isotropization and hydrodynamization in weakly coupled heavy-ion collisions," *Phys. Rev. Lett.*, vol. 115, no. 18, p. 182 301, 2015. DOI: 10.1103/PhysRevLett.115.182301. arXiv: 1506.06647 [hep-ph].

[14] M. P. Heller and V. Svensson, "How does relativistic kinetic theory remember about initial conditions?" *Phys. Rev. D*, vol. 98, no. 5, p. 054 016, 2018. DOI: 10.1103/PhysRevD.98.054016. arXiv: 1802.08225 [nucl-th].

[15] A. Kurkela, S. F. Taghavi, U. A. Wiedemann, and B. Wu, "Hydrodynamization in systems with detailed transverse profiles," *Phys. Lett. B*, vol. 811, p. 135 901, 2020. DOI: 10.1016/j.physletb.2020.135901. arXiv: 2007.06851 [hep-ph].

[16] S. Schlichting and D. Teaney, "The First fm/c of Heavy-Ion Collisions," *Ann. Rev. Nucl. Part. Sci.*, vol. 69, pp. 447–476, 2019. DOI: 10.1146/annurev-nucl-101918-023825. arXiv: 1908.02113 [nucl-th].

[17] J. Berges, M. P. Heller, A. Mazeliauskas, and R. Venugopalan, "QCD thermalization: Ab initio approaches and interdisciplinary connections," *Rev. Mod. Phys.*, vol. 93, no. 3, p. 035 003, 2021. DOI: 10.1103/RevModPhys.93.035003. arXiv: 2005.12299 [hep-th].

[18] J. Berges, K. Boguslavski, S. Schlichting, and R. Venugopalan, "Universal attractor in a highly occupied non-Abelian plasma," *Phys. Rev. D*, vol. 89, no. 11, p. 114 007, 2014. DOI: 10.1103/PhysRevD.89.114007. arXiv: 1311.3005 [hep-ph].

[19] J. Berges, K. Boguslavski, S. Schlichting, and R. Venugopalan, "Basin of attraction for turbulent thermalization and the range of validity of classical-statistical simulations," *JHEP*, vol. 05, p. 054, 2014. DOI: 10.1007/JHEP05(2014)054. arXiv: 1312.5216 [hep-ph].

[20] M. P. Heller and M. Spalinski, "Hydrodynamics Beyond the Gradient Expansion: Resurgence and Resummation," *Phys. Rev. Lett.*, vol. 115, no. 7, p. 072 501, 2015. DOI: 10.1103/PhysRevLett.115.072501. arXiv: 1503.07514 [hep-th].

[21] M. Spaliński, "On the hydrodynamic attractor of Yang–Mills plasma," *Phys. Lett. B*, vol. 776, pp. 468–472, 2018. DOI: 10.1016/j.physletb.2017.11.059. arXiv: 1708.01921 [hep-th].

[22] M. Strickland, J. Noronha, and G. Denicol, "Anisotropic nonequilibrium hydrodynamic attractor," *Phys. Rev. D*, vol. 97, no. 3, p. 036 020, 2018. DOI: 10.1103/PhysRevD.97.036020. arXiv: 1709.06644 [nucl-th].

[23] M. Strickland, "The non-equilibrium attractor for kinetic theory in relaxation time approximation," *JHEP*, vol. 12, p. 128, 2018. DOI: 10.1007/JHEP12(2018)128. arXiv: 1809.01200 [nucl-th].

[24] M. Spaliński, "Universal behaviour, transients and attractors in supersymmetric Yang–Mills plasma," *Phys. Lett. B*, vol. 784, pp. 21–25, 2018. DOI: 10.1016/j.physletb.2018.07.003. arXiv: 1805.11689 [hep-th].

[25] G. Giacalone, A. Mazeliauskas, and S. Schlichting, "Hydrodynamic attractors, initial state energy and particle production in relativistic nuclear collisions," *Phys. Rev. Lett.*, vol. 123, no. 26, p. 262 301, 2019. DOI: 10.1103/PhysRevLett.123.262301. arXiv: 1908.02866 [hep-ph].

[26] A. Kurkela, W. van der Schee, U. A. Wiedemann, and B. Wu, "Early- and Late-Time Behavior of Attractors in Heavy-Ion Collisions," *Phys. Rev. Lett.*, vol. 124, no. 10, p. 102 301, 2020. DOI: 10.1103/PhysRevLett.124.102301. arXiv: 1907.08101 [hep-ph].

[27] G. S. Denicol and J. Noronha, "Exact hydrodynamic attractor of an ultrarelativistic gas of hard spheres," *Phys. Rev. Lett.*, vol. 124, no. 15, p. 152 301, 2020. DOI: 10.1103/PhysRevLett.124.152301. arXiv: 1908.09957 [nucl-th].

[28] D. Almaalol, A. Kurkela, and M. Strickland, "Nonequilibrium Attractor in High-Temperature QCD Plasmas," *Phys. Rev. Lett.*, vol. 125, no. 12, p. 122 302, 2020. DOI: 10.1103/PhysRevLett.125.122302. arXiv: 2004.05195 [hep-ph].

[29] M. P. Heller, R. Jefferson, M. Spaliński, and V. Svensson, "Hydrodynamic Attractors in Phase Space," *Phys. Rev. Lett.*, vol. 125, no. 13, p. 132 301, 2020. DOI: 10.1103/PhysRevLett.125.132301. arXiv: 2003.07368 [hep-th].

[30] X. Du and S. Schlichting, "Equilibration of the Quark-Gluon Plasma at Finite Net-Baryon Density in QCD Kinetic Theory," *Phys. Rev. Lett.*, vol. 127, no. 12, p. 122 301, 2021. DOI: 10.1103/PhysRevLett.127.122301. arXiv: 2012.09068 [hep-ph].

[31] J.-P. Blaizot and L. Yan, "Attractor and fixed points in Bjorken flows," *Phys. Rev. C*, vol. 104, no. 5, p. 055 201, 2021. DOI: 10.1103/PhysRevC.104.055201. arXiv: 2106.10508 [nucl-th].

[32] C. Chattopadhyay, S. Jaiswal, L. Du, U. Heinz, and S. Pal, "Non-conformal attractor in boost-invariant plasmas," *Phys. Lett. B*, vol. 824, p. 136 820, 2022. DOI: 10.1016/j.physletb.2021.136820. arXiv: 2107.05500 [nucl-th].

[33] X. Du, M. P. Heller, S. Schlichting, and V. Svensson, "Exponential approach to the hydrodynamic attractor in Yang-Mills kinetic theory," *Phys. Rev. D*, vol. 106, no. 1, p. 014 016, 2022. DOI: 10.1103/PhysRevD.106.014016. arXiv: 2203.16549 [hep-ph].

[34] B. B. Abelev *et al.*, "Multiparticle azimuthal correlations in p -Pb and Pb-Pb collisions at the CERN Large Hadron Collider," *Phys. Rev. C*, vol. 90, no. 5, p. 054 901, 2014. DOI: 10.1103/PhysRevC.90.054901. arXiv: 1406.2474 [nucl-ex].

[35] M. Aaboud *et al.*, "Measurement of multi-particle azimuthal correlations in *pp*, *p*+Pb and low-multiplicity Pb+Pb collisions with the ATLAS detector," *Eur. Phys. J. C*, vol. 77, no. 6, p. 428, 2017. DOI: 10.1140/epjc/s10052-017-4988-1. arXiv: 1705.04176 [hep-ex].

[36] A. M. Sirunyan *et al.*, "Observation of Correlated Azimuthal Anisotropy Fourier Harmonics in *pp* and $p+Pb$ Collisions at the LHC," *Phys. Rev. Lett.*, vol. 120, no. 9, p. 092 301, 2018. DOI: 10.1103/PhysRevLett.120.092301. arXiv: 1709.09189 [nucl-ex].

[37] K. Dusling, W. Li, and B. Schenke, "Novel collective phenomena in high-energy proton–proton and proton–nucleus collisions," *Int. J. Mod. Phys. E*, vol. 25, no. 01, p. 1 630 002, 2016. DOI: 10.1142/S0218301316300022. arXiv: 1509.07939 [nucl-ex].

[38] C. Loizides, "Experimental overview on small collision systems at the LHC," *Nucl. Phys. A*, vol. 956, Y. Akiba *et al.*, Eds., pp. 200–207, 2016. DOI: 10.1016/j.nuclphysa.2016.04.022. arXiv: 1602.09138 [nucl-ex].

[39] J. L. Nagle and W. A. Zajc, "Small System Collectivity in Relativistic Hadronic and Nuclear Collisions," *Ann. Rev. Nucl. Part. Sci.*, vol. 68, pp. 211–235, 2018. DOI: 10.1146/annurev-nucl-101916-123209. arXiv: 1801.03477 [nucl-ex].

[40] M. Bahr *et al.*, "Herwig++ Physics and Manual," *Eur. Phys. J. C*, vol. 58, pp. 639–707, 2008. DOI: 10.1140/epjc/s10052-008-0798-9. arXiv: 0803.0883 [hep-ph].

[41] T. Sjöstrand *et al.*, "An introduction to PYTHIA 8.2," *Comput. Phys. Commun.*, vol. 191, pp. 159–177, 2015. DOI: 10.1016/j.cpc.2015.01.024. arXiv: 1410.3012 [hep-ph].

[42] U. A. Wiedemann, "HIP and HEP," Jan. 2021. arXiv: 2101.01971 [hep-ph].

[43] P. Bozek, "Collective flow in p-Pb and d-Pd collisions at TeV energies," *Phys. Rev. C*, vol. 85, p. 014 911, 2012. DOI: 10.1103/PhysRevC.85.014911. arXiv: 1112.0915 [hep-ph].

[44] P. Bozek and W. Broniowski, "Correlations from hydrodynamic flow in p-Pb collisions," *Phys. Lett. B*, vol. 718, pp. 1557–1561, 2013. DOI: 10.1016/j.physletb.2012.12.051. arXiv: 1211.0845 [nucl-th].

[45] P. Bozek and W. Broniowski, "Size of the emission source and collectivity in ultra-relativistic p-Pb collisions," *Phys. Lett. B*, vol. 720, pp. 250–253, 2013. DOI: 10.1016/j.physletb.2013.02.014. arXiv: 1301.3314 [nucl-th].

[46] P. Bozek and W. Broniowski, "Collective dynamics in high-energy proton-nucleus collisions," *Phys. Rev. C*, vol. 88, no. 1, p. 014 903, 2013. DOI: 10.1103/PhysRevC.88.014903. arXiv: 1304.3044 [nucl-th].

[47] P. Bozek, W. Broniowski, and G. Torrieri, "Mass hierarchy in identified particle distributions in proton-lead collisions," *Phys. Rev. Lett.*, vol. 111, p. 172 303, 2013. DOI: 10.1103/PhysRevLett.111.172303. arXiv: 1307.5060 [nucl-th].

[48] A. Bzdak, B. Schenke, P. Tribedy, and R. Venugopalan, "Initial state geometry and the role of hydrodynamics in proton-proton, proton-nucleus and deuteron-nucleus collisions," *Phys. Rev. C*, vol. 87, no. 6, p. 064 906, 2013. DOI: 10.1103/PhysRevC.87.064906. arXiv: 1304.3403 [nucl-th].

[49] G.-Y. Qin and B. Müller, "Elliptic and triangular flow anisotropy in deuteron-gold collisions at $\sqrt{s_{NN}} = 200$ GeV at RHIC and in proton-lead collisions at $\sqrt{s_{NN}} = 5.02$ TeV at the LHC," *Phys. Rev. C*, vol. 89, no. 4, p. 044 902, 2014. DOI: 10.1103/PhysRevC.89.044902. arXiv: 1306.3439 [nucl-th].

[50] K. Werner, M. Bleicher, B. Guiot, I. Karpenko, and T. Pierog, "Evidence for Flow from Hydrodynamic Simulations of p-Pb Collisions at 5.02 TeV from ν_2 Mass Splitting," *Phys. Rev. Lett.*, vol. 112, no. 23, p. 232 301, 2014. DOI: 10.1103/PhysRevLett.112.232301. arXiv: 1307.4379 [nucl-th].

[51] A. Ortiz Velasquez, P. Christiansen, E. Cuautle Flores, I. Maldonado Cervantes, and G. Paić, "Color Reconnection and Flowlike Patterns in pp Collisions," *Phys. Rev. Lett.*, vol. 111, no. 4, p. 042 001, 2013. DOI: 10.1103/PhysRevLett.111.042001. arXiv: 1303.6326 [hep-ph].

[52] I. Kozlov, M. Luzum, G. Denicol, S. Jeon, and C. Gale, "Transverse momentum structure of pair correlations as a signature of collective behavior in small collision systems," May 2014. arXiv: 1405.3976 [nucl-th].

[53] B. Schenke and R. Venugopalan, "Eccentric protons? Sensitivity of flow to system size and shape in p+p, p+Pb and Pb+Pb collisions," *Phys. Rev. Lett.*, vol. 113, p. 102 301, 2014. DOI: 10.1103/PhysRevLett.113.102301. arXiv: 1405.3605 [nucl-th].

[54] P. Romatschke, "Light-Heavy Ion Collisions: A window into pre-equilibrium QCD dynamics?" *Eur. Phys. J. C*, vol. 75, no. 7, p. 305, 2015. DOI: 10.1140/epjc/s10052-015-3509-3. arXiv: 1502.04745 [nucl-th].

[55] C. Shen, J.-F. Paquet, G. S. Denicol, S. Jeon, and C. Gale, "Collectivity and electromagnetic radiation in small systems," *Phys. Rev. C*, vol. 95, no. 1, p. 014 906, 2017. DOI: 10.1103/PhysRevC.95.014906. arXiv: 1609.02590 [nucl-th].

[56] R. D. Weller and P. Romatschke, "One fluid to rule them all: viscous hydrodynamic description of event-by-event central p+p, p+Pb and Pb+Pb collisions at $\sqrt{s} = 5.02$ TeV," *Phys. Lett. B*, vol. 774, pp. 351–356, 2017. DOI: 10.1016/j.physletb.2017.09.077. arXiv: 1701.07145 [nucl-th].

[57] H. Mäntysaari, B. Schenke, C. Shen, and P. Tribedy, "Imprints of fluctuating proton shapes on flow in proton-lead collisions at the LHC," *Phys. Lett. B*, vol. 772, pp. 681–686, 2017. DOI: 10.1016/j.physletb.2017.07.038. arXiv: 1705.03177 [nucl-th].

[58] B. Schenke, C. Shen, and P. Tribedy, "Hybrid Color Glass Condensate and hydrodynamic description of the Relativistic Heavy Ion Collider small system scan," *Phys. Lett. B*, vol. 803, p. 135 322, 2020. DOI: 10.1016/j.physletb.2020.135322. arXiv: 1908.06212 [nucl-th].

[59] B. Schenke, "The smallest fluid on earth," Feb. 2021. arXiv: 2102.11189 [nucl-th].

[60] S. Demirci, T. Lappi, and S. Schlichting, "Hot spots and gluon field fluctuations as causes of eccentricity in small systems," *Phys. Rev. D*, vol. 103, no. 9, p. 094 025, 2021. DOI: 10.1103/PhysRevD.103.094025. arXiv: 2101.03791 [hep-ph].

[61] B. Schenke, S. Schlichting, and R. Venugopalan, "Azimuthal anisotropies in p+Pb collisions from classical Yang–Mills dynamics," *Phys. Lett. B*, vol. 747, pp. 76–82, 2015. DOI: 10.1016/j.physletb.2015.05.051. arXiv: 1502.01331 [hep-ph].

[62] L. McLerran and V. Skokov, "Finite Numbers of Sources, Particle Correlations and the Color Glass Condensate," *Nucl. Phys. A*, vol. 947, pp. 142–154, 2016. DOI: 10.1016/j.nuclphysa.2015.12.005. arXiv: 1510.08072 [hep-ph].

[63] B. Schenke, S. Schlichting, P. Tribedy, and R. Venugopalan, "Mass ordering of spectra from fragmentation of saturated gluon states in high multiplicity proton-proton collisions," *Phys. Rev. Lett.*, vol. 117, no. 16, p. 162 301, 2016. DOI: 10.1103/PhysRevLett.117.162301. arXiv: 1607.02496 [hep-ph].

[64] K. Dusling, M. Mace, and R. Venugopalan, "Multiparticle collectivity from initial state correlations in high energy proton-nucleus collisions," *Phys. Rev. Lett.*, vol. 120, no. 4, p. 042 002, 2018. DOI: 10.1103/PhysRevLett.120.042002. arXiv: 1705.00745 [hep-ph].

[65] K. Dusling, M. Mace, and R. Venugopalan, "Parton model description of multiparticle azimuthal correlations in pA collisions," *Phys. Rev. D*, vol. 97, no. 1, p. 016 014, 2018. DOI: 10.1103/PhysRevD.97.016014. arXiv: 1706.06260 [hep-ph].

[66] M. Greif, C. Greiner, B. Schenke, S. Schlichting, and Z. Xu, "Importance of initial and final state effects for azimuthal correlations in p+Pb collisions," *Phys. Rev. D*, vol. 96, no. 9, p. 091 504, 2017. DOI: 10.1103/PhysRevD.96.091504. arXiv: 1708.02076 [hep-ph].

[67] M. Mace, V. V. Skokov, P. Tribedy, and R. Venugopalan, "Hierarchy of Azimuthal Anisotropy Harmonics in Collisions of Small Systems from the Color Glass Condensate," *Phys. Rev. Lett.*, vol. 121, no. 5, p. 052 301, 2018, [Erratum: Phys.Rev.Lett. 123, 039901 (2019)]. DOI: 10.1103/PhysRevLett.121.052301. arXiv: 1805.09342 [hep-ph].

[68] M. Mace, V. V. Skokov, P. Tribedy, and R. Venugopalan, "Systematics of azimuthal anisotropy harmonics in proton–nucleus collisions at the LHC from the Color Glass Condensate," *Phys. Lett. B*, vol. 788, pp. 161–165, 2019, [Erratum: Phys.Lett.B 799, 135006 (2019)]. DOI: 10.1016/j.physletb.2018.09.064. arXiv: 1807.00825 [hep-ph].

[69] A. Kovner and V. V. Skokov, "Does shape matter? v_2 vs eccentricity in small x gluon production," *Phys. Lett. B*, vol. 785, pp. 372–380, 2018. DOI: 10.1016/j.physletb.2018.09.001. arXiv: 1805.09297 [hep-ph].

[70] M. Greif, C. Greiner, S. Plätzer, B. Schenke, and S. Schlichting, "Hadronization of correlated gluon fields," *Phys. Rev. D*, vol. 103, no. 5, p. 054 011, 2021. DOI: 10.1103/PhysRevD.103.054011. arXiv: 2012.08493 [hep-ph].

[71] P. Agostini, T. Altinoluk, and N. Armesto, "Multi-particle production in proton–nucleus collisions in the color glass condensate," *Eur. Phys. J. C*, vol. 81, no. 8, p. 760, 2021. DOI: 10.1140/epjc/s10052-021-09475-0. arXiv: 2103.08485 [hep-ph].

[72] M. E. Carrington, A. Czajka, and S. Mrowczynski, "Physical characteristics of glasma from the earliest stage of relativistic heavy ion collisions," May 2021. arXiv: 2105.05327 [hep-ph].

[73] B. Schenke, S. Schlichting, and P. Singh, "Rapidity dependence of initial state geometry and momentum correlations in p+Pb collisions," *Phys. Rev. D*, vol. 105, no. 9, p. 094 023, 2022. DOI: 10.1103/PhysRevD.105.094023. arXiv: 2201.08864 [nucl-th].

[74] H. Heiselberg and A.-M. Levy, "Elliptic flow and HBT in noncentral nuclear collisions," *Phys. Rev. C*, vol. 59, pp. 2716–2727, 1999. DOI: 10.1103/PhysRevC.59.2716. arXiv: nucl-th/9812034.

[75] N. Borghini and C. Gombeaud, "Anisotropic flow far from equilibrium," *Eur. Phys. J. C*, vol. 71, p. 1612, 2011. DOI: 10.1140/epjc/s10052-011-1612-7. arXiv: 1012.0899 [nucl-th].

[76] P. Romatschke, "Azimuthal Anisotropies at High Momentum from Purely Non-Hydrodynamic Transport," *Eur. Phys. J. C*, vol. 78, no. 8, p. 636, 2018. DOI: 10.1140/epjc/s10052-018-6112-6. arXiv: 1802.06804 [nucl-th].

[77] N. Kersting, N. Borghini, and S. Feld, "Anisotropic flow in the few collisions regime: application to bottomonia," *MDPI Proc.*, vol. 10, no. 1, J. Albacete *et al.*, Eds., p. 16, 2019. DOI: 10.3390/proceedings2019010016. arXiv: 1811.06195 [nucl-th].

[78] A. Kurkela, U. A. Wiedemann, and B. Wu, "Nearly isentropic flow at sizeable η/s," *Phys. Lett. B*, vol. 783, pp. 274–279, 2018. DOI: 10.1016/j.physletb.2018.06.064. arXiv: 1803.02072 [hep-ph].

[79] N. Borghini, S. Feld, and N. Kersting, "Scaling behavior of anisotropic flow harmonics in the far from equilibrium regime," *Eur. Phys. J. C*, vol. 78, no. 10, p. 832, 2018. DOI: 10.1140/epjc/s10052-018-6313-z. arXiv: 1804.05729 [nucl-th].

[80] A. Kurkela, U. A. Wiedemann, and B. Wu, "Flow in AA and pA as an interplay of fluid-like and non-fluid like excitations," *Eur. Phys. J. C*, vol. 79, no. 11, p. 965, 2019. DOI: 10.1140/epjc/s10052-019-7428-6. arXiv: 1905.05139 [hep-ph].

[81] A. Kurkela, A. Mazeliauskas, and R. Törnkvist, "Collective flow in single-hit QCD kinetic theory," Apr. 2021. arXiv: 2104.08179 [hep-ph].

[82] N. Borghini, M. Borrell, and H. Roch, "Early time behavior of spatial and momentum anisotropies in kinetic theory across different Knudsen numbers," Jan. 2022. arXiv: 2201.13294 [nucl-th].

[83] M. Borrell and N. Borghini, "Early time behavior of spatial and momentum anisotropies in a kinetic approach to nuclear collisions," *Eur. Phys. J. C*, vol. 82, no. 6, p. 525, 2022. DOI: 10.1140/epjc/s10052-022-10492-w. arXiv: 2109.15218 [nucl-th].

[84] B. Bachmann, N. Borghini, N. Feld, and H. Roch, "Even anisotropic-flow harmonics are from Venus, odd ones are from Mars," Mar. 2022. arXiv: 2203.13306 [nucl-th].

[85] L. He, T. Edmonds, Z.-W. Lin, F. Liu, D. Molnar, and F. Wang, "Anisotropic parton escape is the dominant source of azimuthal anisotropy in transport models," *Phys. Lett. B*, vol. 753, pp. 506–510, 2016. DOI: 10.1016/j.physletb.2015.12.051. arXiv: 1502.05572 [nucl-th].

[86] H. Roch and N. Borghini, "Fluctuations of anisotropic flow from the finite number of rescatterings in a two-dimensional massless transport model," *Eur. Phys. J. C*, vol. 81, no. 5, p. 380, 2021. DOI: 10.1140/epjc/s10052-021-09147-z. arXiv: 2012.02138 [nucl-th].

[87] C. M. Ko, Q. Li, and R.-C. Wang, "Relativistic Vlasov Equation for Heavy Ion Collisions," *Phys. Rev. Lett.*, vol. 59, pp. 1084–1087, 1987. DOI: 10.1103/PhysRevLett.59.1084.

[88] B. Blattel, V. Koch, W. Cassing, and U. Mosel, "Covariant Boltzmann-Uehling-Uhlenbeck approach for heavy-ion collisions," *Phys. Rev. C*, vol. 38, pp. 1767–1775, 1988. DOI: 10.1103/PhysRevC.38.1767.

[89] V. A. Abramovsky, E. V. Gedalin, E. G. Gurvich, and O. V. Kancheli, "Long Range Azimuthal Correlations in Multiple Production Processes at High-energies," *JETP Lett.*, vol. 47, pp. 337–339, 1988.

[90] Q. Li, J. Q. Wu, and C. M. Ko, "Relativistic Vlasov-Uehling-Uhlenbeck equation for nucleus-nucleus collisions," *Phys. Rev. C*, vol. 39, pp. 849–852, 1989. DOI: 10.1103/PhysRevC.39.849.

[91] W. Botermans and R. Malfliet, "Quantum transport theory of nuclear matter," *Phys. Rept.*, vol. 198, pp. 115–194, 1990. DOI: 10.1016/0370-1573(90)90174-Z.

[92] S. A. Bass *et al.*, "Microscopic models for ultrarelativistic heavy ion collisions," *Prog. Part. Nucl. Phys.*, vol. 41, pp. 255–369, 1998. DOI: 10.1016/S0146-6410(98)00058-1. arXiv: nucl-th/9803035.

[93] Z. Xu and C. Greiner, "Thermalization of gluons in ultrarelativistic heavy ion collisions by including three-body interactions in a parton cascade," *Phys. Rev. C*, vol. 71, p. 064 901, 2005. DOI: 10.1103/PhysRevC.71.064901. arXiv: hep-ph/0406278.

[94] Z. Xu, C. Greiner, and H. Stocker, "PQCD calculations of elliptic flow and shear viscosity at RHIC," *Phys. Rev. Lett.*, vol. 101, p. 082 302, 2008. DOI: 10.1103/PhysRevLett.101.082302. arXiv: 0711.0961 [nucl-th].

[95] Z.-W. Lin, C. M. Ko, B.-A. Li, B. Zhang, and S. Pal, "A Multi-phase transport model for relativistic heavy ion collisions," *Phys. Rev. C*, vol. 72, p. 064 901, 2005. DOI: 10.1103/PhysRevC.72.064901. arXiv: nucl-th/0411110.

[96] W. Cassing and E. L. Bratkovskaya, "Parton-Hadron-String Dynamics: an off-shell transport approach for relativistic energies," *Nucl. Phys. A*, vol. 831, pp. 215–242, 2009. DOI: 10.1016/j.nuclphysa.2009.09.007. arXiv: 0907.5331 [nucl-th].

[97] J. Weil *et al.*, "Particle production and equilibrium properties within a new hadron transport approach for heavy-ion collisions," *Phys. Rev. C*, vol. 94, no. 5, p. 054 905, 2016. DOI: 10.1103/PhysRevC.94.054905. arXiv: 1606.06642 [nucl-th].

[98] E. Rutherford, "The scattering of alpha and beta particles by matter and the structure of the atom," *Phil. Mag. Ser. 6*, vol. 21, pp. 669–688, 1911. DOI: 10.1080/14786440508637080.

[99] J. D. Bjorken, "Asymptotic Sum Rules at Infinite Momentum," *Phys. Rev.*, vol. 179, pp. 1547–1553, 1969. DOI: 10.1103/PhysRev.179.1547.

[100] H. Abramowicz *et al.*, "Combination of measurements of inclusive deep inelastic $e^{\pm}p$ scattering cross sections and QCD analysis of HERA data," *Eur. Phys. J. C*, vol. 75, no. 12, p. 580, 2015. DOI: 10.1140/epjc/s10052-015-3710-4. arXiv: 1506.06042 [hep-ex].

[101] V. N. Gribov and L. N. Lipatov, "Deep inelastic e p scattering in perturbation theory," *Sov. J. Nucl. Phys.*, vol. 15, pp. 438–450, 1972.

[102] G. Altarelli and G. Parisi, "Asymptotic Freedom in Parton Language," *Nucl. Phys. B*, vol. 126, pp. 298–318, 1977. DOI: 10.1016/0550-3213(77)90384-4.

[103] Y. L. Dokshitzer, "Calculation of the Structure Functions for Deep Inelastic Scattering and e+ e- Annihilation by Perturbation Theory in Quantum Chromodynamics.," *Sov. Phys. JETP*, vol. 46, pp. 641–653, 1977.

[104] F. D. Aaron *et al.*, "Combined Measurement and QCD Analysis of the Inclusive e+- p Scattering Cross Sections at HERA," *JHEP*, vol. 01, p. 109, 2010. DOI: 10.1007/JHEP01(2010)109. arXiv: 0911.0884 [hep-ex].

[105] J. Adam *et al.*, "Centrality dependence of particle production in p-Pb collisions at $\sqrt{s_{\mathrm{NN}}}$= 5.02 TeV," *Phys. Rev. C*, vol. 91, no. 6, p. 064 905, 2015. DOI: 10.1103/PhysRevC.91.064905. arXiv: 1412.6828 [nucl-ex].

[106] B. W. Lee, *Chiral Dynamics*. Gordon and Breach Science Publishers, New York, 1972, ISBN: 9780677013800.

[107] M. Tanabashi *et al.*, "Review of Particle Physics," *Phys. Rev. D*, vol. 98, no. 3, p. 030 001, 2018. DOI: 10.1103/PhysRevD.98.030001.

[108] R. D. Pisarski and F. Wilczek, "Remarks on the Chiral Phase Transition in Chromodynamics," *Phys. Rev. D*, vol. 29, pp. 338–341, 1984. DOI: 10.1103/PhysRevD.29.338.

[109] N. Astrakhantsev, V. Braguta, and A. Kotov, "Temperature dependence of shear viscosity of $SU(3)$–gluodynamics within lattice simulation," *JHEP*, vol. 04, p. 101, 2017. DOI: 10.1007/JHEP04(2017)101. arXiv: 1701.02266 [hep-lat].

[110] N. Y. Astrakhantsev, V. V. Braguta, and A. Y. Kotov, "Temperature dependence of the bulk viscosity within lattice simulation of $SU(3)$ gluodynamics," *Phys. Rev. D*, vol. 98, no. 5, p. 054 515, 2018. DOI: 10.1103/PhysRevD.98.054515. arXiv: 1804.02382 [hep-lat].

[111] U. W. Heinz, "Towards the Little Bang Standard Model," *J. Phys. Conf. Ser.*, vol. 455, J. Cleymans, Ed., p. 012 044, 2013. DOI: 10.1088/1742-6596/455/1/012044. arXiv: 1304.3634 [nucl-th].

[112] J. Bartels, K. J. Golec-Biernat, and H. Kowalski, "A modification of the saturation model: DGLAP evolution," *Phys. Rev. D*, vol. 66, p. 014 001, 2002. DOI: 10.1103/PhysRevD.66.014001. arXiv: hep-ph/0203258.

[113] M. L. Miller, K. Reygers, S. J. Sanders, and P. Steinberg, "Glauber modeling in high energy nuclear collisions," *Ann. Rev. Nucl. Part. Sci.*, vol. 57, pp. 205–243, 2007. DOI: 10.1146/annurev.nucl.57.090506.123020. arXiv: nucl-ex/0701025.

[114] B. Schenke, P. Tribedy, and R. Venugopalan, "Fluctuating Glasma initial conditions and flow in heavy ion collisions," *Phys. Rev. Lett.*, vol. 108, p. 252 301, 2012. DOI: 10.1103/PhysRevLett.108.252301. arXiv: 1202.6646 [nucl-th].

[115] J. S. Moreland, J. E. Bernhard, and S. A. Bass, "Alternative ansatz to wounded nucleon and binary collision scaling in high-energy nuclear collisions," *Phys. Rev. C*, vol. 92, no. 1, p. 011 901, 2015. DOI: 10.1103/PhysRevC.92.011901. arXiv: 1412.4708 [nucl-th].

[116] C. Gale, J.-F. Paquet, B. Schenke, and C. Shen, "Multimessenger heavy-ion collision physics," *Phys. Rev. C*, vol. 105, no. 1, p. 014 909, 2022. DOI: 10.1103/PhysRevC.105.014909. arXiv: 2106.11216 [nucl-th].

[117] D. Liyanage, D. Everett, C. Chattopadhyay, and U. Heinz, "Pre-hydrodynamic evolution and its impact on quark-gluon plasma signatures," May 2022. arXiv: 2205.00964 [nucl-th].

[118] S. Chatrchyan *et al.*, "Multiplicity and Transverse Momentum Dependence of Two- and Four-Particle Correlations in pPb and PbPb Collisions," *Phys. Lett. B*, vol. 724, pp. 213–240, 2013. DOI: 10.1016/j.physletb.2013.06.028. arXiv: 1305.0609 [nucl-ex].

[119] S. Schlichting, "Event-by-event pre-equilibrium dynamics in high-energy heavy-ion collisions," Initial Stages 2019, 2019.

[120] V. Khachatryan *et al.*, "Evidence for collectivity in pp collisions at the LHC," *Phys. Lett. B*, vol. 765, pp. 193–220, 2017. DOI: 10.1016/j.physletb.2016.12.009. arXiv: 1606.06198 [nucl-ex].

[121] C. Cercignani and G. M. Kremer, *The relativistic Boltzmann equation: theory and applications*. Basel, Switzerland: Birkhäuser Verlag, 2002.

[122] W. Florkowski, *Phenomenology of Ultra-Relativistic Heavy-Ion Collisions*. World Scientific, 2010, ISBN: 978-981-4280-66-2.

[123] N. Pottier, *Nonequilibrium Statistical Physics*. Oxford University Press, 2010, ISBN: 9780198712275.

[124] G. S. Denicol and D. H. Rischke, *Microscopic Foundations of Relativistic Fluid Dynamics*. Springer Cham, 2021. DOI: 10.1007/978-3-030-82077-0.

[125] J. Anderson and H. Witting, "A relativistic relaxation-time model for the boltzmann equation," *Physica*, vol. 74, no. 3, pp. 466–488, 1974. DOI: 10.1016/0031-8914(74)90355-3.

[126] J. Anderson and H. Witting, "Relativistic quantum transport coefficients," *Physica*, vol. 74, no. 3, pp. 489–495, 1974. DOI: 10.1016/0031-8914(74)90356-5.

[127] G. S. Rocha, G. S. Denicol, and J. Noronha, "Novel Relaxation Time Approximation to the Relativistic Boltzmann Equation," *Phys. Rev. Lett.*, vol. 127, no. 4, p. 042 301, 2021. DOI: 10.1103/PhysRevLett.127.042301. arXiv: 2103.07489 [nucl-th].

[128] A. Bazavov *et al.*, "Equation of state in (2+1)-flavor QCD," *Phys. Rev. D*, vol. 90, p. 094 503, 2014. DOI: 10.1103/PhysRevD.90.094503. arXiv: 1407.6387 [hep-lat].

[129] S. Borsanyi *et al.*, "Calculation of the axion mass based on high-temperature lattice quantum chromodynamics," *Nature*, vol. 539, no. 7627, pp. 69–71, 2016. DOI: 10.1038/nature20115. arXiv: 1606.07494 [hep-lat].

[130] P. Kovtun, "First-order relativistic hydrodynamics is stable," *JHEP*, vol. 10, p. 034, 2019. DOI: 10.1007/JHEP10(2019)034. arXiv: 1907.08191 [hep-th].

[131] P. Romatschke, "Retarded correlators in kinetic theory: branch cuts, poles and hydrodynamic onset transitions," *Eur. Phys. J. C*, vol. 76, no. 6, p. 352, 2016. DOI: 10.1140/epjc/s10052-016-4169-7. arXiv: 1512.02641 [hep-th].

[132] A. Kurkela and U. A. Wiedemann, "Analytic structure of nonhydrodynamic modes in kinetic theory," *Eur. Phys. J. C*, vol. 79, no. 9, p. 776, 2019. DOI: 10.1140/epjc/s10052-019-7271-9. arXiv: 1712.04376 [hep-ph].

[133] F. S. Bemfica, F. S. Bemfica, M. M. Disconzi, M. M. Disconzi, J. Noronha, and J. Noronha, "Nonlinear Causality of General First-Order Relativistic Viscous Hydrodynamics," *Phys. Rev. D*, vol. 100, no. 10, p. 104 020, 2019, [Erratum: Phys.Rev.D 105, 069902 (2022)]. DOI: 10.1103/PhysRevD.100.104020. arXiv: 1907.12695 [gr-qc].

[134] I. Muller, "Zum Paradoxon der Warmeleitungstheorie," *Z. Phys.*, vol. 198, pp. 329–344, 1967. DOI: 10.1007/BF01326412.

[135] W. Israel, "Nonstationary irreversible thermodynamics: A Causal relativistic theory," *Annals Phys.*, vol. 100, pp. 310–331, 1976. DOI: 10.1016/0003-4916(76)90064-6.

[136] W. Israel and J. M. Stewart, "Transient relativistic thermodynamics and kinetic theory," *Annals Phys.*, vol. 118, pp. 341–372, 1979. DOI: 10.1016/0003-4916(79)90130-1.

[137] R. Baier, P. Romatschke, D. T. Son, A. O. Starinets, and M. A. Stephanov, "Relativistic viscous hydrodynamics, conformal invariance, and holography," *JHEP*, vol. 04, p. 100, 2008. DOI: 10.1088/1126-6708/2008/04/100. arXiv: 0712.2451 [hep-th].

[138] A. Jaiswal, "Relativistic dissipative hydrodynamics from kinetic theory with relaxation time approximation," *Phys. Rev. C*, vol. 87, no. 5, p. 051 901, 2013. DOI: 10.1103/PhysRevC.87.051901. arXiv: 1302.6311 [nucl-th].

[139] E. Molnár, H. Niemi, G. S. Denicol, and D. H. Rischke, "Relative importance of second-order terms in relativistic dissipative fluid dynamics," *Phys. Rev. D*, vol. 89, no. 7, p. 074 010, 2014. DOI: 10.1103/PhysRevD.89.074010. arXiv: 1308.0785 [nucl-th].

[140] V. E. Ambrus, E. Molnár, and D. H. Rischke, "Transport coefficients of second-order relativistic fluid dynamics in the relaxation-time approximation," Jul. 2022. arXiv: 2207.05670 [nucl-th].

[141] A. Kurkela, A. Mazeliauskas, J.-F. Paquet, S. Schlichting, and D. Teaney, "Matching the Nonequilibrium Initial Stage of Heavy Ion Collisions to Hydrodynamics with QCD Kinetic Theory," *Phys. Rev. Lett.*, vol. 122, no. 12, p. 122 302, 2019. DOI: 10.1103/PhysRevLett.122.122302. arXiv: 1805.01604 [hep-ph].

[142] P. B. Arnold, G. D. Moore, and L. G. Yaffe, "Effective kinetic theory for high temperature gauge theories," *JHEP*, vol. 01, p. 030, 2003. DOI: 10.1088/1126-6708/2003/01/030. arXiv: hep-ph/0209353.

[143] L. Keegan, A. Kurkela, A. Mazeliauskas, and D. Teaney, "Initial conditions for hydrodynamics from weakly coupled pre-equilibrium evolution," *JHEP*, vol. 08, p. 171, 2016. DOI: 10.1007/JHEP08(2016)171. arXiv: 1605.04287 [hep-ph].

[144] S. Kamata, M. Martinez, P. Plaschke, S. Ochsenfeld, and S. Schlichting, "Hydrodynamization and nonequilibrium Green's functions in kinetic theory," *Phys. Rev. D*, vol. 102, no. 5, p. 056 003, 2020. DOI: 10.1103/PhysRevD.102.056003. arXiv: 2004.06751 [hep-ph].

[145] A. Kurkela, A. Mazeliauskas, J.-F. Paquet, S. Schlichting, and D. Teaney, *KøMPøST*, https://github.com/KMPST/KoMPoST, 2018.

[146] V. Ambrus, L. Bazzanini, A. Gabbana, D. Simeoni, R. Tripiccione, and S. Succi, "Fast kinetic simulator for relativistic matter," Jan. 2022. arXiv: 2201.09277 [physics.comp-ph].

[147] J.-P. Blaizot and L. Yan, "Analytical attractor for Bjorken flows," *Phys. Lett. B*, vol. 820, p. 136 478, 2021. DOI: 10.1016/j.physletb.2021.136478. arXiv: 2006.08815 [nucl-th].

[148] A. H. Mueller, "The Boltzmann equation for gluons at early times after a heavy ion collision," *Phys. Lett. B*, vol. 475, pp. 220–224, 2000. DOI: 10.1016/S0370-2693(00)00084-8. arXiv: hep-ph/9909388.

[149] J.-Y. Ollitrault, "Anisotropy as a signature of transverse collective flow," *Phys. Rev. D*, vol. 46, pp. 229–245, 1992. DOI: 10.1103/PhysRevD.46.229.

[150] S. Voloshin and Y. Zhang, "Flow study in relativistic nuclear collisions by Fourier expansion of Azimuthal particle distributions," *Z. Phys. C*, vol. 70, pp. 665–672, 1996. DOI: 10.1007/s002880050141. arXiv: hep-ph/9407282.

[151] N. Borghini, P. M. Dinh, and J.-Y. Ollitrault, "A New method for measuring azimuthal distributions in nucleus-nucleus collisions," *Phys. Rev. C*, vol. 63, p. 054 906, 2001. DOI: 10.1103/PhysRevC.63.054906. arXiv: nucl-th/0007063.

[152] H. Song and U. W. Heinz, "Causal viscous hydrodynamics in 2+1 dimensions for relativistic heavy-ion collisions," *Phys. Rev. C*, vol. 77, p. 064 901, 2008. DOI: 10.1103/PhysRevC.77.064901. arXiv: 0712.3715 [nucl-th].

[153] I. Karpenko, P. Huovinen, and M. Bleicher, "A 3+1 dimensional viscous hydrodynamic code for relativistic heavy ion collisions," *Comput. Phys. Commun.*, vol. 185, pp. 3016–3027, 2014. DOI: 10.1016/j.cpc.2014.07.010. arXiv: 1312.4160 [nucl-th].

[154] *Nist digital library of mathematical functions*, http://dlmf.nist.gov/, Release 1.1.2 of 2021-06-15, F. W. J. Olver, A. B. Olde Daalhuis, D. W. Lozier, B. I. Schneider, R. F. Boisvert, C. W. Clark, B. R. Miller, B. V. Saunders, H. S. Cohl, and M. A. McClain, eds. [Online]. Available: http://dlmf.nist.gov/.

[155] D. Teaney and L. Yan, "Triangularity and Dipole Asymmetry in Heavy Ion Collisions," *Phys. Rev. C*, vol. 83, p. 064904, 2011. DOI: 10.1103/PhysRevC.83.064904. arXiv: 1010.1876 [nucl-th].

[156] R. S. Bhalerao, M. Luzum, and J.-Y. Ollitrault, "Determining initial-state fluctuations from flow measurements in heavy-ion collisions," *Phys. Rev. C*, vol. 84, p. 034910, 2011. DOI: 10.1103/PhysRevC.84.034910. arXiv: 1104.4740 [nucl-th].

[157] T. Epelbaum and F. Gelis, "Pressure isotropization in high energy heavy ion collisions," *Phys. Rev. Lett.*, vol. 111, p. 232301, 2013. DOI: 10.1103/PhysRevLett.111.232301. arXiv: 1307.2214 [hep-ph].

[158] B. Alver and G. Roland, "Collision geometry fluctuations and triangular flow in heavy-ion collisions," *Phys. Rev. C*, vol. 81, p. 054905, 2010, [Erratum: Phys.Rev.C 82, 039903 (2010)]. DOI: 10.1103/PhysRevC.82.039903. arXiv: 1003.0194 [nucl-th].

[159] F. G. Gardim, F. Grassi, M. Luzum, and J.-Y. Ollitrault, "Mapping the hydrodynamic response to the initial geometry in heavy-ion collisions," *Phys. Rev. C*, vol. 85, p. 024908, 2012. DOI: 10.1103/PhysRevC.85.024908. arXiv: 1111.6538 [nucl-th].

[160] D. Teaney and L. Yan, "Non linearities in the harmonic spectrum of heavy ion collisions with ideal and viscous hydrodynamics," *Phys. Rev. C*, vol. 86, p. 044908, 2012. DOI: 10.1103/PhysRevC.86.044908. arXiv: 1206.1905 [nucl-th].

[161] H. Niemi, G. S. Denicol, H. Holopainen, and P. Huovinen, "Event-by-event distributions of azimuthal asymmetries in ultrarelativistic heavy-ion collisions," *Phys. Rev. C*, vol. 87, no. 5, p. 054901, 2013. DOI: 10.1103/PhysRevC.87.054901. arXiv: 1212.1008 [nucl-th].

[162] S. Plumari, G. L. Guardo, F. Scardina, and V. Greco, "Initial state fluctuations from mid-peripheral to ultra-central collisions in a event-by-event transport approach," *Phys. Rev. C*, vol. 92, no. 5, p. 054902, 2015. DOI: 10.1103/PhysRevC.92.054902. arXiv: 1507.05540 [hep-ph].

[163] J. Noronha-Hostler, L. Yan, F. G. Gardim, and J.-Y. Ollitrault, "Linear and cubic response to the initial eccentricity in heavy-ion collisions," *Phys. Rev. C*, vol. 93, no. 1, p. 014909, 2016. DOI: 10.1103/PhysRevC.93.014909. arXiv: 1511.03896 [nucl-th].

[164] H. Niemi, K. J. Eskola, and R. Paatelainen, "Event-by-event fluctuations in a perturbative QCD + saturation + hydrodynamics model: Determining QCD matter shear viscosity in ultrarelativistic heavy-ion collisions," *Phys. Rev. C*, vol. 93, no. 2, p. 024907, 2016. DOI: 10.1103/PhysRevC.93.024907. arXiv: 1505.02677 [hep-ph].

[165] H. Masui, "Anisotropic Flow @ RHIC," Univ. of Tsukuba Mar/03/2007 Heavy Ion Cafe, 2007.

[166] N. Borghini and J.-Y. Ollitrault, "Momentum spectra, anisotropic flow, and ideal fluids," *Phys. Lett. B*, vol. 642, pp. 227–231, 2006. DOI: 10.1016/j.physletb.2006.09.062. arXiv: nucl-th/0506045.

[167] J. Qian, U. W. Heinz, and J. Liu, "Mode-coupling effects in anisotropic flow in heavy-ion collisions," *Phys. Rev. C*, vol. 93, no. 6, p. 064 901, 2016. DOI: 10.1103/PhysRevC.93.064901. arXiv: 1602.02813 [nucl-th].

[168] J. Vredevoogd and S. Pratt, "Universal Flow in the First Stage of Relativistic Heavy Ion Collisions," *Phys. Rev. C*, vol. 79, p. 044 915, 2009. DOI: 10.1103/PhysRevC.79.044915. arXiv: 0810.4325 [nucl-th].

[169] G. Guennebaud, B. Jacob, *et al.*, *Eigen v3*, http://eigen.tuxfamily.org, 2010.

[170] P. Romatschke, M. Mendoza, and S. Succi, "A fully relativistic lattice Boltzmann algorithm," *Phys. Rev. C*, vol. 84, p. 034 903, 2011. DOI: 10.1103/PhysRevC.84.034903. arXiv: 1106.1093 [nucl-th].

[171] V. E. Ambruș and R. Blaga, "High-order quadrature-based lattice Boltzmann models for the flow of ultrarelativistic rarefied gases," *Phys. Rev. C*, vol. 98, no. 3, p. 035 201, 2018. DOI: 10.1103/PhysRevC.98.035201. arXiv: 1612.01287 [physics.flu-dyn].

[172] S. Succi, *The Lattice Boltzmann Equation: For Complex States of Flowing Matter*. Oxford, UK: Oxford Univ. Press, Jun. 2018, ISBN: 978-0-199-59235-7. DOI: 10.1093/oso/9780199592357.001.0001.

[173] A. Gabbana, D. Simeoni, S. Succi, and R. Tripiccione, "Relativistic Lattice Boltzmann Methods: Theory and Applications," *Phys. Rept.*, vol. 863, pp. 1–63, 2020. DOI: 10.1016/j.physrep.2020.03.004. arXiv: 1909.04502 [hep-lat].

[174] L. Bazzanini, A. Gabbana, D. Simeoni, S. Succi, and R. Tripiccione, "A Lattice Boltzmann Method for Relativistic Rarefied Flows in (2 + 1) Dimensions," Nov. 2020. DOI: 10.1016/j.jocs.2021.101320. arXiv: 2011.06856 [physics.flu-dyn].

[175] A. Kurkela, U. A. Wiedemann, and B. Wu, "Opacity dependence of elliptic flow in kinetic theory," *Eur. Phys. J. C*, vol. 79, no. 9, p. 759, 2019. DOI: 10.1140/epjc/s10052-019-7262-x. arXiv: 1805.04081 [hep-ph].

[176] P. Romatschke and M. Strickland, "Collective modes of an anisotropic quark gluon plasma," *Phys. Rev. D*, vol. 68, p. 036 004, 2003. DOI: 10.1103/PhysRevD.68.036004. arXiv: hep-ph/0304092.

[177] E. Molnár, H. Niemi, and D. H. Rischke, "Closing the equations of motion of anisotropic fluid dynamics by a judicious choice of a moment of the Boltzmann equation," *Phys. Rev. D*, vol. 94, no. 12, p. 125 003, 2016. DOI: 10.1103/PhysRevD.94.125003. arXiv: 1606.09019 [nucl-th].

[178] I. P. Mysovskikh, "Cubature formulae that are exact for trigonometric polynomials," *Dokl. Akad. Nauk SSSR*, vol. 296, p. 023 006, 2003, Sov. Math. Dokl. **36**, 229 (1988). DOI: 10.1103/PhysRevD.68.023006.

[179] L. Mieussens, "Discrete-velocity models and numerical schemes for the boltzmann-bgk equation in plane and axisymmetric geometries," *Journal of Computational Physics*, vol. 162, no. 2, pp. 429–466, 2000, ISSN: 0021-9991. DOI: https://doi.org/10.1006/jcph.2000.6548.

[180] L. R. Weih, A. Gabbana, D. Simeoni, L. Rezzolla, S. Succi, and R. Tripiccione, "Beyond moments: relativistic Lattice-Boltzmann methods for radiative transport in computational astrophysics," *Mon. Not. Roy. Astron. Soc.*, vol. 498, no. 3, pp. 3374–3394, 2020. DOI: 10.1093/mnras/staa2575. arXiv: 2007.05718 [physics.comp-ph].

[181] C.-W. Shu and S. Osher, "Efficient implementation of essentially non-oscillatory shock-capturing schemes," *J. Comput. Phys.*, vol. 77, pp. 439–471, 1988. DOI: 10.1016/0021-9991(88)90177-5.

[182] S. Gottlieb and C.-W. Shu, "Total variation diminishing Runge-Kutta schemes," *Math. Comp.*, vol. 67, pp. 73–85, 1998. DOI: 10.1090/S0025-5718-98-00913-2.

[183] G. S. Jiang and C. W. Shu, "Efficient Implementation of Weighted ENO Schemes," *J. Comput. Phys.*, vol. 126, pp. 202–228, 1996. DOI: 10.1006/jcph.1996.0130.

[184] L. Rezzolla and O. Zanotti, *Relativistic hydrodynamics*. Oxford, UK: Oxford University Press, 2013.

[185] S. Busuioc and V. E. Ambruș, "Lattice Boltzmann models based on the vielbein formalism for the simulation of flows in curvilinear geometries," *Phys. Rev. E*, vol. 99, p. 033 304, 2019. DOI: 10.1103/PhysRevE.99.033304.

[186] J. E. Bernhard, J. S. Moreland, S. A. Bass, J. Liu, and U. Heinz, "Applying Bayesian parameter estimation to relativistic heavy-ion collisions: simultaneous characterization of the initial state and quark-gluon plasma medium," *Phys. Rev. C*, vol. 94, no. 2, p. 024 907, 2016. DOI: 10.1103/PhysRevC.94.024907. arXiv: 1605.03954 [nucl-th].

[187] G. S. Denicol, S. Jeon, and C. Gale, "Transport Coefficients of Bulk Viscous Pressure in the 14-moment approximation," *Phys. Rev. C*, vol. 90, no. 2, p. 024 912, 2014. DOI: 10.1103/PhysRevC.90.024912. arXiv: 1403.0962 [nucl-th].

[188] A. Kurkela, A. Mazeliauskas, J.-F. Paquet, S. Schlichting, and D. Teaney, "Effective kinetic description of event-by-event pre-equilibrium dynamics in high-energy heavy-ion collisions," *Phys. Rev. C*, vol. 99, no. 3, p. 034 910, 2019. DOI: 10.1103/PhysRevC.99.034910. arXiv: 1805.00961 [hep-ph].

[189] N. Borghini, M. Borrell, N. Feld, H. Roch, S. Schlichting, and C. Werthmann, "Statistical analysis of initial state and final state response in heavy-ion collisions," Sep. 2022. arXiv: 2209.01176 [hep-ph].

[190] M. Martinez and M. Strickland, "Dissipative Dynamics of Highly Anisotropic Systems," *Nucl. Phys. A*, vol. 848, pp. 183–197, 2010. DOI: 10.1016/j.nuclphysa.2010.08.011. arXiv: 1007.0889 [nucl-th].

[191] W. Florkowski and R. Ryblewski, "Highly-anisotropic and strongly-dissipative hydrodynamics for early stages of relativistic heavy-ion collisions," *Phys. Rev. C*, vol. 83, p. 034 907, 2011. DOI: 10.1103/PhysRevC.83.034907. arXiv: 1007.0130 [nucl-th].

[192] W. Florkowski, R. Ryblewski, and M. Strickland, "Testing viscous and anisotropic hydrodynamics in an exactly solvable case," *Phys. Rev. C*, vol. 88, p. 024 903, 2013. DOI: 10.1103/PhysRevC.88.024903. arXiv: 1305.7234 [nucl-th].

[193] M. Martinez, R. Ryblewski, and M. Strickland, "Boost-Invariant (2+1)-dimensional Anisotropic Hydrodynamics," *Phys. Rev. C*, vol. 85, p. 064 913, 2012. DOI: 10.1103/PhysRevC.85.064913. arXiv: 1204.1473 [nucl-th].

[194] M. McNelis, D. Bazow, and U. Heinz, "Anisotropic fluid dynamical simulations of heavy-ion collisions," *Comput. Phys. Commun.*, vol. 267, p. 108 077, 2021. DOI: 10.1016/j.cpc.2021.108077. arXiv: 2101.02827 [nucl-th].

List of Figures

List of Tables